Tsunami Modelling along the East Queensland Coast

Report 5: Gold Coast

Australian Government

Queensland Government

Prepared by: Queensland Government Hydraulics Laboratory, Department of Environment and Science

The Department of Environment and Science acknowledges Aboriginal peoples and Torres Strait Islander peoples as the Traditional Owners and custodians of the land. We recognise their connection to land, sea and community, and pay our respects to Elders past and present.

The department is committed to respecting, protecting and promoting human rights, and our obligations under the Human Rights Act 2019.

Citation

Boswood PK, Mardani N, Li Y, Naderi N, and Atkinson A. 2023. Tsunami Modelling along the East Queensland Coast, Report 5: Gold Coast. Brisbane: Department of Environment and Science, Queensland Government.

September 2023

Doc Version	Change	Editor
DRAFTv01	Document version for City of Gold Coast. Not for public release.	Paul Boswood, Neda Mardani, Youkai Li, Nick Naderi and Alex Atkinson
DRAFTv02	Incorporation of comments from QFES, GA and DES.	Paul Boswood and Alex Atkinson
DRAFTv03	Comments from internal review	John Ryan and Paul Pinjuh
FINAL	Inclusion of previous comments	Paul Boswood

Acknowledgements

This project is a joint initiative of the Australian and Queensland Government through the Queensland Resilience and Risk Reduction Fund with funding from City of Gold Coast.

Tsunami scenarios were provided by Geoscience Australia. The authors wish to particularly thank Dr Gareth Davies for his advice and support. The authors also wish to thank the City of Gold Coast and Tweed Shire Council for their guidance, support and provision of data.

The project was steered by a Working Group comprising:

- Luke Connery, City of Gold Coast
- Natarsha Baker, City of Gold Coast
- Nicole Gordon, City of Gold Coast
- Heidi Turner, City of Gold Coast
- Ben King, City of Gold Coast
- Renae Philipson, City of Gold Coast
- Miranda Lyons, City of Gold Coast
- David Youssef, City of Gold Coast
- Mark Ryan, City of Gold Coast
- Jane Sexton, Queensland Fire and Emergency Services
- Matthew Chesnais, Queensland Fire and Emergency Services
- Brenton Philips, Queensland Fire and Emergency Services
- Gareth Davis, Geoscience Australia
- Hannah Power, University of Newcastle
- Kendall Mollison, University of Newcastle
- Doreen Harwood, Tweed Shire Council
- Nick Kuster, NSW State Emergency Services

The support and guidance of the Working Group is greatly appreciated.

Executive summary

The 2004 Indian Ocean tsunami that devastated Indonesia, Thailand and Sri Lanka, brought about a heightened interest and focus into the science and disaster management for this hazard. In 2011, the Queensland Government commenced a project, through the Natural Disaster Mitigation Programme (NDMP) to better understand potential earthquake generated tsunami hazards along the east Queensland coastline, which was informed by the national tsunami hazard assessments conducted by Geoscience Australia. The first stage undertook nearshore tsunami modelling to identify regions of increased hazard to focus on future detailed inundation modelling.

The current project has been undertaken through the Queensland Resilience and Risk Reduction Fund, with funding from the City of Gold Coast, to assess the potential for tsunami inundation within and around the Gold Coast from both earthquake and landslide generated tsunami. Landslide generated tsunami modelling was undertaken separately by the University of Newcastle and is not part of this report. This study examines potential inundation from earthquake generated tsunami. In-kind support was provided by various organisations, including the City of Gold Coast, Tweed Shire Council, Geoscience Australia, Queensland Fire and Emergency Services, and NSW State Emergency Services.

The current study was achieved through demonstrated examples of hypothetical earthquake generated tsunami events for various average recurrence intervals (ARI) from Geoscience Australia's (GA) revised probabilistic tsunami hazard assessment (PTHA18) event database. The original probabilistic tsunami hazard assessment undertaken by GA in 2008 was revised in 2018 to incorporate many advances in modelling earthquake tsunami scenarios and frequencies. Hydrodynamic modelling was undertaken using DHI's Mike21 flexible mesh software for events originating from 7 PTHA18 earthquake source-zones, including those prominent in the PTHA18 hazard deaggregation and other nearby south-west Pacific source-zones (even if less prominent). Although 7 source zones were considered, the contribution of some source zones reduces with increasing ARI. The ARIs are defined based on the PTHA18 wave height exceedance-rates in deep water offshore of the Gold Coast. The 4 ARI values chosen, based on international literature research in consultation with GA and the Working Group as representative of possible credible and extreme (worst-case) conditions, were 100, 500, 2,000, and 10,000 years. This is a variation from previous Queensland studies, which used 750, 3,000 and 10,000 years based on previous studies by Geosciences Australia. The 100-yr ARI is consistent with United States studies, whereas the 500-yr ARI is consistent with both United States and New Zealand studies. The 10,000-yr ARI has been adopted as a worst-case scenario by various Australian studies. Although not directly relating to tsunami, the guidelines for the design of maritime structures for wind waves suggest 2,000 years for residential developments with high risk to people. This variation is considered an improvement to previous studies where arbitrary ARI were selected. Two events from each subduction zone for each ARI were modelled at Mean Sea Level (MSL) to examine the influence of the stage of the tide. All scenarios were also modelled at the Highest Astronomical Tide (HAT) to represent a worst-case and to acknowledge that tsunami events occur over several hours, at which point a high tide could occur. The selection of MSL and HAT is consistent with previous studies. Including sea level rise, a total of 90 runs were modelled.

The study area was defined by Logan River in the north to Dreamtime Beach in the south incorporating the City of Gold Coast and the north region of Tweed Shire Council. The model was calibrated against predicted tides and validated against the 2007 Solomon Islands tsunami event captured by the then Queensland Environmental Protection Agency's (EPA) Storm Tide Monitoring network.

The modelling provides insight into tsunami propagation characteristics within the study area, which can be summarised as follows:

1. Arrival Times

   Arrival times are governed by the distance between the Gold Coast and the subduction zone from which they are generated. Those from the Outer-rise New Hebrides and Puysegur have the shortest arrival time of just over three and a half hours, while events from South America arrive much later at over 18 hours. Once the leading wave reaches the coast, the additional time it takes to reach upstream locations within the waterways is consistently between 30 minutes and 2 hours.

2. Maximum Water levels

   The maximum water levels (above the still water level) range from 0.5 m (100-year ARI) to 7 m (10,000-year ARI) at 5 m depth (at mean sea level) along the coast. In the waterways, the upstream maximum water levels range between 0.1 and 1 metre. The highest levels attributable to the South America events. There is a definite trend of decreasing attenuation with longer wave periods for upstream locations within the waterways.

3. Maximum Currents

   The maximum currents are generally greater in the entrances to waterways reaching up to 12 metres per second. Currents are still strong on the ebb shoals to the waterway entrances. For the 10,000-year ARI, there

are also very strong currents as the tsunami inundates the coast (up to 12 m/s). To put this in perspective, a person would find it difficult to remain stable in currents of 1.5 m/s in 0.5 m depth. The marine hazard is greatest for waterway entrances and along the coast.

4. Inundation

   In general, the inundation hazard is greatest for the coastal sites when considering average recurrence intervals of 2,000 years and above, with substantial inundation along the coast for the 10,000-year ARI. The inundation for the 100- and 500-year ARI is mostly contained to the beaches. In the waterways there is inundation at Highest Astronomical Tide (HAT), commencing with the 100-year ARI and increasing to the 2,000-year ARI. This is a result of less wave attenuation occurring for the South America scenarios due to their longer wave periods. Note that South America scenarios were not considered at the 10,000-year ARI because PTHA18 suggests they are very unlikely (compared to other source zones) to produce correspondingly large waves offshore of the Gold Coast. For populated areas within the Waterways, the inundation is most significant for Paradise Point to Labrador, with substantial inundation behind Palm Beach between Tallebudgera and Currumbin Creeks for the 2,000-year ARI. It is noted that Paradise Point to Labrador is in the Broadwater where the modelled maximum water levels are the greatest for the waterways.

The South America events produced the greatest overall inundation for the 100-yr to 500-yr ARI and the greatest inundation of waterways for all average recurrence intervals. These events are unique in that they are very long-period waves (wave period in the order of 90 min), and their amplitudes appear to increase with subsequent waves for the Gold Coast region. This pattern is similar across all ARI modelled. It is plausible that the 90-min period of the South America events are experiencing some shelf resonance that explains the growth in amplitude for subsequent waves, which is not apparent from the offshore time series or further south of the Gold Coast, which has a markedly narrower continental shelf width. Notably, some of the most significant events were generated on the South American subduction zone in 1868, 1877, and 1960.

The digital elevation model (DEM) is a fixed bare earth model in that only ground points have been included, thereby removing all structures and vegetation. The influence of these features on inland inundation is introduced implicitly by the introduction of roughness factors. The DEM is also assumed to be static and non-erodible. Should a tsunami cause significant erosion of the dune system or entrance shoals to waterways, then the extent of inundation may differ to these model results. The hazard considered relates to potential inundation and broad-scale currents. Secondary impacts, which may be associated with the tsunami, such as coastal erosion, are not addressed in this study.

The use of a static water level to represent tide levels may not be suitable for low-lying areas upstream of waterways where tidal attenuation may occur. The underlying DEM may also not be of sufficient resolution to capture the height of riverbanks. This is particularly so with the 5 m DEM for Tweed Shire Council. Raising the water level to the adopted HAT level shows widespread inundation in the upper reaches of the Tweed River. Although the model was developed to capture the ridges of riverbanks, the resolution may not fully capture the height of the riverbank. The inundation in these areas will be conservative and should be considered with caution when making any decisions. Further modelling of the Tweed River would be required with more representative HAT levels to assess the impact in the upstream reaches of this river.

The events were selected using the ‘logic-tree-mean’ tsunami maxima exceedance-rate curves from the PTHA18. The actual frequency of large tsunamis is uncertain, in large part because of uncertainties in the frequency of large earthquakes. PTHA18 represents this using a weighted set of alternative earthquake-frequency models, and the ‘logic-tree-mean’ curve used herein is the average of these. However, because of the uncertainties, it is possible that even larger tsunamis could occur. There are also other uncertainties associated with the modelling, including source zone assumptions, the DEM, spatial resolution of the model, and limited validation scenarios with no measured inundation levels. Disaster managers may wish to consider appropriate factors of safety in any decisions based on the information provided through this study.

Overall, the study provides planners and disaster managers with a better understanding of the potential tsunami hazard within the Gold Coast and northern Tweed Shire.

Contents

List of Tables

List of Figures

1 Introduction

Following the 2004 Indian Ocean tsunami that devastated Indonesia, Thailand and Sri Lanka, the Australian Government, through Geoscience Australia (GA), the Bureau of Meteorology (BoM) and Emergency Management Australia (EMA), developed the Australian Tsunami Warning System (ATWS) to provide independent advice of potential tsunami events through the Joint Australian Tsunami Warning Centre (JATWC).

To support the end-to-end warning system, GA undertook a probabilistic assessment of tsunami hazard (PTHA) along the Australian coastline in terms of tsunami amplitude (water level height above MSL) at the 100 m depth contour (Burbidge et al., 2008a and 2008b). The study was funded by EMA as part of the community awareness and capacity building component of the ATWS. The study was intended to assist the relevant state government departments in assessing the tsunami risk along the coast and prioritising regions that require further detailed assessment. However, the study was limited in that for Queensland, the 100 m depth contour is offshore of the continental shelf and the Great Barrier Reef (GBR). Therefore, the influence of these significant features on tsunami propagation was uncertain.

To better understand the impact of the complex bathymetric features across the Australian continental shelf on tsunami propagation, GA undertook a national nearshore modelling study to examine the relative amplification of tsunami at 20 m depth compared to the 100 m depth contour for select locations (Fountain et al., 2009b). However, that study did not include some locations along the Queensland Coast.

In 2012, the then Department of Science, Information Technology, Innovation and the Arts (DSITIA) was awarded a Natural Disaster Mitigation Program (NDMP) grant to further assess the tsunami hazard along the Queensland coast. The project was undertaken in two stages. Stage 1 undertook nearshore tsunami modelling to supplement the work undertaken by GA (Boswood, 2013a and 2013c). The study utilised hydrodynamic modelling software developed by the Danish Hydraulic Institute (DHI) together with the latest detailed digital elevation model (DEM) to examine the nearshore amplification to 10 m depth along the east Queensland coast from Cooktown to the NSW border. Stage 1 identified that south-east Queensland (SEQ) from Fraser Island to the NSW border was at higher risk of larger tsunami propagation than the rest of the east Queensland coast. The report identified the following regions of higher nearshore tsunami hazard in decreasing order of magnitude:

- Gold Coast (completed by GA (Fountain et al., 2009a))
- Ocean side of Bribie, Moreton, and Stradbroke Islands
- Sunshine Coast (completed by DSITIA (Boswood, 2013b))
- Fraser Island
- Bundaberg
- Flying Fish Point
- Capricorn Coast
- Agnes Waters
- Hervey Bay.

The report also concluded that detailed inundation modelling would be required to assess the full risk to coastal communities.

Tsunami inundation modelling for the Gold Coast had previously been undertaken by GA (Fountain et al., 2009a), by examining three scenarios: an event representing the JATWC land inundation warning wave amplitude of 0.3 m at the 100 m depth contour (1 in 200-year event); an event representing overtopping of the coastal dunes; and the largest credible event (1 in 10,000-year event) based on the first iteration of the PTHA. These scenarios were modelled at Mean Sea Level (MSL) and Highest Astronomical Tide (HAT). DES has subsequently completed tsunami inundation studies for Moreton Bay, Sunshine Coast (Boswood, 2013b) and Hervey Bay. A methodology similar to GA was used whereby three scenarios representing average recurrence intervals (ARI) of 750, 3,000 and 10,000 years were modelled at both MSL and HAT. The lowest ARI was chosen to represent an event that produces inundation beyond the beach.

In 2018, Geoscience Australia updated the PTHA based on improvements in the science (Davies and Griffin, 2018). The study updated the offshore tsunami hazard for Australia.

In 2021, the City of Gold Coast was successful in obtaining funding through the Queensland Resilience and Risk Reduction Fund (QRRRF) to undertake both landslide and far-field earthquake generated tsunami inundation modelling for the City of Gold Coast, including the northern beaches of Tweed Shire Council with oversight from the Working Group comprising representatives from City of Gold Coast, Tweed Shire Council, Geoscience Australia, Queensland Fire and Emergency Services, and NSW State Emergency Services. The land-slide tsunami modelling was undertaken by the University of Newcastle. DES undertook the far-field earthquake generated tsunami modelling. This report describes the modelling undertaken by DES and is structured as follows.

Section 2 briefly describes tsunami dynamics, with a more detailed description provided in Appendix A. Section 3 provides an historical context of observed tsunami events, followed by Sections 4 and 5, which describe the scope and locality of the study. Section 6 elaborates on the model development process, while Section 7, Appendix B, and Appendix C focus on the model calibration and validation. The scenario selection process is outlined in Section 8. The results of the model are presented in Section 9, and Section 10 discusses specific aspects of the modelling approach. Section 11 concludes the work and provides recommendations. Finally, Appendices D to F provide additional details related to the model, and Appendix G presents a detailed analysis of the potential for shelf resonance.

2 Tsunami Dynamics

To better understand tsunami hazard, this section briefly describes the processes that influence tsunamis. In basic terms, a tsunami is a series of long-period waves generated by a disturbance in the ocean water column arising from abrupt geophysical events. These disturbances are more likely from the movement of tectonic plates along faults in the form of submarine earthquakes, but could also be from submarine landslides, volcanic eruptions, or a possible meteorite strike (in the extreme). More than 80 per cent of the world's tsunamis were caused by earthquakes (IOC, 2016). The earthquake scenario is the focus of this report.

A simple analogy would be dropping a pebble in a pond. The pebble generates a deformation of the water surface. This in turn creates a wave or series of waves that radiate or spread away from the source in concentric circles of increasing circumference as they propagate away. As the circumference increases, the amplitude decreases or attenuates due to energy being transferred along the wave crest. In reality, tsunami generation is not a point source but a complex pattern of bed movements. The three main stages are: tsunami generation; propagation; and run-up/inundation.

The main source of tsunamigenic earthquakes (that is, capable of generating tsunami) that could produce tsunami hazard along the east Queensland coast come from the subduction zones along the Pacific Rim. Friction between the continental and oceanic plates opposes movement, resulting in an energy build-up that is released when the plates suddenly slip past one another, generating an earthquake. The resulting uplift of the seabed generates a vertical rise in the full water column, which propagates as a tsunami in all directions along the water's surface. The resulting tsunami propagates as a set of waves whose energy is concentrated at wavelengths corresponding to the horizontal earth movements (~100 km), with wave heights also determined by the vertical displacement (but typically <1 m far from the immediate source area), and at wave directions determined initially by fault shape and orientation, and later by the adjacent coastline bathymetry and geometry. Because each earthquake is unique, every tsunami has unique wavelengths, wave heights, and directionality (NOAA, 2018).

As the displacement occurs through the entire water column, and wave lengths are much greater than depth, the tsunami behaves as a shallow water wave even in the deep ocean. The wave period is typically in the range of 5 to 40 minutes. In general, the tsunami may experience the same processes that influence shorter period waves (e.g., wind waves and swell), not limited to attenuation, shoaling, scattering, focusing, diffraction, reflection, trapping and resonance, but at a larger scale and greater depths. These processes produce an extended wave train of many waves even though the original source was a single impulse. The latter stages of a tsunami often feature very complicated waves patterns which are difficult to model accurately. Hence, only the observations of the first few waves at a site are used for comparison with model simulations and estimation of the earthquake source parameters (Mofjeld et al., 2004), and comparisons of models and observations for late arriving waves tend to focus on summary statistics rather than seeking a detailed agreement of time-series (Davies et al., 2020). A tsunami event can therefore last for several hours, and the first wave may not necessarily be the largest.

As the tsunami approaches the coastline, it is influenced by coastal features (such as bays and headlands) and nearshore bathymetry such that the amplitude can amplify and vary along the coastline. Unlike wind waves, which steepen, break and dissipate on beaches, a tsunami's wavelength-to-wave-height ratio rarely steepens to the breaking point. As a result, the approaching tsunami can appear as a fast-moving tide or surge as it reaches the coast. The leading edge of some may decay and can appear like a fast-moving tidal bore. The flow is horizontal in pattern (more like river flow) and can be very strong and turbulent. The momentum of these waves can push water much further inland than wind waves, and the currents can be too strong for a person to remain upright.

Of course, the ability to inundate depends on several factors including tsunami height and period, stage of tide, topography, the presence and height of any barriers (such as seawalls and beach dunes), obstacles (such as buildings), and land coverage (for example a dense forest will impede tsunami movement more than cleared pastoral land). For small amplitude tsunamis, the stage of tide may be a critical factor. As well as inundating low-lying coastal regions, tsunamis will also propagate up rivers and waterways much faster than they inundate some coastal zones.

For coastal structures such as ports and marinas, strong currents can develop at the entrances. Within the port, circulation systems can develop as well as potential resonance that will amplify the tsunami amplitude.

Further detail about tsunami dynamics is provided in Appendix A.

3 Historic Context

The following information was provided courtesy of Geoscience Australia.

Eastern Australia has a low or moderate earthquake-tsunami hazard by global standards (AIDR, 2018; Davies and Griffin, 2020). Because it is situated in the middle of a tectonic plate, the Australian coast is not exposed to near-field tsunami impacts generated by the largest subduction zone earthquakes. Historically these near-field inundation events tend to be the most hazardous; examples include inundation from the 2011 Japan tsunami on the Sendai plain in Japan, and the 2004 Sumatra tsunami in Aceh, Indonesia.

Although near-field tsunamis tend to be the most damaging, it is well-established that large tsunamis can also be dangerous at far-field distances, thousands of kilometres from the earthquake source (AIDR, 2018; Davies, 2019). This is possible because tsunamis can be highly directional and travel long distances in the deep ocean with little energy loss. Examples of tsunami fatalities in the far-field include:

- the 2004 Sumatra–Andaman earthquake (Mw 9.2) and tsunami led to 300 deaths in Somalia
- the 1960 Chile earthquake (Mw 9.5) and tsunami led to 61 deaths in Hawaii, 140 in Japan, and 21 in the Philippines (https://www.ga.gov.au/news-events/features/how-the-worlds-largest-earthquake-made-waves-in-australia)
- the 1946 Aleutian Islands earthquake (Mw 8.6) and tsunami led to 159 deaths in Hawaii.

The key point is that large, suitably located earthquakes can generate waves that are deadly even at trans-oceanic distances. Thus, it would be good to understand the hazards associated with such events at the Gold Coast.

History shows that the east Australian coast is exposed to far-field tsunamis generated on Pacific subduction zones. The larger events that occurred during the historical period were not particularly well located to direct waves to Australia, and the impacts have been restricted to marine hazards and some minor inundation (AIDR, 2018). Some of the most significant events were generated on the South American subduction zone in 1868, 1877, and 1960:

- The 1868 tsunami was generated by an earthquake near Peru (Mw ~9) that occurred on (GMT Time) 13/08/1968 20:45. It resulted in ‘unusual tides’ in Moreton Bay on 15 August. Newspaper reports evidence a significant marine hazard and minor inundation hazard in eastern Australia (with inundation being most prominent in the Tasmanian reports).
- The 1877 tsunami resulted from an earthquake in Northern Chile, and one report suggests it generated a maximum peak-to-trough oscillation of 42 inches at Fort Denison in Sydney (Josephson, 1878). This is larger than the waves reported for either the 1868 or 1960 events.
    - However, this large value (42 inches) should be treated with caution as it is not captured by the Fort Denison tide gauge record (also presented in Josephson, 1878). While it could be erroneous, it may alternatively reflect problems with the gauge; Josephson (1878: p103) states that ‘the gauge could not record the full force of the wave’ and mentions the possibility of seaweed interference.
- The 1960 Chile tsunami was widely observed in south-east Australia. Rynn (1994) states that unusually high tides were observed at Coolangatta and Tweed Heads. Lynam (2020) cites Rynn (1994) as stating that near Brisbane:
    - ‘Boats moved from moorings in Cabbage Tree Creek, Shorncliffe. A 24-inch rise in sea level measured at the Pile Light gauge showing 16 rises over a 12-hour period’.
    - Within a few days of the 1960 tsunami arriving, there are newspaper reports of severe erosion on the Gold Coast, possibly due to elevated water levels enhancing the erosive capacity of ocean swell waves.

There is also some evidence of a large 15th century tsunami occurring on the Kermadec-Tonga trench (Goff et al., 2022). The latter study identifies a large number of paleotsunami deposits in the south-west Pacific as consistent with this event. One such deposit is in Batemans Bay, eastern Australia. Goff et al. (2022) modelled the tsunami as generated by a magnitude 9.4 earthquake. Such a large event would be expected to produce significant tsunami waves in much of eastern Australia, including the Gold Coast.

In addition to the above provided by GA, there have also been other earthquake generated tsunami events affecting the Gold Coast that were captured by DES and MSQ tide gauges. A summary is provided in Table 1. The maximum water level reached for these events (excluding tides and meteorological effects) are below 0.2 metres.

Table 1 – Select tsunami events recorded by DES and MSQ tide gauges.

Event	Magnitude (Mw)	Date of record	Location	Maximum water level (m)
2004 Indian Ocean tsunami	9.1	27/12/2004	Gold Coast Seaway	0.1
2007 Solomon Islands tsunami	8.1	02/04/2007	Gold Coast Seaway	0.07
2010 Chile tsunami	8.8	28/02/2010	Gold Coast Seaway	0.13
2011 Japan tsunami	9.0	12/03/2011	Mooloolaba	0.13
South-east of Loyalty Island	7.6	11/02/2021	Gold Coast Seaway	0.1
South-east of Loyalty Island	7.6	11/02/2021	Tweed sand bypass jetty	0.16
Tonga Ridge	8.1	05/03/2021	Tweed sand bypass jetty	0.04

Apart from the above, there have also been other tsunami events not driven by earthquakes that have impacted the Gold Coast in recent times. In December 2016 a meteorological tsunami (meteotsunami) generated by a fast-moving severe thunderstorm generated a maximum wave height (crest to trough) of 0.3 metres. Meteotsunami have characteristics similar to earthquake generated tsunami; however, the driving force behind them is air pressure disturbances associated with fast moving weather systems, such as the series of sudden falls followed by a consequent rise in atmospheric pressure during the passage of a low-pressure trough across the south-east coast for the December 2016 event (DSITI, 2017).

Hunga Tonga–Hunga Ha‘apai is a submarine volcano near Tonga on the Kermadec-Tonga subduction zone. In January 2022 a massive eruption and resulting pressure wave generated a tsunami with a maximum water level of 0.5 m at the Gold Coast sand bypass jetty, 0.4 m at the Tweed sand bypass jetty, and 0.3 m at the Gold Coast Seaway.

This study only considers tsunami generated on the subduction zones from earthquakes.

4 Scope

The overall aim of this work is to provide local government authorities and disaster managers with a better understanding of the potential tsunami hazards (focused on inundation) along the east Queensland coastline, through demonstrated examples of hypothetical tsunami events for various average recurrence intervals (ARI), where the latter are defined based on the PTHA18 at deep-water sites offshore of the Gold Coast.

This study is one in a series of reports to assess the tsunami hazard through numerical modelling. The project, Tsunami Modelling along the East Queensland Coast, originated in 2011. Two reports were completed in 2013 (Boswood, 2013a and 2013b) and a further two regions were completed in 2018 (Boswood et al., 2018 and Boswood et al., 2019). The current study is a continuation of the initial project by examining tsunami inundation for the City of Gold Coast, including the northern beaches of Tweed Shire Council (Stage 5).

This is Report 5, which describes Stage 5 model development and hazard assessment.

The report focuses on earthquake generated tsunamis from GA's revised PTHA18, and the broad-scale inundation on the open coast and the major river systems where bathymetry data is available. The study is limited to the data available at the time of the project, as detailed in the following sections.

All reports can be accessed through the Queensland Government website (https://www.qld.gov.au/environment/coasts-waterways/beach/studies), and the Queensland Government Open Data Portal (https://data.qld.gov.au/).

5 Locality

The Stage 5 study region comprises the Gold Coast and northern Tweed Shire Local Government Areas (LGAs) (Figure 1), with a cumulative coastline of approximately 63 km in length including South Stradbroke Island to Dreamtime Beach. Gold Coast is a prime tourist destination with numerous high-rise buildings. The Gold Coast population is 625,087 (as of the 2021 Census, ABS, 2022), and the region covers approximately 137,550 hectares. In addition, the Gold Coast is one of the most popular tourist destinations, with an estimated 4.2 million visitors a year (DTIS, 2022). Tweed Shire has a population of 97,392 as of the 2021 census, with an area of 130,300 hectares.

The coastline of the Gold Coast is heavily developed, with numerous revetments and groynes to protect infrastructure. The Gold Coast is known for its sandy beaches along the open coast. Most of the coastline consists of essentially straight beaches facing east to north-east. In the southern Gold Coast, there are a few prominent headlands and the beaches curve to face more northerly at Coolangatta. In the study area, there are 2 beaches in the Tweed region: Letitia Spit and Dreamtime Beach, separated by a headland at Fingal Head. There are a few offshore reefs in the study area, including those at Palm Beach, Kirra, and Cook Island.

Within the Gold Coast, there are numerous waterways comprising rivers, creeks, and canal estates that connect to the ocean through the Broadwater and Gold Coast seaway entrance. The Primary waterways in the study area include Coomera River, Nerang River, Tallebudgera Creek, Currumbin Creek and Tweed River.

Figure 1 – Stage 5 study region.

6 Model Development

6.1 Modelling Approach

The tsunami inundation modelling was undertaken using DHI's MIKE21 flexible mesh hydrodynamic modelling software (MIKE21FM), which was successfully applied to Stages 1 to 4. The hydrodynamic model is based on the numerical solution of the two-dimensional (depth-averaged) incompressible Reynolds averaged Navier-Stokes equations (RANSE) invoking the Boussinesq approximation and assumption of hydrostatic pressure (DHI, 2017a). The model consists of the continuity, momentum, temperature, salinity and density equations, and it is closed by a turbulent closure scheme. The spatial discretisation of the primitive equations is performed using a cell-centred finite volume method. Unstructured meshes can be generated comprising both triangular and quadrilateral elements in either Cartesian or spherical coordinate systems. An explicit scheme is adopted for time integration.

Modelling software that solves the shallow water equations have been successfully applied to tsunami propagation and inundation. Horrillo et al. (2014) undertook benchmarking of several models ranging from full 3D Navier-Stokes implementations to 2D long-wave models with frequency dispersion (Boussinesq) or without dispersion (nonlinear shallow water equations – similar to the selected modelling software). The results indicated that all models tested were suitable for inundation modelling for the benchmark problems investigated. Further details on the suitability of this software can be found in Boswood (2013a).

The modelling approach involves developing a mesh of the study area that represents the topographic and bathymetric characteristics that will influence tsunami propagation, including bed roughness characteristics, and applying forcing conditions that represent the range of conditions expected within the study area. The following sections will go through the data and model development in more detail.

6.2 Supporting Data

6.2.1 Bathymetric and Topographic Data

Several bathymetric and topographic datasets were sourced during the project to develop the digital elevation model (DEM) employed for mesh interpolation (refer to Section 6.3 for more detail). Table 2 details the datasets and sources.

Table 2 – Bathymetric and topographic data sources.

Source	Description	Resolution	Usage
National Geophysical Data Center (NGDC), an office of the National Oceanic and Atmospheric Administration (NOAA)	ETOPO1 Global Relief Model, https://www.ncei.noaa.gov/products/etopo-global-relief-model	1 Arcminute	Solomon Validation Model (areas outside the GA250 extent – refer below).
Geoscience Australia (GA)	Australian Bathymetry and Topography, June 2009 (GA250) (Webster, 2005), https://data.gov.au/dataset/australian-bathymetry-and-topography-grid-june-2009	250 m	Solomon Validation Model (areas outside the gbr100 extent – refer below). Gold Coast tsunami model (areas outside the gbr30 extent – refer below)
James Cook University (JCU)	High-resolution depth model for the Great Barrier Reef and Coral Sea 2017 (gbr100) (Beaman, 2010), https://www.deepreef.org/bathymetry/65-3dgbr-bathy.html	100 m	Solomon Validation Model.
GA/Dr R Beaman	High-resolution depth model for the Great Barrier Reef – 30 m (gbr30) (GA, 2017), http://pid.geoscience.gov.au/dataset/ga/115066	30 m	Gold Coast tsunami model.

Source	Description	Resolution	Usage
GA	Digital Elevation Model (DEM) of Australia derived from LiDAR 5 Metre Grid – State Mosaic QLD and NSW, https://data.gov.au/dataset/digital-elevation-model-dem-of-australia-derived-from-lidar-5-metre-grid	5 m	Gold Coast tsunami model.
GA/City of Gold Coast	Gold Coast Digital Terrain Model (DTM), 2020, https://data.gov.au/data/dataset/digital-elevation-models-dem	2 m	Gold Coast tsunami model.
GA	NSW Marine LiDAR Topo-Bathy 2018 Geotiff, https://datasets.seed.nsw.gov.au/dataset/marine-lidar-topo-bathy-2018	5 m	Gold Coast tsunami model.
City of Gold Coast	Location of Gold Coast weirs shapefile	N/A	Gold Coast tsunami model.
Tweed Shire Council	Tweed River hydrographic survey data (XYZ)	N/A	Gold Coast tsunami model.
Queensland Government	Queensland Land Use Mapping Program (QLUMP), https://www.qld.gov.au/environment/land/vegetation/mapping/qlump	N/A	Roughness Map.
Queensland Government	Queensland Digital Cadastral Database (DCDB) https://www.business.qld.gov.au/running-business/support-assistance/mapping-data-imagery/data/digital-cadastral	N/A	Roughness Map.
Queensland Government	Queensland Wetland Mapping, https://wetlandinfo.ehp.qld.gov.au/wetlands/facts-maps/wetland-background/	N/A	Roughness Map.
New South Wales Government	New South Wales vegetation Mapping https://datasets.seed.nsw.gov.au/dataset/nsw-bionet-vegetation-map-catalogue-collection36515	N/A	Roughness Map.
New South Wales Government	NSW Cadastre Web Service https://datasets.seed.nsw.gov.au	N/A	Roughness Map.
New South Wales Government	Biodiversity Wetlands NSW https://datasets.seed.nsw.gov.au/dataset/nsw-wetlands047c7	N/A	Roughness Map.

6.2.2 Tide Data

For calibration purposes, tidal predictions at the monitoring sites were provided by DES.

The Highest Astronomical Tide (HAT) levels used to determine the tsunami modelling scenario static water levels were obtained from Maritime Safety Queensland (MSQ, 2022) and DES. The obtained tidal levels are reproduced below in Table 3 and Table 4 for the ocean side and within the waterways of the study area, respectively.

Table 3 – Highest Astronomical Tide (HAT) levels (ocean sites)

Site	MSL (m LAT)	HAT (m LAT)	HAT (m MSL)	Source
Gold Coast sand pumping jetty	0.78	2.11	1.13	DES
Tweed sand bypass jetty	1.00	1.91	1.15	DES
Kingscliff	0.76	2.24	1.22	MSQ
Snapper Rocks	1.02	2.16	1.23	MSQ
AVERAGE:	**0.89**	**2.07**	**1.18**	

Table 4 – Highest Astronomical Tide (HAT) levels within Waterways.

Site	MSL (m LAT)	HAT (m LAT)	HAT (m MSL)	Source
Couran Cove	0.96	2.02	1.06	DES
Sovereign Island North	0.77	1.81	1.04	DES
Wavebreak Island Labrador Channel	0.87	2.01	1.14	DES
Wavebreak Island North Channel	0.87	2.01	1.14	DES
Gold Coast Seaway	0.80	1.97	1.17	DES
Roes Kamp	0.81	1.84	1.03	DES
Coombabah Creek	0.80	1.64	0.84	DES
Coombabah Lake North	0.15	0.89	0.74	DES
Coombabah Lake South	0.20	0.89	0.69	DES
Jumpinpin	1.06	2.13	1.07	DES
Isle of Capri	0.72	1.66	0.94	MSQ
Gold Coast Bridge	0.88	2.04	1.16	MSQ
Grand Hotel Jetty	0.85	1.93	1.08	MSQ
Nerang Township	0.63	1.53	0.90	MSQ
Paradise Point	0.69	1.71	1.02	MSQ
Runaway Bay	0.67	1.69	1.02	MSQ
Coomera River (Saltwater Creek)	0.72	1.69	0.97	MSQ
Sanctuary Cove	0.72	1.69	0.97	MSQ
The Bedroom	0.81	1.87	1.06	MSQ

Site	MSL (m LAT)	HAT (m LAT)	HAT (m MSL)	Source
AVERAGE:	**0.74**	**1.74**	**1.00**	

6.2.3 Probabilistic Tsunami Hazard Assessment Database

Geoscience Australia (GA) provides a national offshore Probabilistic Tsunami Hazard Assessment (PTHA) for major earthquake source zones, with the first iteration being released in 2008 (Burbidge et al., 2008a) and a major update being released in 2018 (Davies and Griffin, 2018). The purpose of the offshore PTHA is to:

- Estimate the chance that earthquake-generated tsunamis of any size will reach waters offshore of Australia.
- Help to identify sites requiring more detailed tsunami inundation hazard assessment.
- Provide a nationally consistent database of earthquake-tsunami scenarios and return periods that can be used for detailed hazard studies (in conjunction with site-specific inundation models).

The original assessment provided deep water return period curves for maximum tsunami amplitude along the 100 m depth contour and relative tsunami hazard rankings for locations around Australia. Tsunami propagation modelling was undertaken using a finite difference model based on the linear shallow water equations. Over 70,000 tsunamis were modelled, and the time series were recorded at points along the 100 m depth contour. GA developed the Tsunami Data Access Tool (TsuDAT) so that state governments could access this database to assess the potential hazard along their coastline and to undertake inundation modelling (GA, 2010).

In 2018, GA revised the PTHA (PTHA18). Compared to the previous study, it incorporated many advances in modelling earthquake tsunami scenarios and frequencies. It also included extensive validation using high quality deep ocean tsunami observations (the latter was unavailable for the 2008 PTHA). Specifically, the update utilised:

- Updated representations of subduction zone geometries via Slab1.0 (Hayes et al., 2012) and Slab2.0 (Hayes et al., 2018). Slab2.0 was used for sources that were previously not covered or had changed substantially since Slab1.0.
- Subduction zones discretised at a resolution of 50 x 50 km^2 (previously 100 x 50 km^2).
- Earthquake scenario models that represent the natural variability of earthquake slip with ~1,000,000 scenarios (previously uniform-slip with 70,000 scenarios).
- Tests of the synthetic tsunamis with data for 18 historic tsunamis (Davies, 2019) showed good agreement between the statistical properties of modelled and observed tsunamis (no such testing was possible previously).
- New methods to model earthquake frequencies and characterise uncertainties in these frequencies (Davies and Griffin, 2020). The new models often predict higher earthquake frequencies than the 2008 study and appear to agree better with observed global earthquake frequencies (Davies and Griffin, 2018: p93).

The revision also provides some flexibility with output locations, which are available along the RL −20 m, RL −100 m and RL −1000 m contour lines, as well as an offshore grid of points. The format of the return period curves has also been updated to account for uncertainty by including the mean, median and percentile confidence intervals. This study selected events based on the mean exceedance rate curve (see Section 8 for more detail).

6.3 Digital Elevation Model (DEM)

A tsunami is a long wave that affects the whole water column, even in relatively deep water. As such, the propagation of the tsunami will be sensitive to the underlying bathymetric data used in the model. Considerable effort was therefore directed towards producing a DEM that best represented the overland, nearshore and deep-water bathymetry within the model domain based on the most complete set of available data.

The Stage 5 model DEM was developed from a range of sources, including (see Table 2):

- bathymetry and topography from the gbr30
- topography from the 5 m State Mosaic Qld and NSW DEM
- Digital Terrain Model of the Gold Coast LGA
- Tweed River bathymetric data from Tweed Shire Council.

The gbr30 is a comprehensive compilation of available bathymetric and topographic data collected from 1967 to 2017 covering the GBR and Coral Sea extending along the entire Queensland east coast. The dataset is provided in raster format with a spatial resolution of 0.0003 decimal degrees (approximately 30 metres). It is noted that although the gbr30 is of relatively high resolution, the underlying bathymetry data within the nearshore can be sparse. The intertidal zone can be dynamic, particularly on the beaches exposed to the open ocean.

The Digital Terrain Model (DTM) of the Gold Coast LGA is the primary data source and comprises topographic and bathymetric data from an airborne Light Detection and Ranging (LiDAR) survey in 2018 and other hydrographic surveys completed over numerous years. The DTM is provided at a two-metre horizontal resolution.

Hydrographic survey data of the Tweed River was provided by Tweed Shire Council and incorporated into the five-metre spatial resolution of the Topographic LiDAR.

The developed overland DEM is a bare earth model in that only ground points have been included, thereby removing all structures and vegetation. The influence of these features on overland inundation is implemented through roughness factors. The DEM is also assumed to be static and non-erodible. Should a tsunami cause significant damage to soft/natural defences (such as dune systems), this could significantly impact the inundation extent provided in this report.

All model validation and scenario modelling were undertaken with the final DEM, which is a layered compilation of all quality assured DEMs to maintain available spatial resolution.

6.4 Model Domain and Mesh Development

The entire model domain for Stage 5 is shown in Figure 2. Multiple test runs using a 10,000-year ARI event with sea level rise (refer to Section 8) were undertaken to optimise the inland extent of the model and mesh resolution offshore to maintain feasible computation times whilst reducing numerical dispersion (Luger and Harris, 2010) and adequately representing key geomorphological features within the critical region of the model domain.

The offshore boundary was set to correspond with the output locations of GA's PTHA event database. For this study, the offshore boundary was offshore of the continental slope to reduce potential boundary effects. The land boundary allows for flooding and drying associated with inundation. The extension of the model domain to the north and south of the study area allows tsunami propagation into the study region and mitigates numerical boundary effects.

MLITT (2012) suggests that grid sizes should be selected such that at least 20 grid points represent a wavelength. For wave periods in the range of 5 to 10 minutes, this would suggest grid sizes of 1.5 to 3.0 km at 1000 m depth, and 150 to 300 m at 10 m depth. Generally, finite volume models refer to mesh area rather than mesh dimension. Mesh size was reduced inshore in the study area to ensure changes in maximum water level were minimised. A balance is required to ensure the processes that influence tsunami inundation are replicated whilst maintaining reasonable computation times based on the number of elements and the time step for model stability governed by the Courant-Friedrich-Lévy (CFL) number (DHI, 2017b).

The final mesh comprises 3,842,852 triangular mesh elements. The maximum offshore resolution is 4,000,000 m^2 (an equivalent spatial resolution (side of triangle or *dx*) of about 2,800 m based on a right-angle triangle of equal sides), reducing to 4,000 m^2 close to the coast ($dx \approx 90$ m). A resolution of 20,000 m^2 ($dx \approx 200$ m) was adopted for the southern region of Moreton Bay to replicate tsunami propagation in the northern extent of the study area. A finer mesh was chosen in the waterways, reducing to 100 m^2 ($dx \approx 14$ m) in the narrow canals.

Meshes for developed inland areas are typically 300 m^2 ($dx \approx 25$ m). This overland mesh size was considered adequate for emergency management purposes as it approximately represents a large residential lot but is not too fine to cause unreasonable simulation times. This mesh size will provide general inundation extents but will not provide detailed flow characteristics around buildings or along residential streets. Sensitivity testing on overland mesh size indicated that coarser meshes would be more conservative. In undeveloped inland areas, a coarser resolution of 1,250 m^2 ($dx \approx 50$ m) was adopted. Care was taken to capture potential barriers to tsunami inundation, such as coastal ridges, dunes, and the crest of revetments.

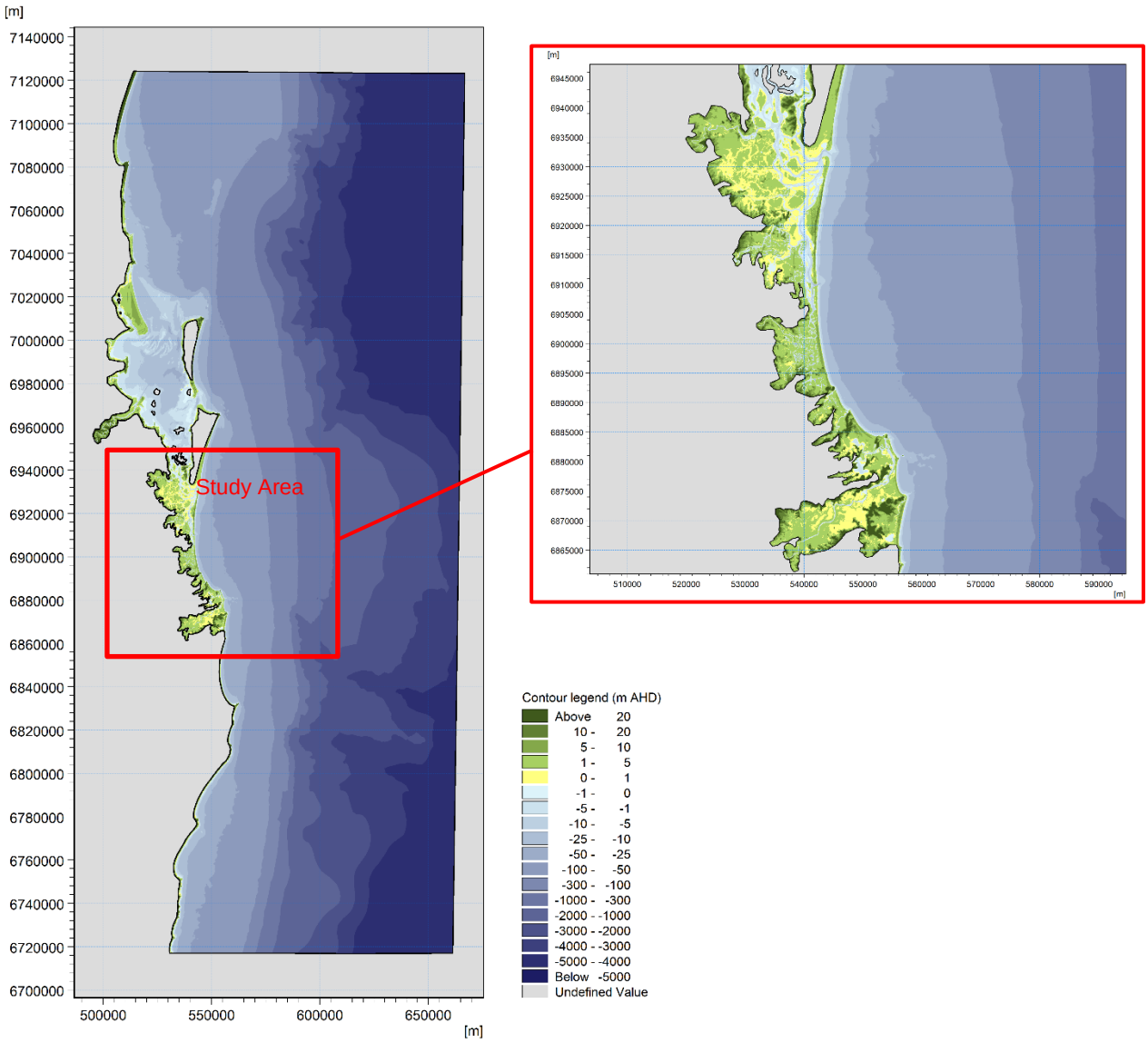

Figure 2 – Stage 5 model domain. Inset shows the study area.

7 Model Calibration, Validation and Sensitivity

7.1 Approach

The standard approach to calibrating 2D hydrodynamic models involves adjusting model parameters such as bed roughness, horizontal eddy viscosity, and bathymetry to match measured water level and/or velocity data collected within the study area. This may involve a range of conditions expected to influence the local hydrodynamics. Once calibrated, the model is then validated against other measured events.

As explained in Boswood (2013a), the availability of measured tsunami events along the Queensland coast is scarce, and inundation mapping from historical events is non-existent. As water level data associated with tides are more readily available, the 2013 study (Stage 1) calibrated the regional models against tidal predictions for 83 sites over a spring tide period from January to February 2011. The calibrated models were then validated for a specific tsunami event originating from the Solomon Islands in 2007 that was measured by the DES storm tide network (EPA, 2007). GA provided boundary conditions consisting of water level time series.

To have further confidence in the detailed mesh developed for the current project, this process of calibration and validation was undertaken again, the detail of which is provided in Appendix B and Appendix C for calibration and validation, respectively.

Calibration was undertaken against astronomical tides for 13 prediction sites that were available within the study area: Tweed Sand Bypass Jetty, Gold Coast Sand Bypass Jetty, Gold Coast Seaway, Wavebreak Island Labrador Channel, Wavebreak Island (North Channel), Roes Kamp, Coombabah Lake North, Coombabah Creek, Sovereign Island North, Couran Cove, Jumpinpin, Russell Island West, and Mooloolaba. For the validation event, only 2 sites were available within the model domain: Gold Coast Seaway; and Mooloolaba. The only calibration parameter considered was seabed roughness. Horizontal eddy viscosity has been considered in previous studies and found not to be a primary factor (Boswood et al., 2018).

Overall, the model performed well in reproducing both the tides and 2007 Solomon Islands tsunami event in the study area with minimal adjustment required to the parameters. However, the model performed better for tides in Coombabah Lake and Russell Island West with a seabed Manning's roughness of 0.02. For the 2007 Solomon Islands event, there was no noticeable sensitivity for either parameter. However, the Solomon event was a small magnitude tsunami, in the order of 10 cm on the open coast, compared to the 10,000-year event with maximum amplitudes of up to 5 metres along the open coast. To further test the sensitivity of the model to seabed roughness, a 10,000-year ARI event provide by GA (refer to Appendix C) was investigated. The results indicated minimal sensitivity along the open coast, supporting previous findings of Cardno (2013) for the NSW coast. However, the model is more sensitive to roughness within the bay. The model was found to be more sensitive to mesh size. An initial nearshore mesh size area of 50,000 m^2 (length of approximately 300 m) was compared with the final nearshore mesh size area of 4,000 m^2 (approximate length of 90 m). The finer mesh size increased the maximum water levels by up to 27 per cent. Further reductions in mesh size produced a minimal change in maximum water levels but considerably increased computation times.

7.2 Adopted Parameters

Given the lack of validation data within the Gold Coast area and the findings of the sensitivity analysis described above, the final parameter settings were chosen on the more conservative side to produce slightly higher amplitudes but within commonly accepted values for coastal applications.

7.2.1 Seabed and Waterway Roughness

The Manning's coefficient (n) defines seabed roughness, a commonly adopted parameter for both riverine and coastal applications. Calibration suggested a constant seabed value of 0.02, which is consistent with studies undertaken for NSW (Cardno, 2013).

7.2.2 Overland Roughness

As a tsunami travels overland, it will experience obstacles and land cover that will obstruct or impede its motion. The adoption of a 'bare earth' topography requires the application of overland roughness values that represent the expected effect of the removed obstacles on inundation extent for each overland cell. Roughness coefficients are typically adjusted to match measured inundation levels. However, such data for a tsunami event is lacking for the study region.

Bricker et al. (2015) conclude that tsunami models would benefit from leveraging roughness values from open channel flow literature and cites the work of Bunya et al. (2010), which provides an extensive list of Manning's

values based on land use mapping for a storm surge modelling study. The approach applied to the current study was the development of a detailed roughness map based on land use. Further detail is provided in Appendix D.

Manning's values for overland areas were chosen following a literature review of values as discussed in Appendix D. The final list of values is reproduced in Table 5, based on the work of Bricker et al. (2015), Bunya et al. (2010), and Cardno (2013). This list has been purposely kept to a minimum to prevent undue complexity that cannot presently be verified. It is expected that this approach will produce a conservative result.

Table 5 – Table of Overland' Manning's values used within the model domain.

Land Use Category	Manning's n	Manning's M (1/n)
Coastal Waters	0.020	50.00
Roads	0.020	50.00
Wetland Barren	0.030	33.33
Wetland Shrub	0.045	22.22
Grassland	0.030	33.33
Farmland	0.040	25.00
Coastal Woody Wetland	0.070	14.28
Forest	0.070	14.28
Low Density Urban	0.050	20.00
Medium Density Urban	0.100	10.00

8 Scenarios

The scenarios and associated model time series were provided by GA and were selected using a multi-gauge-based scenario selection process (Giblin et al., 2021) with associated tutorial here[1]. This approach involves combining the PTHA18 tsunami return period information with subjective judgements to identify scenarios to model while ensuring the choice is not dominated by unusual results at a single gauge. The gauges considered in this study are located shoreward of the Gold Coast hydrodynamic model offshore boundary, with depths ranging from 650–4000 m (Figure 3). The linear hydrodynamic theory underlying PTHA18 is expected to perform well in these depths.

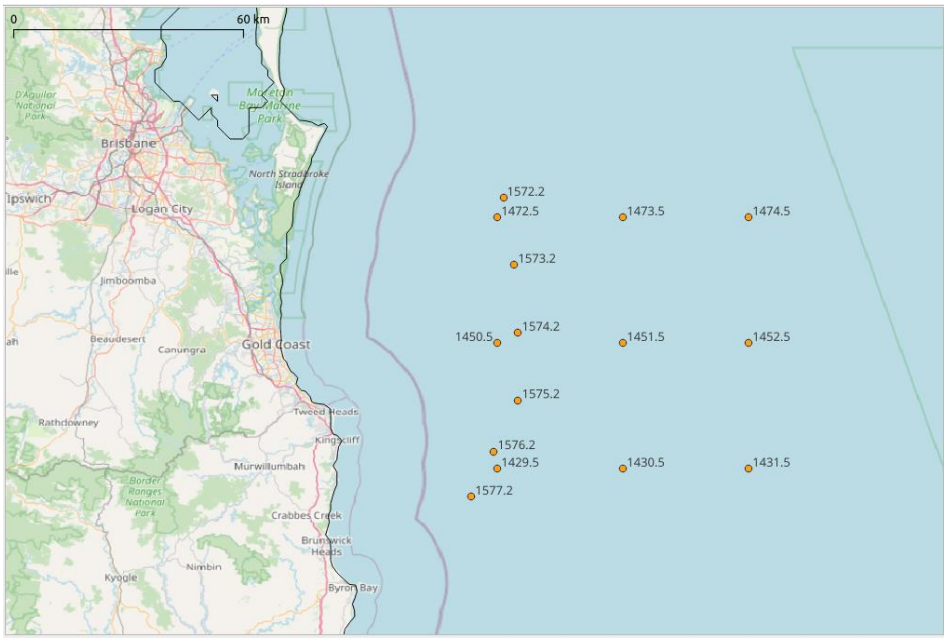

Figure 3 – PTHA gauge location consider for multi-gauge-based selection process (Source: GA).

Scenarios are selected based on their maximum positive amplitude (i.e., maximum stage) at each gauge, with reference to the corresponding maximum stage exceedance-rates (exceedance-rate = 1/ARI). An example of the exceedance rate curve for gauge 1574.2 located in 1000 m depth is provided in Figure 4. It is not expected that any scenario will exactly match the desired ARI maximum stage at all the considered offshore gauges. In the multi-gauge scenario selection process, we first reduce the choice of scenarios to those with a maximum stage within 10 per cent of the target value at 5 or more of the considered offshore gauges (excluding scenarios more than 10 per cent greater at any considered gauge). In other words, we consider scenarios close to the desired ARI at a range of offshore gauges and exclude those that greatly exceed the target at any gauge. They key benefit of the multi-gauge approach is that the scenario selection becomes less sensitive to results at any single gauge (Giblin et al., 2022).

Based on a literature review of previous hazard studies, the desired scenario ARIs were chosen to represent a range of credible and worst-case events that could affect the Gold Coast. The ARI chosen are 100, 500, 2,000, and 10,000 years. U.S. studies undertaken for insurance purposes have considered the 100- and 500-year events (González et al., 2009 and Tsunami Pilot Study Working Group, 2006). In New Zealand the yellow zone, being the inundation level that all maximum credible tsunami events including the highest impact events can reach, is defined as the 2,500-year event at an 84 per cent confidence level, erring on the side of caution in relation to uncertainty factors. Whereas the orange zone, used for official warnings of distant tsunami is defined by the 500-year event (Ministry of Civil Defence & Emergency Management, 2016). In Australia, various recurrence intervals have been adopted for tsunami inundation studies (e.g., Cardno, 2013 and Boswood et al., 2013) with an upper limit of 10,000 years. AIDR (2018) refers to the credible worst-case. For a tsunami inundation study in Western Australia (Hall et al., 2008), the plausible worst-case was chosen as the 10,000-year event. Although not directly relating to

[1] https://github.com/GeoscienceAustralia/ptha/blob/master/ptha_access/example_event_access_scripts/multi_site_scenario_selection/example_usage.md

tsunami, the guidelines for the design of maritime structures suggests recurrence intervals for design wind wave events (Standards Australia, 2005). For residential developments with high risk to people, it is suggested to use the 2,000-year event.

Scenarios were selected from a range of subduction zones based on an examination of the source-zone deaggregation information included in the standard PTHA18 outputs for the chosen gauges. Although these results vary from site to site, they suggest that the following earthquake sources are of primary significance (Figure 5):

- Kermadec-Tonga (KDT)
- New Hebrides (NH)
- South America (SA).

For the first two subduction zones, we also included outer-rise normal fault earthquakes:

- Outer-rise Kermadec-Tonga (OKDT)
- Outer-rise New Hebrides (ONH).

These outer-rise sources appeared among the top 10 sources in the PTHA18 hazard deaggregation for some of the considered sites and ARIs but were typically less significant than their corresponding thrust sources. It was decided to include them to give a fuller characterisation of the different kinds of earthquake generated tsunamis that may be generated on these nearby sources.

Although less significant according to the PTHA18 logic-tree-mean hazard model, 2 other regionally significant earthquake source-zones were selected:

- Solomons (S)
- Puysegur (P).

The above choices ensure that scenarios are included from a variety of source-zones considered relevant to eastern Australia.

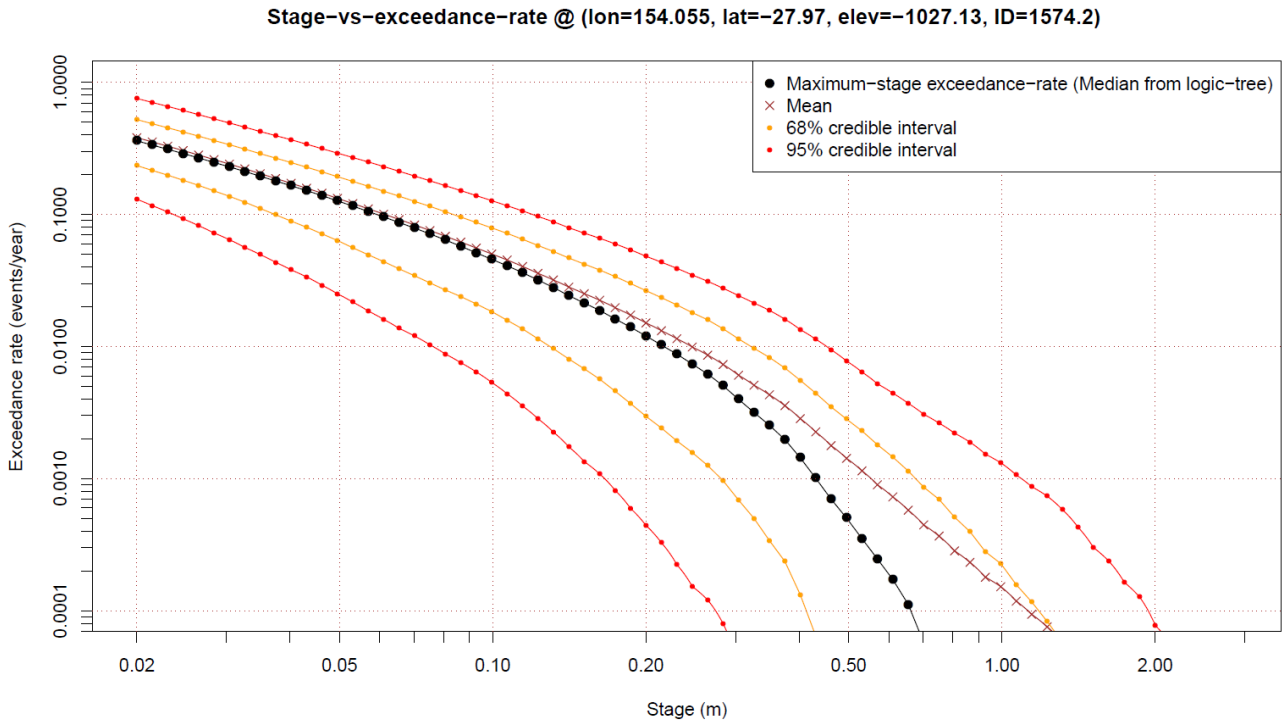

Figure 4 – Sample exceedance rate for one location offshore the Gold Coast at 1000 m depth.

Scenarios were selected for each ARI and source zone unless the source-zone had no scenarios (or was very unlikely according to the PTHA18) at a particular ARI:

- The New Hebrides, New Hebrides outer-rise and Kermadec-Tonga source-zones were included at all return periods.
- The following source-zones were included at return periods less than 10,000 years:
  - Solomon
  - South America

  - Kermadec-Tonga outer-rise
- The Puysegur source-zone was only included at the 100-year return period.

Although we include a variety of source zones for each ARI, we note that according to the PTHA18, the source-zones are not 'equal contributors' to the hazard. While results can vary from gauge to gauge, the PTHA18 generally suggests a tsunami with 500-year return period is most likely to be produced by the Kermadec-Tonga, South American, and New-Hebrides thrust source-zones. It also suggests tsunamis with rarer return periods, such as 2,500-year, are less likely to come from the distant South American source than from the nearer Kermadec-Tonga and New Hebrides thrust sources, and that the outer-rise events are generally much less likely than the thrust events.

For each combination of ARI and source-zone, 2 scenarios were selected. To do this, we first searched for all PTHA18 scenarios on the source-zone with maximum stage matching the desired return period value (within 10%) at our target gauge locations (Figure 3). A scenario will not usually meet this requirement simultaneously at all gauges but was considered if they met the requirement at five or more gauges simultaneously and without exceeding the desired maximum-stage by more than 10 per cent at any other gauge.

The final two scenarios were chosen subjectively from among this subset. Preference was given to scenarios with the following characteristics:

- Scenarios that were more likely to be possible according to the PTHA18.
  - Note that because maximum-magnitudes are uncertain on each source-zone, PTHA18 considers that sufficiently large magnitude earthquakes may or may not be possible. This uncertainty is represented probabilistically.
- Scenarios that met the maximum stage criteria at more than the minimum 5 gauges.
- Scenarios with moderate peak-slip (dependent on their magnitude, refer to Appendix A.2.1).
- Scenarios with tsunami energies comparable to known historical events (with similar magnitude).
- Scenarios with modelled tsunami maxima occurring within 12 hours of the initial tsunami arrival.

The PTHA18 considers only earthquakes as a source of tsunami hazard, contributing to approximately 80 per cent of all tsunami events (Davies et al., 2017 and Appendix A).

It is noted that although the study has adopted the logic-tree mean exceedance rate, there can be considerable spread in maximum stage between the 95 per cent creditable intervals (Figure 4). So, although some of the events modelled may seem extreme, according to the PTHA18, we cannot exclude the possibility that they can occur, and they may be more or less common than suggested by the mean exceedance rates.

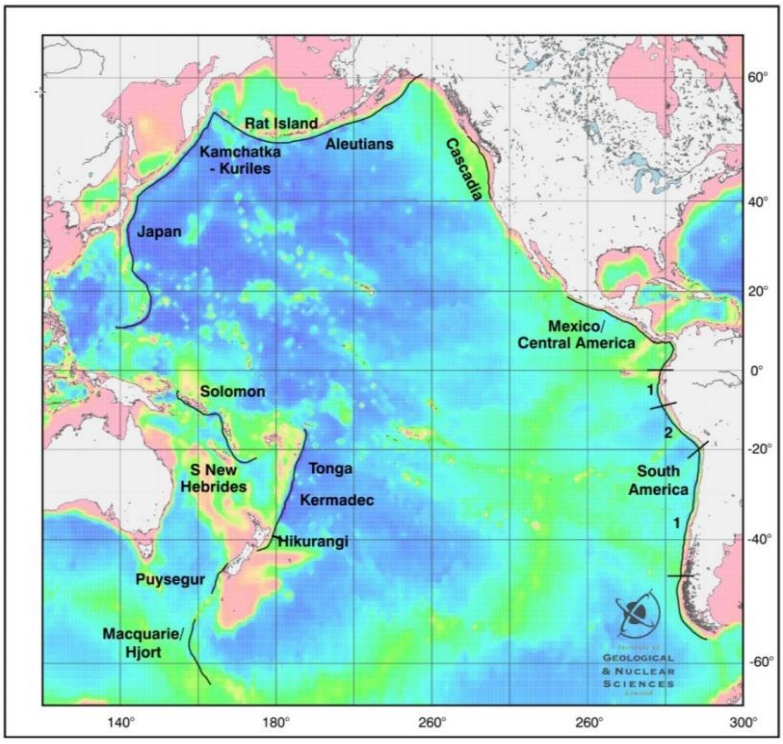

Figure 5 – Subduction zones around the Pacific Rim (Power, 2013).

The model run schedule is shown in Appendix F, listing all Stage 5 runs varying over ARI, subduction zone and still water level. Models were run with still water levels at MSL, HAT, and HAT with sea level rise (SLR). The MSL

condition is provided to demonstrate an average tide condition and is the level applied to the PTHA. Given that a tsunami event can persist over several hours, it is likely that some waves will occur on high tide. The runs are also undertaken at HAT to demonstrate variations between different tide stages. Adopting HAT will provide a conservative result and is consistent with other Australian studies (e.g., Kain et al., 2020; Cardno, 2013; and AIDR, 2018). HAT values at ocean sites and within waterways are provided in Table 3 and Table 4, respectively. The average difference between both is only 0.18 m, so it was decided to apply one HAT level at 1.1 metres. While this level is representative of the coast and downstream locations within waterways, tidal attenuation occurs within the waterways such that the static increase of 1.1 m above MSL results in the inundation of low-lying areas for upstream locations (as indicated in Figure 6 and Figure 7). The modelling has attempted to capture the height of waterway banks, but the underlying DEM and resolution of the model may not have captured all the peaks, resulting in more inundation. For example, the narrow ridge along the banks of the Tweed River is close to the adopted HAT in height. Even the 5 m horizontal resolution DEM results in inundation at the adopted HAT. The modelling will result in an overestimate of the inundation in these areas.

Following the Coastal Hazard Technical Guide (EHP, 2013), an additional water level increase of 0.8 m has been applied to account for the projected sea level rise by the year 2100, in addition to the tide. The ARI provided by the PTHA is only based on the tsunami size and does not consider tides, but impacts are expected to worsen at higher sea-levels. SLR was only considered for the 10,000-yr ARI worst-case event. For this study, 2 runs were considered (Outer-rise New Hebrides event ID 7700 and Kermadec-Tonga event ID 43313), representing the upper limit of the hazard for all scenarios for the waterways and coast. Statistical properties of each event time series at an offshore boundary point corresponding to gauge 1452.5 (depth of approximately 3,700 m) are summarised in Table 6. A spectral analysis was performed based on the Welch method with a Hann window of 17.07 hrs and 50 per cent overlap. The time series was 36 hr in length at 30-second intervals commencing from the initiation of the tsunami at the source. This means that the available data differs for each event based on the arrival time. In the table, T_p is the spectral peak period, and *T02* is the average wave period from the spectra, and the arrival time is the arrival of the first wave at the offshore boundary point.

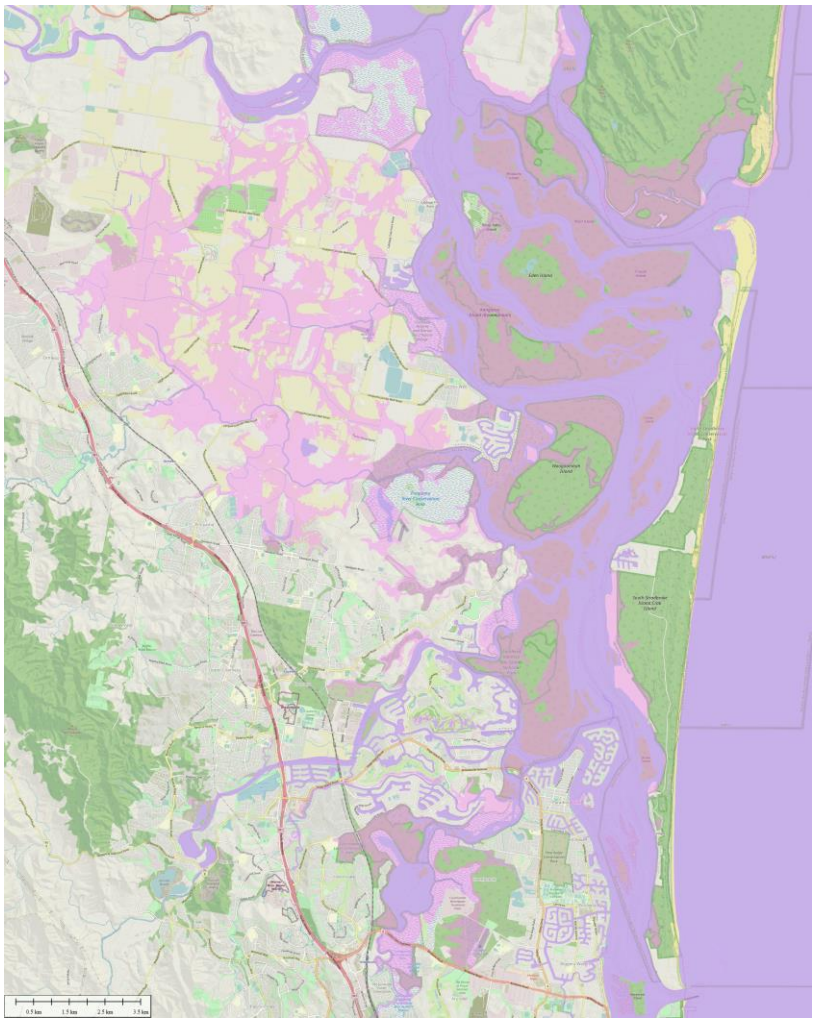

Figure 6 – HAT (1.1 m above MSL) extent for northern Gold Coast (at a 10 m resolution).

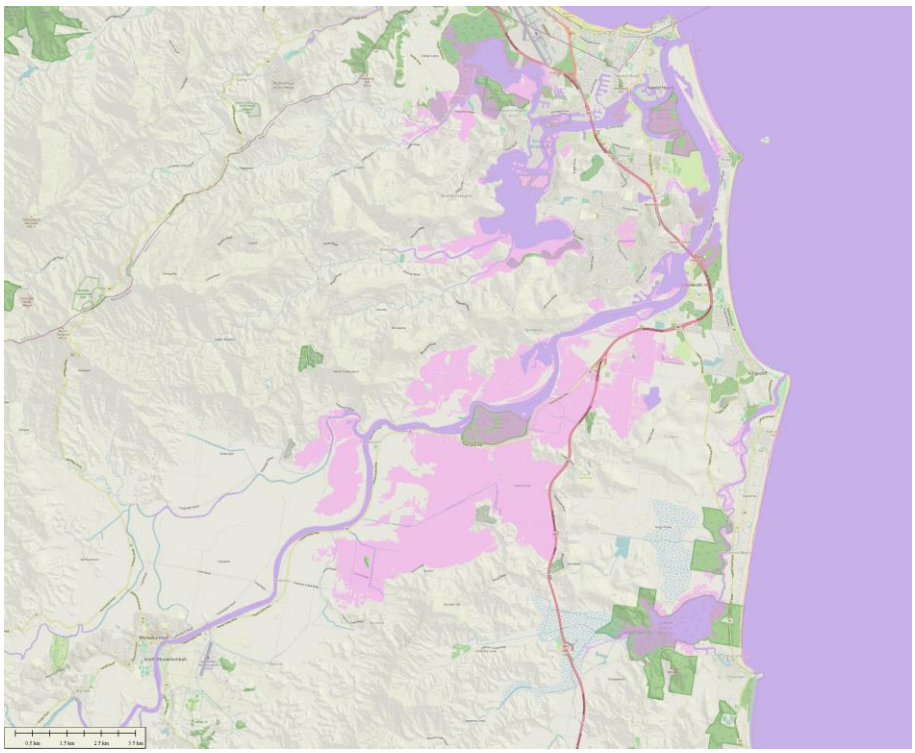

Figure 7 – HAT (1.1 m above MSL) extent for Tweed (at 10 m resolution).

Table 6 provides a snapshot of the statistical properties at one location along the offshore boundary. The properties will vary throughout the domain. To demonstrate this, Figure 8 shows the variation of the maximum water level along the offshore boundary for 10,000-year ARI events. The peak of many of these plotted lines coincides with gauges offshore of the Gold Coast where the continental slope is wider such that these gauges are located on the toe of the continental slope. However, there is some variation for different source zones. Figure 9 shows the variation of the maximum water level along the offshore boundary for 100-year ARI events. The Puysegur event (ID 3188) shows an increasing trend southward whereas the Solomon event (ID 14181) demonstrates a slight reduction southward. In total, 90 scenarios were modelled, representing a range of ARI, source zones and water levels.

Table 6 – Statistical Summary of event time series at gauge 1452.5.

PTHA Event ID	Source	ARI	Max Amplitude (m)	Earth-quake Mag. (Mw)	T_p (h:mm:ss)	T02 (h:mm:ss)	Arrival Time (h:mm)
38319	Kermadec-Tonga	100	0.12	8.7	0:20:57	0:13:14	4:13
38395	Kermadec-Tonga	100	0.16	8.9	0:17:39	0:13:42	4:11
8399	New Hebrides	100	0.16	8.1	0:15:31	0:12:48	3:11
9905	New Hebrides	100	0.16	8.4	0:23:21	0:15:10	3:08
10788	Outer-rise Kermadec-Tonga	100	0.13	8.5	0:21:00	0:05:38	4:27
11435	Outer-rise Kermadec-Tonga	100	0.14	8.6	0:21:03	0:06:13	4:28
4578	Outer-rise New Hebrides	100	0.15	8.1	0:23:14	0:06:24	3:11
6071	Outer-rise New Hebrides	100	0.15	8.4	0:28:29	0:06:21	3:02
3188	Puysegur	100	0.14	8.5	0:08:11	0:04:51	2:47

PTHA Event ID	Source	ARI	Max Amplitude (m)	Earth-quake Mag. (Mw)	T_p (h:mm:ss)	T02 (h:mm:ss)	Arrival Time (h:mm)
3269	Puysegur	100	0.13	8.5	0:32:22	0:05:48	2:47
14181	Solomon	100	0.16	8.8	0:18:57	0:13:24	3:07
14659	Solomon	100	0.16	8.9	2:27:49	0:12:29	3:12
138376	South America	100	0.16	9.1	1:43:50	0:41:09	19:57
139765	South America	100	0.17	9.2	1:45:16	0:50:50	18:01
40294	Kermadec-Tonga	500	0.25	8.9	0:20:57	0:13:17	4:09
40814	Kermadec-Tonga	500	0.24	9.0	0:22:55	0:10:28	4:12
10423	New Hebrides	500	0.31	8.5	0:28:09	0:11:37	3:07
10881	New Hebrides	500	0.30	8.6	0:28:06	0:15:26	3:07
12160	Outer-rise Kermadec-Tonga	500	0.22	8.7	0:07:32	0:05:57	4:27
12188	Outer-rise Kermadec-Tonga	500	0.22	8.7	0:09:16	0:06:02	4:27
5564	Outer-rise New Hebrides	500	0.28	8.3	0:10:03	0:05:58	3:08
6484	Outer-rise New Hebrides	500	0.27	8.5	0:15:34	0:07:25	2:52
15018	Solomon2	500	0.31	9.0	0:18:57	0:13:59	3:03
15034	Solomon2	500	0.33	9.0	1:13:39	0:11:33	3:07
143881	South America	500	0.27	9.4	1:45:53	0:49:46	17:43
143914	South America	500	0.28	9.4	1:46:30	0:37:10	17:37
41602	Kermadec-Tonga	2000	0.41	9.1	0:22:09	0:13:46	4:17
42273	Kermadec-Tonga	2000	0.39	9.2	0:22:55	0:13:48	4:14
10877	New Hebrides	2000	0.45	8.6	0:28:06	0:13:57	3:07
11290	New Hebrides	2000	0.46	8.7	0:20:53	0:14:55	3:10
12851	Outer-rise Kermadec-Tonga	2,000	0.32	8.8	0:21:02	0:05:56	4:27
12858	Outer-rise Kermadec-Tonga	2,000	0.41	8.8	0:07:28	0:05:27	4:26
6503	Outer-rise New Hebrides	2,000	0.33	8.5	0:13:26	0:06:29	2:58
6915	Outer-rise New Hebrides	2,000	0.34	8.6	0:15:28	0:07:15	2:58
15551	Solomon2	2,000	0.49	9.2	1:13:48	0:13:16	3:02

PTHA Event ID	Source	ARI	Max Amplitude (m)	Earth-quake Mag. (Mw)	T_p (h:mm:ss)	T02 (h:mm:ss)	Arrival Time (h:mm)
15725	Solomon2	2,000	0.47	9.2	1:13:39	0:12:59	3:03
147780	South America	2,000	0.46	9.6	1:46:05	0:45:58	17:32
147918	South America	2,000	0.45	9.6	1:46:28	0:46:28	17:32
43313	Kermadec-Tonga	10,000	0.62	9.4	0:20:59	0:15:21	4:07
43443	Kermadec-Tonga	10,000	0.57	9.4	0:21:00	0:13:19	4:06
11664	New Hebrides	10,000	0.67	8.8	0:28:07	0:15:45	3:02
12034	New Hebrides	10,000	0.72	8.9	0:28:09	0:15:37	3:01
7380	Outer-rise New Hebrides	10,000	0.58	8.7	0:13:26	0:06:34	2:54
7700	Outer-rise New Hebrides	10,000	0.62	8.8	0:15:36	0:07:04	2:53

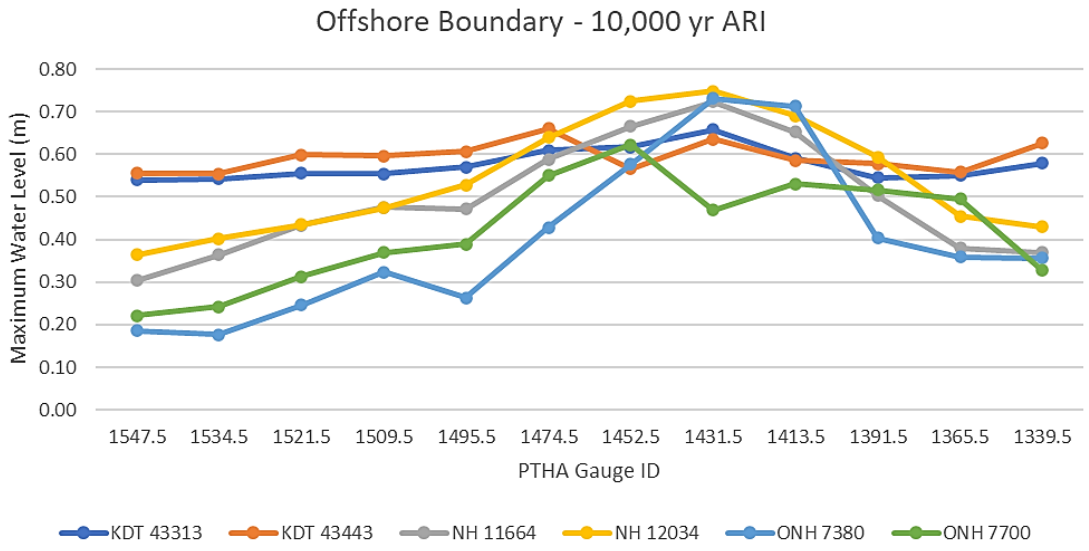

Figure 8 – Variation in maximum water level along the offshore boundary for 10,000 yr ARI events.

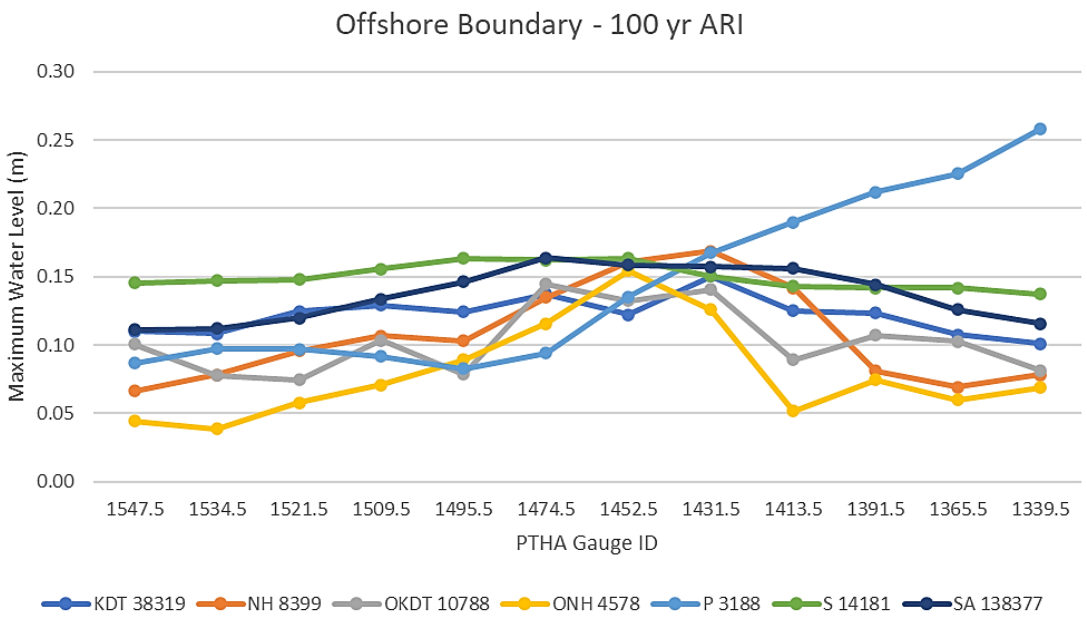

Figure 9 – Variation in maximum water level along the offshore boundary for 100 yr ARI events.

9 Results

9.1 Analysis Approach

Model outputs include spatial data of maximum water depth and maximum current speed within the study area and time series data at select locations along the coast and within the waterways. The time series were used to compute the maximum water level and arrival time for select locations. The spatial data were analysed to provide inundation extents, inundation depths, maximum water levels, and maximum currents. The maximum envelope for each of these parameters for a given ARI was then calculated by determining the maximum at every element in the study area from all events for a given ARI. The worst-case scenario was also determined based on inundation extent to calculate the flux (depth x velocity) map. For some ARI, there were two worst-cases, one for waterways and the other for the coast. The worst-case scenarios were rerun to produce a spatial depth and velocity time series (large file sizes restricted creating them for all scenarios). The flux was then calculated for each time step and the maximum for all time steps was determined. The 10,000-year ARI worst-case scenario was also used to model the SLR scenario. The worst-case scenario for each ARI is provided in Table 7.

Table 7 – Worst-case scenario for each ARI.

ARI (years)	Run No.	Source	PTHA18 Event ID	Location
100	28	South America	139765	Coast and Waterways
500	50	South America	143881	Coast and Waterways
2,000	68	Outer-rise New Hebrides	6915	Coast
2,000	74	South America	147780	Waterways
10,000	78	Kermadec-Tonga	43313	Waterways
10,000	88	Outer-rise New Hebrides	7700	Coast

Table 8 provides a summary of provided Stage 5 result formats. Refer to these appendices for further context to the following sections. The separate documents and datasets listed in Table 8 can be accessed through the Queensland Government website (https://www.qld.gov.au/environment/coasts-waterways/beach/studies) and the Queensland Government Open Data Portal (https://data.qld.gov.au/).

Table 8 – Stage 3 results summary.

Name	Description	Format
Appendix H	Spatial maximum envelope of maximum water level (amplitude) and current speed at HAT.	Separate PDF Map Booklets
Appendix I	Select study location maps of maximum inundation extent for each ARI at MSL.	Separate PDF Map Booklet
Appendix J	Select study location maps of maximum inundation extent for each ARI at HAT.	Separate PDF Map Booklet
Appendix K	Select study location maps of modelled inundation extent of SLR scenario (Kermadec-Tonga).	Separate PDF Map Booklet
GIS Database	Entire study domain GIS files of maximum envelope for each ARI.	Separate ESRI Database

9.2 General Overview

The following sections provide a summary of the results from the modelling.

9.2.1 Wave Propagation

This section provides a general description of tsunami propagation within Gold Coast based on observation of the model results. Each tsunami will be different, but there will be characteristics that will be more generic based on

coastline shape and bathymetric features. These characteristics will assist in understanding the potential hazard for Gold Coast and are summarised below. In general, tsunami propagation into the study region can be characterised by:

- The first or leading wave, in the absence of any ambient conditions, is well formed and continuous across the study region (Figure 10).
- The first wave is not always preceded by a recession or drop in water level (also referred to as leading depression N-wave or LDN). Of the model scenarios considered, those from Kermadec-Tonga, Outer-rise New Hebrides, Outer-rise Kermadec-Tonga and Puysegur subduction zone were LDN; whereas, those generated from the New Hebrides, Solomons and South America had no or minimal initial recession (leading elevation N-waves or LEN). The characteristics of tsunami generated from the Puysegur subduction zone are difficult to ascertain given that only two scenarios were considered.
- The first wave is not necessarily the largest, although for the New Hebrides and Outer-rise New Hebrides sources, the largest wave was either the first wave or within 2 hrs of the first wave. For the other source zones, the largest wave was within 2 to 14 hrs after the arrival of the first wave. Of the scenarios modelled, the offshore leading wave is typically the largest wave. However, as the tsunami reaches the coast, interactions with the coastline and the shelf produce complicated patterns between the incident and reflected waves in both space and time, such that the resulting time series can look much different to the offshore wave train.
  The timing of the largest wave will depend on these interactions. The timing of the maximum water level will also depend on the stage of the tide. Figure 11 shows an example of the offshore and nearshore tsunami time series for a New Hebrides scenario.
- In general, due to the configuration of the coastline and continental shelf, the first wave of the tsunami time series will impact northern NSW first being further eastward than the rest of the coast, regardless of the directionality of the source zone. The tsunami impacts north and south of the Gold Coast first due to the concave shape of the coastline and the shape of the continental shelf, converging near the Gold Coast Seaway entrance in less than 10 minutes.
- Subsequent waves interact with reflected waves to set up a complex pattern of frequency-dependent nodes and antinodes that influence local water level fluctuations.
- In addition to the reflected wave interactions, the presence of shelf trapped waves and coastal trapped edge waves will influence the timing and spatial distribution of the largest tsunami amplitude, as well as the duration that the tsunami event will persist.
- Tsunamis propagate up waterways and canal estates. The tsunami dissipates as it travels upstream and is influenced by the presence of weirs.
- Although not modelled, there is potential for shorter steep waves to form with the tsunami in areas where the tsunami wave steepens (refer Appendix A.4).

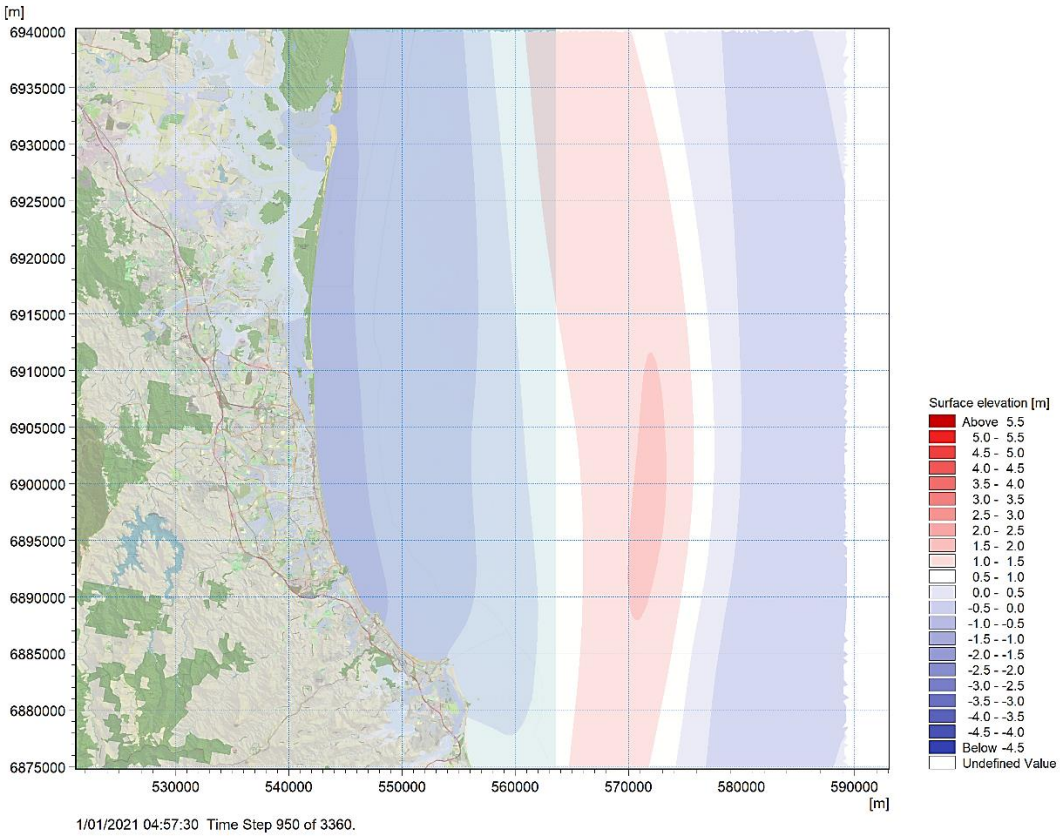

Figure 10 – Leading wave approaching the coast for run 78 (Kermadec-Tonga, 10,000 yr ARI).

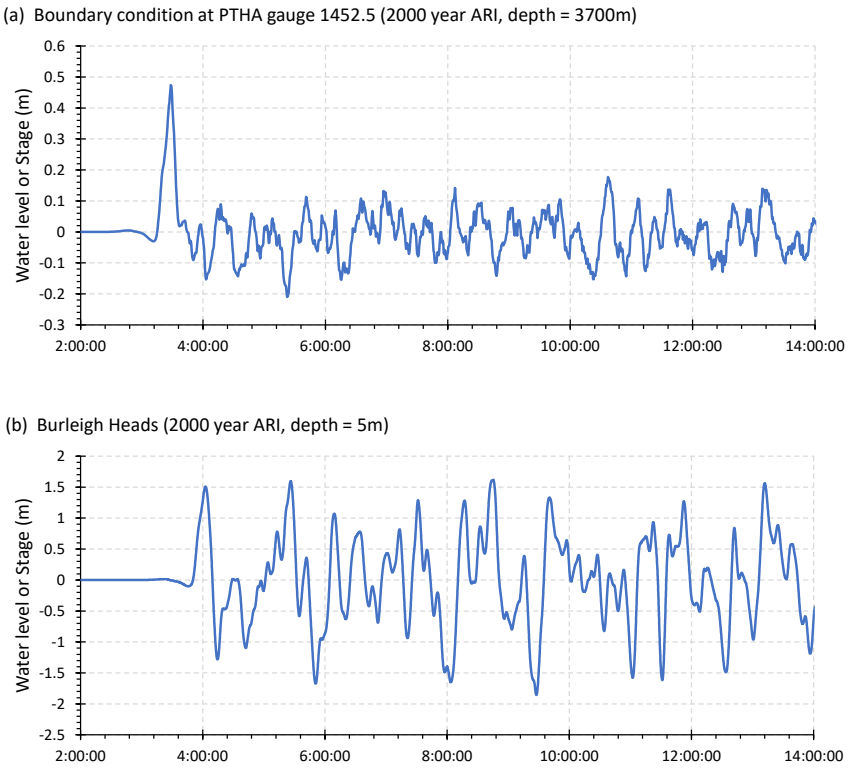

Figure 11 – Example of tsunami time series for a 2,000-year ARI event from New Hebrides at HAT (Run 58). Although the offshore gauge (plot a) shows the first wave is the largest, this is not clear in the time series at the coast (plot b) due to the various complex interactions occurring.

9.2.2 Maximum Water Levels

The following provides a summary of maximum water levels above the still water level (SWL) for each source zone. The analysis is based only on the HAT runs. The upstream levels are based on the upstream limit of the model. The maximum envelope for each ARI is provided in Appendix H.

9.2.2.1 Kermadec-Tonga

There is little variation in the maximum water levels along the coast for the 100- and 500-year ARI runs. For the 2,000- and 10,000-year ARI runs, the maximum water level is greatest to the north of the Gold Coast Seaway entrance and south of the Tweed River (south of Currumbin Creek for run 78). Energy dissipates rapidly through waterway entrances, with attenuation continuing as the wave propagates upstream.

The maximum water level along the coast occurs about 2–6 hrs after the arrival of the first wave. For the waterways, the maximum water level occurs 2–11 hrs after the arrival of the first wave at each location. Table 9 provides the range of maximum water levels for locations within the study area.

Table 9 – Range of maximum water levels (m above SWL) for select locations from Kermadec-Tonga source zone.

ARI	Coast	Broadwater (near Wavebreak Island)	Upstream Nerang/ Coomera R	Upstream Tallebudgera Ck	Upstream Currumbin Ck	Upstream Tweed R
100	0.5–1.5	1.0	0.1–0.2	0.2	0.2	<0.1
500	1.0–3.0	1.5	0.1–0.2	0.3	0.4	<0.1
2,000	2.0–3.5	2.0	0.1–0.3	0.4	0.5	0.1
10,000	3.0–5.0	4.0	0.1–0.4	1.0	1.5	0.1–0.2

9.2.2.2 New Hebrides

There is not much variation in maximum water levels along the coast for the 100- and 500-year ARI runs, except for Snapper Rocks where the maximum water levels were the lowest. For the 2,000- and 10,000-year ARI runs, the maximum water level is consistent along the coast, with lower levels near the entrances to waterways. Energy dissipates rapidly through waterway entrances, with attenuation continuing as the wave propagates upstream.

The maximum water level along the coast occurs for most sites on the first wave but can be up to 2 hrs after the arrival of the first wave. For the waterways, the maximum water level occurs 3–11 hrs after the arrival of the first wave at each location. Table 10 provides the range of maximum water levels for locations within the study area.

Table 10 – Range of maximum water levels (m above SWL) for select locations from the New Hebrides source zone.

ARI	Coast	Broadwater (near Wavebreak Island)	Upstream Nerang/ Coomera R	Upstream Tallebudgera Ck	Upstream Currumbin Ck	Upstream Tweed R
100	0.5–1.5	1.0	0.1–0.2	0.2	0.2	<0.1
500	1.0–2.5	1.0	0.1–0.2	0.3	0.4	<0.1
2,000	1.5–4.0	2.0	0.1–0.3	0.4	0.5	0.1
10,000	2.0–6.0	3.0	0.1–0.3	0.8	1.0	0.2

9.2.2.3 Outer-rise Kermadec-Tonga

For all runs, the maximum water level is greatest for South Stradbroke Island to Burleigh Heads and Letitia Spit. Energy dissipates rapidly through waterway entrances, with attenuation continuing as the wave propagates upstream.

The maximum water level along the coast occurs within 2–3 hrs after the arrival of the first wave. For the waterways, the maximum water level occurs 4–9 hrs after the arrival of the first wave at each location. Table 11 provides the range of maximum water levels for locations within the study area.

Table 11 – Range of maximum water levels (m above SWL) for select locations from the Outer-rise Kermadec-Tonga source zone.

ARI	Coast	Broadwater (near Wavebreak Island)	Upstream Nerang/ Coomera R	Upstream Tallebudgera Ck	Upstream Currumbin Ck	Upstream Tweed R
100	1.0–2.0	1.0	0.1–0.2	0.1	0.2	<0.1
500	1.5–5.0	1.5	0.1–0.2	0.2	0.2	<0.1
2,000	2.0–6.0	2.0	0.1–0.2	0.3	0.3	<0.1

9.2.2.4 Outer-rise New Hebrides

There is variability in the location of the maximum water level for each run but for higher ARI, there is a pattern of higher water levels south of the Gold Coast Seaway, with the largest maximum water level at Letitia Spit. For run 88, the maximum water level on the beaches is up to 8 m from Main Beach to Miami, with the greatest water level at Letitia Spit (9 m). Energy dissipates rapidly through waterway entrances, with attenuation continuing as the wave propagates upstream.

The maximum water level along the coast occurs for most sites on the first wave but can be up to 2 hrs after arrival of the first wave. For the waterways, the maximum water level occurs 5–10 hrs after the arrival of the first wave at each location. Table 12 provides the range of maximum water levels for locations within the study area.

Table 12 – Range of maximum water levels (m above SWL) for select locations from the Outer-rise New Hebrides source zone.

ARI	Coast	Broadwater (near Wavebreak Island)	Upstream Nerang/ Coomera R	Upstream Tallebudgera Ck	Upstream Currumbin Ck	Upstream Tweed R
100	0.5–2.5	1.0	<0.1	0.1–0.2	0.1–0.2	<0.1
500	1.0–4.0	1.0–2.0	0.1–0.2	0.1–0.3	0.1–0.3	<0.1
2,000	2.0–6.0	3.0	0.1–0.2	0.2–0.4	0.3–0.4	<0.1
10,000	6.0–9.0	3.5	0.1–0.3	0.3–0.5	0.5–0.8	0.2–0.3

9.2.2.5 Puysegur

Events from Puysegur were only run for 100-year ARI. The maximum water level is consistent along the coast. The wave periods are relatively shorter than other source zones and remain elevated for a considerable time. Energy dissipates rapidly through waterway entrances, with attenuation continuing as the wave propagates upstream.

The maximum water level along the coast occurs up to 7 hrs after the arrival of the first wave. For the waterways, the maximum water level occurs 10–11 hrs after the arrival of the first wave at each location. Table 13 provides the range of maximum water levels for locations within the study area.

Table 13 – Range of maximum water levels (m above SWL) for select locations from the Puysegur source zone.

ARI	Coast	Broadwater (near Wavebreak Island)	Upstream Nerang/ Coomera R	Upstream Tallebudgera Ck	Upstream Currumbin Ck	Upstream Tweed R
100	0.5–1.0	0.5	<0.1	0.1	0.1	<0.1

9.2.2.6 Solomon

The maximum water level is consistent along the coast for the 100- and 500-year ARI runs. For the 2,000- and 10,000-year ARI runs, the maximum water level is consistent along the coast with lower levels near the entrances to waterways and Snapper Rocks. Energy dissipates rapidly through waterway entrances, with attenuation

continuing as the wave propagates upstream.

The maximum water level along the coast occurs up to 11–14 hrs after the arrival of the first wave. For the waterways, the maximum water level occurs 11–13 hrs after the arrival of the first wave at each location. Table 14 provides the range of maximum water levels for locations within the study area.

Table 14 – Range of maximum water levels (m above SWL) for select locations from the Solomon source zone.

ARI	Coast	Broadwater (near Wavebreak Island)	Upstream Nerang/ Coomera R	Upstream Tallebudgera Ck	Upstream Currumbin Ck	Upstream Tweed R
100	0.5–1.5	0.5	0.1–0.3	0.3–0.4	0.3–0.4	0.1
500	1.0–2.5	1.0	0.1–0.3	0.1–0.4	0.1–0.5	0.1
2,000	1.5–3.0	1.0	0.1–0.4	0.6	0.7	0.2

9.2.2.7 South America

The waves produced from the South American scenarios have very long periods of 1.5 hrs along the coast, resulting in water levels elevated above SWL for about 45 minutes. This allows the waves to penetrate further into the waterways with less attenuation. The maximum water level is consistent along the coast for the 100-year ARI runs, with run 26 indicating higher levels between The Spit and Main Beach, reducing further north and south. For the 500-year ARI, waves are consistent along the coast with lower levels near the entrances to waterways and Snapper Rocks. For the 2,000-year ARI runs, maximum water levels are greatest between South Stradbroke Island and Burleigh Heads, reducing southwards. Energy dissipates through waterway entrances, with attenuation continuing as the wave propagates upstream.

The maximum water level along the coast occurs within 4–11 hrs after arrival of the first wave. For the waterways, the maximum water level occurs 9–11 hrs after the arrival of the first wave at each location. Table 15 provides the range of maximum water levels for locations within the study area.

Table 15 – Range of maximum water levels (m above SWL) for select locations from the South American source zone.

ARI	Coast	Broadwater (near Wavebreak Island)	Upstream Nerang/ Coomera R	Upstream Tallebudgera Ck	Upstream Currumbin Ck	Upstream Tweed R
100	0.5–2.0	1.5	0.2–0.5	0.4–0.8	0.4–1.0	0.2
500	1.5–3.0	2.0	0.2–0.7	1.0	1.2	0.2
2,000	3.0–5.0	4.0	0.3–1.0	1.3–2.0	2.0	0.3–0.7

9.2.2.8 Variation for ARI

lists the maximum water level statistics at select coastal locations for all scenarios (MSL and HAT) modelled at each ARI. The average maximum water levels suggest that the levels are slightly higher for the coast between The Spit and Burleigh Heads. Variation of the averages increases with increasing ARI, from 0.2 m for the 100-yr ARI to 1.5 m for the 10,000-yr ARI.

The maximum water level statistics for select locations in the waterways are provided in Table 17. It confirms the attenuation of waves as they propagate up the waterways. In Tallebudgera and Currumbin creeks, the water levels are higher than the longer waterways of Nerang and Coomera rivers. Maximum water levels at the mouth of Logan River do not exceed 0.5 m (2000-yr ARI). Note that the 2000-yr ARI maximum levels are higher than those of the 10,000-yr because of the long-period tsunamis arriving from South America (not modelled for the 10,000-yr ARI) that enhanced wave propagation upstream. Broadwater's average maximum water levels range from 0.6 m (100-yr ARI) to 2.5 m (10,000-yr ARI). Upstream, the average maximum water levels range from 0.1 m (100-yr ARI) to 0.3 m (10,000-yr ARI). The higher maximum water levels upstream are associated with the South American scenarios. The results emphasise that offshore wave heights or ARIs do not completely characterise onshore wave heights or ARIs, and thus the importance of considering a range of scenarios for hazard assessment.

Table 16 – Variation in maximum water level (in metres above SWL) at select coast sites.

	Sth Stradbroke 2	Seaworld-seaside	Surfers Paradise Beach	Mermaid Beach	Burleigh Beach 1	Palm Beach 2	Bilinga Beach	Kirra Beach	Letitia Spit	Kingscliff 2
Easting	542543	542749	543443	544811	546123	549551	551961	554893	555927	542543
Northing	6907457	6902811	6897843	6893137	6890854	6886381	6884759	6883515	6878946	6907457
Depth (m MSL)	5	5	5	5	5	5	5	5	5	5
100-yr ARI										
Average	0.9	1.1	1.1	1.1	1.0	1.0	1.0	0.9	0.9	1.0
Standard Deviation	0.3	0.4	0.4	0.4	0.3	0.4	0.3	0.3	0.3	0.3
Max	1.8	2.0	2.0	1.9	1.8	1.8	1.6	1.4	1.6	1.7
Min	0.6	0.6	0.6	0.5	0.5	0.4	0.4	0.4	0.5	0.5
Max Range	1.2	1.4	1.4	1.4	1.3	1.4	1.2	1.0	1.1	1.2
500-yr ARI										
Average	2.2	2.5	2.4	2.4	2.2	2.2	1.7	1.6	1.9	1.6
Standard Deviation	1.0	0.9	0.8	0.7	0.6	0.5	0.7	0.6	0.6	0.5
Max	4.3	4.3	3.9	3.8	3.6	3.0	2.9	2.5	3.0	2.6
Min	1.2	1.1	1.2	1.3	1.3	1.2	0.4	0.5	1.0	0.7
Max Range	3.1	3.2	2.7	2.5	2.3	1.8	2.5	2.0	2.0	1.9
2,000-yr ARI										
Average	2.8	3.3	3.3	3.3	3.0	3.1	3.0	2.5	2.7	2.7
Standard Deviation	0.9	0.9	0.9	0.8	0.8	0.6	0.6	0.7	0.8	0.7
Max	4.7	4.8	5.0	4.8	4.3	4.3	3.9	3.8	4.0	3.9
Min	1.6	1.8	1.8	1.9	1.6	2.1	1.9	1.6	1.4	1.7
Max Range	3.1	3.0	3.2	2.9	2.7	2.3	2.0	2.2	2.6	2.2
10,000-yr ARI										
Average	3.8	5.1	5.2	5.3	4.6	4.8	5.3	4.1	4.6	5.2

	Sth Stradbroke 2	Seaworld-seaside	Surfers Paradise Beach	Mermaid Beach	Burleigh Beach 1	Palm Beach 2	Bilinga Beach	Kirra Beach	Letitia Spit	Kingscliff 2
Standard Deviation	0.6	0.8	1.0	1.1	0.4	0.9	1.1	0.5	1.5	1.1
Max	5.0	6.7	7.0	7.1	5.2	6.1	6.6	4.9	6.9	6.6
Min	2.8	4.2	4.0	4.0	3.7	3.5	3.5	3.4	2.9	3.3
Max Range	2.2	2.5	3.0	3.1	1.5	2.6	3.2	1.5	4.0	3.3

Table 17 – Variation in maximum water level (in metres above SWL) at select waterway sites.

	Logan R Mouth	Gold Coast Seaway S	Coomera River - Dreamtime Parkway	Lake Coombabah	Nerang R – Big Tree Park	Bond Uni	Lilys Beach	Mainsail St S	Tweed entrance	Tweed R – Bosun Blvd
Easting	531819	541352	531727	535058	534642	541190	544331	545470	554523	553399
Northing	6935702	6909591	6916426	6903678	6913299	6895007	6891203	6885659	6883908	6876323
Depth (m MSL)	2.6	3.9	3.0	1.8	0.23	2.2	3.4	1.4	6.2	2.6
100-yr ARI										
Average	0.06	0.63	0.06	0.02	0.13	0.10	0.43	0.28	0.71	0.13
Standard Deviation	0.07	0.21	0.09	0.05	0.11	0.10	0.22	0.23	0.23	0.10
Max	0.20	1.30	0.40	0.20	0.50	0.40	1.20	1.10	1.20	0.40
Min	0.00	0.30	0.00	0.00	0.00	0.00	0.20	0.10	0.40	0.00
Max Range	0.20	1.00	0.40	0.20	0.50	0.40	1.00	1.00	0.80	0.40
500-yr ARI										
Average	0.11	1.10	0.13	0.06	0.20	0.16	0.74	0.46	1.31	0.20
Standard Deviation	0.10	0.25	0.13	0.10	0.19	0.16	0.33	0.31	0.36	0.13
Max	0.30	1.60	0.50	0.30	0.70	0.50	1.60	1.30	2.00	0.50
Min	0.00	0.80	0.00	0.00	0.00	0.00	0.50	0.10	0.80	0.10
Max Range	0.30	0.80	0.50	0.30	0.70	0.50	1.10	1.20	1.20	0.40

	Logan R Mouth	Gold Coast Seaway S	Coomera River - Dreamtime Parkway	Lake Coombabah	Nerang R – Big Tree Park	Bond Uni	Lilys Beach	Mainsail St S	Tweed entrance	Tweed R – Bosun Blvd
2,000-yr ARI										
Average	0.18	1.63	0.21	0.14	0.31	0.25	1.13	0.75	1.88	0.31
Standard Deviation	0.14	0.49	0.22	0.17	0.30	0.26	0.60	0.56	0.59	0.22
Max	0.49	2.88	0.82	0.66	1.02	0.89	2.69	2.15	2.86	0.88
Min	0.05	1.06	0.03	0.00	0.07	0.06	0.69	0.25	1.02	0.08
Max Range	0.45	1.82	0.79	0.66	0.95	0.83	2.00	1.90	1.83	0.79
10,000-yr ARI										
Average	0.22	2.54	0.19	0.13	0.26	0.23	1.35	0.96	3.55	0.34
Standard Deviation	0.10	0.33	0.09	0.07	0.09	0.08	0.17	0.28	1.37	0.07
Max	0.37	3.10	0.37	0.29	0.40	0.40	1.77	1.49	5.49	0.44
Min	0.09	2.06	0.07	0.04	0.14	0.11	1.10	0.50	1.87	0.20
Max Range	0.27	1.04	0.30	0.25	0.26	0.29	0.67	0.99	3.61	0.24

9.2.3 Maximum Currents

The following provides a summary of maximum currents for each source zone. The analysis is based only on the HAT runs. The upstream levels for the waterways are based on the upstream limit of the model. The maximum envelope for each ARI is provided in Appendix H. The relationship between current velocity and impact is difficult as there is limited recorded information available during events. Instead post-event analysis has relied on numerical modelling, which also has limitations (refer Sections 10.5, 10.6 and Appendix A.5). For marine hazard, it has been suggested that the initiation of damage occurs at 1.5 m/s with extreme/complete damage above 4.6 m/s (Lynett et al., 2014). For overland inundation, Koshimura (2007, 2009a, 2009b) suggests building collapse when inundation depths exceeding 2 m and current velocities exceed 3 to 5 m/s. However, this is specific to the locations considered and based on modelled velocities, so are only a rough estimate of the potential impact and may not apply to Australian conditions.

9.2.3.1 Kermadec-Tonga

The maximum currents are strongest in the entrances of waterways, entrance ebb shoals, near prominent headlands and off Kirra. Strong currents exist over the entrance shoals within Currumbin Creek. For the more extreme cases, there are very strong currents over the Gold Coast Seaway training walls. Offshore of Fingal, currents range from 2 to 9 m/s. Table 18 provides the range of maximum currents for locations within the study area.

Table 18 – Range of maximum currents (m/s) for select locations from Kermadec-Tonga source zone.

ARI	Coast	Broadwater	Waterway entrances	Upstream of waterways	Tweed River
100	0.5–2	2–3	4–5	0.1–0.2	2
500	1–3	3–4	5–7	0.1–0.3	2–4
2,000	1–3	5	6–7	0.1–0.3	3–4
10,000	2–4	5–6	8–12	0.2–0.3	5

9.2.3.2 New Hebrides

The maximum currents are strongest in the entrances of waterways, entrance ebb shoals, near prominent headlands, Palm Beach, and Kirra to Snapper Rocks. Strong currents exist over the entrance shoals within Currumbin Creek. For the more extreme cases, there are very strong currents over the Gold Coast Seaway training walls. Offshore of Fingal, currents range from 2 to 9 m/s. Table 19 provides the range of maximum currents for locations within the study area.

Table 19 – Range of maximum currents (m/s) for select locations from New Hebrides source zone.

ARI	Coast	Broadwater	Waterway entrances	Upstream of waterways	Tweed River
100	0.5–1.5	2.5	4	<0.1	2
500	0.5–3	3–4	6	0.1–0.2	4.5
2,000	1–5	4–5	7–10	0.1–0.2	5–6
10,000	2–5	5–6	10–11	0.2	6–7

9.2.3.3 Outer-rise Kermadec-Tonga

For 500-yr ARI and above, the maximum currents are strongest from South Stradbroke Island to The Spit, with the largest currents adjacent to the north training wall to the Gold Coast Seaway. There are also strong currents adjacent to prominent headlands and entrance ebb shoals. Offshore of Fingal, currents are up to 5 m/s. Table 20 provides the range of maximum currents for locations within the study area.

Table 20 – Range of maximum currents (m/s) for select locations from Outer-rise Kermadec-Tonga source zone.

ARI	Coast	Broadwater	Waterway entrances	Upstream of waterways	Tweed River
100	0.5–3	2–3	3–4	0.1	1.5–2
500	1.5–7	3	5.5	0.1	3
2,000	2–10	3–5	6–7	0.1–0.2	3–5

9.2.3.4 Outer-rise New Hebrides

For 100- to 500-yr ARI, the maximum currents are strongest in the entrances to waterways and north of prominent headlands. For the 2,000-yr ARI, maximum currents are strongest south of the Gold Coast Seaway entrance and to the north of prominent headlands. For the 10,000-yr ARI, there are very strong currents along the coast from Surfers Paradise to Miami and Kirra to Fingal, as well as the entrances to waterways and north of headlands. There are also very strong currents over training walls to waterway entrances. At Fingal, currents reach 12 m/s. Table 21 provides the range of maximum currents for locations within the study area.

Table 21 – Range of maximum currents (m/s) for select locations from Outer-rise New Hebrides source zone.

ARI	Coast	Broadwater	Waterway entrances	Upstream of waterways	Tweed River
100	0.5–1.5	2.5	4	<0.1	2
500	0.5–5	2–4	7	0.1–0.2	4.5
2,000	1–9	3–4	7–8	0.1–0.2	6
10,000	2–12	5–6	6–10	0.1–0.2	7–8

9.2.3.5 Puysegur

Events from Puysegur were only run for 100-year ARI. The maximum currents are consistent along the coast. The maximum currents are greatest in entrances to waterways. Table 22 provides the range of maximum currents for locations within the study area.

Table 22 – Range of maximum currents (m/s) for select locations from Puysegur source zone.

ARI	Coast	Broadwater	Waterway entrances	Upstream of waterways	Tweed River
100	<0.5–1.5	2	3	<0.1	1

9.2.3.6 Solomon

Maximum currents are greatest in waterway entrances and near prominent headlands. In the nearshore at Fingal, the currents are up to 4 m/s for the 2,000-yr ARI. Table 23 provides the range of maximum currents for locations within the study area.

Table 23 – Range of maximum currents (m/s) for select locations from Solomon source zone.

ARI	Coast	Broadwater	Waterway entrances	Upstream of waterways	Tweed River
100	<0.5–1	2	3–4	0.1	1–1.5
500	0.5–1.5	3	5	0.1–0.2	2.5
2,000	0.5–2	3–4	6–7	0.1–0.2	4

9.2.3.7 South America

Currents are greater near waterway entrances and prominent headlands. For the 2,000-yr ARI, currents are also stronger from Kirra to Fingal. In the nearshore at Fingal, currents reach up to 6 m/s. Table 24 provides the range of maximum currents for locations within the study area.

Table 24 – Range of maximum currents (m/s) for select locations from South American source zone.

ARI	Coast	Broadwater	Waterway entrances	Upstream of waterways	Tweed River
100	0.5–1.5	2–4	3.5–6	0.1–0.2	2-3
500	0.5–1.5	5	7	0.1–0.3	3.5
2,000	0.5–3	7	10–11	0.1–0.4	5–6

9.2.3.8 Variation for ARI

Table 25 lists the maximum currents statistics at select coastal locations for all runs (MSL and HAT) at each ARI. Except for the 10,000-yr ARI, there is little variation in maximum currents along the coast for each ARI, with slightly higher currents at Burleigh Beach. This location is close to the headland at Burleigh Heads. For the 10,000-yr ARI, the maximum of the maximum currents is greatest between Surfers Paradise and Burleigh Beach. This is associated with worst-case for the coast (run 88, Outer-rise New Hebrides). There is considerable variation in

maximum currents for each ARI, as indicated by the maximum range. This variation increases for increasing ARI with up to 7.6 m/s range for the 10,000-yr ARI.

The maximum current statistics for select locations in the waterways are provided in Table 26. The maximum current in the mouth of the Logan River reaches 0.8 m/s with an average of up to 0.4 m/s. Upstream in the waterways connected to the Broadwater, there is little variation in the maximum currents with averages in the order of 0.1 to 0.3 m/s. The maximum of 0.6 m/s in the Nerang River is associated with the South American events. In the Broadwater, the currents are much higher than upstream, with an increasing trend with increasing ARI. At Gold Coast Seaway, the currents reach 4.3 m/s (2,000-yr ARI), which again is associated with the South American events. In Tallebudgera and Currumbin Creeks, the upstream currents are higher than the longer waterways of Nerang and Coomera Rivers. Currents at the Tweed River entrance site increase with increasing ARI, reaching a maximum of 6.3 m/s for the 10,000-yr ARI.

Table 25 – Variation in maximum currents (m/s) at select coast sites.

	Sth Stradbroke 2	Seaworld-seaside	Surfers Paradise Beach	Mermaid Beach	Burleigh Beach 1	Palm Beach 2	Bilinga Beach	Kirra Beach	Letitia Spit	Kingscliff 2
Easting	542543	542749	543443	544811	546123	549551	551961	554893	555927	542543
Northing	6907457	6902811	6897843	6893137	6890854	6886381	6884759	6883515	6878946	6907457
Depth (m below MSL)	5	5	5	5	5	5	5	5	5	5
100-yr ARI										
Average	0.9	1.1	1.1	1.1	1.0	1.0	1.0	0.9	0.9	1.0
Standard Deviation	0.3	0.4	0.4	0.4	0.3	0.4	0.3	0.3	0.3	0.3
Max	1.8	2.0	2.0	1.9	1.8	1.8	1.6	1.4	1.6	1.7
Min	0.6	0.6	0.6	0.5	0.5	0.4	0.4	0.4	0.5	0.5
Max Range	1.2	1.4	1.4	1.4	1.3	1.4	1.2	1.0	1.1	1.2
500-yr ARI										
Average	0.9	1.3	1.2	1.2	1.5	1.1	1.0	1.1	1.2	0.8
Standard Deviation	0.7	1.0	0.8	0.7	0.8	0.6	0.5	0.4	0.5	0.4
Max	2.5	3.1	2.5	2.8	3.2	2.8	2.1	2.0	2.4	2.0
Min	0.3	0.3	0.3	0.3	0.5	0.4	0.4	0.4	0.6	0.4
Max Range	2.2	2.8	2.2	2.5	2.7	2.4	1.7	1.6	1.8	1.6
2,000-yr ARI										
Average	1.4	1.8	1.7	1.6	1.9	1.7	1.3	1.4	1.8	1.2

	Sth Stradbroke 2	Seaworld-seaside	Surfers Paradise Beach	Mermaid Beach	Burleigh Beach 1	Palm Beach 2	Bilinga Beach	Kirra Beach	Letitia Spit	Kingscliff 2
Standard Deviation	1.0	1.3	1.2	1.2	1.0	0.9	0.7	0.5	0.7	0.5
Max	3.7	4.1	4.6	4.9	4.4	4.1	3.3	2.5	3.7	2.6
Min	0.5	0.5	0.6	0.6	0.7	0.7	0.6	0.6	0.9	0.5
Max Range	3.2	3.6	4.0	4.3	3.7	3.4	2.8	2.0	2.9	2.1
10,000-yr ARI										
Average	2.2	3.3	3.7	3.6	4.0	3.7	3.4	3.1	4.0	3.1
Standard Deviation	0.5	1.8	2.2	2.8	2.3	2.1	2.0	1.5	2.4	1.9
Max	3.1	6.8	8.0	8.9	8.2	7.5	7.2	6.2	8.9	6.8
Min	1.5	1.8	1.7	1.4	2.0	2.1	1.4	1.4	1.9	1.6
Max Range	1.6	5.0	6.2	7.6	6.1	5.4	5.8	4.8	7.0	5.3

Table 26 – Variation in maximum currents (m/s) at select waterway sites.

	Logan R Mouth	Gold Coast Seaway S	Coomera River - Dreamtime Parkway	Lake Coombabah	Nerang R – Big Tree Park	Bond Uni	Lilys Beach	Mainsail St S	Tweed entrance	Tweed R - Bosun Blvd
Easting	531819	541352	531727	535058	534642	541190	544331	545470	554523	553399
Northing	6935702	6909591	6916426	6903678	6913299	6895007	6891203	6885659	6883908	6876323
Depth (m below MSL)	2.6	3.9	3	1.8	0.23	2.2	3.4	1.4	6.2	2.6
100-yr ARI										
Average	0.2	1.1	0.1	0.1	0.2	0.1	1.2	0.8	1.6	0.4
Standard Deviation	0.1	0.5	0.1	0.1	0.1	0.0	0.3	0.2	0.6	0.3
Max	0.5	2.7	0.2	0.2	0.5	0.2	1.7	1.2	2.9	0.9
Min	0.1	0.5	0.0	0.0	0.1	0.0	0.6	0.6	0.7	0.1

	Logan R Mouth	Gold Coast Seaway S	Coomera River - Dreamtime Parkway	Lake Coombabah	Nerang R – Big Tree Park	Bond Uni	Lilys Beach	Mainsail St S	Tweed entrance	Tweed R - Bosun Blvd
Max Range	0.4	2.2	0.2	0.2	0.4	0.2	1.1	0.6	2.2	0.8
500-yr ARI										
Average	0.2	1.8	0.1	0.1	0.3	0.1	1.6	1.0	3.3	0.6
Standard Deviation	0.1	0.6	0.1	0.1	0.1	0.1	0.3	0.1	0.8	0.3
Max	0.5	3.1	0.2	0.3	0.6	0.2	2.1	1.3	4.6	1.1
Min	0.1	0.9	0.0	0.0	0.1	0.0	1.1	0.8	1.6	0.2
Max Range	0.4	2.2	0.2	0.3	0.5	0.2	1.0	0.5	3.0	0.9
2,000-yr ARI										
Average	0.3	2.5	0.1	0.2	0.3	0.1	2.2	1.3	4.3	0.6
Standard Deviation	0.2	0.9	0.1	0.1	0.1	0.0	0.4	0.2	0.7	0.3
Max	0.7	4.3	0.3	0.3	0.6	0.2	2.8	1.7	5.3	1.1
Min	0.1	1.2	0.0	0.0	0.2	0.1	1.4	0.8	3.0	0.3
Max Range	0.6	3.1	0.2	0.3	0.5	0.1	1.4	0.9	2.3	0.9
10,000-yr ARI										
Average	0.4	2.9	0.1	0.1	0.3	0.2	2.8	1.5	5.2	0.7
Standard Deviation	0.2	0.5	0.0	0.1	0.1	0.1	0.3	0.2	0.4	0.3
Max	0.8	3.7	0.2	0.2	0.4	0.4	3.3	1.9	6.3	1.2
Min	0.1	2.1	0.1	0.1	0.2	0.1	2.3	1.0	4.8	0.3
Max Range	0.7	1.6	0.1	0.2	0.2	0.3	1.0	0.9	1.5	0.9

9.2.4 Arrival Times

Arrival times depend on the distance the tsunami needs to travel from its generation, and the water depths through which it propagates. As tsunamis travel as shallow water waves across the open ocean, it is expected that arrival times will be similar at a given location for events from the same subduction zone, with some variations to account for differences in the particular fault zone location. For the study region, tsunamis will typically reach the northern New South Wales beaches first, being the most eastward coastline. However, it will reach the rest of the coast within 10 minutes of arrival at the northern New South Wales beaches. The tsunami then continues to slow down as it enters the shallower waterways such as Logan River, Nerang River, Tallebudgera, and Currumbin Creek.

Appendix E provides the arrival times of the leading wave for several locations and subduction zones. The tables have been categorised into broad regions: Ocean side (Northern and Southern Beaches); Northern Seaway including Logan River; Southern Seaway; Tallebudgera and Currumbin Creek; and Tweed. In general, events from the Outer-rise New Hebrides and Puysegur have the shortest arrival time on the coast, just over 3.5 hours after the earthquake, with events from South America arriving much later at over 18 hours.

Another way to examine this data is to consider the time differences relative to the first arrival of the tsunami within the study region. Calculating the travel time relative to arrival times at the coast gives an indication of expected arrival times within waterways once the tsunami first reaches the coast. This approach also leads to reduced variations for a given location across all events as the speed of propagation is related directly to depth based on linear shallow wave theory (Table 27). In general, once the tsunami reaches different entrances, it will take between 30 min and 1.5 hours for the tsunami to arrive upstream, and about 2 hours to reach Coombabah Creek within the Northern Seaway. The South American subduction zone has been excluded from the calculation of travel time differences because its long wave periods lead to a substantially delayed arrival at the coast and waterways compared to other zones due to the slow rise in water level.

The tsunami waves generated from South America for water level HAT over all ARI for Burleigh Beach (longitude 153.27° east, latitude 28.104° south) at a depth of 5 m is shown in Figure 11. It is seen that the leading wave is not necessarily the wave with the highest amplitude, and that larger waves can potentially arrive several hours after the initial wave.

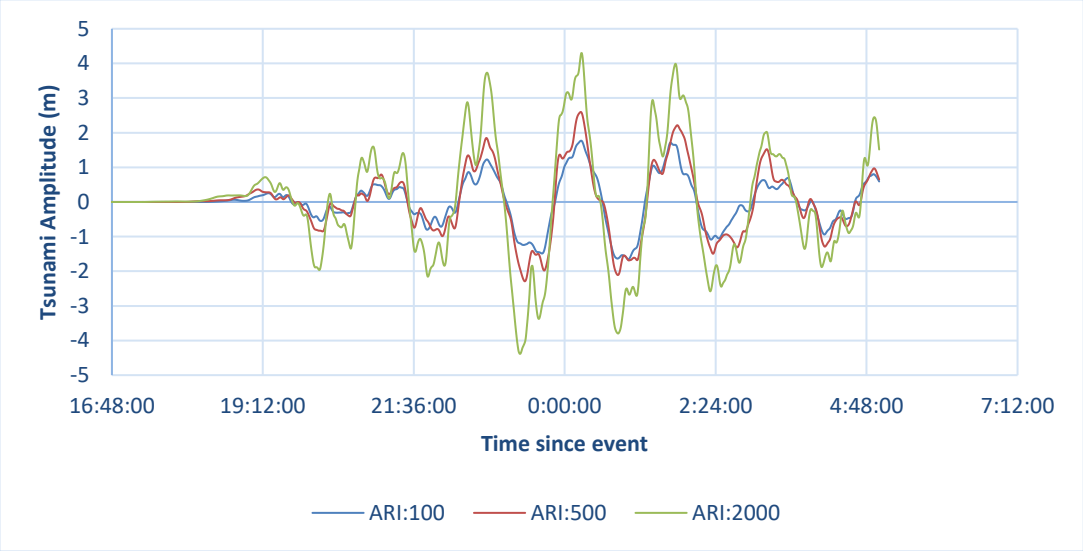

Figure 12 – South American wave heights by ARI at Burleigh Beach for tide level HAT.

Table 27 – Arrival times at waterway sites after arrival at the Coast.

Region	Location	Average arrival time (hrs:min)	Std Deviation of arrival time (hrs:min)
Northern Seaway	Logan River – Boat Ramp	1:21	0:03
	Coomera River – Jiboora Island	1:32	0:03
	Coombabah Creek	2:00	0:03
Southern Seaway	Nerang River – Big Tree Park	0:51	0:03
	Nerang River – Witt Ave	0:46	0:03
	Nerang River–River Cres	0:38	0:03
	Bond university	0:44	0.03
Tallebudgera	Conservation Park	0:04	0:02
	Schuster Park	0:25	0.02

Region	Location	Average arrival time (hrs:min)	Std Deviation of arrival time (hrs:min)
Currumbin	Mainsail St. (N)	0:02	0:02
Tweed	Charles–Trutes Bay	0:41	0:02
	Tweed River_Bosun Blvd	0:31	0:02
	Tweed River_Murwillumbah	1:38	0:02

9.3 Inundation

Below are specific comments that relate to areas within the study domain. Note that inundation maps provided in Appendices I and J (refer Table 8) are for the extreme upper limit of the modelled scenarios for each ARI.

9.3.1 South Stradbroke Island

Minor inundation is seen in properties for 100-yr and 500-yr ARI at MSL scenarios. For higher ARI, inundation is more pronounced, causing flooding in Couran Cove and properties near Brown Island. Considerable inundation occurs for HAT scenarios, with low variability between ARI for populated areas because of the steep topography. The areas surrounding the north and south of the Island, which are mostly non-infrastructure areas, experience significant flooding during 2,000-yr and 10,000-yr ARI events.

9.3.2 The Spit to Broadbeach

In the case of the 100-yr and 500-yr ARI at MSL scenarios, Marine Parade in Labrador, and the low-lying regions along the coast experience most of the flooding. However, for higher ARI events, all the coastal areas including The Spit, Sea World, Main Beach, Surfers Paradise, Broadbeach, and Labrador are significantly inundated. Additionally, residential areas in the vicinity of Loders Creek are at a high risk of flooding.

Regarding the 100-yr and 500-yr ARI at HAT events, the west bank of the Broadwater including limited built-up and residential areas, were flooded. There was also considerable flooding in Labrador, some residential areas in Surfers Paradise, and areas near Loders Creek. Coastal regions such as beaches, coastal parks, and Sea World experienced some levels of inundation. For higher ARI events, all the coastal areas, including The Spit, Sea World, Main Beach, Surfers Paradise, Broad Beach, and Labrador, are significantly inundated. The extent of flooding in the western bank of the Broadwater was significantly greater during HAT occurrences as opposed to cases with MSL.

9.3.3 Kurrawa to Burleigh Heads

The extent of flooding that occurs at the 100-yr and 500-yr ARI, both at MSL and HAT, is confined to low-lying areas near beaches or creeks. There is no substantial risk to infrastructure or residential areas.

The degree of flooding experienced during 2,000-yr ARI at MSL is comparable to that observed during 100-yr and 500-yr ARI events. Nonetheless, during 2,000-yr ARI at HAT, certain buildings and roads situated near the beaches in Surfers Paradise, Mermaid Beach, Miami Beach, and Burleigh Heads are susceptible to inundation.

The degree of flooding observed at 10,000-yr ARI for both MSL and HAT is considerable, as it covers nearly all the infrastructure, buildings, and roads from Kurrawa to Burleigh Heads.

9.3.4 Burleigh Heads to Currumbin Creek

While flooding only occurs in low-lying areas near beaches and Tallebudgera Creek with 100-yr and 500-yr ARI at MSL, significant residential areas between Gold Coast highway and Murlong Park, as well as areas near Palm Beach Currumbin State High School, experience inundation during HAT and 2,000-yr ARI at MSL. For 10,000-yr ARI at MSL, there is additional flooding of most regions situated between the Gold Coast highway and coastal beaches, as well as those between Palm Beach Avenue and Fourteenth Avenue.

During 2,000-yr and 10,000-yr ARI at HAT, nearly all regions within a 1 km radius of the shorelines experience complete flooding. Considerable flooding occurred in areas near Tallebudgera Creek and Awonga Lake as a consequence of the 2,000-yr ARI at HAT.

9.3.5 Currumbin to Snapper Rocks

Inundation extent for 100-yr and 500-yr ARI (for both MSL and HAT) is not significant and is limited to low-lying regions near beaches and waterways. However, the area near the Twin Towns services club may experience flooding during these events.

There are three primary regions of flooding for the 2,000-yr ARI, which include the vicinities of Flat Rock Creek, Roughton Park, J E (Bluey) Gray Park and Boundary St.

Most regions within a 300-metre proximity of beaches experience flooding for the 10,000-yr ARI at MSL. In the case of HAT, this inundation reaches an average distance of 700 metres from the beaches.

9.3.6 Letitia Spit to Dreamtime Beach

Infrastructure and residential areas are not at risk of inundation from 100-yr and 500-yr ARI at MSL. However, low-lying areas around Letitia Spit and the entrance of the Tweed River may experience inundation from the 100-yr and 500-yr ARI at HAT and 2,000-yr ARI at MSL. The sporadic flooding of Letitia Road and the surrounding areas of Tweed Holiday Parks can also occur. In addition, Fingal Road and the areas around Wommin Lagoon and Wommin Lake in the southern region are susceptible to flooding.

The coastal areas stretching from Letitia Spit to Dreamtime Beach are likely to be completely flooded, except for the elevated terrain close to Fingal Head for 2,000-yr ARI at HAT and 10,000-yr ARI at MSL and HAT.
The surrounding areas of Tweed River, such as Minjungbal Drive, Dry Dock Road, Philip Parade, and Soorley Street, are also affected by these events, which result in flooding.

9.3.7 Tallebudgera Creek

Although flooding is limited to low-lying regions adjacent to Tallebudgera creek with 100-yr and 500-yr ARI at MSL, significant residential areas are impacted at HAT. In the vicinity of Tallebudgera Drive and Boodera Road area, a substantial portion of properties is inundated on the downstream side of the creek, close to the Tallebudgera Creek bridge. At Tallebudgera Cove, including Little Scholars School, areas are experiencing 1.5 m inundation just before the Pacific Motorway. Upstream, due to wave attenuation, inundation is decreasing, posing no serious threat to the community. The 2,000-yr ARI at MSL produces flooding in properties near Kevin Gates Park and Elanora Drive Park in addition to the inundation extent mentioned earlier, which is comparable to the 100-yr and 500-yr ARI at HAT cases.

It is worth noting that the severity of flooding caused by the 2,000-yr ARI is greater than that caused by the 10,000-yr ARI. Note that South American scenarios were not considered at the 10,000-year ARI because PTHA18 suggests they are very unlikely (compared to other source zones) to produce correspondingly large waves offshore of the Gold Coast. The 2,000-yr ARI at HAT results in substantial flooding in all properties and infrastructure near Awong Lake, Mallawa Sport Complex, Japonica Drive, West Burleigh, and Koala Park. It is interesting to observe that there is not much attenuation as one moves upstream, and the low-lying areas close to the creek remain flooded.

9.3.8 Currumbin Creek

The Currumbin Creek region is highly susceptible to changes in water levels. Although flooding is restricted to low-lying areas adjacent to Currumbin Creek with 100-yr and 500-yr ARI at MSL, significant residential areas are inundated during HAT events. These areas include Palm Beach Currumbin State High School, Sarawak Ave, Winders Park, Currumbin State School, Preston Park, Palmer Family Park, Merv Craig Sporting Complex, and Chown Ave. As one moves further upstream, the water level diminishes, and flooding is limited only to the vicinity of the creek.

As with Tallebudgera Creek, the flooding caused by the 2,000-yr ARI is more severe than that caused by the 10,000-yr ARI. The 2,000-yr and 10,000-yr ARI at HAT can cause severe flooding in all properties and infrastructure within a ~1 km radius of the main creek channel. However, in the upstream area near Currumbin Valley, flooding is limited to low-lying areas close to the creek.

9.3.9 Logan River

No inundation is seen to properties along the Logan River for MSL scenarios across all ARI within the model extent. Inundation occurs for HAT scenarios with higher inundation levels for larger ARI's. However, this is mostly limited to non-infrastructure areas along the river and does not generally affect coastal properties. Properties near Muriel Street may experience minor inundation.

9.3.10 Broadwater

No inundation is seen to properties along the Broadwater for MSL scenarios across 100-yr and 500-yr ARI. Marine Parade in Labrador could experience some minor flooding. However, for the 100-yr and 500-yr ARI at HAT conditions, the west bank of the Broadwater, including several built-up and residential areas up to 400 metres from the water, can be flooded.

Flood occurrences for events with a 2,000-yr and 10,000-yr ARI at MSL are restricted to specific properties located near Marine Parade in Labrador and Southport Beach. Nonetheless, when considering HAT, properties within approximately 600 metres of the water are vulnerable to flooding. It is noteworthy that the most severe flooding situations are associated with 2,000-yr ARI events due to the South American events that were not considered for the 10,000-yr ARI because PTHA18 suggested it was very unlikely.

9.3.11 Coomera River

No inundation is seen to properties along the Coomera River for MSL scenarios across all ARI within the model extent. In HAT situations, flooding is typically confined to non-residential zones, including Coomera Island, Phil Hill Park, and low-lying regions near Oaky Creek, Bullock Head Creek, and Eleven Lake. Nonetheless, flooding is anticipated in Paradise Point (from Aurora Square to Columbus Drive) as well as in properties located in the vicinity of Tom and Jean Ruddy Park.

It is noteworthy that the most severe flooding situations are associated with 2,000-yr ARI events, rather than 10,000-yr ARI.

9.3.12 Coombabah Creek/Lake

No inundation is seen to properties along the Coombabah Creek/Lake area for MSL scenarios across all ARI within the model extent. In HAT situations, flooding is typically confined to non-residential zones, including Coombabah Lake Conservation Park. Nonetheless, flooding occurs for the majority of residential buildings in Hope Island from Boykambil Esplanade to Crescent Avenue as well as in properties located in the vicinity of the Esplanade Park. It is noteworthy that the most severe flooding situations are associated with 2,000-yr ARI events, rather than 10,000-yr ARI.

9.3.13 Nerang River

Inundation is anticipated in low-lying areas for all MSL scenarios and ARI within the model extent, but there will be additional flooding in certain residential areas. Specifically, flooding is expected in the Surfers Paradise region between Norfolk Avenue and Cypress Avenue, as well as the areas between Appel Park and Lionel Perry Park. However, properties located on the upstream side of the Nerang River will not be affected. The HAT scenarios have the most severe outcomes with the potential to endanger numerous locations surrounding Nerang River with the possibility of flooding. This includes properties situated within a 300 m radius of Pelican Beach, James Overell Park, Matron and Sister Higman Park, Gardiner Creek Reserve, Winchester Park, Wildash Street, Harry Bond Park, as well as many other areas located between Lionel Perry Park and Sunset Boulevard Park. It is noteworthy that the most severe flooding situations are associated with 2,000-yr ARI events, rather than 10,000-yr ARI.

9.4 Climate Change (Sea Level Rise)

Although expected climate change outcomes relate to meteorological changes, the increased water level due to sea level rise (SLR) will make low-lying areas more susceptible to inundation and may impact on tsunami amplitudes because of potentially less shoaling. An increase of 1.9 m (HAT + SLR) alone inundates low-lying areas as shown in Figure 13. There is significant inundation of Norwell and Woogoolba, Tweed, and Coombabah Lake.

The SLR scenario was based on the worst-case event for the 10,000-yr ARI. For this study, there were two worst-case events. The Outer-rise New Hebrides event (PTHA ID 7700) at HAT (run 88) produced the greatest inundation for the coast, whereas the Kermadec-Tonga event (PTHA ID 43313) at HAT (run 78) produced the greatest inundation for the waterways. The corresponding SLR runs are 89 and 90, respectively (refer to Appendix F).

The overall impact is an increase in inundation extent. The changes to maximum water depth and currents for the area mainly occur on the coast and are presented in Figure 14. The increase in inland water depths on the coast is typically less than 0.8 m (i.e., increase for SLR). The increase in currents inland is associated with the increase in inundation depth and inundation extent. Figure 15 shows the inundation extent for the Outer-rise New Hebrides event at both HAT (to run 88) and HAT + SLR (run 89). The figure also shows the static inundation extent for HAT and HAT+SLR alone (i.e., no tsunami). There has been some increase in extent along the coast, but most of the increase is in the waterways near low-lying areas, mostly contributable to the SLR increase. A similar figure is

provided in Figure 16 for the Kermadec-Tonga event (run 90) showing the same pattern to Figure 15 except there is less inundation along the coast.

The maximum water level and currents for select coastal and waterway sites are presented in Table 28 (Outer-rise New Hebrides event) and Table 29 (Kermadec-Tonga event), respectively. For the coastal sites, the increase in depth resulted in a slight reduction in maximum water level (above SWL) with a reduction of less than 10 per cent. This is an expected outcome as the increased depth would reduce shoaling of the waves. There was generally a reduction in maximum current for the coastal sites considered at 5 m depth. Palm Beach showed a one per cent increase in currents, but this is not considered significant.

For the waterways, the maximum water level remained the same or slightly decreased. Although the percentage change is higher than that for the coast, it is noted that the water levels are much lower and only reported to one significant figure. Maximum currents within the waterway sites considered remained the same or increased, except for upstream in Currumbin Creek where the currents reduced.

The above discussion on maximum water levels and currents is based on select points in the study area and may not represent the spatial variability. To consider this, spatial difference plots (HAT + SLR scenario – HAT scenario) of maximum currents for the Kermadec-Tonga event are provided in Figure 17. The figure illustrates that in the waterways there is variability in the changes to current speed with regions of increase and decrease associated with the complex bathymetry. The changes to maximum water level for the Outer-rise New Hebrides event (Figure 18) shows a distinct reduction in the nearshore as the waves approach the coast because of less wave shoaling.

To summarise: the main impact of SLR is increased inundation extent, particularly in low-lying areas within the waterways. This scenario only considers the existing topography and does not consider possible future remediation works that may be undertaken to offset the impacts of SLR. Further discussion on the impact of increasing still water level is provided in Section 10.1.

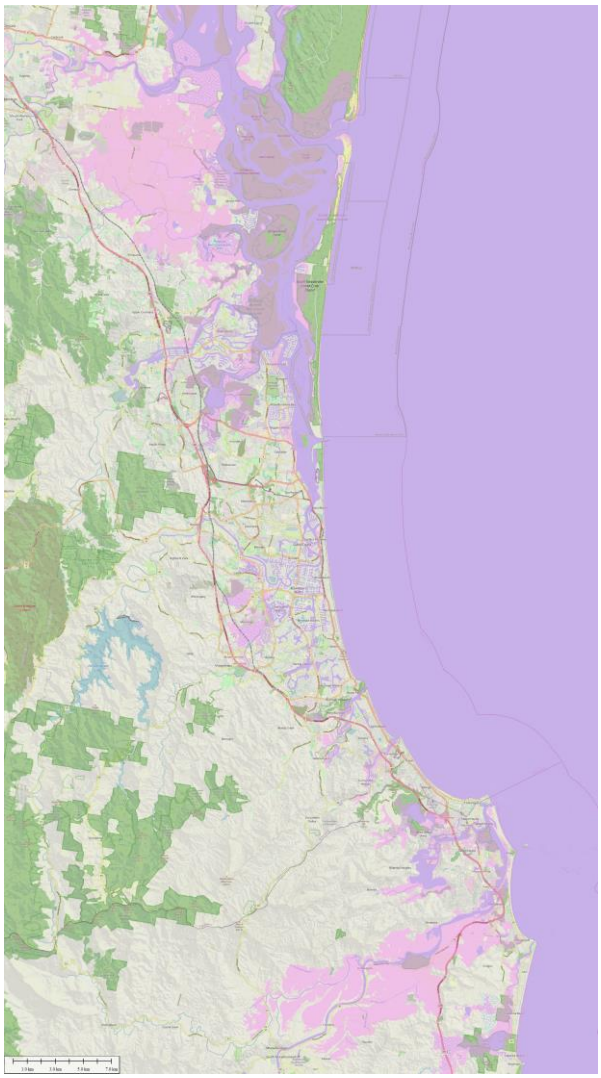

Figure 13 – Inundation extent of static water level increase for HAT and SLR (1.9 m above MSL).

Table 28 – Variation in maximum water levels (WL above SWL) and maximum currents (m/s) for select coastal sites from Outer-rise New Hebrides event with (run 89) and without (run 88) SLR.

	Sth Stradbroke 2	Seaworld-seaside	Surfers Paradise Beach	Mermaid Beach	Burleigh Beach 1	Palm Beach 2	Bilinga Beach	Kirra Beach	Letitia Spit	Kingscliff 2
Easting	542543	542749	543443	544811	546123	549551	551961	554893	555927	542543
Northing	6907457	6902811	6897843	6893137	6890854	6886381	6884759	6883515	6878946	6907457
Depth (m MSL)	5	5	5	5	5	5	5	5	5	5
Max WL (m) (Run 88, HAT)	4.8	6.5	6.8	6.8	4.7	5.6	6.4	4.4	6.6	6.3
Max WL (m) (Run 89, HAT and SLR)	4.6	6.4	6.6	6.6	4.6	5.4	6.3	4.0	6.4	6.1
% change in WL (positive increase)	**−4**	**−2**	**−3**	**−3**	**−2**	**−4**	**−2**	**−9**	**−3**	**−3**
Max current (m/s) (Run 88, HAT)	2.7	6.4	7.7	8.8	8.1	7.4	7.0	5.5	8.4	6.5
Max current (m/s) (Run 89, HAT and SLR)	2.4	6.1	7.5	8.5	7.7	7.5	6.4	5.0	7.6	6.0
% change in current (positive increase)	**−11**	**−5**	**−3**	**−3**	**−5**	**1**	**−9**	**−9**	**−10**	**−8**

Table 29 – Variation in maximum water levels (WL above SWL) and maximum currents (m/s) for select waterway sites from Kermadec-Tonga event with (run 90) and without (run 78) SLR.

	Logan R Mouth	Gold Coast Seaway S	Coomera River - Dreamtime Parkway	Lake Coombabah	Nerang R - Big Tree Park	Bond Uni	Lilys Beach (Tallebudgera Ck)	Mainsail St S (Currumbin Ck)	Tweed entrance	Tweed R - Bosun Blvd
Easting	531819	541352	531727	535058	534642	541190	544331	545470	554523	553399
Northing	6935702	6909591	6916426	6903678	6913299	6895007	6891203	6885659	6883908	6876323
Depth (m MSL)	2.6	3.9	3	1.8	0.23	2.2	3.4	1.4	6.2	2.6
Max WL (m) (Run 78, HAT)	0.3	2.9	0.2	0.2	0.3	0.2	1.4	1.3	2.6	0.3
Max WL (m) (Run 90, HAT and SLR)	0.2	3.1	0.2	0.1	0.3	0.2	1.1	1.0	2.4	0.2
% change in WL (positive increase)	**−33**	**7**	**0**	**−50**	**0**	**0**	**−21**	**−23**	**−8**	**−33**
Max current (m/s) (Run 78, HAT)	0.5	3.4	0.2	0.1	0.4	0.2	3.0	1.4	4.9	0.4
Max current (m/s) (Run 90, HAT and SLR)	0.8	3.7	0.2	0.1	0.4	0.2	3.3	1.1	5.3	0.4
% change in current (positive increase)	**60**	**9**	**0**	**0**	**0**	**0**	**10**	**−21**	**8**	**0**

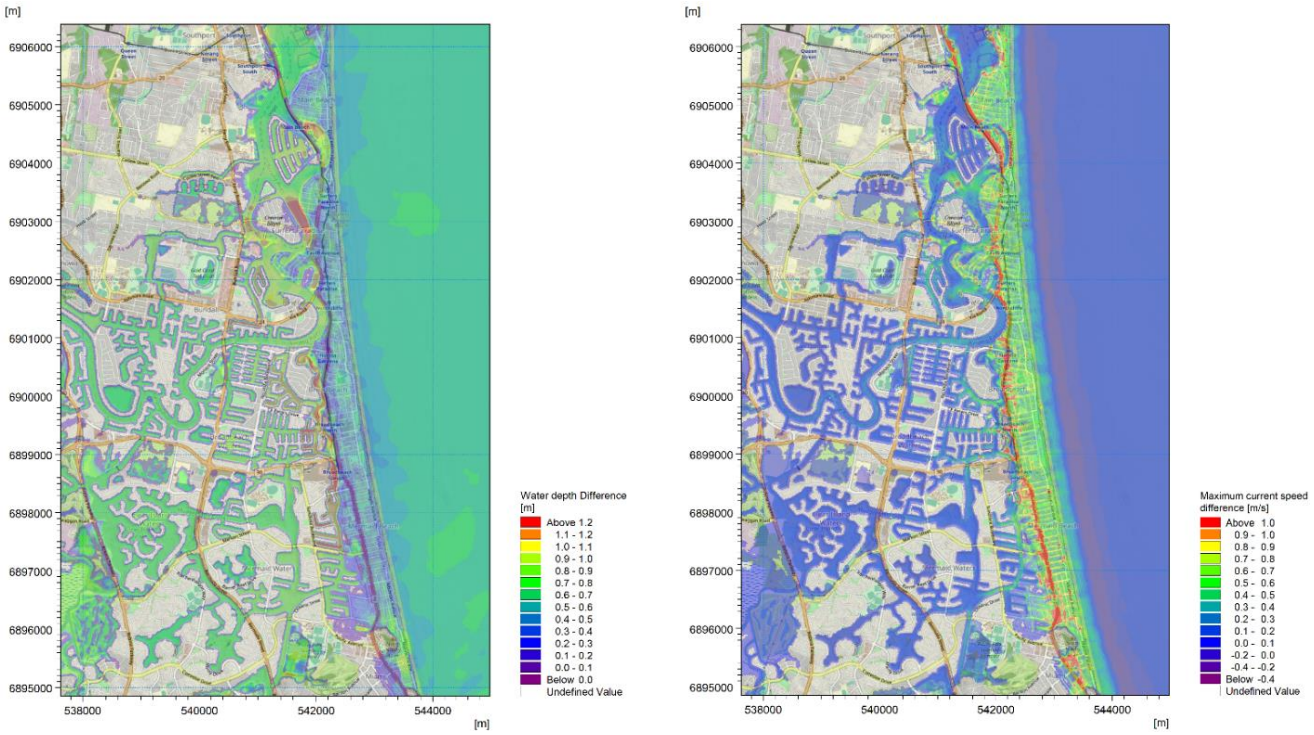

Figure 14 – Changes in water depth and currents as a result of SLR for the Outer-rise New Hebrides event (Run 88 (HAT) and Run 89 (HAT + SLR)).

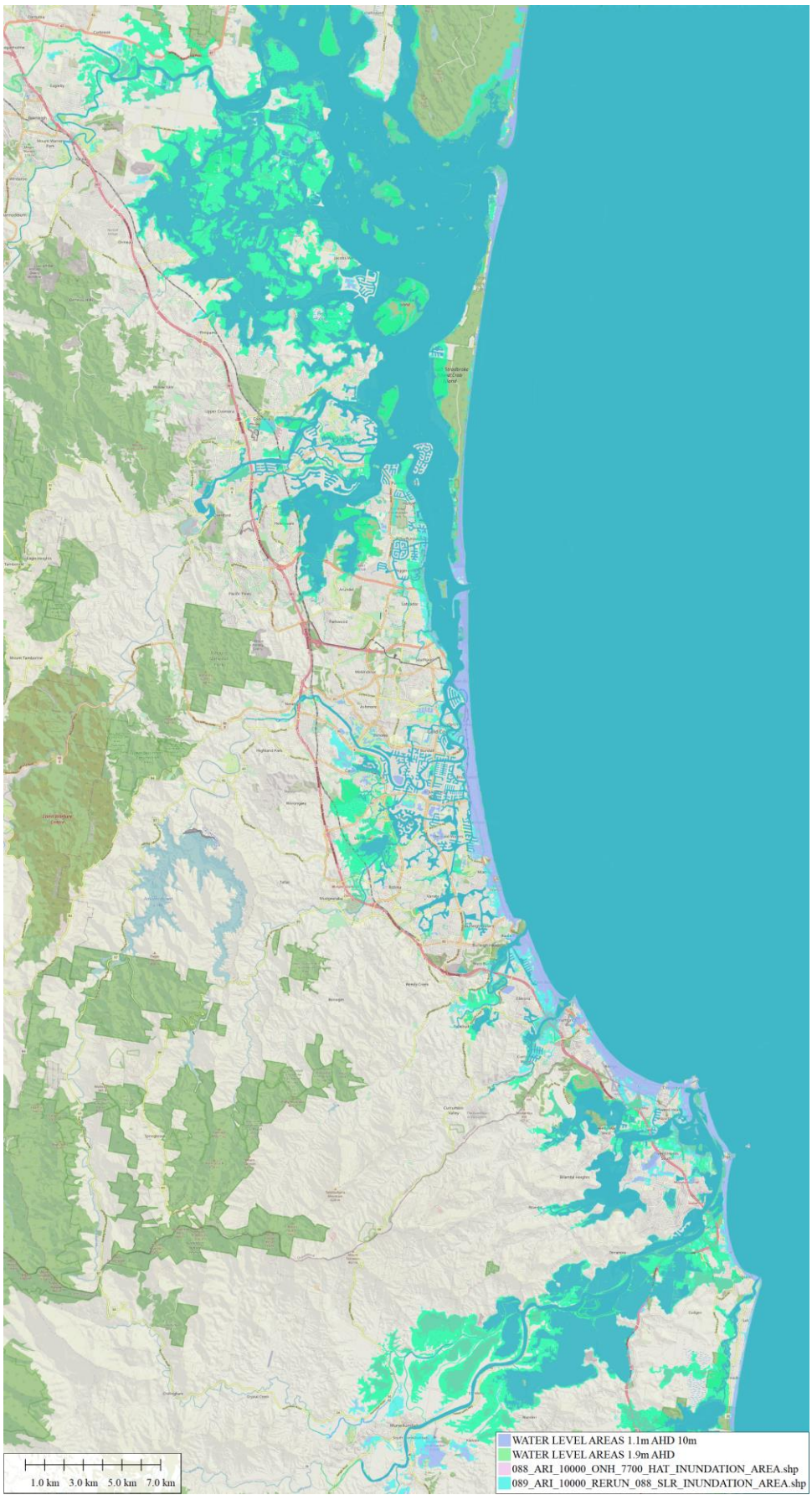

Figure 15 – Inundation extent for Outer-rise New Hebrides event with SLR (run 89). Dark blue is HAT extent, green is SLR extent, pink/purple is extent for Kermadec-Tonga event at HAT (run 88) and light blue is extent for run 89 (HAT + SLR).

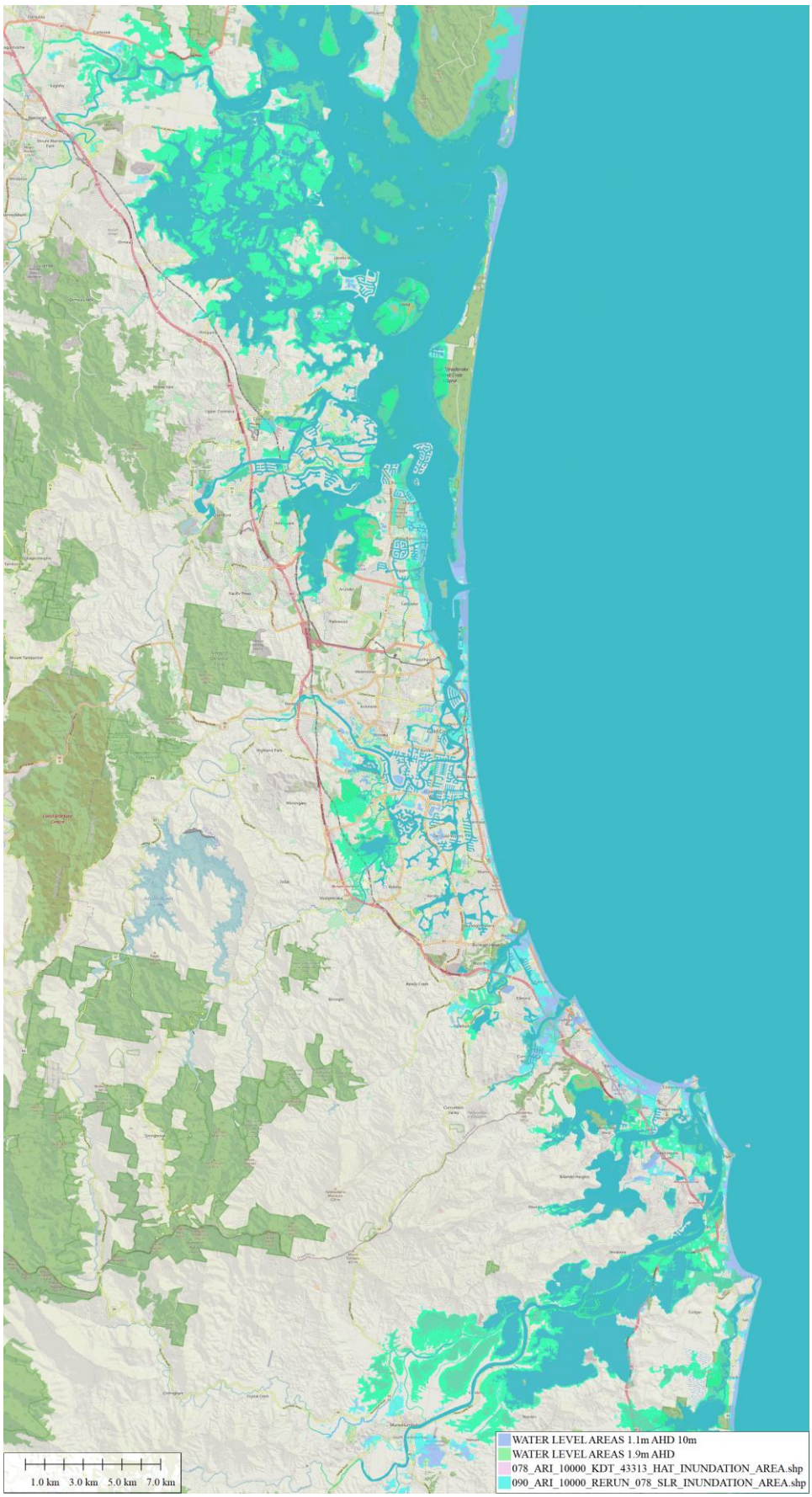

Figure 16 – Inundation extent for Kermadec-Tonga event with SLR (run 90). Dark blue is HAT extent, green is SLR extent, pink/purple is extent for Kermadec-Tonga event at HAT (run 78) and light blue is extent for run 90 (HAT + SLR).

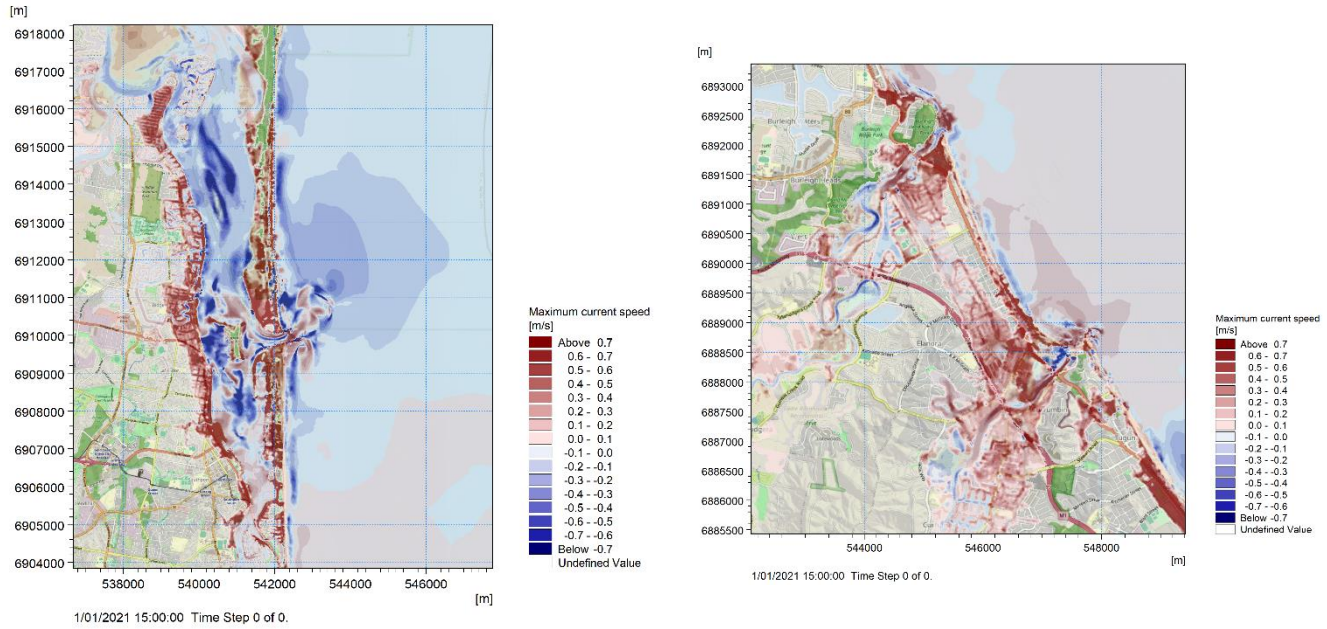

Figure 17 – Changes in Current Speed within the Broadwater (left) and Currumbin Creek (right) for the Kermadec-Tonga event (HAT + SLR scenario – HAT scenario).

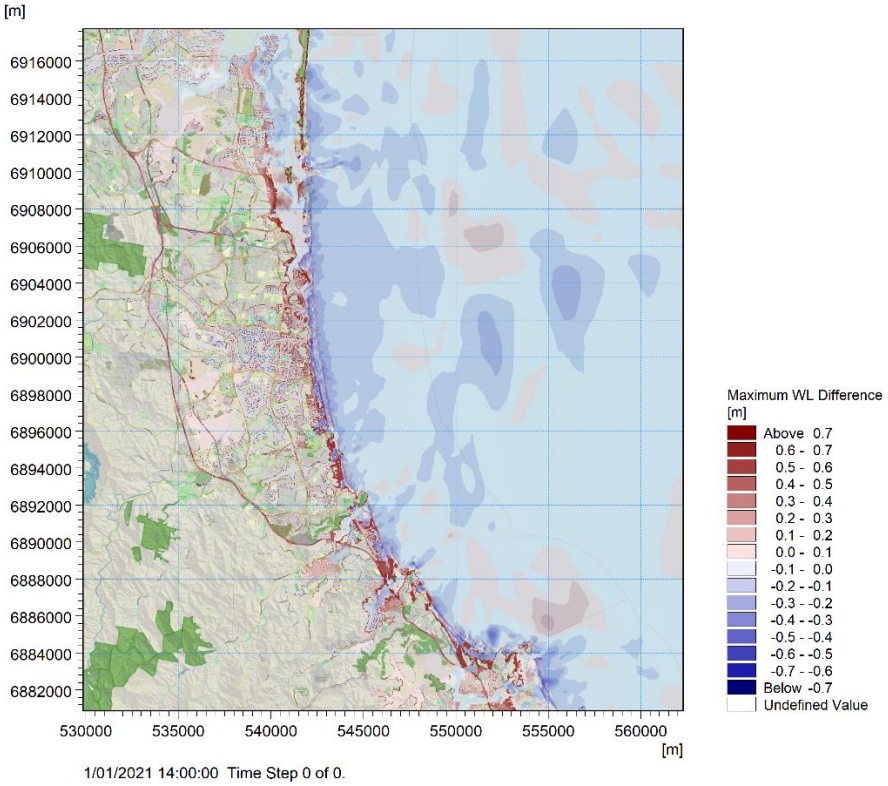

Figure 18 – Changes in maximum water level for the Outer-rise New Hebrides event (HAT + SLR scenario – HAT scenario).

10 Discussion

10.1 Stage of Tide and Inundation

Modelling undertaken of three still water levels (SWL) allow us to consider the influence of the stage of tide on tsunami inundation for the study area. The 10,000-yr ARI Outer-rise New Hebrides event (ID 7700) was run for MSL (run 87), HAT (run 88) and HAT with SLR (run 89). Superimposing the inundation extent for these runs (Figure 19, Figure 20 and Figure 21) provides an indication of the influence of the stage of tide.

On the coast, there is some increase in inundation extent despite there being a slight reduction in maximum tsunami amplitude for increasing water depth (0.2 to 0.8 m reduction at sites in 5 m depth at MSL) as a result of less wave shoaling (refer Table 28). Even with this reduction, the maximum water levels are still extreme for this scenario (ranging from 4 to 7 m at select sites in 5 m depth at MSL).

In the waterways, there is attenuation of the waves such that upstream of the larger waterways the maximum water levels (above SWL) are typically 0.1 to 0.4 metres. There is no trend in maximum water levels (above SWL) as seen for the coastal sites, with some sites increasing and others decreasing with increasing water depth.
The changes in maximum water level (above SWL) are typically in the order of 0.2 m upstream. However, the change in inundation extent can be significant with increasing still water levels as low-lying areas become inundated. At MSL, there is little inundation of the waterways showing they are sensitive to the stage of tide.

Mofjeld et al. (2007) examined the influence of tides on the maximum water level by superimposing theoretical tsunami wave time series based on an exponential decay coefficient of two days over a duration of 5 days (based on measurements within the Pacific Ocean), on tides typical for Oregon, USA. The results showed that for small tsunami amplitudes, the maximum water levels tend to occur near mean higher high water with little spread. As the tsunami amplitude increases, the maximum water level tends towards a limit of MSL plus the tsunami amplitude (for tsunami amplitudes greater than the tide range). Although the principle of an exponentially decaying tsunami time series may be applicable in the open Pacific Ocean, the nearshore tsunami time series in this study is complicated by interaction of reflections, shelf trapped waves and coastal trapped waves. Therefore, the consideration of tides in this study is expected to provide a conservative result.

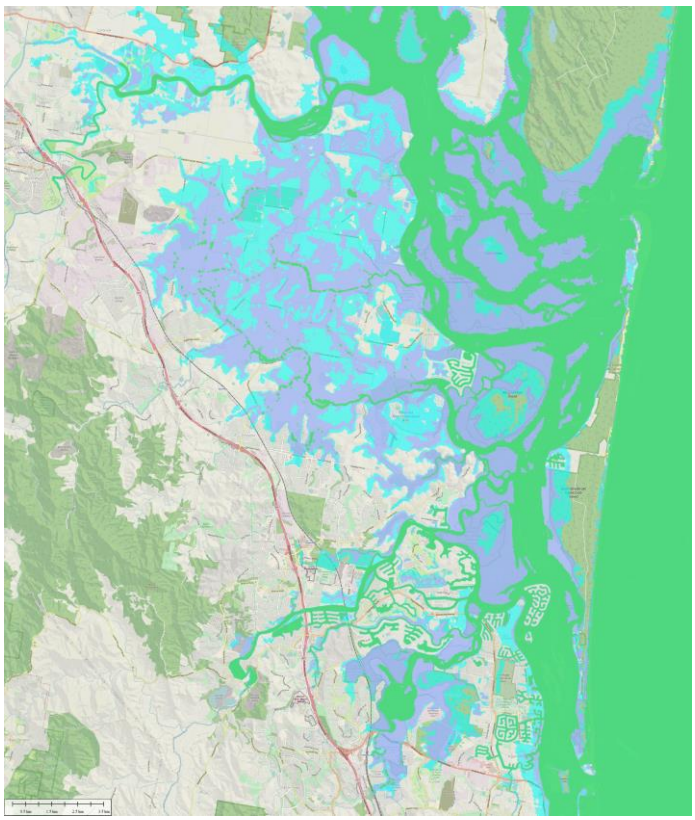

Figure 19 – Impact of stage of tide on inundation for northern Gold Coast, 10,000-yr ARI Outer-rise New Hebrides. Green is at MSL, purple at HAT and blue at HAT and SLR.

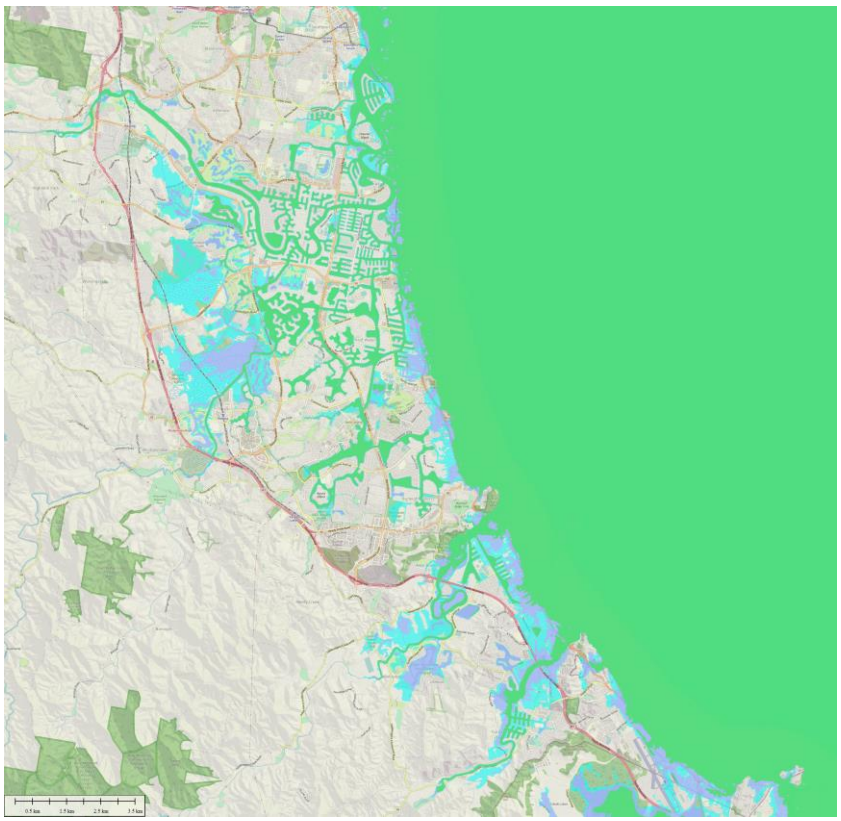

Figure 20 – Impact of stage of tide on inundation for southern Gold Coast, 10,000-yr ARI Outer-rise New Hebrides. Green is at MSL, purple at HAT and blue at HAT and SLR.

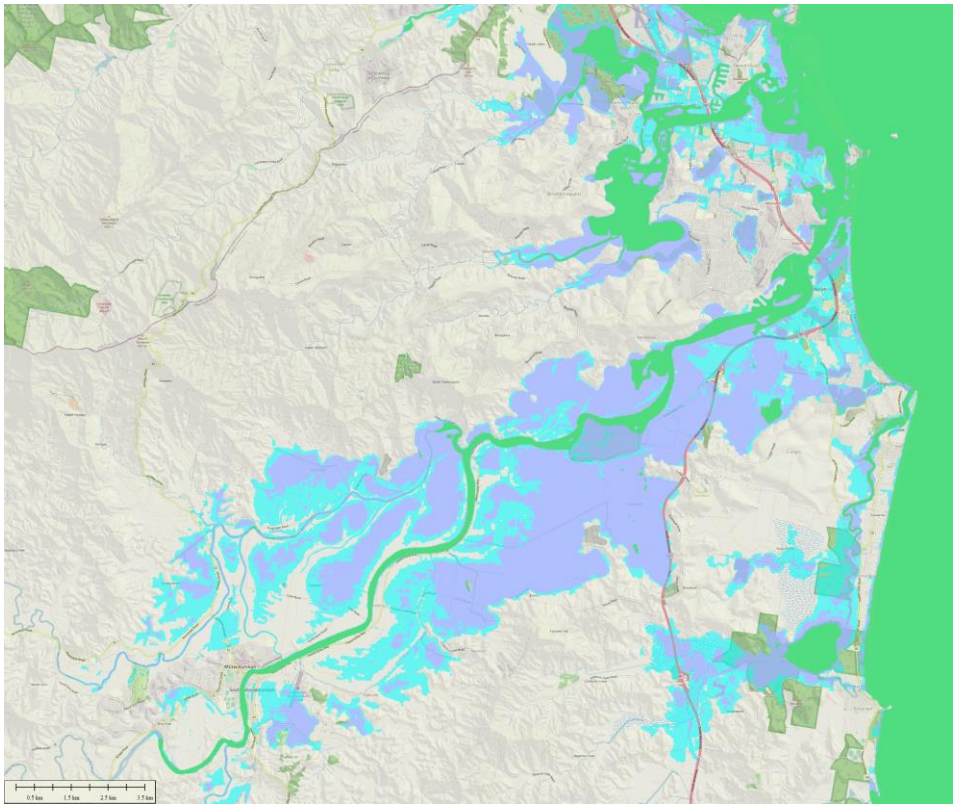

Figure 21 – Impact of stage of tide on inundation for Tweed, 10,000-yr ARI Outer-rise New Hebrides. Green is at MSL, purple at HAT and blue at HAT and SLR.

10.2 Tsunami Attenuation in Waterways

Section 9.2.2.7 refers to the maximum water levels for South American events. It was observed that the South American events had much longer wave periods than other source zones and produced less attenuation in the waterways compared to other events. To examine this further, select runs from each source zone for the 2,000-yr ARI have been analysed to examine the influence of wave period on upstream maximum water levels. A spectral analysis was performed on the wave signal from the Seaworld-seaside site to determine the wave period statistics prior to entering the waterways. This was then compared to the maximum water level for several upstream sites. Table 30, Figure 22 and Figure 23 present the results of this analysis. From Figure 22, there is no notable trend for the coastal site Seaworld-seaside, with a drop in maximum water level occurring before an increase for the South American event. However, the upstream sites show a distinct trend of decreasing attenuation with increasing wave period. It is therefore plausible that source zones that produce longer period waves (such as South America) will result in less attenuation in the waterways.

To account for the variability in the maximum water levels between the different events at Seaworld-seaside, Figure 23 plots the relative maximum water levels (WL_{rel}) against the tsunami period. The relative maximum water level is non-dimensional and calculated by $WL_{rel} = WL_{WW}/WL_{SW}$ where WL_{WW} and WL_{SW} represent the maximum water level at each waterway site and Seaworld-seaside, respectively. This data appears to indicate that WL_{rel} may increase with period up to ~24-minutes. Beyond this, there is no apparent increase in WL_{rel} between the 24-minute Solomon event and the 56-minute South American tsunami. However, more data would be required to consider this further. In addition, the figure indicates variability in the relative maximum water levels at each of the sites analysed, with Lilys beach consistently the highest WL_{rel} and the lowest observed at Lake Coombabah.

Table 30 – Maximum water levels above SWL for select coastal and waterways sites (2,000-yr ARI).

Run	Source	Peak Period (Tp)	Average Period (T02)	Seaworld-seaside	Coomera River Mouth	Lake Coombabah	Bond University	Lilys Beach (Tallebudgera Ck)	Mainsail St S (Currumbin Ck)	Tweed R - Bosun Blvd
62	OKDT	0:07:42	0:08:13	3.71	0.17	0.03	0.09	0.82	0.31	0.08
68	ONH	0:12:59	0:10:14	4.34	0.22	0.05	0.12	0.90	0.38	0.13
54	KDT	0:17:26	0:15:56	3.41	0.29	0.06	0.14	0.87	0.52	0.22
60	NH	0:17:39	0:17:55	2.93	0.30	0.05	0.15	0.89	0.55	0.19
70	S	1:00:29	0:24:16	1.92	0.32	0.11	0.26	1.00	0.66	0.31
74	SA	1:29:47	0:56:20	4.77	0.76	0.37	0.76	2.21	1.80	0.68

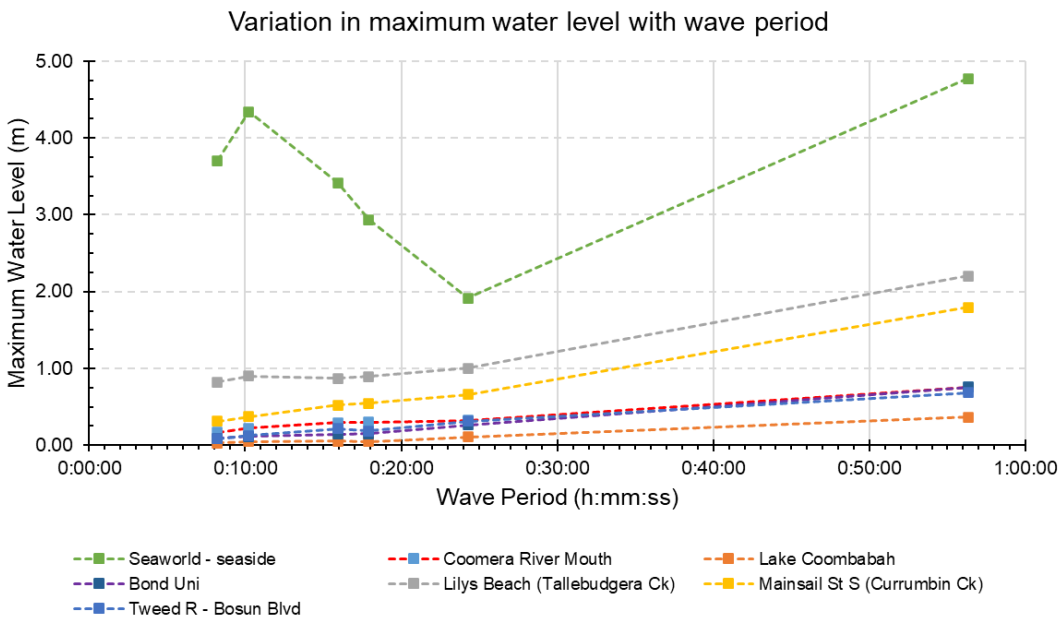

Figure 22 – Variation in upstream waterway maximum water level with average wave period (Table 30).

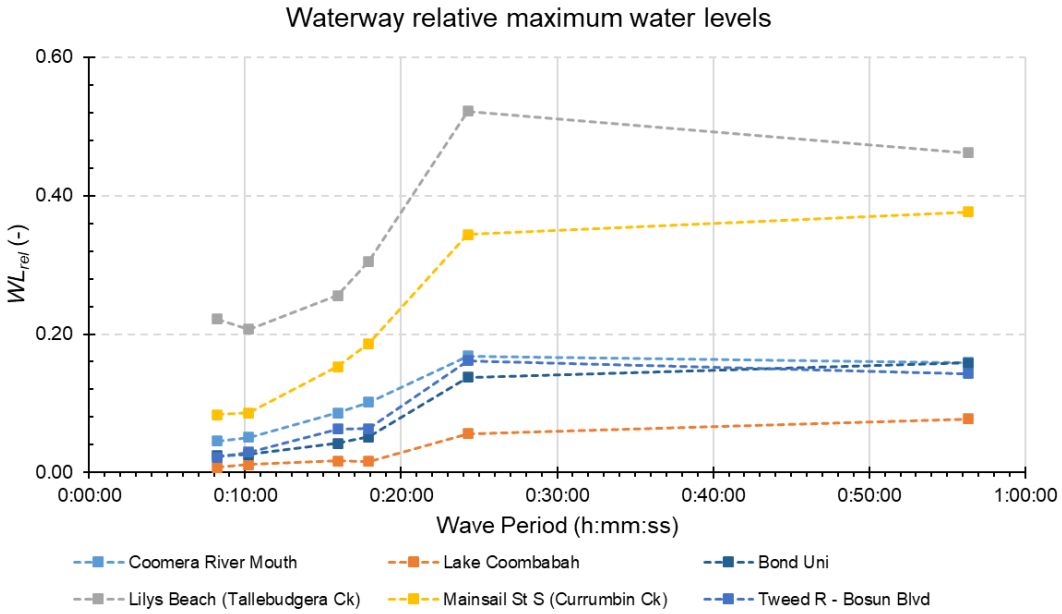

Figure 23 – Variation in relative maximum water levels ($WL_{rel} = \frac{WL_{WW}}{WL_{SW}}$) for selected waterways (WL_{WW}) relative to the Seaworld-seaside site (WL_{SW}) with average wave period (Table 30).

10.3 South American Events

The South American events produced the greatest inundation for the 100-yr to 500-yr ARI and the greatest inundation of waterways for all ARI. These events are unique in that they are very long period waves (wave period in the order of 90 min) and their amplitudes appear to increase with subsequent waves (Figure 12) on the Gold Coast. This pattern is similar across all ARI modelled for the Gold Coast. Further south (northern New South Wales), there is no increase in amplitude with subsequent waves. Appendix G provides an analysis of the South American events as well as a comparison against a shorter period event from Kermadec-Tonga. A simple calculation of the resonant period for the Gold Coast based on linear wave theory, is about 100 min and 66 min for the narrower continental shelf in northern New South Wales. This fits well with the spectral analysis undertaken for the South American events for Burleigh and Wooyung. Although the Kermadec-Tonga event exhibits much shorter wave periods than the South American event, the spectral analysis close to shore shows a growth in energy for these frequencies.

Therefore, it is plausible that the 90-minute period of the tsunami originating from South America could undergo shelf resonance upon reaching the continental shelf adjacent to the Gold Coast. This resonance might account for the increase in amplitude for subsequent waves, a phenomenon that is not apparent from the offshore time series.

10.4 Anthropogenic Structures

The structures at risk of scour and potential failure are coastline-exposed revetments and buildings with shallow foundations. Experiences from the 2004 Indian Ocean and the 2011 Great East Japan tsunami events have shown that as the tsunami overtops sea defences such as revetments, they can scour behind the structure, causing failure. In addition, houses can be damaged by impact forces of the water and the debris it may carry, scour and liquefaction.

Although most of the revetments are covered by dunes, the severe events will result in significant erosion. There are also significant currents over the entrance training walls for the more severe events, which may compromise their stability.

10.5 Community Vulnerability

Although a complete exposure, vulnerability and risk assessment is beyond the scope of this study, it is useful to examine metrics that would assist disaster managers in assessing their risk. The vulnerability of a community to tsunami hazard can be categorized into physical, social, economic, and environmental (UNESCO, 2015 and UNISDR, 2017). The physical aspects relate to factors such as human casualties, building damage and loss of infrastructure. The concept and quantification of vulnerability is well understood for other water hazards that occur more frequently such as riverine flooding and storm surge (refer Section A.5).

Research into vulnerability measures for tsunami hazard has mostly developed post-2004, but particularly following the 2011 Great East Japan tsunami. As such, the tsunami research community is still in the early stages of understanding how to quantify physical and social vulnerability. Research into the vulnerability of buildings has focused on developing empirical damage or fragility functions (probability of exceeding a given damage state based on a measure of tsunami intensity, e.g., Charvet et al., 2015) for a range of structure types and predefined damage states based on post-event assessments and laboratory experiments. However, there is still a degree of uncertainty associated with the fragility estimations as well as variability for different locations, limiting their generic use (Charvet et al., 2015). This is affected by several factors, including the current state of understanding of the primary tsunami intensity measures, variability in the classification and assessment of building type and damage state, variability in building quality, locality-specific influences (bathymetry, topography, typology), incomplete field survey databases, and the statistical approaches adopted (Charvet et al., 2017). They also do not capture all failure mechanisms such as debris impact, foundation scour and liquefaction. Further information is provided in Section A.5.2.

UNESCO (2015) provides some generic median damage states from Nanayakkara and Dias (2013) for single-storey buildings constructed from commonly used materials based on inundation depth. Figure 24 summarises these based on the lower limits for timber structures. Complete damage for masonry (M) and reinforced concrete (RC) are also shown as lines. The figure also includes the human stability criteria from Wijetunge (2009), based on the experimental results of Takahashi (2005). Data from the 2011 Great East Japan tsunami were intentionally omitted as these structures performed better given they were newly constructed with proper quality controls. It is likely that Australian building codes would also have higher quality controls. Maqsood et al. (2014) developed tsunami vulnerability models for the south-east Asia and Pacific region as part of the Global Assessment Report on Disaster Risk Reduction (GAR). Whilst this work considered a different set of building types, such an approach of describing vulnerability as the percentage of damage for depth above ground floor level, is consistent with other vulnerability research conducted in Australia for severe wind, earthquake and flood through the Bushfire and Natural Hazard Cooperative Research Centre (see research outputs at https://www.bnhcrc.com.au/research/cluster/built-environment). The Severe Wind Hazard Assessment for south-east Queensland (Edwards et al., 2022) has highlighted a range of future research areas, including the need for storm surge vulnerability research which could be used to inform future tsunami vulnerability assessments in Queensland.

The 10,000-yr ARI worst-case for the coast (run 88) indicates depths of up to 2 m with the arrival of the first wave (the largest wave for this area) and currents up to 2 m/s for the region between Surfers Paradise and Broadbeach South (Figure 25). This would indicate complete damage. However, as mentioned above, the design of the vulnerability curve does not consider engineered buildings and is likely overly conservative for the Gold Coast.

Further research is required to develop tsunami vulnerability curves specific to the Australian built environment. Should overland flow velocity become an important variable, then a finer model mesh may be required to resolve velocity patterns around buildings. No sound decisions can be made from the current state of knowledge.

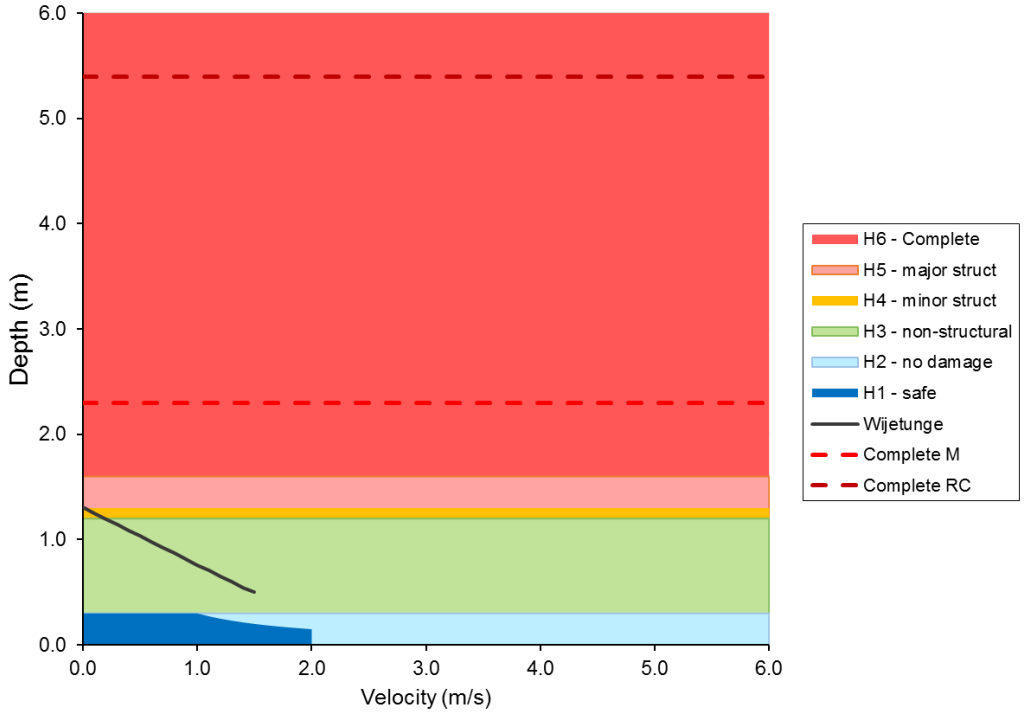

Figure 24 – Combination of general vulnerability curves for tsunami inundation.

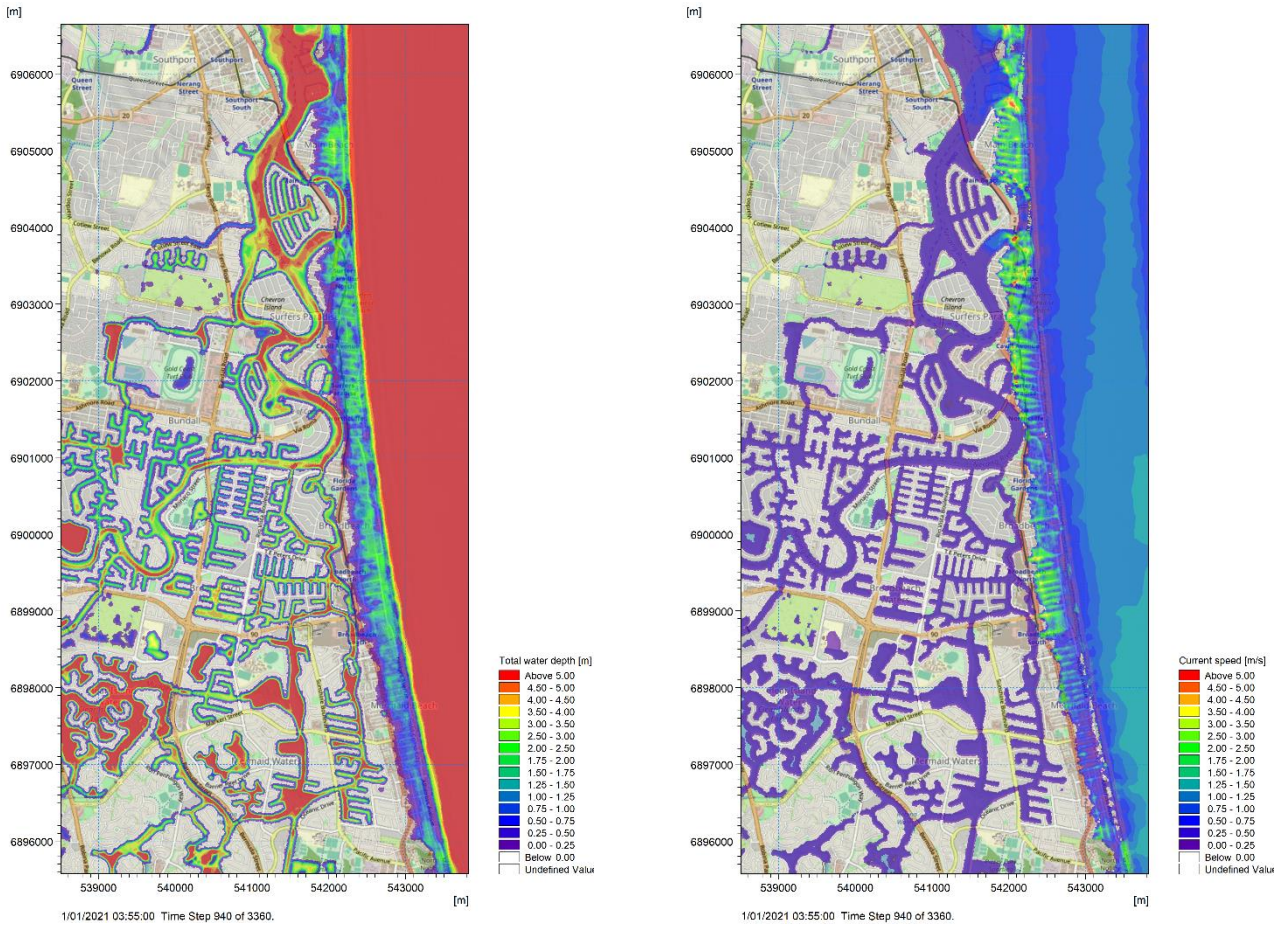

Figure 25 – Water depths (left) and currents (right) for inundation from first wave for Run 88.

10.6 Marine Hazard and Vulnerability

Although tsunami inundation is perhaps the most considerable and obvious risk to the public, there can still be significant damage to maritime facilities from events that do not pose an inundation threat. Within ports and marinas, maritime assets are vulnerable to significant damage from strong currents and associated drag forces (Lynett et al., 2014).

Lynett et al. (2014) undertook a review of recorded vessel damage against measured and modelled tsunami current speeds within ports and harbours, predominantly in California following the 2010 Chile and 2011 Great East Japan tsunamis, to note distinct damage thresholds as summarised in Table 31. Further detail is provided in Section A.5.1.1. This damage criteria are based on far-field tsunami events and so could be applicable to Queensland. However, the authors are not aware of any specific studies undertaken for the east coast of Australia.

The criteria were applied to the maximum current speeds for run 88, being the coastal worst-case for the 10,000-year ARI (Figure 26 and Figure 27). The figures show the potential for extreme marine damage along the open coastline and the entrances to the waterways.

Table 31 – Marine facility damage classification from Lynett et al. (2014).

Damage Index	Damage Type	Threshold Velocity (m/s)
0	no damage/impacts	<1.5
1	small buoys moved	<1.5
2	1–2 docks/small boats damaged and/or large buoys moved	1.5
3	Moderate dock/boat damage (<25% of docks/vessels damaged) and/or midsized vessels off moorings	1.5
4	Major dock/boat damage (<50% of docks/vessels damaged) and/or large vessels off moorings	3
5	Extreme/complete damage (>50% of docks/vessels damaged)	4.6

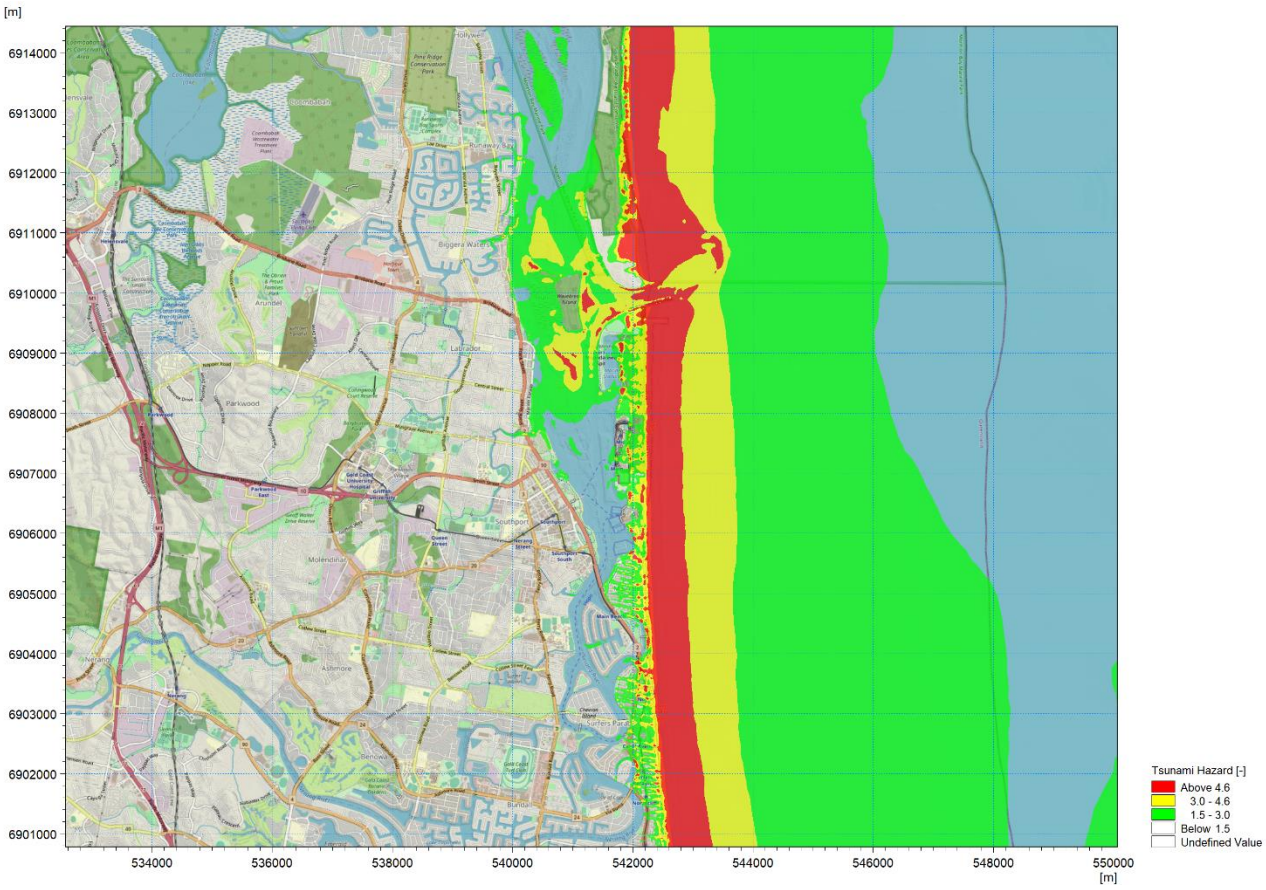

Figure 26 – Marine hazard classification for Run 88, Broadwater.

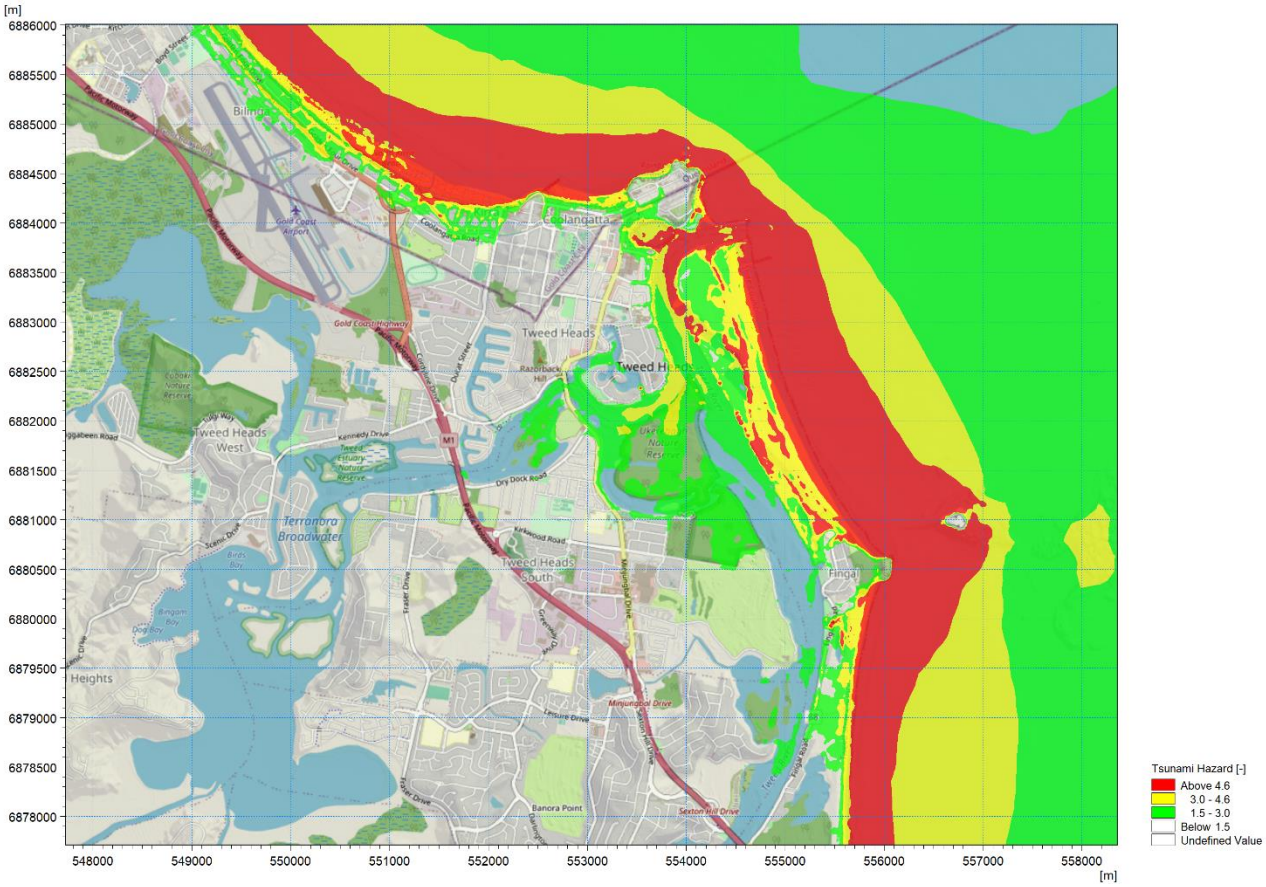

Figure 27 – Marine hazard classification for Run 88, Tweed River entrance.

10.7 Comparison with GA study

Tsunami inundation modelling for the Gold Coast had previously been undertaken and detailed in a report by GA (Fountain et al., 2009a). GA examined 3 scenarios: (i) an event representing the JATWC land inundation warning wave amplitude of 0.3 m at the 100 m depth contour (200-yr ARI event); (ii) an event representing overtopping of the coastal dunes (5,000-yr ARI event); and (iii) the largest credible event (10,000-yr ARI event) based on the first iteration of the PTHA. All 3 events originated from the New Hebrides source zone. Table 32 compares each ARI event's maximum water levels from the first iteration of the PTHA (PTHA08) against the PTHA18 at 100 m depth. Gauge ID 1431.1 was used for the PTHA18 hazard. It is not clear what gauge was used for the GA study. Although the hazard can vary for different gauges, the table suggests that the revised PTHA18 has increased hazard for all ARI, with lower ARIs exhibiting a more significant change. Additionally, the maximum water level for the 2,500-yr ARI based on the PTHA18 is 1.65 m (not shown), close to that of the 5,000-yr ARI for the PTHA08. The GA study was modelled at both MSL and HAT of 1.1 m above MSL (the same as the present study).

Table 32 – Comparison of maximum water level (m) at 100 m depth off the Gold Coast for PTHA08 and PTHA18. PTHA18 based on gauge ID 1431.1.

ARI	Maximum Water Level (m) (PTHA08)	Maximum water Level (m) (PTHA18)
200	0.3	0.6
5,000	1.7	2.0
10,000	2.3	2.4

Although the results of the GA report cannot be shown here as the report is marked 'in-confidence', the following provides a descriptive comparison between the inundation extents for the two studies at HAT. The inundation extent within the waterways for the 5,000-yr event is similar to that of the maximum envelope of all 500-yr ARI scenarios in the present study. In the Broadwater, the inundation from the 2,000-yr ARI maximum envelope in the present study is greater than the 10,000-yr event in the GA study. It is difficult to ascertain the inundation associated with the waterways from that of the coast between Tallebudgera and Currumbin creeks for the GA study. However, as previously discussed in Sections 10.2 and 10.3, the greatest inundation extents within the waterways for the 500-yr and 2,000-yr ARI in the present study are mostly contributable to the South American events, which were not modelled for the GA study.

Along the coast, the 2,000-yr ARI maximum envelope for the present study shows a greater inundation extent than the 5,000-yr event for the GA study for all the coast except Coolangatta where the present study shows slightly less inundation. Comparison of the 10,000-yr ARI inundation extents for both studies shows similar coastal inundation from the Spit to Miami. The GA study shows a greater inundation extent from Miami to Coolangatta.

For MSL, the inundation extents for the 2,000-yr ARI maximum envelope (present study) and the 5,000-yr event (GA study) are similar except for adjacent to Tallebudgera and Currumbin creeks where the present study shows greater inundation extents. The 10,000-yr ARI inundation extents at MSL are further inland for the present study, except for Nobby Beach.

The GA study also stated that the highest current speeds were found within the Broadwater, Tallebudgera and Currumbin creek entrances and across the beachfront and offshore at Coolangatta and Palm Beach, which is consistent with the present study's findings. For the 10,000-yr event, current speeds may exceed 20 m/s in some areas, while for the 5,000-yr event, speeds are generally less than 15 m/s. Current speeds for the 200-yr event are much lower and rarely exceed 4 m/s. For the present study, maximum currents for the 10,000-yr ARI maximum envelope are typically under 12 m/s. However, currents exceed 20 m/s over the Gold Coast Seaway training walls. For the 2,000-yr ARI maximum envelope, currents are typically less than 10 m/s, but reach 13 m/s within the Gold Coast Seaway entrance. For the 100-yr ARI maximum envelope, currents do not exceed 5 m/s, with the strongest currents within waterway entrances.

Several factors would influence the differences between these two studies, including:

- The two studies were undertaken for different ARI. A direct comparison is only available for the 10,000-yr ARI.
- The present study considered more scenarios from different source zones, whereas the GA study only considered three events from the New Hebrides.
- The stage versus exceedance rate curve has changed since the first iteration of the PTHA08. The PTHA18 maximum water levels at 100 m depth are now higher than in the first iteration.
- The present study utilised a 2 m spatial resolution DEM whereas the GA study used a 30 m DEM.
- The present study used a detailed roughness map based on land use. It is unclear what was used for the GA study.

- A finer mesh was developed and applied here for inland and waterways than that of the GA study.

The comparison highlights the importance of DEM resolution and modelling a large set of scenarios from various major source zones to consider their influence on the hazard at the study site.

11 Conclusion and Recommendations

A total of 90 scenarios were modelled, representing a range of average recurrence intervals (ARIs), water levels (MSL, HAT and SLR) and source zones. The tsunami modelling undertaken has contributed valuable insights into the details of tsunami propagation and potential inundation, affecting areas from South Stradbroke Island to Dreamtime Beach along the Gold Coast and Tweed. Although the mean exceedance rate curve was used to select specific events, it is important to consider the confidence limits associated with these estimates (due to uncertainties in the frequencies of large earthquakes as modelled by PTHA18). For example, the mean 100-yr ARI event is about 0.25 m but could also be between 0.08 and 0.45 metres at Gauge 1574.2 (1000 m depth), the upper limit being close to the mean for 500-yr ARI. Furthermore, our results show that even when the offshore ARI is fixed, the onshore results can vary significantly for different scenarios. Thus, the results herein may change to some extent if using a different set of scenarios. Notwithstanding these limitations, the following key aspects have been identified in this study:

- The stage of tide is important for inundation in the waterways. The adopted HAT level of 1.1 m above MSL inundates low-lying northern Gold Coast and Tweed River areas. As the tide will attenuate in waterways, the results should be considered conservative in these areas.
- There is a relationship between tsunami attenuation in the waterways and tsunami wave period, with decreasing attenuation for longer wave periods. The South American scenarios that were modelled have wave periods in the order of 90 minutes, producing the greatest inundation in the waterways for the 100-yr to 2,000-yr ARI. The inundation extent in the waterways for the 2,000-yr ARI worst-case event was larger than the 10,000-yr ARI inundation. There was no South American scenario for the 10,000-yr ARI because PTHA18 suggested it was very unlikely. While we cannot say that all South American scenarios would exhibit such long wave periods, the results highlight important relations between wave periods and attenuation in the waterways.
- The 100-yr ARI maximum envelope shows little inundation for the MSL case and inundation of low-lying areas within the waterways for the HAT case. Along the coast, the inundation is contained to the beaches and dunes. In the waterways at HAT, inundation affects areas in Couran Cove, Paradise Point, Biggera Waters, Labrador, Surfers Paradise, Currumbin Creek, and Fingal Road.
- The 500-yr ARI maximum envelope shows some inundation for the MSL case that is mostly contained to unpopulated areas adjacent to waterways as well as Marine Parade in Labrador. There is increased inundation of low-lying areas within the waterways for the HAT case. Along the coast at HAT, the inundation is contained to the beaches and dunes. In the waterways there is increased inundation at HAT of the areas identified for the 100-yr ARI, as well as Tallebudgera Creek.
- The 2,000-yr ARI maximum envelope shows increased inundation for the MSL case but considerably more for the HAT case. For MSL, there is increased inundation of unpopulated low-lying areas adjacent to waterways as well as populated areas adjacent to the Broadwater, Tallebudgera Creek, Currumbin Creek and The Spit. Along the coast at HAT, there is inundation of The Spit, Main Beach, Surfers Paradise, Broadbeach, Nobby Beach, Palm Beach, Kirra, Coolangatta and Letitia Spit. In the waterways there is increased inundation at HAT of the areas identified for the 500-yr ARI, as well as Hope Island, Main Beach, Chevron Island, low lying areas behind Palm Beach, and Tweed Heads South.
- The 10,000-yr ARI maximum envelope shows extensive inundation for both the MSL and HAT case. Considerable inundation occurs over the entire coast. In the waterways the inundation extent is less than the 2,000-yr ARI case due to no South American event being modelled at an ARI of 10,000 years (as PTHA18 suggested it was very unlikely).
- Arrival times are governed by the subduction zone from which they were generated. Those from the Outer-rise New Hebrides and Puysegur have the shortest arrival time of just over 3.5 hours, while events from South America take over 18 hours to arrive.
- Once the leading wave reaches the coast, the additional time it takes to reach upstream locations within the waterways varies between 30 minutes and 2 hours, depending on the distance travelled and the depth of the waterway.
- The first wave is not necessarily the largest. The largest wave may occur several hours after the leading wave reaches the coast. For the New Hebrides and Outer-rise New Hebrides sources, the largest wave was either the first wave or within 2 hrs of the first wave. For the other source zones the largest wave was within 2 to 14 hrs after the arrival of the first wave.
- There are strong currents that develop within the waterway entrances. As the ARI increases, very strong currents develop along the coast and over inundated areas. These currents can reach up to 12 m/s.
- The marine hazard within waterway entrances and along the coast increases with increasing ARI.
- For the 10,000-yr ARI, dangerous currents develop over the top of entrance training walls.
- Maximum water levels (above the still water level, SWL) on the coast range from 0.5 m (100-yr ARI) to 9 m (10,000-yr ARI). At 5 m depth, the maximum water levels range from 0.4–7.1 m. Upstream of the larger waterways there is considerable attenuation such that maximum water levels are in the order of 0.1–1 metres. There is less attenuation in Tallebudgera and Currumbin Creeks, most likely due to their shorter length.

- The events from South America are unique in that they are very long-period waves (wave period in the order of 90 min), and their amplitudes appear to increase with subsequent waves for the Gold Coast region. It is plausible that the 90 min period of the South American events produces some shelf resonance, leading to the growth in amplitude for subsequent waves, which is not apparent from the offshore time series or to the south of the Gold Coast. This pattern is similar across all ARI modelled, although we cannot conclude that all South American scenarios would exhibit such long periods.
- Although not modelled, there is potential for shorter steep waves to form with the tsunami in areas where the tsunami wave steepens significantly.
- Sea level rise (SLR) associated with climate change will increase inundation extents. This is especially so in the waterways for low-lying areas that are susceptible to changes in still water level (SWL). The increase in SWL shows a decrease in maximum water levels (above the SWL) along the coast, so most of this increase is associated with the increase in SWL. This scenario only considers the existing topography and does not consider possible future remediation works that may be undertaken to offset the impacts of SLR.

The use of a static water level to represent tide levels may not be suitable for low-lying areas upstream of waterways where tidal attenuation may occur. The underlying DEM may also not be sufficient to capture the height of riverbanks. This is particularly so with the 5 m DEM for Tweed Shire Council. Raising the water level to the adopted HAT level shows widespread inundation in the upper reaches of the Tweed River. Although the model was developed to capture the ridges of riverbanks, the resolution may not fully capture the height of the riverbank. The inundation in these areas will be conservative and should be consider when making any decisions.

The developed overland DEM is a fixed bare earth model in that only ground points have been included, thereby removing all structures and vegetation. The influence of these features on inland inundation is introduced implicitly by the introduction of roughness factors. The DEM is also assumed to be static and non-erodible. Should a tsunami cause significant erosion of the dune system or entrance shoals to waterways, then the extent of inundation may differ to these model results. The hazard considered relates to potential inundation and broad-scale currents. There may be secondary impacts associated with the tsunami such as coastal erosion, which have not been addressed in this study.

The events selected represent the mean of the maximum water levels for the chosen ARI based on the revised PTHA. Higher levels can occur within the confidence limits. Disaster managers may wish to consider appropriate factors of safety in any decisions based on the information provided through this study.

Overall, the study provides planners and disaster managers with a better understanding of the potential tsunami hazard within the Gold Coast and northern Tweed areas.

12 Glossary

AEST	Australian Eastern Standard Time
ARI	Average Recurrence Interval
ATWS	Australian Tsunami Warning System
BoM	Bureau of Meteorology
DEM	Digital Elevation Model
DES	Queensland Department of Environment and Science
DHI	Danish Hydraulic Institute
DSITIA	Queensland Department of Science, Information Technology, Innovation and the Arts
EHP	Queensland Department of Environment and Heritage Protection
EMA	Emergency Management Australia
EPA	Queensland Environmental Protection Agency
GA	Geoscience Australia
GBR	Great Barrier Reef
HAT	Highest Astronomical Tide
JATWC	Joint Australian Tsunami Warning Centre
IofA	Index of Agreement
LGA	Local Government Authority (or Area)
MSL	Mean Sea Level
NDMP	Natural Disaster Mitigation Program
NDRP	Natural Disaster Resilience Program
NOAA	National Oceanic and Atmospheric Administration
NSW	New South Wales
NTHA	Nearshore Tsunami Hazard Assessment of Australia
PTHA	Probabilistic Tsunami Hazard Assessment of Australia
R2	Coefficient of Determination
RANSE	Reynolds averaged Navier-Stokes equations
RMSE	Root Mean Square Error
SEQ	South-east Queensland
SWL	Still Water Level
TsuDAT	Tsunami Data Access Tool
USGS	United States Geological Survey

13 References

Australian Bureau of Statistics (ABS), 2022. 2021 Census Data by Local Government Areas, URL: https://abs.gov.au/census/find-census-data/quickstats/2021/LGA33430

Australian Institute for Disaster Resilience (AIDR), 2018. Australian Disaster Resilience: Tsunami hazard modelling guidelines, Australian Government, p 49.

Beaman, R.J., 2010. Project 3DGBR: A high-resolution depth model for the Great Barrier Reef and Coral Sea. Marine and Tropical Sciences Research Facility (MTSRF) Project 2.5i.1a Final Report, MTSRF, Cairns, Australia, p 13 plus Appendix 1. Available at: http://www.deepreef.org/images/stories/publications/reports/Project3DGBRFinal_RRRC2010.pdf

Boswood, P.K., 2013a. Tsunami Modelling along the East Queensland Coast, Report 1: Regional Modelling. Brisbane: Department of Science, Information Technology, Innovation and the Arts, Queensland Government, p 111.

Boswood, P.K., 2013b. Tsunami Modelling along the East Queensland Coast, Report 2: Sunshine Coast. Brisbane: Department of Science, Information Technology, Innovation and the Arts, Queensland Government, p 96.

Boswood, P.K., 2013c, Tsunami Modelling along the East Queensland Coast, Coasts and Ports 2013, Engineers Australia, Sydney, 13–15 November, p 7.

Boswood P.K., Wall R., Peach L. 2018. Tsunami Modelling along the East Queensland Coast, Report 3: Moreton Bay. Brisbane: Department of Environment and Science, Queensland Government.

Boswood P.K., Wall R., Peach L. 2019. Tsunami Modelling along the East Queensland Coast, Report 4: Hervey Bay. Brisbane: Department of Environment and Science, Queensland Government.

Bricker, J.D., Gibson, S., Takagi, H., and Imamura, F., 2015. On the Need for Larger Manning's Roughness Coefficients in Depth-Integrated Tsunami Inundation Models. Coastal Engineering Journal, volume 57(2), June, p 13, https://doi.org/10.1142/S0578563415500059

Bunya, S., Deitrich, J.C., Westerink, J.J., Ebersole, B.A., Smith, J.M., Atkinson, J.H., Jensen, R., Resio, D.T., Luettich, R.A., Dawson, C., Cardone, V.J., Cox, A.T., Powell, M.D., Westerink, H.J., and Roberts, H.J., 2010. A High-Resolution Coupled Riverine Flow, Tide, Wind, Wind Wave, and Storm Surge Model for Southern Louisiana and Mississippi. Part I: Model Development and Validation, Monthly Weather Review, Vol. 18, pp 345–377.

Burbidge, D., Cummins, P., Mleczko, R., and Thio, H., 2008b. A Probabilistic Tsunami Hazard Assessment for Western Australia, Pure and Applied Geophysics 165 (11), pp 2059–2088.

Burbidge, D., Mleczko, R., Thomas, C., Cummins, P., Nielsen, O., and Dhu, T., 2008a. A Probabilistic Tsunami Hazard Assessment for Australia, Geoscience Australia Professional Opinion 2008/04.

Cardno, 2013. NSW Tsunami Inundation Modelling and Risk Assessment, Report prepared for the NSW State Emergency Service and the Office of Environment and Heritage, p 64.

Charvet, I., Macabuag, J., and Rossetto, T., 2017. Estimating Tsunami-Induced Building Damage through Fragility Functions: Critical Review and Research Needs, Front. Built Environ., Vol 3(36), p 22, doi: 10.3389/fbuil.2017.00036.

Charvet, I., Suppasri, A., Kimura, H., Sugawara, D., and Imamura, F, 2015. Fragility estimations for Kesennuma City following the 2011 Great East Japan Tsunami based on maximum flow depths, velocities and debris impact, with evaluation of the ordinal model's predictive accuracy, Nat.Hazards 79, pp 2073–2099, doi:10.1007/s11069-015-1947-8.

Dames and Moore, 1980. Design and Construction Standards for Residential Construction in Tsunami-Prone Areas in Hawaii, prepared by Dames & Moore for the Federal Emergency Management Agency, Washington D.C.

Davies, G., 2019. Tsunami variability from uncalibrated stochastic earthquake models: tests against deep ocean observations 2006-2016, Geophysical Journal International, 218, pp 1939–1960.

Davies, G., and Griffin, J., 2018. The 2018 Australian probabilistic tsunami hazard assessment: hazard from earthquake generated tsunamis. Record 2018/41. Geoscience Australia, Canberra, p 182. http://dx.doi.org/10.11636/Record.2018.041

Davies, G., and Griffin, J., 2020, Sensitivity of Probabilistic Tsunami Hazard Assessment to Far-Field Earthquake Slip Complexity and Rigidity Depth-Dependence: Case Study of Australia, Pure and Applied Geophysics, 177, pp 1521–1548.

Davies, G., Griffin, J., Løvholt, F., Glimsdal, S., Harbitz, C., Thio, H.K., Lorito, S., Basili, R., Selva, J., Geist, E., and Baptista, M.A., 2017. A global probabilistic tsunami hazard assessment from earthquake sources, In: Tsunamis:

Geology, Hazards and Risks, Geological Society, London, Special Publications (2018), 456 (1): 219 https://doi.org/10.1144/SP456.5

Davies, G., Romano, F., and Lorito, S., 2020. Global Dissipation Models for Simulating Tsunamis at Far-Field Coasts up to 60 hours Post Earthquake: Multi-Site Tests in Australia, Frontiers in Earth Sci. 8:598235, doi: 10.3389/feart.2020.598235.

Department of Environment and Heritage Protection (EHP), 2013. Coastal Hazard Technical Guide, Determining Coastal Hazard Areas, Queensland Government, p 18.

Department of Science, Information Technology and Innovation (DSITI), 2017. Meteotsunami in Queensland, Coastal Impacts Unit, p 2.

Department of Tourism, Innovation and Sport (DTIS), 2022. Gold Coast, URL: https://www.dtis.qld.gov.au/your-region/gold-coast

DHI, 2017a. MIKE 21 & MIKE 3 Flow Model FM, Hydrodynamic and Transport Module, Scientific Documentation, Mike Powered by DHI, October, p 64.

DHI, 2017b. MIKE 21 & MIKE 3 Flow Model FM, Hydrodynamic Module, User Guide, Mike Powered by DHI, p 148.

Edwards, M. R., Arthur, C., Wehner, M., Allen, N., Henderson, D., Parackal, K., Dunford, M., Mason, M., Rahman, M., Hewison, R., Ryu, H., Corby, N., and Butt, S., 2022. Severe Wind Hazard Assessment for South East Queensland: Technical Report. Record 2022/45. Geoscience Australia, Canberra. http://dx.doi.org/10.11636/Record.2022.045

Environmental Protection Agency (EPA), 2007. Solomon Islands tsunami, Fact Sheet, FS 2007-2, May, p 3.

Fountain, L., Griffin, J., Van Putten, K., Sexton, J., Nielsen, O., and Wilson, R., 2009a. Capacity building for tsunami planning and preparation: inundation models for the Gold Coast, Geoscience Australia Professional Opinion 2009/08.

Fountain, L., Van Putten, K., Griffin, J., Hingee, M., Wilson, R., Burbidge, D., Sexton, J., Nielsen, O., and Mleczko, R., 2009b. A Nearshore Tsunami Hazard Assessment for Australia, Geoscience Australia Professional Opinion 2009/06.

Geoscience Australia (GA), 2010. Tsunami Data Access Tool (TsuDAT) User Guide, Version 1.0, p 27.

Geoscience Australia (GA), 2017. High-resolution depth model for the Great Barrier Reef – 30m, URL: http://pid.geoscience.gov.au/dataset/115066

Giblin, J.; Damlamian, H.; Davies, G.; Weber, R. & Wilson, K., 2022. Earthquake Scenario Selection for Tsunami Inundation Hazard Assessment: Guidelines on using the 2018 Probabilistic Tsunami Hazard Assessment in the Pacific, SPC and Geoscience Australia, https://repository.oceanbestpractices.org/handle/11329/2062

Goff, J.; Borrero, J. & Easton, G., 2022. In search of Holocene trans-Pacific palaeotsunamis, Earth-Science Reviews, 233, 104194.

González, F.I., Geist, E.L., Jaffe, B., Kanoglu, U., Mofjeld, H., Synolakis, C.E., Titov, V.V., Arcas, D., Bellomo, D., Carlton, D., Horning, T., Johnson, J., Newman, J., Parsons, T., Peters, R., Peterson, C., Priest, G., Venturato, A., Weber, J., Wong, F., and Yalciner, A., 2009. Probabilistic tsunami hazard assessment at Seaside, Oregon, for near- and far-field seismic sources, J. Geophys. Res., 114 (C11023), doi: 10.1029/2008JC005132

Hall, G., Stevens, R., and Sexton, J., 2008. Tsunami planning and preparation in Western Australia: application of scientific modelling and community engagement, The Australian Journal of Emergency Management, Vol. 23 No. 4, November, p 7.

Hayes, G. P.; Moore, G. L.; Portner, D. E.; Hearne, M.; Flamme, H.; Furtney, M. and Smoczyk, G. M., 2018. Slab2, a comprehensive subduction zone geometry model, Science.

Hayes, G.P., Wald, D.J., and Johnson, R.L., 2012. Slab1.0: A three-dimensional model of global subduction zone geometries, J. Geophys. Res., 117, B01302, doi:10.1029/2011JB008524.

Horrillo, J., Grilli, S.T., Nicolsky, D., Roeber, V., and Zhang, J., 2014. Performance Benchmarking Tsunami Models for NTHMP's Inundation Mapping Activities, Pure and Applied Physics, July, p 16, DOI 10.1007/s00024-014-0891-y.

Intergovernmental Oceanographic Commission (IOC), 2016. Tsunami Glossary, Third Edition, Paris, UNESCO, IOC Technical Series 85. (English, French, Spanish, Arabic, Chinese) (IOC/2008/TS/85 rev.2).

Josephson, J. P., 1878. Some facts about the Great Tidal Wave, May 1877, Journal and proceedings of the Royal Society of New South Wales, 12, pp 103–116.

Kain, C.L., Lewarn, B., Rigby, E.H., and Mazengarb, C., 2020. Tsunami Inundation and Maritime Hazard Modelling for a Maximum Credible Tsunami Scenario in Southeast Tasmania, Australia, Pure Appl. Geophys. 177, pp 1549–1568.

Koshimura, S. and Yanagisawa, H. 2007. Developing fragility curves for tsunami damage estimation using the numerical model and satellite imagery, Proceedings of the 5th International Workshop on Remote Sensing for Disaster Response, George Washington University, Washington, United States, 10–12 September.

Koshimura, S., Matsuoka, M., and Kayaba, S. 2009a. Tsunami hazard and structural damage inferred from the numerical model, aerial photos and SAR imageries, Proceedings of the 7th International Workshop on Remote Sensing for Post Disaster Response, University of Texas, Texas, United States, 22–23 October.

Koshimura, S., Oie, T., Yanagisawa, H., and Imamura, F. 2009b. Developing fragility curves for tsunami damage estimation using numerical model and post-tsunami data from Banda Aceh, Indonesia, Coast. Eng. J., 51, pp 243–273.

Luger, S.A., and Harris, R.L., 2010. Modelling Tsunamis Generated by Earthquakes and Submarine Slumps Using MIKE 21, International MIKE by DHI Conference, Copenhagen, 6–8 September 2010, p 13.

Lynam, C. 2020. On a Fine Day in Shorncliffe the Sea Came Boiling Upwards Across the Bathers ..., Proceedings of The Royal Society of Queensland, 128.

Lynett, P. J., Borrero, J., Son, S., Wilson, R., and Miller, K., 2014. Assessment of the tsunami-induced current hazard, Geophys. Res. Lett., 41, pp 2048–2055, doi:10.1002/2013GL058680.

Maqsood, T., Wehner, M., Ryu, H., Edwards, M., Dale, K. and Miller, V., 2014. *GAR15 Vulnerability Functions: Reporting on the UNISDR/GA SE Asian Regional Workshop on Structural Vulnerability Models for the GAR Global Risk Assessment, 11–14 November, 2013, Geoscience Australia, Canberra, Australia*. Record 2014/38. Geoscience Australia: Canberra. http://dx.doi.org/10.11636/Record.2014.038

Maritime Safety Queensland (MSQ), 2022. Queensland Tide Tables: Standard Port Tide Times 2023, Department of Transport and Main Roads, Queensland Government, p 132, URL: https://www.msq.qld.gov.au/Tides/Tide-tables

Ministry of Civil Defence & Emergency Management, 2016. Tsunami Evacuation Zones, Director's Guideline for Civil Defence Emergency Management Groups [DGL 08/16], New Zealand, pp 46.

MLITT, 2012. Guide to determining the potential tsunami inundation, Seacoast Office, Water and Disaster Management Bureau, Ministry of Land, Infrastructure, Transport and Tourism, Version 2.0 (temporary translation), p 82.

Mofjeld, H.O., Symons, C.M., Lonsdale, P., González, F.I., and Titov, V.V., 2004. Tsunami Scattering and Earthquake Faults in the Deep Pacific Ocean, Oceanography, Vol 17(1), pp 38–46.

Mofjeld, H.O., González, F.I., Titov, V.V., Venturato, A.J., and Newman, J.C., 2007. Effects of Tides on Maximum Tsunami Wave Heights: Probability Distributions, J. Atmos. Oceanic Technol., 24, 117–123, https://doi.org/10.1175/JTECH1955.1

Murata, S., Imamura, F., Katoh, K., Kawata, Y., Takahashi, S., Takayama, T. (eds), 2010. Tsunami: To Survive from Tsunami, Advanced Series on Ocean Engineering, Volume 32, World Scientific, p 302.

Nanayakkara, K.I.U. and Dias, W.P.S., 2013. Fragility curves for tsunami loading, International Conference on Structural Engineering & Construction Management, Kandy.

NOAA, 2018. Tsunami: The Tsunami Story (web page accessed 2018), URL: https://www.tsunami.noaa.gov/tsunami_story.html.

Power, W.L. (compiler), 2013. Review of Tsunami Hazard in New Zealand (2013 update), GNS Science Consultancy Report 2013/131, p 222.

Rynn, J.M.W., 1994. Tsunamis and their effect on Australia, IN: *Proceedings National Tsunami Workshop*, Brisbane, 25 August 1994.

Standards Australia, 2005. Guidelines for the design of maritime structures, AS 4997-2005.

Takahashi, S., 2005. Tsunami disasters and their prevention in Japan – Toward the performance design of coastal defences, Proc International Symposium on Disaster Reduction on Coasts, Monash University, Melbourne, Australia.

Tsunami Pilot Working Group, 2006. Seaside, Oregon Tsunami Pilot Study – Modernization of FEMA flood hazard maps, NOAA OAR Special Report, NOAA/OAR/PMEL, Seattle, p 94.

United Nations Office for Disaster Risk Reduction (UNISDR), 2017. Words into Action Guidelines: National Disaster

Risk Assessment, 2. Tsunami Hazard and Risk Assessment, p 9.

UNESCO, 2015. Tsunami risk assessment and mitigation for the Indian Ocean; knowing your tsunami risk – and what to do about it, IOC Manual and Guides No 52, Second Edition, p 160.

Webster, M.A., and Petkovic, P., 2005. Australian bathymetry and topography grid, Geoscience Australia Record 2005/12, June, p 27, URL: http://www.ga.gov.au/meta/ANZCW07030080022.html

Wijetunge, J.J., 2009. Demarcation of High Hazard Areas Based on Human Stability Considerations in Tsunami Overland Flow, Engineer, Vol XXXXII (01), Institute of Engineers, Sri Lanka, pp 45–52.

Appendix A Tsunami Dynamics

A.1 Introduction

To better understand tsunami hazard, this section will briefly describe the processes that influence tsunamis. In basic terms, a tsunami is a series of long-period waves generated by a disturbance in the ocean water column arising from abrupt geophysical events. These disturbances are more likely from movement of tectonic plates along faults in the form of submarine earthquakes, but could also be from submarine landslides, volcanic eruptions, or a possible meteorite strike (in the extreme). More than 80 per cent of the world's tsunamis were caused by earthquakes (IOC, 2016). The earthquake scenario is the focus of this report.

A simple analogy would be dropping a pebble in a pond. The pebble generates a deformation of the water surface. This in turn creates a wave or series of waves that radiate or spread away from the source in concentric circles of increasing circumference as they propagate away. As the circumference increases, the amplitude decreases or attenuates due to energy being transferred along the wave crest. In reality, tsunami generation is not a point source but a complex pattern of bed movements. The three main phases are tsunami generation, propagation, and run-up/inundation. These phases will be briefly described below.

The following discussion has attempted to keep the subject matter as basic as possible. However, the topic itself can be complex, and so there is a need to provide some technical content for completeness.

A.2 Tsunami Generation

A.2.1 Earthquake

The main source of tsunamigenic earthquakes (that is, capable of generating tsunami) that have notable effects on Queensland come from the so called 'Ring of Fire', also referred to as the circum-Pacific seismic belt. It is a collection of oceanic trenches, volcanoes and plate movements along the rim of the Pacific Ocean and is responsible for about 70 per cent of the world's tsunamis (IOC, 2016). There are 3 types of plate boundaries: convergent boundaries (where 2 plates are colliding); divergent boundaries (moving apart); and transform boundaries (plates sliding horizontally passed each other) (Figure A. 1). The oceanic crust of a convergent boundary is denser than the continental crust and will be thrust beneath the continental shelf to form subduction zones. Friction between the plates opposes movement until energy build up causes the plates to suddenly slip past one another, generating an earthquake. The surface where the slip occurs is referred to as the fault and energy radiates outward from the fault in all directions in the form of seismic waves that can last for minutes.
The magnitude of the earthquake is related to the length of the fault and the amount of slip. The location or epicentre and time of initiation of the earthquake can be determined from triangulation of available seismogram recordings based on the primary (P-wave) and secondary (S-wave) waves (Kayal, 2006 and USGS, 2018a).

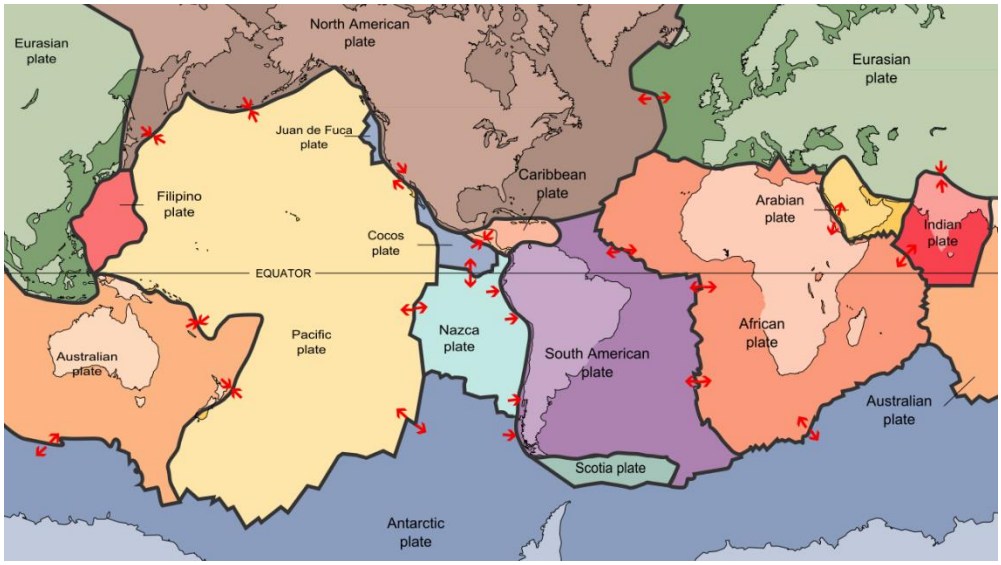

Figure A. 1 – Tectonic plates (source: http://pubs.usgs.gov/publications/text/slabs.html).

In general, a subduction zone slip results in the leading edge of the overriding plate (typically the continental plate) breaking free from its grip with the inducting plate, and to spring seaward. This generates a vertical rise in the full water column, which splits to propagate as a tsunami in all directions (Figure A. 2). Although the tsunami will

propagate out in all directions from the generating area, the main energy propagation is generally orthogonal to the direction of the earthquake fracture zone (IOC, 2016).

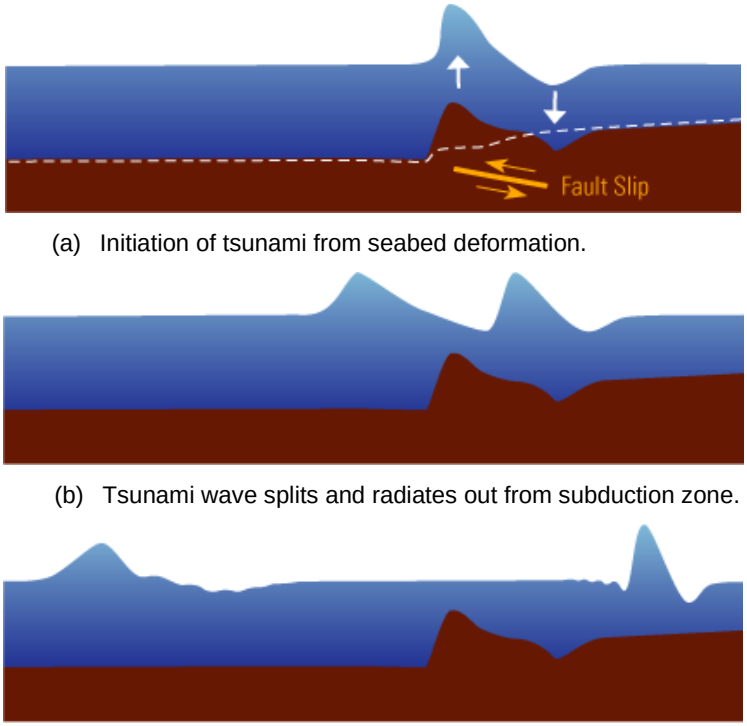

(a) Initiation of tsunami from seabed deformation.

(b) Tsunami wave splits and radiates out from subduction zone.

(c) Deep water wave travels faster, whilst shallow wave shoals.

Figure A. 2 – Tsunami generation (distorted scale) (source: https://walrus.wr.usgs.gov/tsunami/basics.html)

As well as the uplift of the seabed, there can also be some subsidence of the overriding plate as shown in Figure A. 2. Communities that experience the tsunami on the continental shelf side (right in Figure A. 2) will experience a drawdown of the ocean prior to the tsunami reaching the coast. Communities to the left will not experience a drawdown prior to the tsunami. However, this is a simplified explanation, and several factors will influence tsunami generation.

A commonly adopted model for tsunami generation is to discretise the fault area into rectangular sub-faults. The deformation of the seafloor is then defined for each sub-fault using a planar fault model (Okada, 1985 and 1992), which considers parameters such as the depth below the seabed, orientation, and slip (Yamazaki, 2010). For specific events, tsunami waveform inversion analysis such as that proposed by Satake (1987) are used to estimate fault slip distribution (Adriano et al., 2018), as illustrated in Figure A. 3 for the 2016 Fukushima earthquake. The fault model as well as the initiation and rise time for each sub-fault are then used to determine the temporal and spatial seabed deformation, which is translated to sea surface displacement.

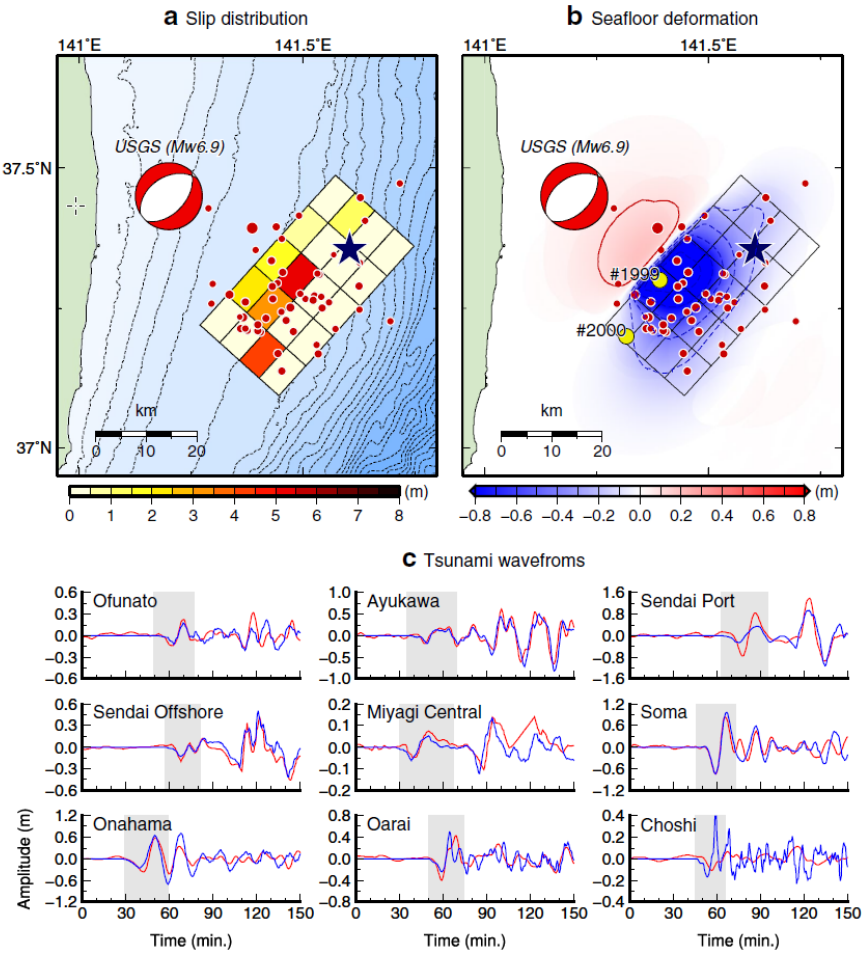

Figure A. 3 – Slip distribution, seafloor deformation and resulting tsunami fit to measurements from an inversion analysis for the 2016 Fukushima Earthquake (Adriano et al., 2018).

Tsunamis amplitudes are governed by the seabed deformation, whereas wave periods are determined by the fault area. Tsunami have very long wavelengths of tens to hundreds of kilometres as the abrupt bottom movements that generated them have large horizontal scales (hundreds of kilometres). Multiple reflections and partial wave trapping, especially near the source, produce an extended wave train of many waves even though the original source was a single impulse. The latter waves in a tsunami wave train form very complicated patterns in which it is difficult to determine the relationship of a latter wave to the initial source. Hence, only the observations of the first few waves at a site are used for comparison with model simulations and estimation of the earthquake source parameters, (Mofjeld et al., 2004), and comparisons of models and observations for late arriving waves tend to focus on summary statistics rather than detailed agreement of time-series (Davies et al., 2020).

A.2.2 Landslide

Although not considered in this study, an introduction into tsunami generation would not be complete without mentioning tsunami generated from landslides. Submarine landslides can occur on continental slopes and are similar to those that occur on land. They can be triggered by earthquakes. The tsunami that devastated Papua New Guinea in 1998 was much greater than expected for the magnitude 7 earthquake that preceded it. A subsequent seafloor survey indicated that a submarine landslide may have been triggered by the earthquake (González, 1999; Synolakis et al., 2002; Bernard et al., 2006; and Tappin et al., 2008), resulting in the unusually high tsunami waves.

The earthquake triggers a mass of seabed to break away and travel down the continental slope by gravity. As with earthquake generated tsunami, this in turn generates a movement in the column of water above the slide.
The tsunami that is generated is related to several factors such as the dimensions of the failed mass and the speed and distance this mass travels down the slope. The closer the landslide speed is to the wave speed, the larger the tsunami (Geist et al., 2009). The impact zone of a tsunami generated by submarine landslide is typically more localised than that generated by earthquakes. As the continental shelf can be narrow, the land adjacent to the landslide may be impacted by powerful tsunamis with little warning. The Papua New Guinea event produced runup heights of over 10 m for a 25 km stretch of coastline, killing over 2,100 people (Synolakis et al., 2002). The tsunami will also travel offshore. Refraction processes as well as coastal and shelf trapped waves may result in tsunamis being felt at further distances for an extended duration. However, the largest waves will occur along the coastline within the immediate vicinity of the landslide.

Geist et al. (2009) found that for continental slope landslides, frequency dispersion and nonlinearity are important in modelling tsunami evolution. They modelled the Currituck landslide in North America with a 1D high resolution model based on the fully nonlinear Boussinesq equations, to show the formation of short period fission waves riding on the tsunami (discussed further in Section A.4) before it breaks into a tsunami bore.

A.3 Tsunami Propagation

A.3.1 Transoceanic Propagation

The resulting earthquake-generated tsunami propagates as a set of waves whose energy is concentrated at wavelengths corresponding to the earth movements (~100 km), at wave heights determined by vertical displacement (but typically <1 m far from the immediate source zone), and at wave directions determined initially by fault shape and orientation, and later by the adjacent coastline geometry. Because each earthquake is unique, every tsunami has unique wavelengths, wave heights, and directionality (NOAA, 2018a).

As the displacement occurs through the entire water column, and wave lengths are much greater than depth, the tsunami behaves as a shallow water wave even in deep water. From linear shallow water wave theory, the speed of the tsunami can be calculated from:

$$c = \sqrt{gD}$$

Equation A.1

Where c is the wave celerity (m/s), g is the acceleration by gravity (about 9.81 m/s^2) and D is depth (m).
This means that the tsunami in deep water can travel very fast (in the order of 600–800 km/hr in 3,000–5,000 m depth).

The wave period is generally in the range of 5 to 40 minutes. If the wave has to travel considerable distances, the shorter period wave energy will dissipate more. Therefore, the period of the tsunami increases with distance travelled. Periods of up to one hour were observed in Japan following the Great Chilean Earthquake of 1960 (Murata et al., 2010).

As the waves propagate away from the source in deep water, they also spread (as in the pebble analogy), causing some attenuation. As tsunamis are sensitive to water depth variations at all ocean depths, submarine features will influence the wave train. Wave refraction (described below) will occur at all depths. Linear features such as such as escarpments and ridges can act as wave guides, redirecting and concentrating wave energy. Other features such as seamounts can scatter wave energy. Basically, submarine features that extend to within 500 m depth can cause significant wave scatter (Mofjeld et al., 2004). Mofjeld et al. (2000 and 2001) mapped the distribution of a scattering index within the Pacific Ocean. They found that the south-western Pacific exhibits the highest density of significant scatter features, which includes Australia, such that any tsunami within this region will experience strong scattering with a tendency to become trapped.

In addition to the above processes, oceanic islands will reflect and scatter wave energy. These processes tend to complicate and extend the tsunami wave train as it approaches the Australian continental slope. At this stage, amplitudes are relatively small and so may go unnoticed by a ship.

A.3.2 Continental Shelf Propagation

As the tsunami reaches the continental slope, the depth can change drastically and abruptly compared to the long wavelength. In general, the tsunami may experience the same processes to that of short period waves, not limited to attenuation, shoaling, scattering, focusing, diffraction, reflection, and resonance, but at a larger scale. The more significant processes will be briefly described below.

A.3.2.1 Refraction, Shoaling and Reflection

As the tsunami approaches shallower water it will slow down, thereby adjusting direction such that the crest will tend to become more parallel with the contours (known as refraction). As the wave slows down, the amplitude will increase (shoaling). For steep coastlines (narrow continental self), such as south-east Queensland, the tsunami amplitude can increase considerably as there is less dissipation as the wave approaches. In areas where there is a wide and shallow continental shelf, or fringing reefs, the wave may dissipate. However, the wave may again increase as it reaches the shoreline due to shoaling. A first approximation of the shoaling wave height from linear wave theory is Green's Law (Synolakis and Skjelbreia, 1993; Geist, 1998; Truong, 2012; and Bryant, 2014):

$$\frac{H_1}{H_o} = \left[\frac{d_o}{d_1}\right]^{1/4}$$

Equation A.2

Where H_1 is the wave height at the intermediate depth, d_1 and H_o is the deep-water wave height at depth d_o.

As the tsunami approaches the coastline, it is influenced by coastal features and nearshore bathymetry. Refraction can focus energy on features such as prominent headlands or diverge energy such as the back beach of an embayment. Complex bathymetry may also cause crossing (superposition) of waves, generating localised amplification. Another feature of tsunami is they can reflect off the coastline. Unlike short waves, which steepen, break, and dissipate on beaches; the length to wave height ratio of tsunamis rarely steepens to breaking point. The tsunami approaches the coast without breaking. Energy is transferred to run-up (refer next section) and reflections. If the coastline is of steep rocky headlands, the reflection will be more pronounced. The reflected wave can then be redirected by refraction and again returns to the coast (Murata et al., 2010). This can occur in V-shaped bays, resulting in higher-than-expected tsunami heights at the back beach as demonstrated in Figure A. 4. There is also potential for amplification within bays should the period of the tsunami be close to a harmonic of the natural period of the bay. If the tsunami travels along a solid surface such as a rocky headland, Mach-stem waves may occur, greatly amplifying the tsunami against the steep surface (Bryant, 2014).

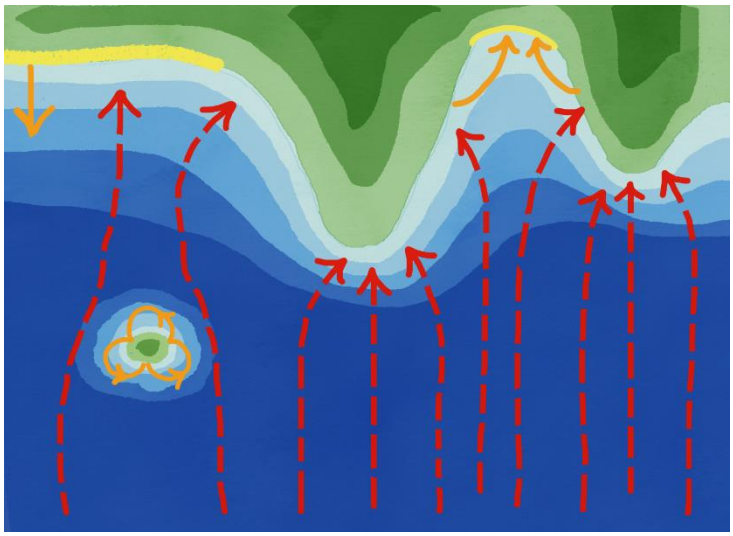

Figure A. 4 – Schematic representation of refraction (red) and reflection (orange) of a tsunami. The curving near the islands is an indication of diffraction.

A.3.2.2 Trapped Waves

A trapped wave is a wave that becomes bound by a particular feature, whether it be the coastline (coastal trapped waves), or the abrupt change in bathymetry (shelf trapped waves). For steep continental shelves where there is an abrupt change in depth over a length scale that is shorter than the tsunami wavelength, there can be partial reflection of the tsunami as it approaches the shelf, and then a further reflection from the coast. This bouncing back and forth is called shelf trapping (Figure A. 5). This process can also occur due to refraction when the tsunami is reflected at an angle to the coast. As the oblique reflected wave reaches the shelf, the rapid depth changes on the continental slope can cause the wave to refract back further along the coast in a leapfrogging pattern (a pattern analogous to skipping a pebble across the water surface).

Coastal trapped or edge waves are surface gravity waves that are trapped against a rigid body (the coastline) by refraction. In the offshore direction, the wave height diminishes rapidly, depending on the wavelength and mode. The fundamental mode (n = 0) producing an exponential decay offshore. Figure A. 6 provides an example of the theoretical profile of the first four modes based on the theory provided in Mei et al. (2005) and González et al. (1995), and in three dimensions in Figure A. 8, while Figure A. 7 shows modelled wave profiles off the coast of North Stradbroke Island for a hypothetical event originating from the Kermadec-Tonga subduction zone.

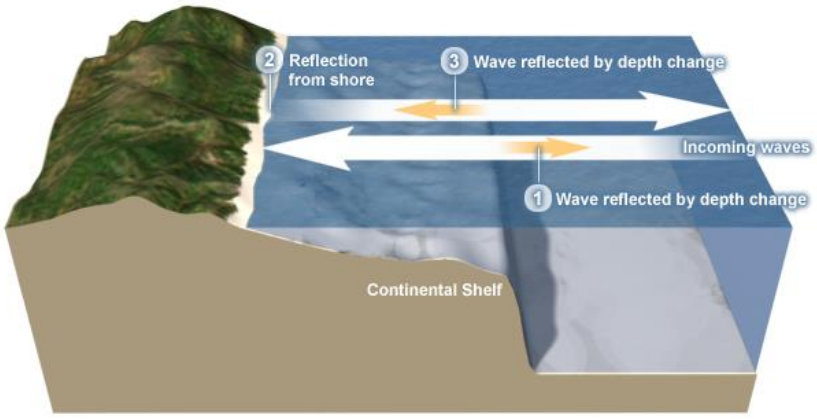

Figure A. 5 – Shelf trapping mechanism (source: COMET® Website at http://meted.ucar.edu/ of the University Corporation for Atmospheric Research (UCAR)).

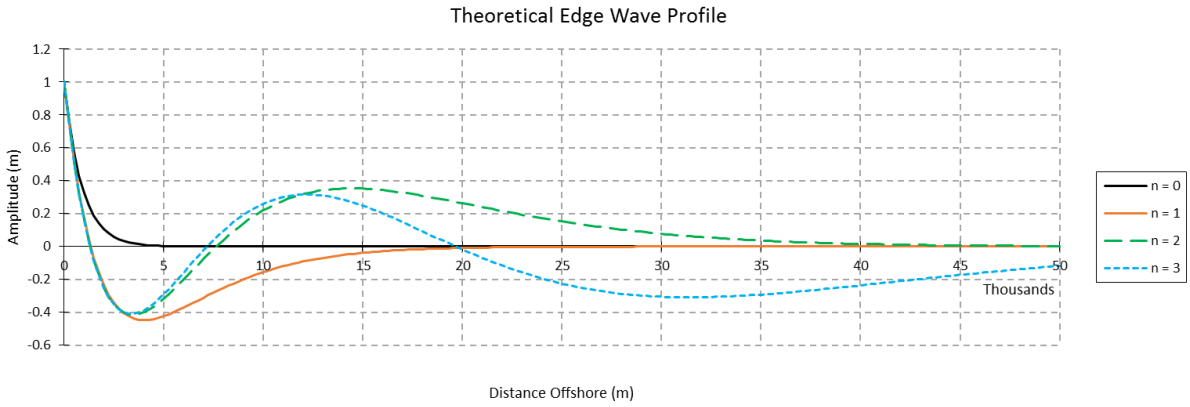

Figure A. 6 – Theoretical edge wave offshore profile for the first four modes (n = 0 to 3) of a long wave (Amplitude = 1m, Period = 10 min).

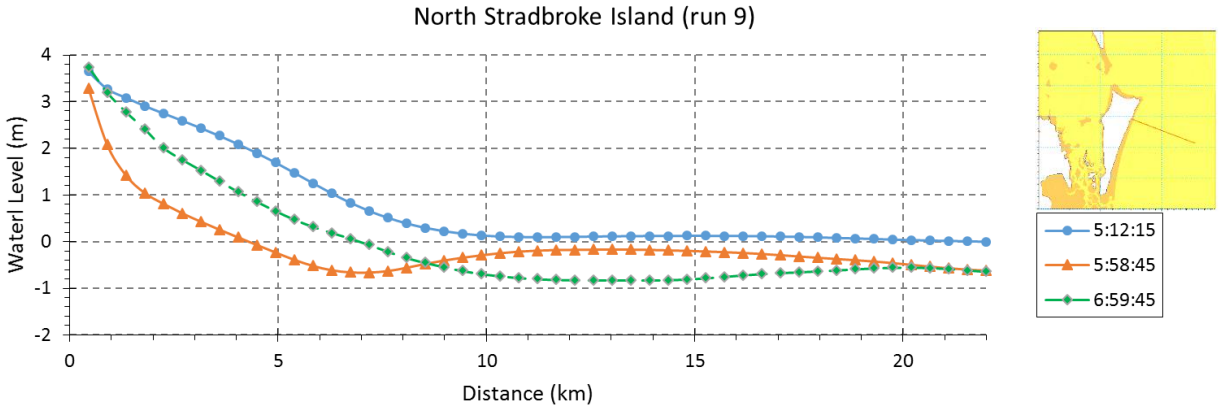

Figure A. 7 – Modelled coastal trapped wave profiles generated off North Stradbroke Island by a hypothetical 3,000-year ARI event from the Kermadec-Tonga subduction zone (times given in hr:min:sec after initial generation).

Coastal trapped waves can be described as either standing (stationary in space but oscillating in time) or progressive (moving along the coastline). However, the progression of these waves is greatly affected by the complexity of the coastline. Progressive edge waves can be steered or guided by sudden drop-off in bathymetry such as the continental shelf.

Coastal and shelf trapped waves have been found to be important phenomena in understanding tsunami hazard along the coastline. The trapped and incident wave can interact, such that the wave train will be complex, of longer duration, and vary along the coast. More importantly, the constructive interaction between edge waves and the non-trapped modes of the tsunami can produce higher than expected secondary waves and associated run-up (Geist, 1998). The literature refers to two broad conditions of exciting trapped waves: those excited by tsunamigenic earthquakes on the continental shelf close to the coastline; and those excited from scattering of the incident tsunami from offshore sources by irregular coastlines.

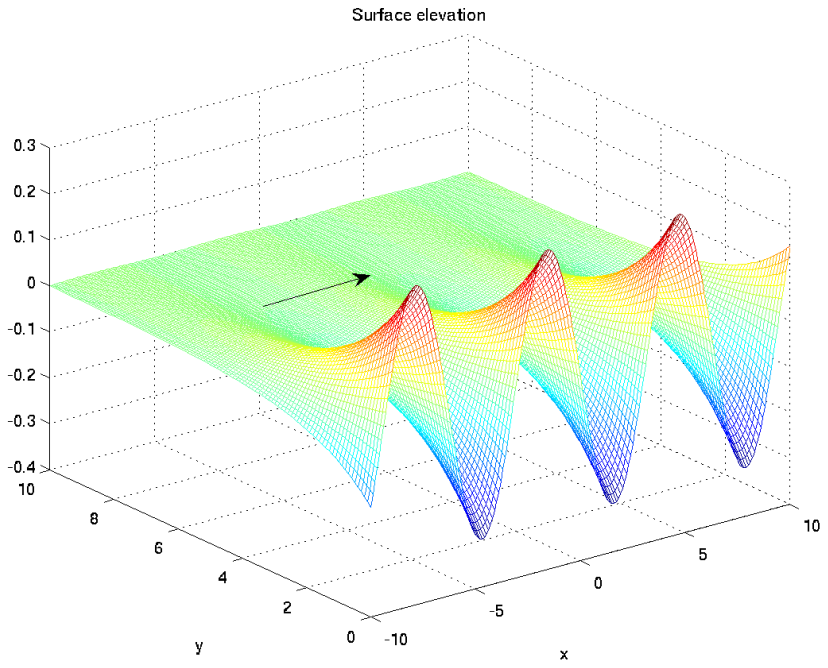

Figure A. 8 – Three dimensional profile of edge waves propagating in the x direction, being the coastline(Source: https://en.wikipedia.org/wiki/Edge_wave).

Trapped edge waves excited from tsunamigenic earthquakes generated on shelves have been documented by González et al. (1995) when they analysed data captured during the April 1992 Cape Mendocino tsunami, which generated both incident and trapped edge waves along the Californian and Oregon Coast from a nearfield earthquake. They found these waves were of the fundamental mode (that is, exponential decay offshore), which propagate much slower than the incident tsunami waves and can travel long distances along the coast. Rabinovich et al. (2006) found the presence of trapped edge waves during the June 2005 tsunami generated by an earthquake offshore of California. The excitation of trapped edge waves from shelf generated tsunamis was also found by Neetu et al. (2011) following a reanalysis of the 1945 tsunami that impacted the Makran coast. They also found that these modes can be trapped in the alongshore direction due to longshore variations in shelf width. Yamazaki and Cheung (2011) modelled the 2010 Chile earthquake that occurred offshore of the central Chilean coast to find that the continental shelf slope refracts and traps the radiated energy initially as progressive edge waves on the shelf. Reflections between headlands and the shelf generated a number of standing waves along the coast.

Fuller and Mysak (1977) demonstrated theoretically that trapped edge waves can be generated on a shelf with a straight coastline with small irregularities, due to energy transfer from scattering effects. They also indicated that the amplitude of trapped edge waves excited by a tsunami is about 70 per cent of the incident amplitude and that they slowly attenuate from scattering along irregular coastlines. The presence of edge waves from tsunami generated offshore can be found in references that also discuss resonance as discussed in the following section.

Figure A. 9 demonstrates a shelf trapped transient wave generated during a modelled 3,000-year average recurrence interval (ARI) tsunami event on the south-east Queensland coast (Boswood et al., 2018). The wave is initially reflected off the Great Sandy National Park coast. As it nears the continental shelf, it is refracted back towards the coast to impact Bribie Island, some 120 km south of the initial reflection. As the wave reaches the Bribie coast, it splits to propagate along the coast in both directions as a coastal trapped wave (Figure A. 10). The combination of the trapped and incident waves resulted in the highest water level at Bribie for this event, about 207 minutes after the leading wave (Figure A. 11). Abraimi (2014) observed a similar phenomenon when analysing the results of modelling the 2010 Chilean Tsunami on the central Chilean coast.

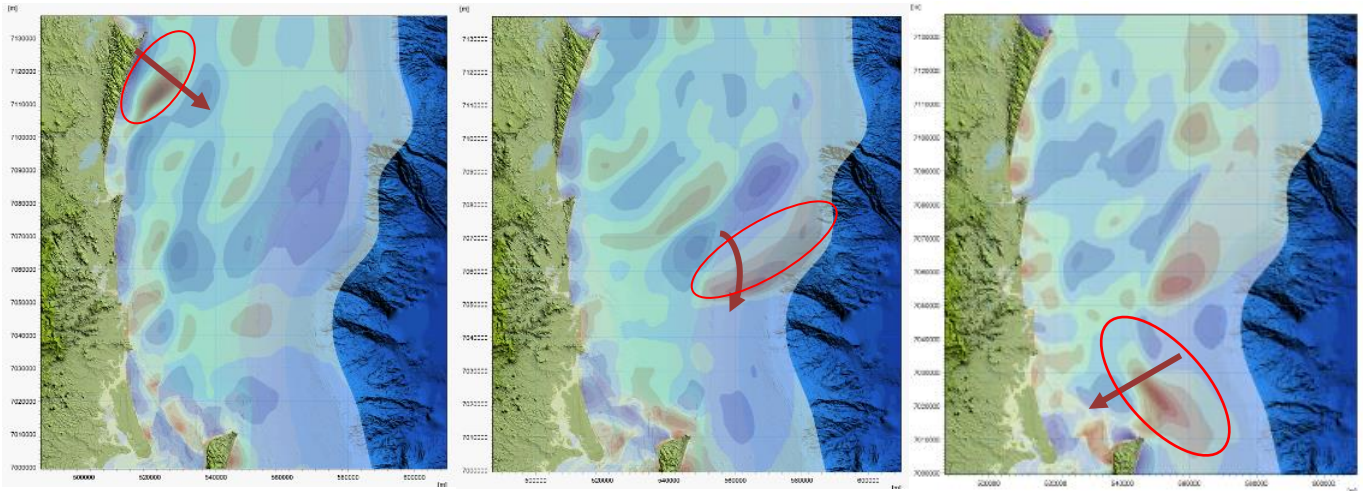

(a) Initial reflection of wave (t = 06:32) (b) Wave refracted on shelf (t = 07:15) (c) Wave approaching Bribie (t = 07:30)

Figure A. 9 – Shelf trapped wave along south-east Queensland coast (3,000-year ARI event). Arrows indicate direction. Dark red shading represents 4 m. Time is elapsed time in hours:minutes (Boswood et al, 2018).

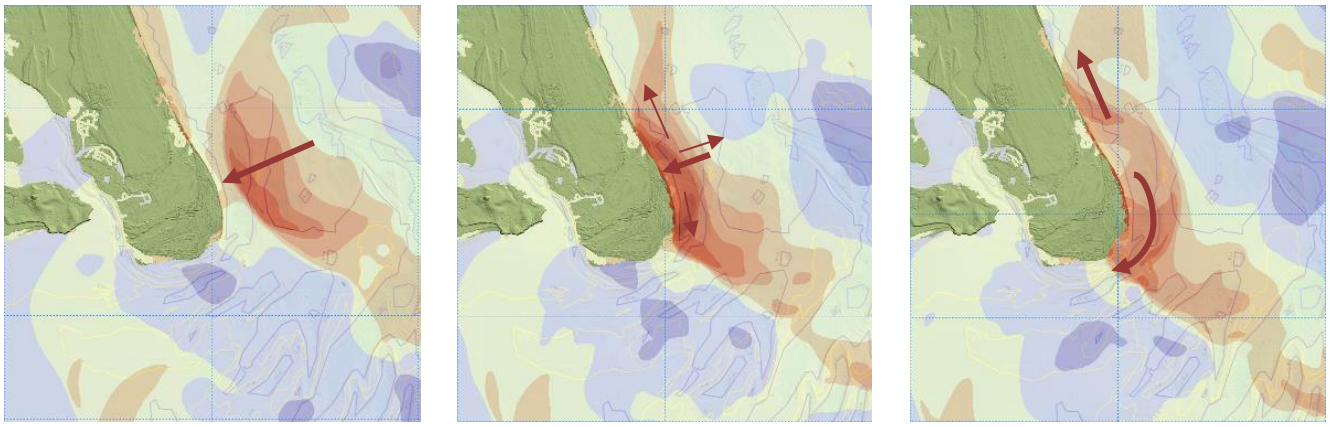

(a) Wave approaching Bribie (t = 08:05) (b) Wave scattering (t = 08:08) (c) Coastal trapped wave formed (t = 08:10)

Figure A. 10 – Coastal trapped wave example for Bribie Island, Queensland. (3,000-year ARI event). Arrows indicate direction. Dark red shading represents 4 m. Time is elapsed time in hours:minutes (Boswood et al, 2018).

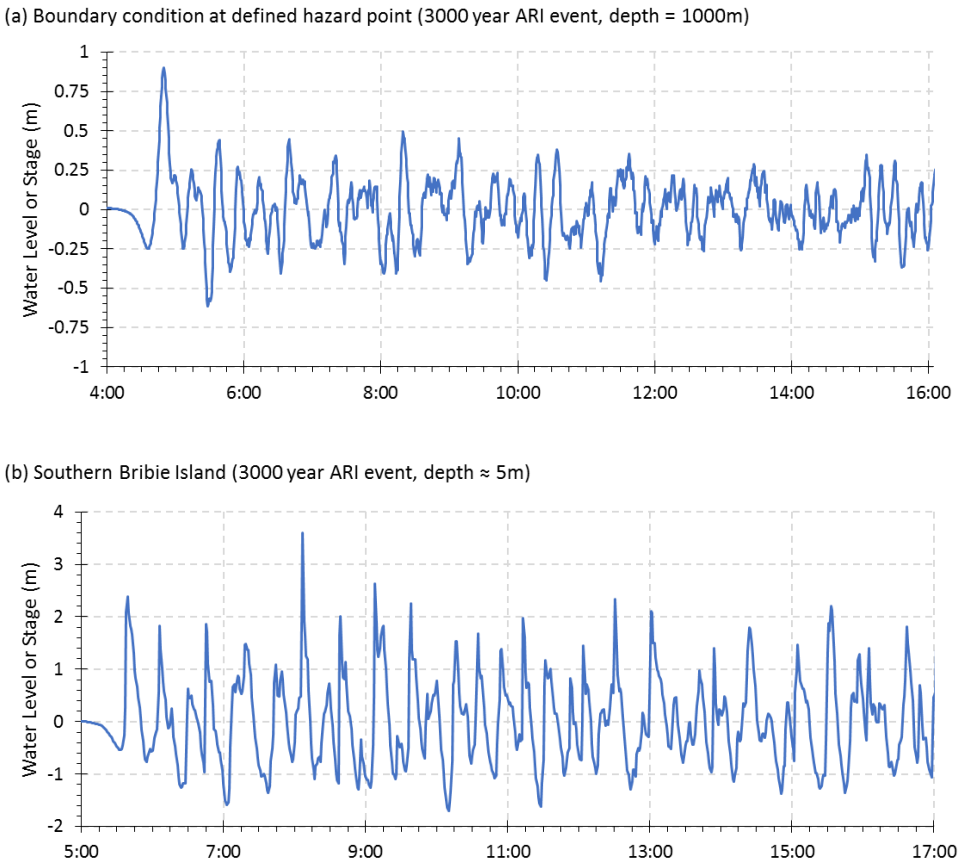

Figure A. 11 – Time series of tsunami near the coast of Southern Bribie Island (3,000-year ARI event).

A.3.2.3 Standing Waves and Resonance

Standing waves is the name given to the combination of two waves travelling in opposite directions at particular periods and timing that their interference creates the appearance of a wave where the crest appears to be stationary. For tsunami, the two waves will be the incoming wave and the reflected wave. Standing waves occur when the wave period (or frequency being the inverse of period) matches a natural period of the water body. In simple terms, when the wave period (or wavelength) of the arriving tsunami matches a harmonic (an integer fraction) of the natural (or eigen) period (or length) of a water body (such as the length of a bay), a standing wave is generated that can amplify the tsunami height. A standing wave is the combination (or superposition) of the incident wave and a reflected wave (Figure A. 12). If the wavelength is an integer factor of the overall length, the reflected and incident wave will combine to form nodes and antinodes in the spatial domain. The nodes are where the two waves are out of phase and so cancel each other out. The water level at nodes will be minimal due to destructive interference. The antinodes are where the two waves are in phase and the amplitude will be at a maximum due to constructive interference.

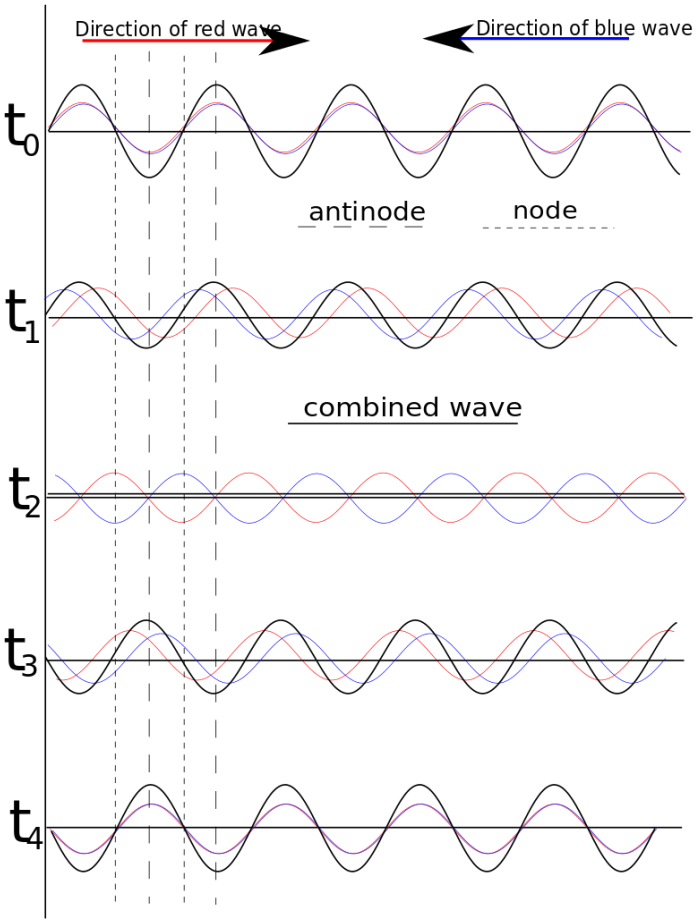

Figure A. 12 – Standing wave example caused by an incident (red) and reflected (blue) wave (Source: https://en.wikipedia.org/wiki/Standing_wave).

The fundamental mode (also referred to as the zero mode or first harmonic) is the simplest mode and is the most commonly seen as it is subject to the least energy dissipation because they involve smaller velocities for a given amplitude (Nielsen, 2012). The wavelength required to generate the fundamental node depends on the end conditions. For a simple condition of a semi-enclosed basin, the node will appear near the entrance. Therefore, the fundamental mode will occur when the basin is a quarter of the wavelength. The wave period can then be calculated with consideration of wave celerity (Equation A.1) giving (Bryant, 2014):

$$T_s = \frac{4L_b}{\sqrt{gD}}$$

Equation A.3

Where L_b is the length of the basin and T_s is the wave period required to initiate seiching. For an edge wave, the wavelength is along the coast with nodes at either end. The fundamental mode will occur when the length between nodes is half the wavelength. In reality, the wave lengths required to generate the modes will be more complicated due to factors such as irregular coastlines, partial reflections, oblique waves, and irregular wave conditions to name a few. As the tsunami wave train consists of many waves over a wide range of wave periods, it is possible that this phenomenon can occur and be excited at a number of modes.

Resonance is always associated with standing waves. To understand resonance, let us consider a wave entering a harbour: reflections will cause the water level to oscillate after the passage of the wave, which will decay rapidly. However, if the wave frequency matches the natural frequency of the harbour, then the waves will continue to oscillate for some considerable time (or resonate). The natural frequency being the frequency at which the harbour tends to oscillate in the absence of any driving or damping force.

If the external wave is a series of waves at the natural period, then each successive wave will add energy to the harbour oscillation which may grow larger than any individual wave in the original wave series. Resonance can appear in everyday life. The coffee in your cup that spills when you increase your walking pace is resonance caused by your motion matching the natural period of the cup. Resonance is a known issue for ports and harbours (referred to as a seiche) and can cause significant damage to moored vessels. Given the wavelength of tsunamis can still be tens of kilometres in the nearshore, the phenomena can also occur at larger scales such as bays and even the continental shelf.

The presence of shelf resonance has contributed to unusually high tsunami wave heights at: Hawaii (Munger and Cheung, 2008) and Crescent City (Horrillo et al., 2008) from the 2006 Kuril Islands tsunami; the American Samoa from the 2009 Samoa tsunami (Roeber et al., 2010); and the Chilean coast following the 2010 Chilean earthquake (Yamazaki and Cheung, 2011). In these examples, standing edge waves resulted in a spatially and temporally complex tsunami patterns that would not be explained by solely examining the leading tsunami wave.

A.3.2.4 Obstructions and Islands

Obstructions such as islands, peninsulas, or capes, may cause the tsunami to circle around to the back of the obstruction with reduced amplitude (referred to as diffraction). The obstruction must be significant enough in size to be felt by the long period tsunami. Murata et al. (2010) suggests the obstruction needs to exceed 500 m in length to have a notable influence.

For short period wind waves, the process of diffraction around islands has been known to produce a region of calmer water (known as the shadow zone) in the lee of the obstruction (such as islands) which may offer protection to the mainland coastline directly behind the obstruction. This concept has been utilised by coastal engineers through the design of detached offshore breakwaters as a coastal defence approach.

The behaviour of tsunamis around features such as islands can be quite different. The combination of refraction and edge waves can cause the wave to wrap around the island to reunite on the leeward side, such that the run-up levels can be as high as on the exposed side (Murata et al., 2010 and Wong et al., 2008). Yamazaki (2010) examined this phenomenon by numerical modelling of a solitary wave approaching a conical island and compared the results against physical model results (Figure A. 13). Stefanakis et al. (2014) undertook 200 simulations of an idealised conical island in front of a coastline. They found that unlike short period waves, tsunamis tend to wrap around the island and form a focusing lens of energy on its lee side, amplifying wave heights on the mainland behind the island. Rasyif et al. (2016) examined the influence of small islands on tsunami propagation on the Sumatran coast by numerical modelling of 3 actual events and 3 hypothetical cases. The report found that under certain conditions (that is, the tsunami propagates from both sides of the island), the tsunami will focus on the lee of the island and amplify the tsunami on mainland communities behind the island.

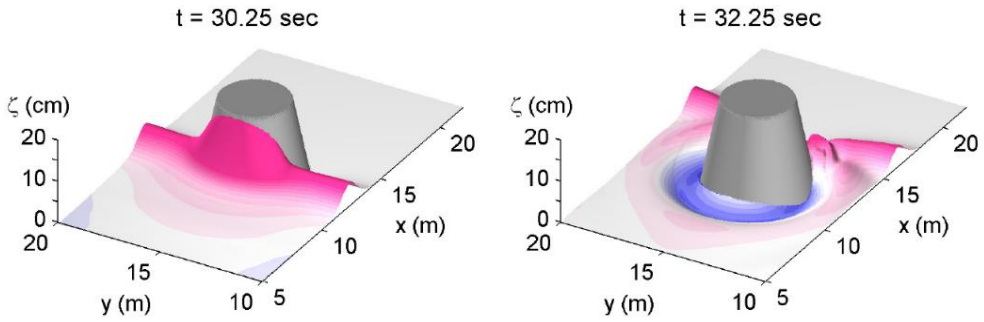

(a) *Solitary wave in front of island*

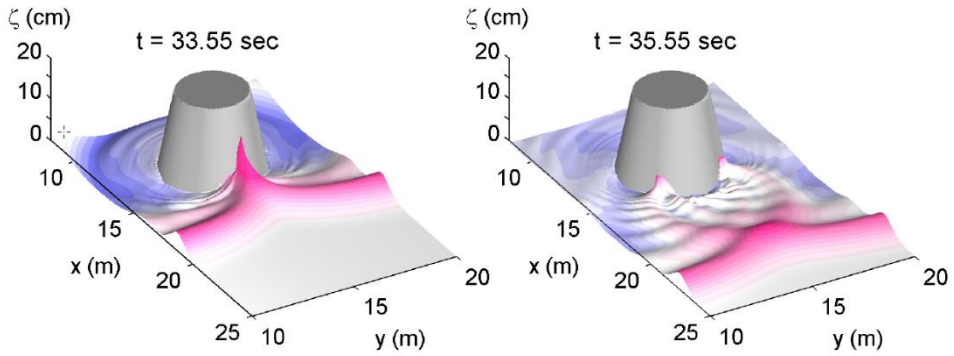

(b) *Solitary wave in lee of island*

Figure A. 13 – Solitary wave wrapping around idealised conical island (Yamazaki, 2010).

A.3.2.5 Ports and Marinas

Because of the long length scale of tsunamis even on the coast, small structures such as marinas and detached breakwaters for coastal erosion works have little influence on wave attenuation, unless their crest is above the tsunami run-up height. Under these conditions, there will be very strong currents at the openings. For ports and marinas, strong currents can develop as well as circulation systems. As flows accelerate around port structures,

boundary shear leads to flow separation that can create transitional turbulent structures. These structures are referred to as coherent eddies or turbulent coherent structures (Borrero et al., 2015) and at first glance can be misconstrued as whirlpools.

A.3.2.6 Wave Characteristics

The theory of waves is a complex subject and will not be discussed in any detail. Some of the more common terminology will be provided. The description of the tsunami wave form relates specifically to the leading wave, being the initial impulse of the tsunamigenic earthquake. Subsequent waves are a result of the processes mentioned earlier. In the deep ocean, the wave train follows an exponentially decaying envelope with the leading wave much larger than subsequent waves (Geist, 2009). As the tsunami approaches the coast, the wave form becomes more complex with no discernible characteristic envelope. However, for one-dimensional waves there has been analytical work undertaken in describing the run-up (described below) in relation to the shape of the leading wave. Early work considered the leading wave as a solitary wave (being the infinite wavelength limit of cnoidal waves). Madsen et al. (2008) examined the solitary wave and concluded that it is not applicable for long waves on a sloping bottom. Tadepalli and Synolakis (1994) introduced the concept of the N-wave (in analogy to dipole waves in gas dynamics – Synolakis and Bernard, 2006) to describe analytical wave run-up from tsunami. They consider 2 forms: leading depression N-waves (LDN), being a drawdown of the ocean before the tsunami hits the coast, and leading elevation N-waves (LEN). These different wave profiles depicted by these theories are depicted in Figure A. 14.

In deep water, tsunami can be described by linear wave theory (assuming small amplitude, homogenous and incompressible fluid). For depths of less than about 50 m, it is suggested that nonlinear wave theory applies (Geist, 1998), as the waveform will change with time. Cnoidal waves are considered nonlinear waves. Therefore, numerical modelling within the coastal region should be undertaken with models based on the nonlinear shallow water equations (NLSWE) or Boussinesq equations.

Tsunami are generally described by the amplitude (height of the crest above the mean water level) and period (time between successive crests). However, the wave train will consist of numerous waves of varying amplitude and period. Short wave statistics can be used to describe the wave train in terms of wave height (crest to trough height, approximately twice the amplitude) and period. Some common parameters include significant wave height (Hs being the average of the highest one-third of wave heights), root-mean-square wave height, peak period (Tp being the period corresponding to the peak spectral energy) and the zero up-crossing period (Tz being the average period based on the time each wave rises above the mean water level).

The water level at a particular moment in time is sometimes referred to as the stage.

All the processes previously mentioned add to the complexity and length of the tsunami wave train. A tsunami event can therefore last for several hours, and the first wave may not necessarily be the largest. As mentioned earlier, all these processes and their complex interactions will decrease the reliability of modelling the longer wave train.

(a) Linear sinusoidal waves

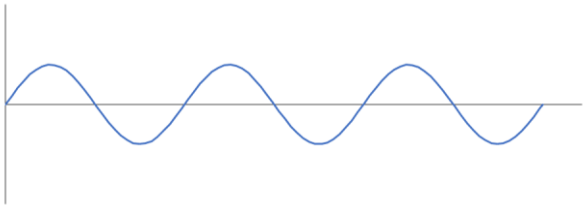

(b) Cnoidal waves

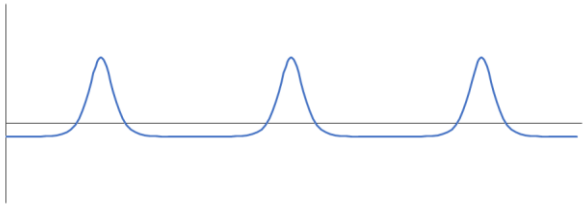

(c) Solitary wave

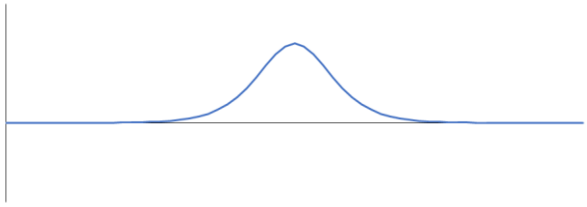

(d) Leading elevation N- wave (LEN)

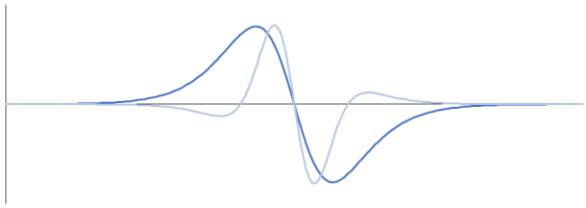

(e) Leading depression N- wave (LDN)

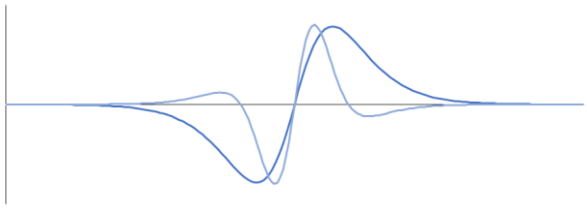

Figure A. 14 – Different nonlinear wave theories adopted in literature to describe the leading tsunami wave. The first plot is based on linear wave theory provided as a reference. The lighter of the lines in the last two plots are double N-waves.

A.3.2.7 Tsunami and Tides

The tide range in the open ocean is small relative to the depths (typically less than one metre). As the tides travel across the Australian continental shelf, amplification occurs. The largest tide ranges within Queensland occur around Central Queensland, with the highest documented tide range 9.1 m at McEwen Islet (MSQ, 2017).

Traditionally to minimise computation times, tsunami forecast, and hazard modelling have decoupled the tides, adopting a constant level of Mean Sea Level (MSL). Mofjeld et al. (2007) examined the influence of tides on the maximum water level by superimposing theoretical tsunami wave time series based on an exponential decay coefficient of 2 days over a duration of 5 days (based on measurements within the Pacific Ocean), on tides typical for Oregon, USA. Maximum envelopes of tide plus tsunami were calculated by stepping the tsunami time series

through a full year of tides representing an average year during the 18.6-year tidal cycle. The results showed that for small tsunami amplitudes, the maximum water levels tend to occur near mean higher high water (MHHW) with little spread. As the tsunami increases, the maximum water level tends towards a limit of MSL plus the tsunami amplitude (for tsunami amplitude > tide range), and the probability density function approaches that of the tides.

Although the principle of an exponentially decaying tsunami time series may be applicable in the open Pacific Ocean, the tsunami time series on the Australian continental shelf will be further complicated by the processes discuss above such that the largest wave my occur several hours after the onset of the leading wave. This is not discussed in the paper, but it is possible that a tsunami time series with large amplitudes persisting for some time may increase the limit from MSL to a tidal plane above MSL.

A.4 Tsunami Run-up/Inundation

The behaviour of tsunamis as they reach the coast is different to the behaviour of wind waves (Figure A. 15). Short period wind waves will continue shoaling until their steepness causes the wave to break. The broken bore will then continue to wash up the beach until its energy has been dissipated (referred to as the swash zone). The vertical height that is reached above the still water level is referred to as the run-up. The run-up depends on wave characteristics and beach slope. The particle motion within wind waves is orbital, becoming more elliptical in shallow water. Depending on wind wave and bathymetry characteristics within the surf zone, current patterns can develop including undertow, rip currents, and longshore currents.

With tsunamis, the wavelength even in very shallow water can still be in the order of kilometres. Bryant (2014) describes that the wave form close to shore appears like either Stokes or *N*-waves. These waves typically do not break, unless they are very large. Instead, they can appear as a fast-moving tide or surge. The leading edge of some may decay into one or more bores or solitons (Bryant, 2014), and can appear like a fast-moving tidal bore. The flow is horizontal in pattern (more like a river flow) and can be very strong and turbulent. The momentum of these waves can push water much further inland than wind waves at rates of 5 to 8 m/s (Bryant, 2014), and the currents can be too strong for a person to remain upright.

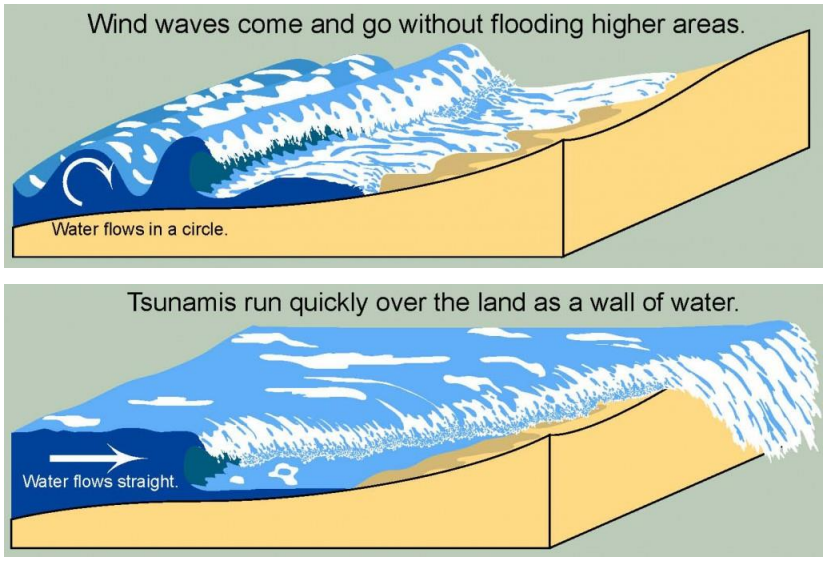

Figure A. 15 – Differences between wind waves and tsunami at the coast. (Source: http://earthweb.ess.washington.edu/tsunami/).

Madsen et al. (2008) investigated the use of solitary waves to model tsunamis, and in doing so, examined some characteristics of long waves as they approach the coastline. With the aid of a high order Boussinesq numerical model based on Madsen et al. (2006), they concluded the following:

1. In general, there is insufficient distance for tsunamis to generate solitons in the ocean or continental shelf.
2. During shoaling from deep to shallow water, wave asymmetry will increase (seen as steepening of the leading face of the wave), whereas skewness remains low.
3. With decreasing water depth, nonlinearity grows rapidly while the effect of dispersion reduces. Nonlinear shallow water equations (NLSWE) provide a good approximation of this process.
4. As the wave propagates close to the beach, the front face of the wave may become steep enough to disintegrate into an undular bore with short and steep transient waves of periods in the order of 10 to 15 seconds riding on top of the tsunami. This process explains the observed short period waves during the 2004 Indian Ocean tsunami (Figure A. 16). Dispersion now becomes important and nonlinear dispersive models

such as Boussinesq models are required to model this phenomenon. Although the NSWE may indicate this process due to numerical dispersion.
5. Even on a flat, shallow, and wide shelf, the asymmetry of the waves will continue to grow until the front face steepens to the point that undular bores develop.
6. Typically, the bores develop close to the coast and hence do not have sufficient time or travel distance to develop leading solitons.
7. Wave breaking that is observed during events is typically related to the short period bores, and not the underlying tsunami.
8. Although these transient waves will have an impact on coastal structures, the run-up and inundation that occurs is a result of the underlying longer period tsunami.
9. Constant depth theory for cnoidal or solitary waves cannot be applied to approximating long waves on sloping bottoms.

(a) Undular bores riding on the underlying tsunami which is not apparent in the photo due to its gentle slope.

(b) Close up of approaching bores.

Figure A. 16 – The 26 December 2004 Indian Ocean tsunami approaching the North Beach of the island Koh Jum, off the coast of Thailand. Photo taken from the top of Mt Pu (Copyright Anders Grawin. Reproduced from http://www.kohjumonline.com/anders.html with permission).

For sloping topography, the inundation extent will be defined by the run-up limit. Murata et al. (2010) suggests that run-up will be greater on a gentle slope. For regions where there is a beach of uniform slope followed by a flat coastal plain, the momentum of the tsunami will travel further inland until friction overcomes it. For regions where the inland region slopes downward (such as behind dunes) the tsunami may accelerate with increased velocity. For both cases, tsunami velocities are slow to dissipate.

Extreme events have been known to destroy buildings, infrastructure and strip vegetation, moving several kilometres inland (inundation extent). With such devastating events, like the 2004 Indian Ocean tsunami, a

booming roar can be heard as the tsunami approaches (UNESCO/IOC, 2010). Circulation patterns can develop along the coast such as large eddies. As the trough of the wave approaches, the water level can recede rapidly generating strong offshore currents that wash obstacles out to sea.

Of course, the ability to inundate depends on several factors including tsunami height and period, stage of tide, height of any barriers (such as seawalls and beach dunes), obstacles (such as buildings), and land coverage (for example a dense forest will impede tsunami movement more than pastoral land). For small amplitude tsunamis, the stage of tide may be a critical factor.

As well as inundating low-lying coastal regions, tsunamis will also propagate up rivers and waterways much faster than they inundate some coastal zones.

A.5 Tsunami hazard and Community Vulnerability

The preceding sections describe the processes that can influence the tsunami hazard at a specific geographic location. Once the hazard is quantified, vulnerability and risk assessments can be undertaken. Charvet et al. (2017) define tsunami risk as:

Tsunami Risk = Tsunami Hazard x Vulnerability x Exposure

Where exposure is the number of people, buildings and infrastructure at risk; and vulnerability is the likelihood of losses, defined as:

Vulnerability = Fragility x Loss Model

Where fragility is the probability of damage given a particular tsunami intensity; and the loss model defines the probable losses (financial and casualty) for a given level of damage. The above definition being consistent with the risk assessment process defined in QFES (2018).

The vulnerability of a community to tsunami hazard can be categorised as physical (human casualties and structural damage), social, economic, and environmental (UNESCO, 2015 and UNISDR, 2017). The following relates to the physical aspects.

The science behind vulnerability and risk assessments is well developed for other coastal hazards that occur more frequently. There is extensive literature and guidelines regarding vulnerability metrics for riverine flood events, based on field and laboratory investigations. The Flood Hazard Guideline published by the Australian Institute for Disaster Resilience (AIDR, 2017) quantifies flood hazard as the product of flood depth and velocity. Figure A. 17 illustrates the combined general flood hazard vulnerability curves provided in the guideline, which set hazard thresholds that relate to the vulnerability of the community when interacting with floodwaters.

Further guidance regarding human stability in riverine flood events can be found in Engineers Australia (2010), which is based on a review of previous laboratory experiments. The results are summarised in Table A. 1 as a function of the product of individual height and mass (HxM) and the product of depth and velocity (DxV).

However, there are fundamental differences in the physics of these two hazards. Riverine flooding of floodplains is generally characterised by the gradual and steady rise in water level over an extended period, with currents being typically low within the floodplain: the main cause of damage being from water damage. Their occurrence is much more frequent, and as such there has been significant field assessments and physical modelling investigations to develop vulnerability relationships.

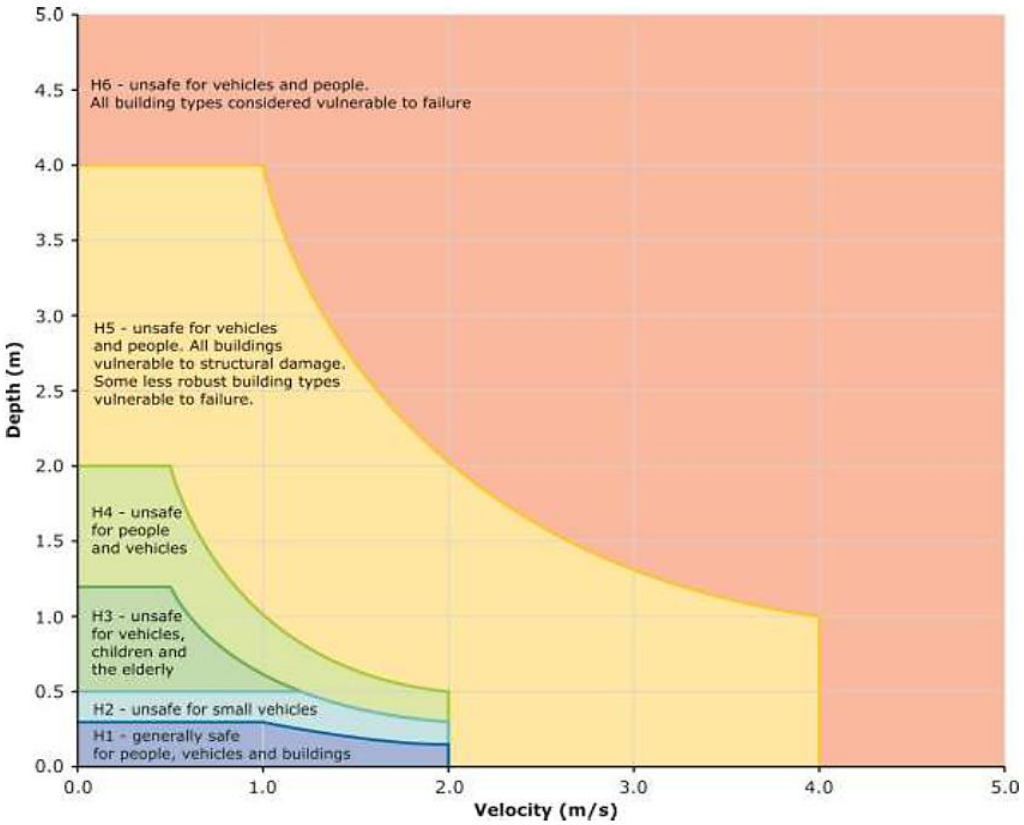

Figure A. 17 – General flood hazard vulnerability curves (AIDR, 2017).

Table A. 1 – Human Stability during flood event (reproduced from Engineers Australia, 2010).

D.V (m/s)	Infants, small children (H.M ≤25) and frail/older persons	Children (H.M = 25 to 50)	Adults (H.M >50)
0	Safe	Safe	Safe
0–0.4	Extreme Hazard; Dangerous to all	Low Hazard	Low Hazard
0.4–0.6		Significant Hazard; Dangerous to most	
0.6–0.8		Extreme Hazard; Dangerous to all	Moderate Hazard; Dangerous to some
0.8–1.2			Significant Hazard; Dangerous to most
>1.2			Extreme Hazard; Dangerous to all

Although the overland flow associated with tsunami is predominantly horizontal (Bryant, 2014), the inundation is more rapid with stronger currents and turbulence. The sequence of a number of waves will see reversing currents. The formation of undular bores (refer Section A.4) can introduce additional forces on structures. Scour can be significant, compromising foundation stability. In addition, the occurrence of tsunami events with recorded damage assessments are much scarcer, relying on documented events post 2004.

The Joint Australian Tsunami Warning Centre (JATWC) provides warnings within Australia based on a no threat, marine warning, or land warning. The following sections consider hazard and vulnerability metrics based on the latter two threats.

A.5.1 Marine Hazard

Although tsunami inundation is the most considerable and obvious risk to the public, there can still be significant damage to maritime facilities from events that do not pose an inundation threat. Within ports and marinas, maritime assets are vulnerable to significant damage from strong currents and associated drag forces (Lynett et al., 2014). The following provides some guidance in relation to vessels and maritime structures.

A.5.1.1 Maritime Users

Hazards to maritime users from tsunami are most acute in nearshore areas as the tsunami wave enters shallower waters close to the shore.

Tsunamis can pose a significant risk to vessels of all sizes in nearshore areas and ports, due to wave steepness, high current velocities, and debris. Tsunami forces on vessels at anchor are likely to impose significant loads on moorings. Due to the impact of tsunamis on the maritime industry from the Indian Ocean 2004 and Japanese 2011 events, a considerable research effort has seen a variety of guides being produced for the marine industry on tsunami, including estimates of impact based on tsunami amplitude and current velocity (Muhari et al. 2015).

Lynett et al. (2014) undertook a review of recorded damage against measured and modelled tsunami current speeds within ports and harbours predominantly in California following the 2010 Chile and 2011 Great East Japan tsunamis. The results demonstrated distinct thresholds for different levels of damage (defined in Table A. 2) as shown in Figure A. 18, with initiation of damage occurring for speeds above 1.5 m/s. Muhari et al. (2015) developed loss functions for marine vessels based on a multivariate analysis of data collected from the 2011 Great East Japan tsunami together with numerical hydrodynamic modelling of flow velocities. Loss estimation surfaces were developed based on tsunami height, velocity, impact (from floating or static obstructions), and boat material. They found that their results were consistent with that of Lynett et al. (2014), with the model being more sensitive to velocity. They also concluded that collision is a major factor in the determination of vessel loss, significantly reducing the velocity and depth thresholds.

For recreational maritime users, Queensland Government guidance is: where possible, moor your vessel and move to high ground. Otherwise, if at sea, move offshore into deep water and stay there until further advised (Queensland Government, 2018). Lynett (2014) undertook hydrodynamic modelling for the Californian coast to examine a ‘safe’ depth for evacuation of vessels should there be sufficient lead time prior to tsunami arrival. The modelling showed that navigable currents was the controlling factor, requiring depths greater than 50 m to reduce currents below 1 m/s, and depths greater than 180 m for currents below 0.5 m/s.

Table A. 2 – Marine facility damage classification from Lynett et al. (2014).

Damage Index	Damage Type
0	no damage/impacts
1	small buoys moved
2	1–2 docks/small boats damaged and/or large buoys moved
3	Moderate dock/boat damage (<25% of docks/vessels damaged) and/or midsized vessels off moorings
4	Major dock/boat damage (<50% of docks/vessels damaged) and/or large vessels off moorings
5	Extreme/complete damage (>50% of docks/vessels damaged)

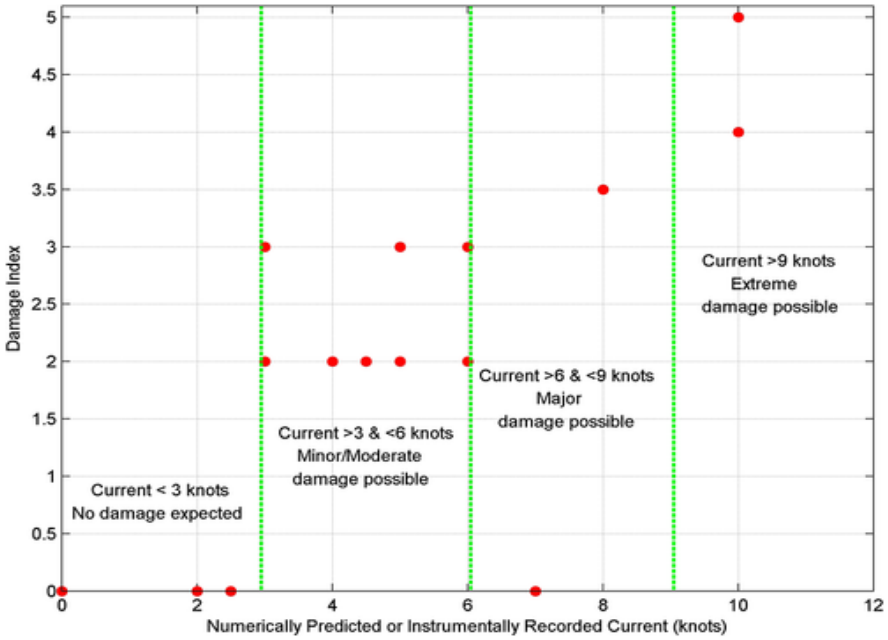

Figure A. 18 – Damage against tsunami current speed from Lynett et al. (2014).

A.5.1.2 Maritime Structures

Tsunamis have the potential to cause significant damage to coastal and estuarine structures due to the significant forces that can be applied to structures as they may be subject to hydraulic forces beyond tolerable design levels.

Tsunami waves apply exceptional hydraulic forces as they propagate over and around structures, dissimilar to surges and wind derived waves, potentially resulting in significant additional loading on a structure from wave impact forces and debris. Structures can also be impacted by scour due to increased current velocities and water depths. Although these forces are relatively well understood in terms of structure design, they are not well understood in the context of tsunami and are the subject of research.

Although the Australian design standards for maritime structures (Council of Standard Australia, 2002 and 2005) are rigorous in their requirements to assess the resilience of structures from a variety of hydraulic impacts, the risk from tsunami is neither specifically identified nor particularly well understood.

For port facilities, some guidance is provided in Lynett et al. (2014) as described in the preceding section.

A.5.2 Land Hazard

The obvious hazards associated with overland progression of tsunamis are inundation or flow depth and extent, high velocities, and debris. Several factors influence building damage including hydrostatic forces, buoyant forces, hydrodynamic forces, surge forces, impact of floating objects, breaking wave forces, inundation duration and footing scour (Tinti, 2011).

Research into vulnerability measures has mostly developed post 2004, but particularly following the 2011 Great East Japan tsunami. As such, the tsunami community is still in the early stages of understanding how to quantify the physical and social vulnerability. Nevertheless, there is literature available that provides rough guidance. Wijetunge (2009) provides human stability criteria based on the experimental results of Takahashi (2005) as reproduced in Table A. 3.

Table A. 3 – Human stability in tsunami based on laboratory experiments (Wijetunge, 2009).

Depth, D (m)	Stability
D <0.5	Stable, if V <1.5 m/s
0.5< D <1.3	Unstable if V > −1.84D + 2.4
D >1.3	Unstable for all V

This criterion is similar to classification H3 from the general flood hazard vulnerability curves (Figure A. 17): the above being based on the stability of people caught in currents and so should be considered only as a first approximation. Other factors will influence human stability such as floating debris.

Building vulnerability research has focused on developing empirical damage or fragility functions (probability of exceeding a given damage state (DS) based on a measure of tsunami intensity) for a range of structure types and predefined damage states based on post event assessments and laboratory experiments. Most of the recent work in this field has come from the 2011 Great East Japan tsunami. Figure A. 19 provides an example of the typical 2-D fragility functions as developed by Charvet et al. (2015) based on flow depth, where the DS relates to the criteria defined by the Japanese Ministry of Land Infrastructure Tourism and Transport as summarized in Table A. 4, noting that they combined DS5 and DS6 as these damage states were seen to not be mutually exclusive.

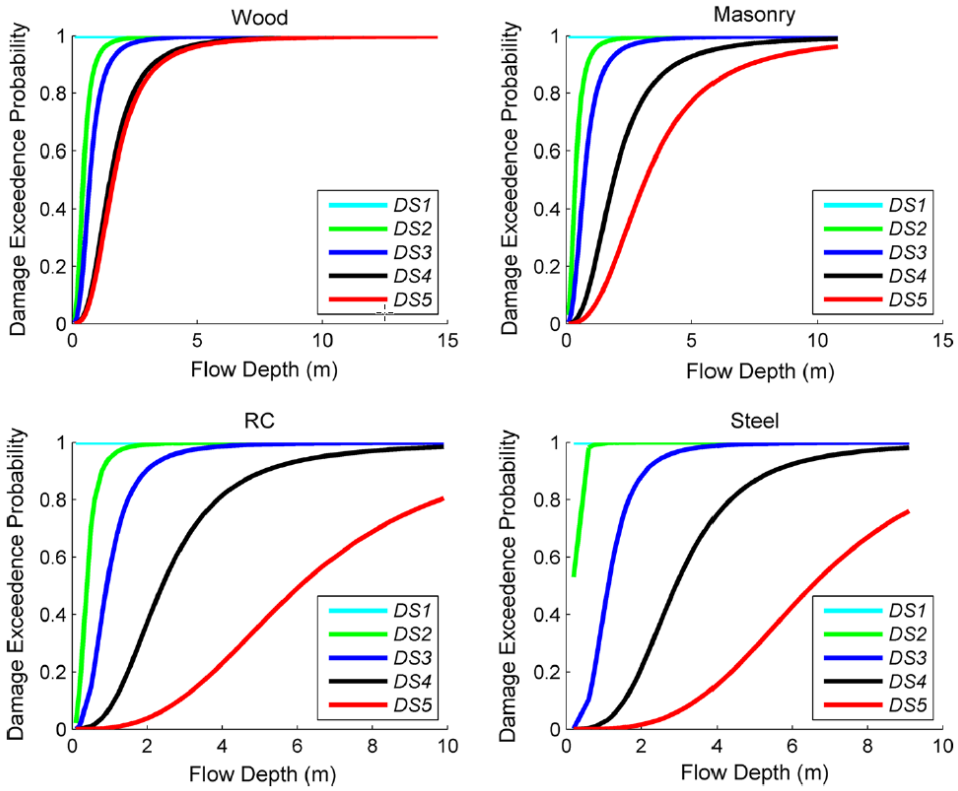

Figure A. 19 – Two-dimensional fragility functions for Kesennuma City following the 2011 Great East Japan tsunami (Charvet et al., 2015).

Charvet et al. (2015) also undertook a multivariate analysis using improved statistical methods to develop 3-D fragility surfaces based on flow depth, velocity, structure material, damage state, and debris impact; an example of which is provided in Figure A. 20. They found that flow depth alone is a poor predictor of damage for the stronger construction types (such as reinforced concrete (RC) and steel) at higher damage states and suggested that both flow velocity and debris impact were important parameters (Figure A. 21). The work concluded that the approach provided better fits to the available damage data, but still showed a high level of uncertainty such that further research is required particularly into debris impact, numerical modelling methods for estimating velocities, scour effects, and the influence of additional parameters such as combined depth and velocity.

Charvet et al. (2017) undertook a review of the current state of knowledge in relation to estimating tsunami-induced building damage through fragility functions. The review found that flow depth is the main measure (referred to as Tsunami Intensity Measure or TIM in the paper) adopted in literature, as it is can be readily determined from field assessments. Other information such as velocity is important at higher damage states, but difficult to measure in the field without pre-deployed instrumentation. Therefore, estimates of velocities rely on hydrodynamic models that are typically only validated for inundation depth or run-up extent. Park et al. (2013 and 2014) examined the sensitivity of modelled tsunami inundation water level, velocity, and momentum flux to overland friction to show that although a tenfold reduction in friction had minor impacts on surface elevation (15 per cent increase), velocity and momentum flux were more sensitive with increases of 95 per cent and 208 per cent respectively. When considering hydrodynamic forces (which are typically proportional to the velocity squared) then the sensitivity can become substantial.

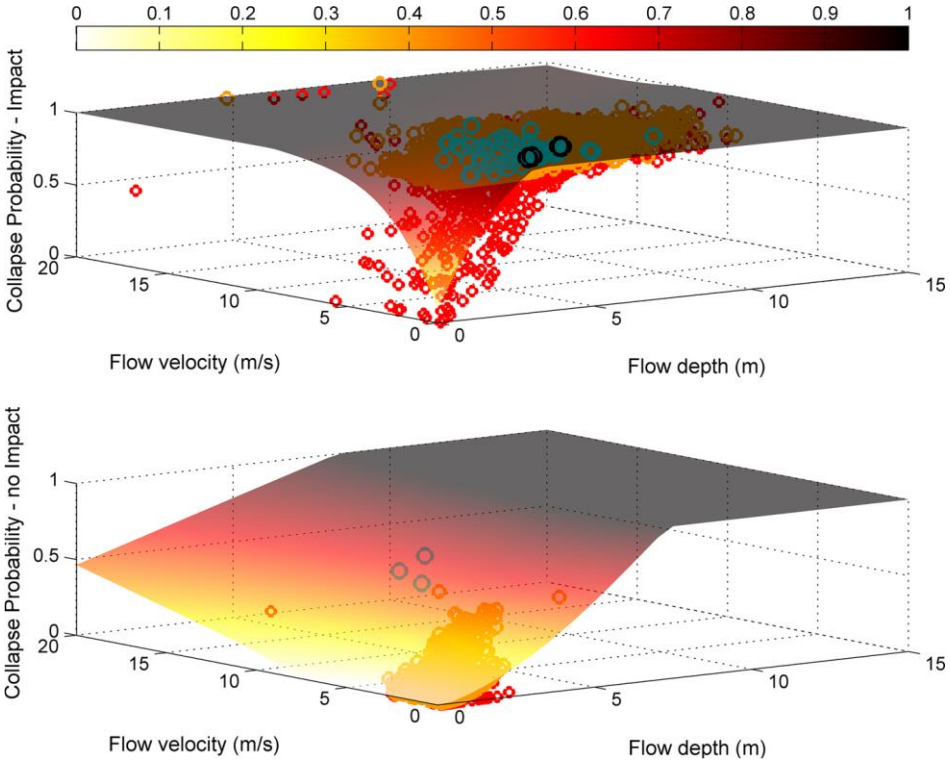

Figure A. 20 – Example fragility surfaces showing the probability of collapse (DS5) for wood buildings, with and without debris impact (radius: 130 m) based on field survey data following the 2011 Great East Japan tsunami (Charvet et al., 2015).

Figure A. 21 – Schematic representation of the contributions of different tsunami intensity measures to the severity of observed damage (Charvet et al., 2015).

Table A. 4 – Damage state definitions used by the Japanese Ministry of Land Infrastructure Tourism and Transport following the 2011 Great East Japan Earthquake (source: Charvet et al., 2017).

Damage	State	Description	Use	Image
DS1	Minor damage	Inundation below ground floor. The building can be reused by removing mud below the floorboards.	Possible to use immediately after minor floor and wall cleanup.	
DS2	Moderate damage	The building is inundated less than 1 m above the floor.	Possible to use after moderate repairs.	
DS3	Major damage	The building is inundated more than 1 m above the floor (below the ceiling)	Possible to use after major repairs	
DS4	Complete damage	The building is inundated above the ground floor level	Major work is required for re-use of the building	
DS5	Collapsed	The key structure is damaged, and difficult to repair to be used as it was before	Not repairable	
DS6	Washed away	The building is completely washed away except for the foundation	Not repairable	

Charvet et al. (2017) also concluded that fragility relationships that have been developed are not necessarily comparable or translatable to other locations due to a number of factors including choice of tsunami intensity

measures, building codes (for example engineered structures in Japan versus non-engineered structures in Indonesia), differences in damage state criteria and mutual exclusiveness of each defined damage state, building classifications, field assessment approach (field survey by qualified personnel or remote sensing), completeness of database records, and variations in statistical approaches. Research into fragility functions following the 2011 Great East Japan tsunami also showed they can be location specific, sensitive to local bathymetry, topographic features, building distribution, and the presence of coastal defences. For locations that were also subject to the earthquake, it is difficult to separate earthquake related damage or contributions such as liquefaction. It was therefore concluded by Charvet et al. (2017) that for the development of fragility functions for locations where damage data is not available, analytical methods for fragility function derivation based on structural analysis are required, incorporating multiple TIMs.

Suppasri et al (2011) developed tsunami fragility curves based on satellite remote sensing and numerical modelling of the 2004 Indian Ocean tsunami in Thailand. The approach classified damage as destroyed or not destroyed based on whether the roof was missing and excluded high-rise buildings and hotels because of their apparently high structural strength. The developed curves did not distinguish between building materials. The fragility curves represent the cumulative probability of damage based on inundation depth, current velocity and hydrodynamic force based on the drag force for two regions: Phang Nga and Phuket. A damage probability of 50 per cent occurred at 2–3 m for inundation depth and 1.5–2 m/s for current velocity. There are differences in the curves for the two regions attributable to the differences in building materials. They concluded that the proposed fragility curves show similar performance to studies of Indonesia (Koshimura and Yanagisawa, 2007; Koshimura et al., 2009c) and Japan (Koshimura et al., 2009b). Buildings start to collapse at 2–3 m inundation depth and collapse entirely at depths exceeding 6 metres. They also noted that the fragility curves should be applied with care because they depend on the characteristics of the tsunami and of building materials that might differ in other countries.

Suppasri et al (2011) also provided a summary of other studies undertaken into tsunami fragility. Koshimura and Yanagisawa, 2007; and Koshimura et al., 2009c developed tsunami fragility curves from satellite imagery and numerical modelling for Banda Aceh, Indonesia. The damage probability rapidly increased when the inundation depth exceeds 2 m, with almost all building destroyed when depths exceed 4 metres. Most buildings collapse when the current velocity exceeds 3 m/s and the hydrodynamic force exceeds 10 kilonewtons per metre. Research undertaken by Koshimura et al (2009a) into the 1993 Hokkaido Nansei-oki tsunami based on aerial photography showed most buildings collapsed when the inundation depth exceed 2 m, the current velocity was greater than 5 m/s, and the hydrodynamic forces exceeded 20 kilonewtons per metre. Matsutomi and Harada (2010) examined building damage from numerous field surveys. Suppasri et al (2011) roughly inferred that severe damage would occur at inundation depths of 2 m for timber, 7 m for concrete block, and 8 m for reinforced concrete. Historical data on damaged buildings in Japan based on the 1896 Meiji-Sanriku, 1933 Showa-Sanriku, and 1960 Chile tsunamis indicated that for a 2 m tsunami there is less than 30 per cent probability that a house would be destroyed and that at least 30 per cent structural damage would result from a tsunami of 2.1–7.4 m height (Koshimura et al, 2009b).

Koshimura et al (2009c) recommended applying the fragility function to inundation depth as the current velocity is mostly calculated by numerical modelling, which is influenced by numerical grid resolution, accuracy and resolution of the topographic data, and assumptions on the roughness coefficients within the model.

In 2013, a workshop was held to assess regional vulnerability functions for the SE Asia and Pacific region for earthquake, severe wind, flood, volcanic ash and tsunami as part of the Global Assessment Report on Disaster Risk Reduction (GAR). The GAR forms part of the United Nations International Strategy for Disaster Reduction (UNISDR) and contributes to achieving the Hyogo Framework for Action (HFA) (Maqsood et al, 2014). Figure A. 22 presents a selection of vulnerability curves developed during the workshop process.

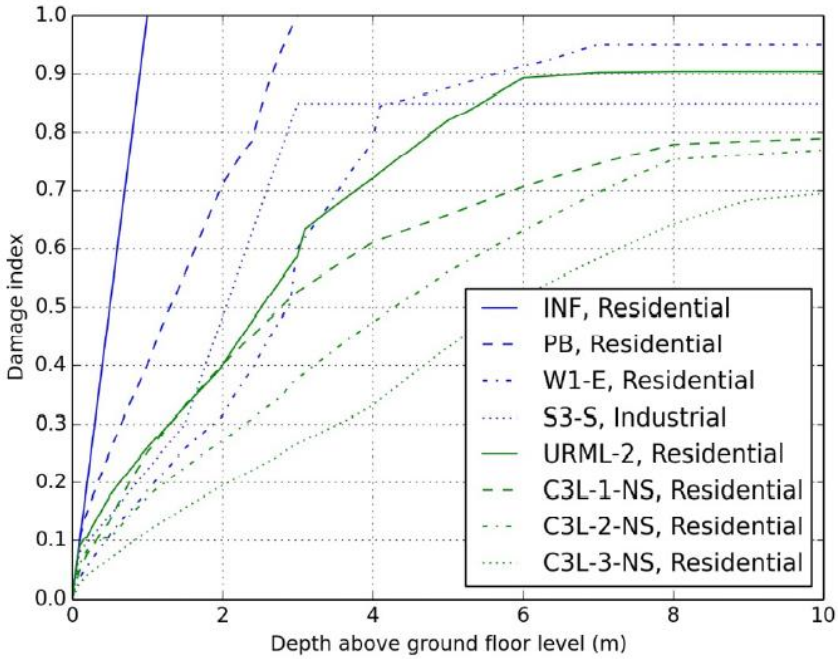

Figure A. 22 – Comparison of vulnerability curves for select building types (Maqsood et al, 2014).

The damage index refers to the total cost of repairing the building fabric of a group of buildings exposed to a severe natural hazard divided by the total cost of fully rebuilding the same assets in the existing locality to current local building regulations. The legend refers to single storey informal settler's house (INF, Residential), single storey pole and beam structure (PB, Residential), single storey Pier and Beam Wood light frame (W1_E, Residential), single storey steel light frame with susceptible cladding (S3-S, Residential), single storey concrete frame with unreinforced masonry infill walls with non-susceptible interior wall (C3L-1-NS, Residential), two-storey concrete frame with unreinforced masonry infill walls with non-susceptible interior wall (C3L-2-NS, Residential), and three-storey concrete frame with unreinforced masonry infill walls with non-susceptible interior wall (C3L-3-NS, Residential).

The above discussion outlines the complexity and issues of developing generic vulnerability curves for tsunami. UNESCO (2015) provides some generic median damage states from Nanayakkara and Dias (2013) for single-storey buildings constructed from commonly used materials based on inundation depth (Table A. 5). The table is based on the median of data from Sri Lanka and Thailand during the 2004 Indian Ocean tsunami, as well as Samoa during the 2009 South Pacific tsunami. Data from the 2011 Great East Japan tsunami were intentionally omitted as these structures performed better given, they were newly constructed with proper quality controls. It is likely that Australian building codes would also have higher quality controls.

Table A. 5 – Median inundation depth ranges by construction and damage state (UNESCO, 2015).

Damage State	Timber (T)	Masonry (M)	Reinforced Concrete (RC)
Complete (H6)	~1.6 m	2.3–2.5 m	5.4–7.3 m
Major structural (H5)	~1.3 m	~1.9 m	~3.5 m
Minor structural (H4)	~1.2 m	1.3 m	1.4–1.9 m
Non-structural (H3)	0.3–0.5 m	0.3–0.5 m	0.3–0.5 m

Figure A. 23 summarises Table A. 1 and Table A. 5 based on the lower limits for timber structures. Complete damage for masonry and reinforced concrete are also shown as lines. In Figure A. 23, H1 relates to "generally safe for people and buildings" adopted from the general riverine flood vulnerability curves (Figure A. 17), and H2 represents no structural damage. The figure only provides a general indication of potential vulnerability and should only be used with due consideration of the limitations mentioned above.

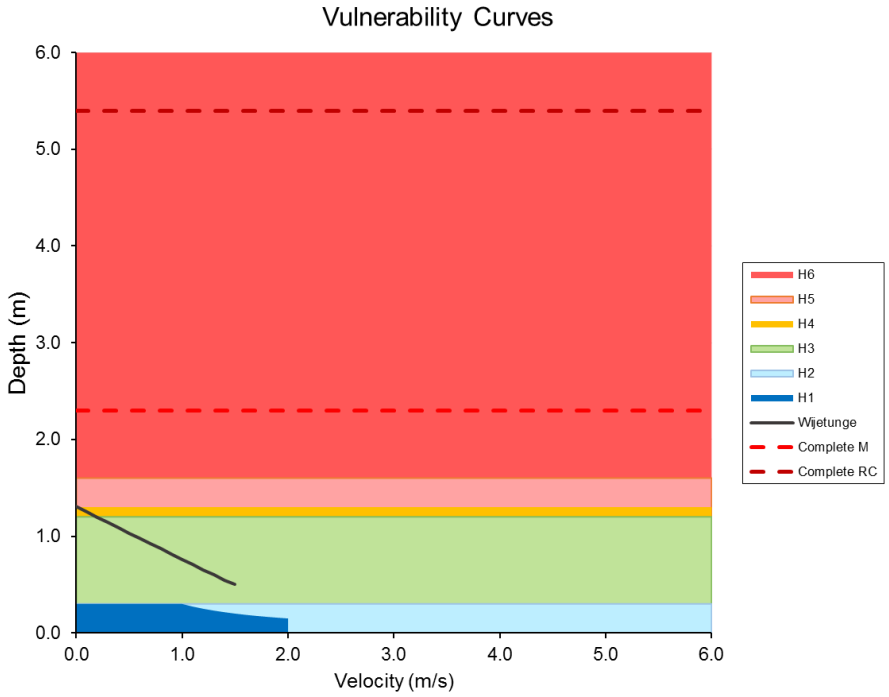

Figure A. 23 – Combination of general vulnerability curves for tsunami inundation.

A.6 Further Information

As discussed above, tsunami generation, propagation and inundation can be complex. Further information can be found in UNESCO/IOC (2010), IOC (2012), IOC (2016), Murata et al. (2010), Bryant (2014), Mofjeld et al. (2004), Geist (1998 and 2009), Synolakis and Bernard (2006), and Borrero et al. (2015). Useful websites include those of National Oceanic and Atmospheric Administration (NOAA, 2018a), the International Tsunami Information Center (ITIC, 2018), and a website produced by the COMET program (UCAR, 2010).

A.7 References

Abraimi, R., 2014. Modelling the 2010 Chilean Tsunami using the H2Ocean unstructured mesh model, MSc thesis, Civil Engineering and Geosciences, TUDelft, p 64, uuid:17166e10-861b-4aa9-8f4d-afb092fd18fd

Adriano, B., Fujii, Y., and Koshimura, S., 2018. Tsunami source and inundation features around Sendai Coast, Japan, due to the November 22, 2016 Mw 6.9 Fukushima earthquake, Geoscience Letters 5:2, p 12, https://doi.org/10.1186/s40562-017-0100-9.

Australian Institute for Disaster Resilience (AIDR), 2017. Flood Hazard, Australian Disaster Resilience Guideline 7-3, 2nd Edition, prepared for the Australian Government Attorney-General's Department, p 30.

Bernard, E.N., Mofjeld, H.O., Titov, V., Synolakis, C.E., and González, F.I., 2006. Tsunami: scientific frontiers, mitigation, forecasting and policy implications, Phil. Trans. R. Soc. A 364, pp 1989–2007, doi:10.1098/rsta.2006.1809.

Borrero, J.C., Lynett, P.J., and Kalligeris, N., 2015. Tsunami currents in ports, Phil. Trans. R. Soc. A 373: 20140372, p 19, http://dx.doi.org/10.1098/rsta.2014.0372.

Boswood P.K., Wall R., Peach L. 2018. Tsunami Modelling along the East Queensland Coast, Report 3: Moreton Bay. Brisbane: Department of Environment and Science, Queensland Government.

Bryant, E., 2014. Tsunami: The Underrated Hazard, Third Edition, Springer, p 222.

Charvet, I., Macabuag, J., and Rossetto, T., 2017. Estimating Tsunami-Induced Building Damage through Fragility Functions: Critical Review and Research Needs, Front. Built Environ., Vol 3(36), p 22, doi: 10.3389/fbuil.2017.00036.

Charvet, I., Suppasri, A., Kimura, H., Sugawara, D., and Imamura, F, 2015. Fragility estimations for Kesennuma City following the 2011 Great East Japan Tsunami based on maximum flow depths, velocities and debris impact, with evaluation of the ordinal model's predictive accuracy, Nat.Hazards 79, pp 2073–2099, doi:10.1007/s11069-015-1947-8.

Council of Standard Australia, 2002. Structural Design Actions – General Principles. (AS /NZS 1170-2002). SAI Global Pty Ltd.

Council of Standard Australia, 2005. Guidelines for the design of maritime structures. (AS /NZS 4997-2005). SAI Global Pty Ltd.

Davies, G., Romano, F., and Lorito, S., 2020. Global Dissipation Models for Simulating Tsunamis at Far-Field Coasts up to 60 hours Post Earthquake: Multi-Site Tests in Australia, Frontiers in Earth Sci. 8:598235, doi: 10.3389/feart.2020.598235.

Engineers Australia, 2010. Appropriate Safety Criteria for People, Stage 1 Report, Australian Rainfall & Runoff Revision Project 10, P10/S1/006, April, p 21.

Fuller, J.D. and Mysak, L.A., 1977. Edge waves in the presence of an irregular coastline, J. Phys. Oceanogr., Vol 7(6), pp 846–855.

Geist, E.L., 1998. Local Tsunamis and Earthquake Source Parameters, Advances in Geophysics, Vol 39, pp 117–209, https://doi.org/10.1016/S0065-2687(08)60276-9.

Geist, E.L., 2009, Chapter 3 - Phenomenology of Tsunamis: Statistical Properties from Generation to Runup, Advances in Geophysics, Vol 51, pp 107–169, https://doi.org/10.1016/S0065-2687(09)05108-5.

Geist, E.L., Lynett, P.J., and Chaytor, J.D., 2009. Hydrodynamic modelling of tsunami from the Currituck landslide, Marine Geology, 264, pp 41–52.

González, F.I., 1999. Tsunami!, Scientific American, May, pp 56–65.

González, F.I., Satake, K., Boss, E.F., and Mofjeld, H.O., 1995. Edge Waves and Non-trapped Modes of the 25 April 1992 Cape Mendocino Tsunami, Pure & Applied Geophysics, Vol 144(3), September, pp 409–426, DOI: 10.1007/BF00874375.

Horrillo, J., Knight, W., and Kowalik, Z., 2008. Kuril Islands tsunami of November 2006: 2. Impact at Crescent City by local enhancement, J. Geophys. Res., Vol 113, C01021, p 12, doi: 10.1029/2007JC004404.

Intergovernmental Oceanographic Commission (IOC), 2012. Tsunami: The Great Waves, Second Revised Edition, Paris, UNESCO, illus. IOC Brochure 2012-4. (English), p 16.

Intergovernmental Oceanographic Commission (IOC), 2016. Tsunami Glossary, Third Edition, Paris, UNESCO, IOC Technical Series 85. (English, French, Spanish, Arabic, Chinese) (IOC/2008/TS/85 rev.2).

International Tsunami Information Center (ITIC), 2018. Web page accessed in 2018, URL: http://itic.ioc-unesco.org/index.php.

Kayal, J.R., 2006. Seismic Waves and Earthquake Location, Geological Survey of India, Lecture notes for a training course: Preparing for the Next Tsunami: Training in Seismology and Tsunami Warnings in the Indian Ocean Region, offered by Mooney, W.D., USGS, URL: https://escweb.wr.usgs.gov/share/mooney/training%20courses.html

Koshimura, S. and Yanagisawa, H. 2007. Developing fragility curves for tsunami damage estimation using the numerical model and satellite imagery, Proceedings of the 5th International Workshop on Remote Sensing for Disaster Response, George Washington University, Washington, United States, 10–12 September.

Koshimura, S., Matsuoka, M., and Kayaba, S. 2009a. Tsunami hazard and structural damage inferred from the numerical model, aerial photos and SAR imageries, Proceedings of the 7th International Workshop on Remote Sensing for Post Disaster Response, University of Texas, Texas, United States, 22–23 October.

Koshimura, S., Namegaya, Y., and Yanagisawa, H. 2009b. Tsunami Fragility – A new measure to assess tsunami damage, Journal of Disaster Research, 4, pp 479–488.

Koshimura, S., Oie, T., Yanagisawa, H., and Imamura, F. 2009c. Developing fragility curves for tsunami damage estimation using numerical model and post-tsunami data from Banda Aceh, Indonesia, Coast. Eng. J., 51, pp 243–273.

Lynett, P. J., Borrero, J., Son, S., Wilson, R., and Miller, K., 2014. Assessment of the tsunami-induced current hazard, Geophys. Res. Lett., 41, pp 2048–2055, doi:10.1002/2013GL058680.

Madsen, P.A., Fuhrman, D.R., and Schäffer, H.A., 2008. On the solitary wave paradigm for tsunamis. J. Geophys. Res., Vol 113, C12012, p 22, doi:10.1029/2008JC004932.

Madsen, P.A., Fuhrman, D.R., and Wang, B., 2006. A Boussinesq-type method for fully nonlinear waves interacting with a rapidly varying bathymetry, Coast. Eng., 53, pp 487–504.

Maritime Safety Queensland (MSQ), 2017. Queensland Tide Tables: Standard Port Tide Times 2018, Dept of Transport and Main Roads, Queensland Government, p 128.

Matsutomi, H. and Harada, K. 2010. Tsunami-trace distribution around building and its practical use, Proceedings of the 3rd International tsunami field symposium, Sendai, Japan, 10–11 April.

Maqsood, T., Wehner, M., Ryu, H., Edwards, M., Dale, K. and Miller, V. 2014. GAR15 Vulnerability Functions: Reporting on the UNISDR/GA SE Asian Regional Workshop on Structural Vulnerability Models for the GAR Global Risk Assessment, 11–14 November, 2013, Geoscience Australia, Canberra, Australia. Record 2014/38. Geoscience Australia: Canberra. http://dx.doi.org/10.11636/Record.2014.038

Mei, C.C., Stiassnie, M., and Yue, D. K.-P., 2005. Theory and Applications of Ocean Surface Waves, Part 1: Linear Aspects, Advanced Series on Ocean Engineering, Vol 23, World Scientific, pp 172–173.

Mofjeld, H.O., González, F.I., Titov, V.V., Venturato, A.J., and Newman, J.C., 2007. Effects of Tides on Maximum Tsunami Wave Heights: Probability Distributions, J. Atmos. Oceanic Technol., 24, 117–123, https://doi.org/10.1175/JTECH1955.1

Mofjeld, H.O., Symons, C.M., Lonsdale, P., González, F.I., and Titov, V.V., 2004. Tsunami Scattering and Earthquake Faults in the Deep Pacific Ocean, Oceanography, Vol 17(1), pp 38–46.

Mofjeld, H.O., Titov, V.V., González, F.I., and Newman, J.C., 2000. Analytic Theory of Tsunami Wave Scattering in the Open Ocean with Application to the North Pacific, NOAA Tech Memo OAR PMEL-116, Jan, p 37.

Mofjeld, H.O., Titov, V.V., González, F.I., and Newman, J.C., 2001. Tsunami scattering provinces in the Pacific Ocean, Geophysical Res Letters, Vol 28(2), Jan 15, pp 335–338.

Muhari, A., Charvet, I., Tsuyoshi, F., Suppasri, A., Imamura, F., 2015 Assessment of tsunami hazards in ports and their impact on marine vessels derived from tsunami models and the observed damage data, Natural Hazards, 78 (2), pp. 1309–1328.

Munger, S., and Cheung, K.F., 2008. Resonance in Hawaii waters from the 2006 Kuril Islands Tsunami, Geophys. Res. Lett., Vol 35, L07605, p 7, doi: 10.1029/2007GL032843.

Murata, S., Imamura, F., Katoh, K., Kawata, Y., Takahashi, S., Takayama, T. (eds), 2010. Tsunami: To Survive from Tsunami, Advanced Series on Ocean Engineering, Volume 32, World Scientific, p 302.

Nanayakkara, K.I.U. and Dias, W.P.S., 2013. Fragility curves for tsunami loading, International Conference on Structural Engineering & Construction Management, Kandy.

Neetu, S., Suresh, I., Shankar, R., Nagarajan, B., Sharma, R., Shenoi, S.S.C., Unnikrishnan, A.S., and Sundar, D., 2011. Trapped waves of the 27 November 1945 Makran tsunami: observations and numerical modeling, Nat. Hazards, Vol 59, pp 1609–1618, DOI: 10.1007/s11069-011-9854-0.

Nielsen, P., 2012. Coastal and Estuarine Processes, Advanced Series on Ocean Engineering, Vol 29, World Scientific, p 343.

NOAA, 2018a. Tsunami: The Tsunami Story (web page accessed 2018), URL: https://www.tsunami.noaa.gov/tsunami_story.html.

Okada, Y., 1985. Surface Deformation due to Shear and Tensile Faults in a Half-Space, Bulletin of the Seismological Society of America, Vol 75(4), August, pp 1135–1154.

Okada, Y., 1992. Internal Deformation due to Shear and Tensile Faults in a Half-Space, Bulletin of the Seismological Society of America, Vol 82(2), April, pp 1018–1040.

Park, H., Cox, D.T., Lynett, P.J., Wiebe, D.M., & Shin, S., 2013. Tsunami inundation modeling in constructed environments: A physical and numerical comparison of free-surface elevation, velocity, and momentum flux, Coastal Engineering, Vol 79, pp 9–21, doi: https://doi.org/10.9753/icce.v34.currents.1

Park, H., Wiebe, D., and Cox, D.T., 2014. Tsunami inundation modeling: sensitivity of velocity and momentum flux to bottom friction with application to building damage at Seaside, Oregon, Coast. Eng. Proc., No 34, Korea, p 12. URL: https://icce-ojs-tamu.tdl.org/icce/index.php/icce/article/view/7557/pdf_985

Queensland Fire and Emergency Services (QFES), 2018. Queensland Emergency Risk Management Framework (QERMF) Risk Assessment Process Handbook, Queensland Government, p 53.

Queensland Government, 2018. Tsunami, URL: https://www.qld.gov.au/emergency/dealing-disasters/disaster-types/tsunami.

Rabinovich, A.B., Stephenson, F.E., and Thomson, R.E., 2006. The California tsunami of 15 June 2005 along the coast of North America, Atmosphere-Ocean, Vol 44(4), pp 415-427. DOI: 10.3137/ao.440406.

Rasyif, T.M, Kato, S., Syamsidik, Okabe, T., 2016. Influence of Small Islands against Tsunami Wave: Impact along Sumatra Island, Journal of Japan Society of Civil Engineers, Vol 72(2), pp I_331–I_336.

Roeber, V., Yamazaki, Y., and Cheung, K. F., 2010. Resonance and impact of the 2009 Samoa tsunami around Tutuila, American Samoa, Geophys. Res. Lett., Vol 37(21), L21604, p 8, doi: 10.1029/2010GL044419.

Satake, K., 1987. Inversion of Tsunami Waveforms for the Estimation of a Fault Heterogeneity: Method and Numerical Experiments, J. Phys. Earth, Vol 35, pp 241–254.

Stefanakis, T.S., Contal, E., Vayatis, N., Dias, F., Synolakis, C.E., 2014. Can small islands protect nearby coasts from tsunamis? An active experimental design approach, Proceedings of the Royal Society A, 470:20140575, p 20.

Suppasri, A., Koshimura, S., and Imamura, F. 2011. Developing tsunami fragility curves based on the satellite remote sensing and the numerical modeling of the 2004 Indian Ocean tsunami in Thailand, Nat. Hazards Earth Syst. Sci., 11, pp 173–189.

Synolakis, C.E., Bardet, J.P., Borrero, J.C, Davies, H.L., Okal, E.A., Silver, E.A., Sweet, S., and Tappin, D.R., 2002. The slump origin of the 1998 Papua New Guinea Tsunami, Proc. R. Soc. A, Vol. 458, pp 763–789; DOI: 10.1098/rspa.2001.0915.

Synolakis, S.E., and Bernard, E.N., 2006. Tsunami science before and beyond Boxing Day 2004, Phil. Trans. R. Soc. A, Vol 364, Issue 1847, pp 2231–2265, doi:10.1098/rsta.2006.1824.

Synolakis C.E., and Skjelbreia J.E., 1993. Evolution of Maximum Amplitude of Solitary Waves on Plane Beaches, J. Waterway, Port, Coastal, and Ocean Engineering, Vol 119(3), ASCE, May, pp 323–342, doi: 10.1061/(ASCE)0733-950X(1993)119:3(323)

Tadepalli, S., and Synolakis, C.E., 1994. The run-up of N-waves on sloping beaches. Proc. R. Soc. Lond. A, 445, pp 99–112, DOI: 10.1098/rspa.1994.0050.

Tappin, D.R., Watts, P., and Grilli, S.T., 2008. The Papua New Guinea tsunami of 17 July 1998: anatomy of a catastrophic event, Natural Hazards and Earth System Sciences, 8, pp 243-266, https://doi.org/10.5194/nhess-8-243-2008.

Tinti, S., Tonini, R., Bressan, L., Armigliato, A., Gardi, A., Guillande, R., Valencia, N., and Scheer, S., 2011. Handbook on tsunami hazards and damage scenarios: SCHEMA, Project No. 030963, JRC Scientific and Technical Reports, EUR 24691 EN, European Union, p 40.

Truong, H.V.P, 2012. Wave-Propagation Velocity, Tsunami Speed, Amplitudes, Dynamic Water-Attenuation Factors, Proc. 15th World Conf. on Earthquake Engineering, Lisbon, p 10.

UNESCO, 2015. Tsunami risk assessment and mitigation for the Indian Ocean; knowing your tsunami risk – and what to do about it, IOC Manual and Guides No 52, Second Edition, p 160.

UNESCO/IOC, 2010. Where the First Wave Arrives in Minutes: Indonesian Lessons on Surviving Tsunamis Near Their Sources, IOC Brochure 2010-4, pp 36.

United Nations Office for Disaster Risk Reduction (UNISDR), 2017. Words into Action Guidelines: National Disaster Risk Assessment, 2. Tsunami Hazard and Risk Assessment, p 9.

University Corporation for Atmospheric Research (UCAR), 2010. Tsunami: Produced by the COMET Program (web site accessed 2018), URL: http://www.torbenespersen.dk/Publish/tsunami/index.htm

USGS, 2018a. The Science of Earthquakes (web page accessed in 2018), Earthquake Hazards Program, URL: https://earthquake.usgs.gov/learn/kids/eqscience.php

Wijetunge, J.J., 2009. Demarcation of High Hazard Areas Based on Human Stability Considerations in Tsunami Overland Flow, Engineer, Vol XXXXII (01), Institute of Engineers, Sri Lanka, pp 45–52.

Wong, R.H.C., Lin, H.Y., Chau, K.T., and Wai, O.W.H., 2008. Experimental study on edge wave effect inducing by tsunami at Phi-Phi Island (Thailand), 14th World Conference on Earthquake Engineering, Oct 12-17, Beijing, China, pp 9.

Yamazaki, Y., 2010. Depth-Integrated, Non-hydrostatic Model with Grid Nesting for Tsunami Generation, Propagation, and Run-up, PhD Thesis, UniversitI of Hawai'i, Manoa, pp 107.

Yamazaki, Y., and Cheung, K.F., 2011. Shelf resonance and impact of near-field tsunami generated by the 2010 Chile earthquake, Geophys. Res. Lett., Vol 38, L12605, p 8, doi: 10.1029/2011GL047508.

Appendix B Model Calibration

B.1 Introduction

The standard approach to calibrating 2D hydrodynamic models involves adjusting model parameters such as bed roughness, horizontal eddy viscosity, and bathymetry to match measured water level and/or velocity data collected within the study area. This may involve a range of conditions that are expected to influence the local hydrodynamics. Once calibrated, the model is then validated against measured events.

As explained in Boswood (2013), the availability of measured tsunami events along the Queensland coast is scarce, and inundation mapping from historic events is non-existent. As tidal water level data are more readily available, the 2013 study (Stage 1) calibrated the regional models against tide water level predictions for 83 sites over a spring tide period in January to February 2011.

For consistency, the current study undertook to calibrate against predicted tides for the same period considered in the Stage 1 study (Boswood, 2013). However, due to the computation time required to model tides over the 39-day period for the fine resolution Stage 5 mesh, a subset of four days from 20–23 January 2011 was considered. This represented spring tides close to HAT.

B.2 Tide Data and Boundary Conditions

Calibration is based on astronomical tides only (no meteorological component). Model results are compared against predicted tides for sites where tidal constituents are available. This provides a good measure of model skill with minimal complication from uncertainty in model boundary condition data that can occur by introducing meteorological components from forecast or hindcast models.

Boundary conditions were provided by the DHI global tide model (DHI, 2020). For this study, 13 prediction sites with predictions were considered: (Tweed Sand Bypass Jetty; Gold Coast Sand Bypass Jetty; Gold Coast Seaway; Wavebreak Island Labrador Channel; Wavebreak Island (North Channel); Roes Kamp; Coombabah Lake North; Coombabah Creek; Sovereign Island North; Couran Cove; Jumpinpin; Russell Island West; and Mooloolaba). It is noted that the Mooloolaba site is outside the fine mesh region.

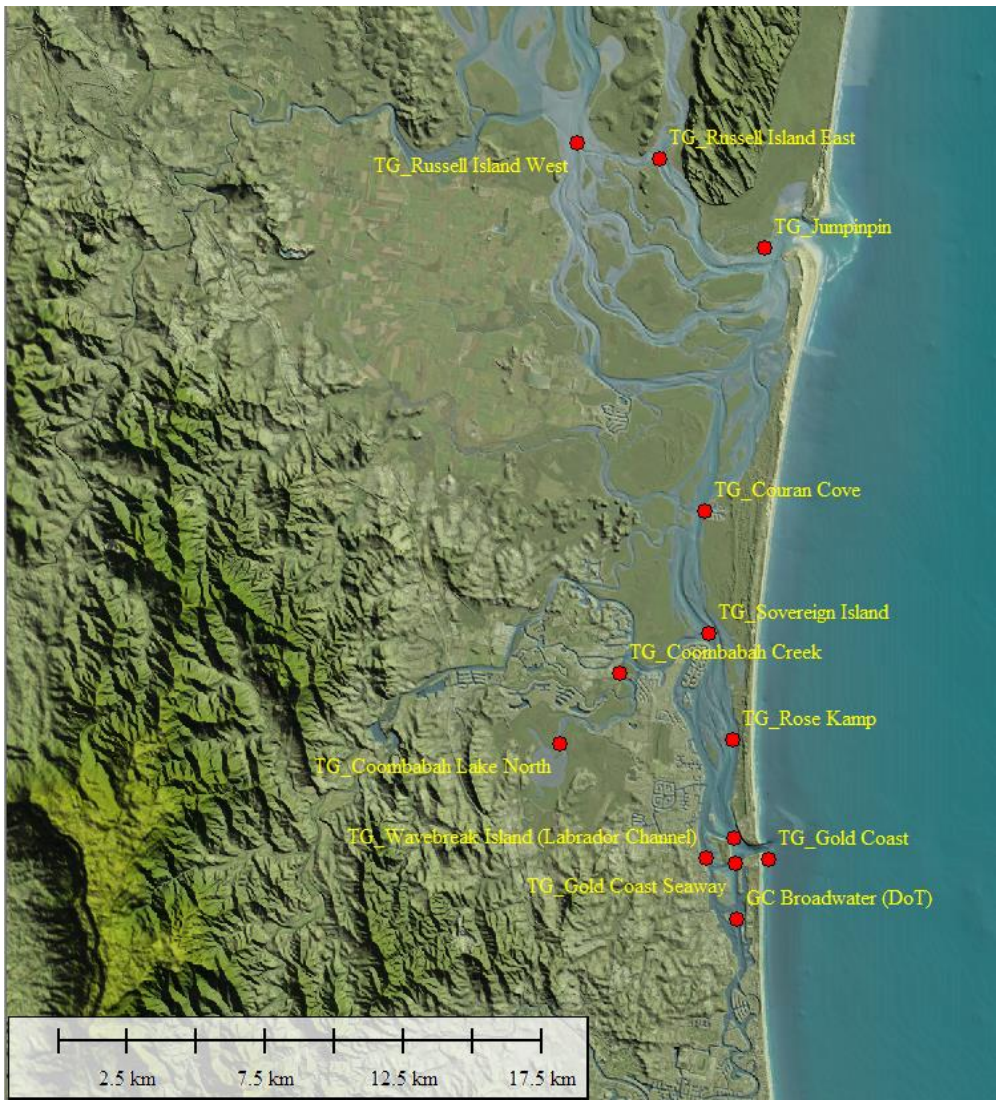

Figure B. 1 – Tide sites within Gold Coast.

B.3 Assessment Approach

The calibration undertaken in Stage 1 involved assessing the skill of the model. The assessment was based on the Index of Agreement (IofA) (Wilmott, 1981), the Coefficient of Determination (R^2) (Kreyszig, 1999), along with the Root Mean Square Error (RMSE) normalised to the amplitude of the Highest Astronomical Tide (HAT) (that is, the height of HAT above Mean Sea Level (MSL)). The criteria adopted are detailed in Table B. 1. The skill scores provide a statistical measure of agreement between the observed (predicted tides) and modelled data.

Table B. 1 – Skill score classification (Boswood, 2013).

Criteria	IofA	R^2	Normalised RMSE (percentage)
excellent	>0.95	>0.925	<10
satisfactory	0.85–0.95	0.85–0.925	10–20
poor	0.5–0.85	0.5–0.85	20–30
reject	<0.5	<0.5	>30

B.4 Calibration Results

Previous studies (Boswood, et al., 2018) considered a range of uniform ocean and waterway Manning's roughness values between n=0.02 to 0.03 (Manning's M = 50 to 33.3), as well as horizontal eddy viscosity based on depth

dependent values, and a constant value using the Smagorinsky formulation (Smagorinsky, 1963). The study found that increases in roughness had little influence on the open coast sites due to the narrow continental shelf. Changes in eddy viscosity had little impact on the tides.

Based on previous studies, only a Manning's roughness of n=0.02 and 0.025 was considered with a constant eddy viscosity (0.28 as applied to previous studies). The results for n=0.02 are provided below and the resulting skill scores are provided in Table B. 2.

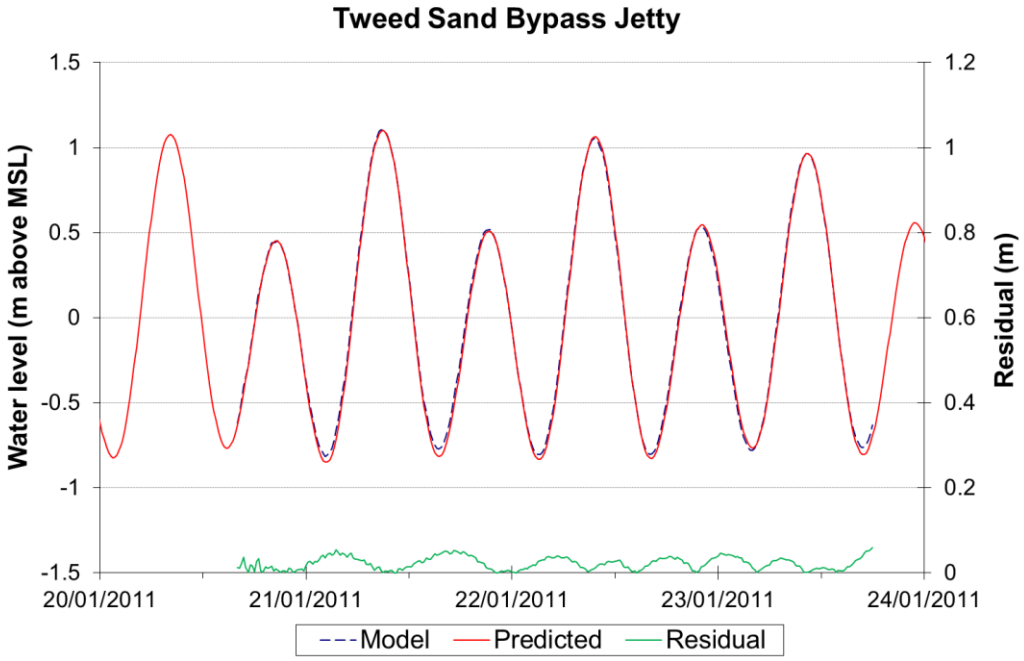

Figure B. 2 – A comparison of the modelled results for the final calibration scenario at Tweed.

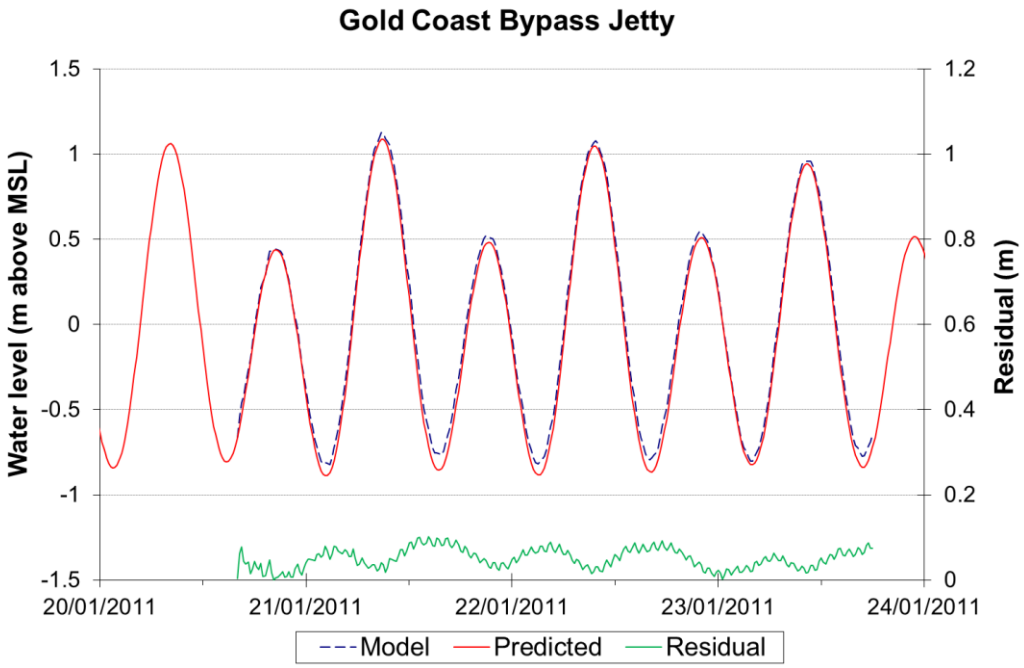

Figure B. 3 – A comparison of the modelled results for the final calibration scenario at Gold Coast Bypass Jetty.

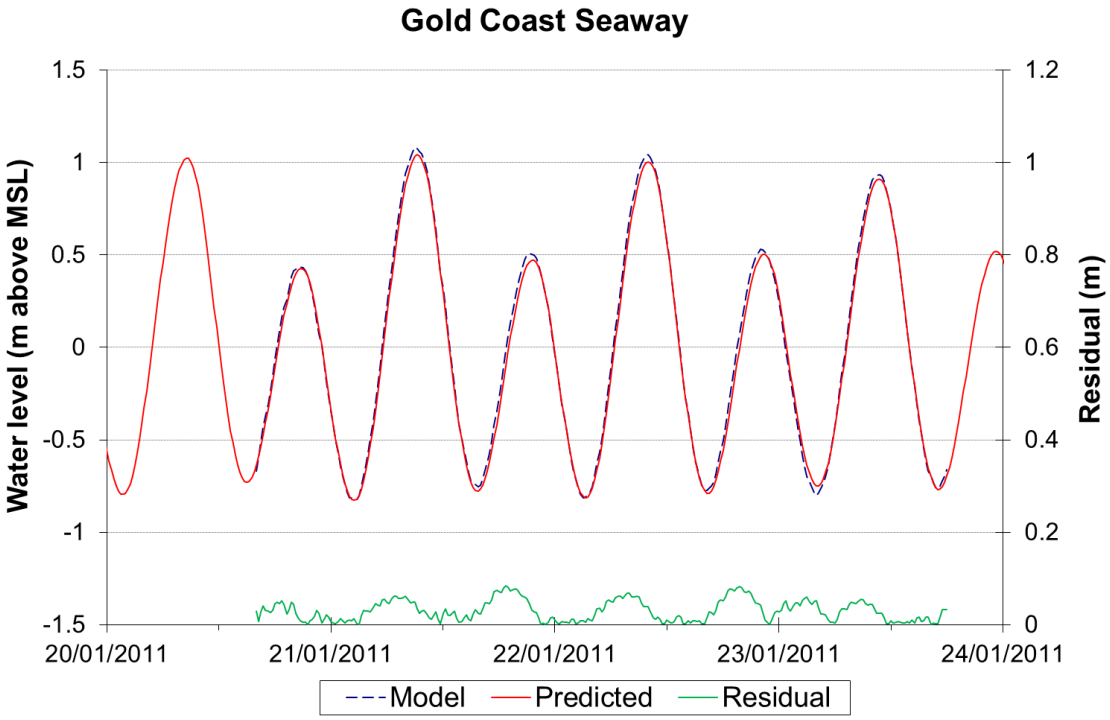

Figure B. 4 – A comparison of the modelled results for the final calibration scenario at Gold Coast Seaway.

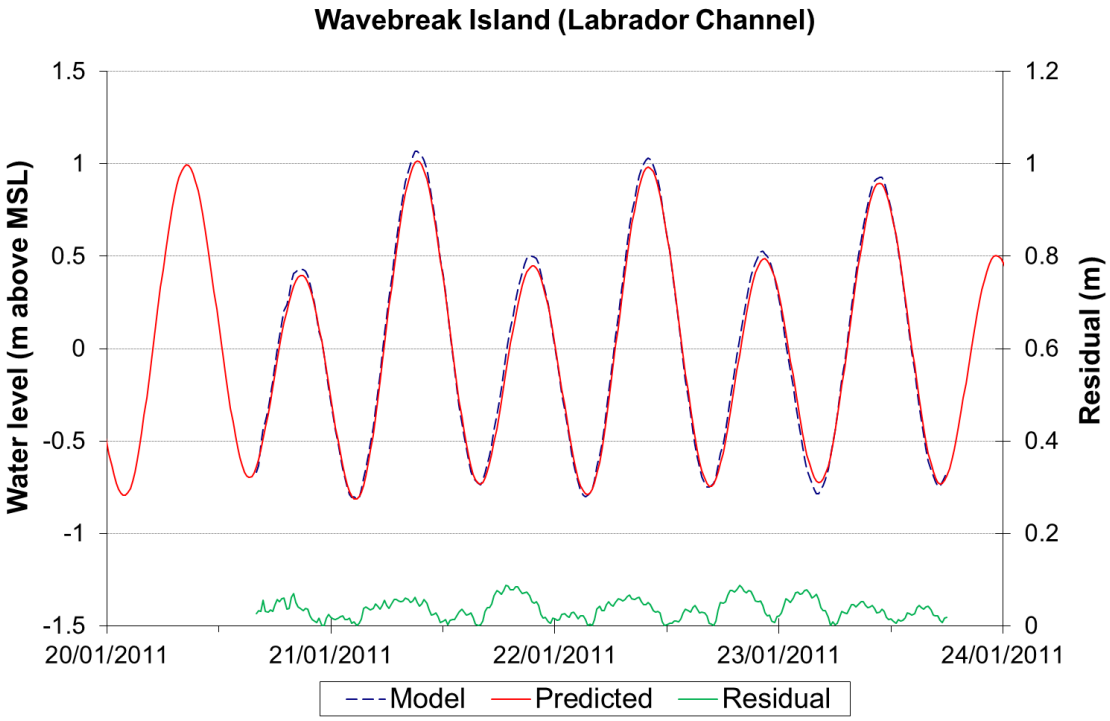

Figure B. 5 – A comparison of the modelled results for the final calibration scenario at Wavebreak Island (Labrador Channel).

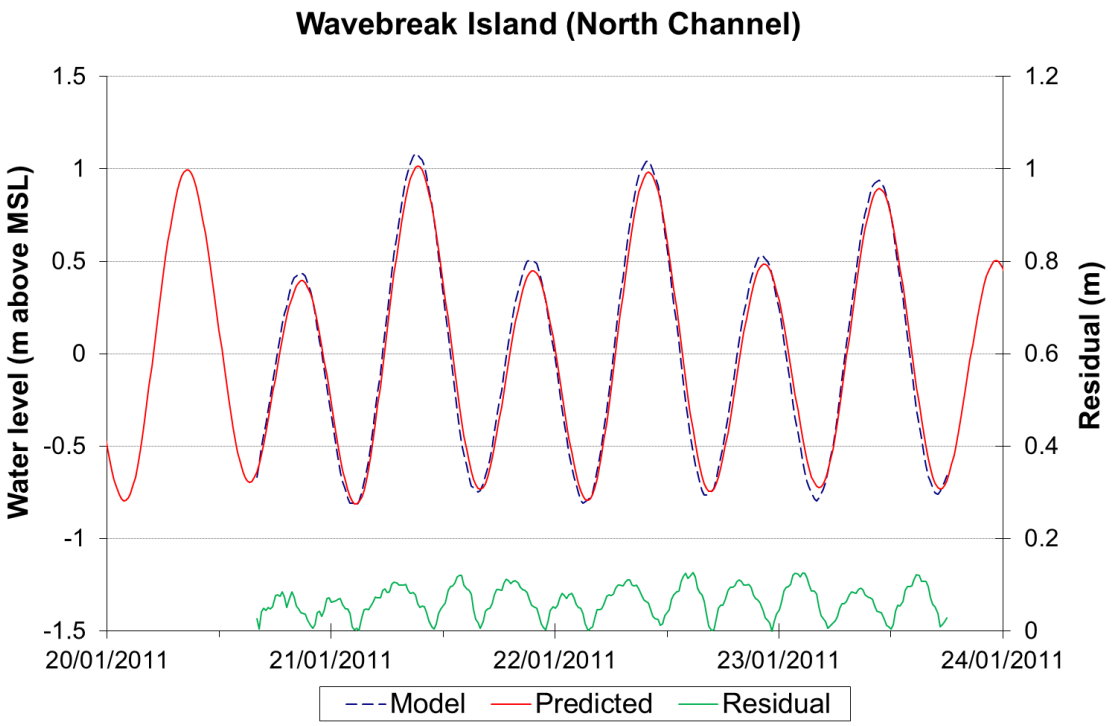

Figure B. 6 – A comparison of the modelled results for the final calibration scenario at Wavebreak Island (North Channel).

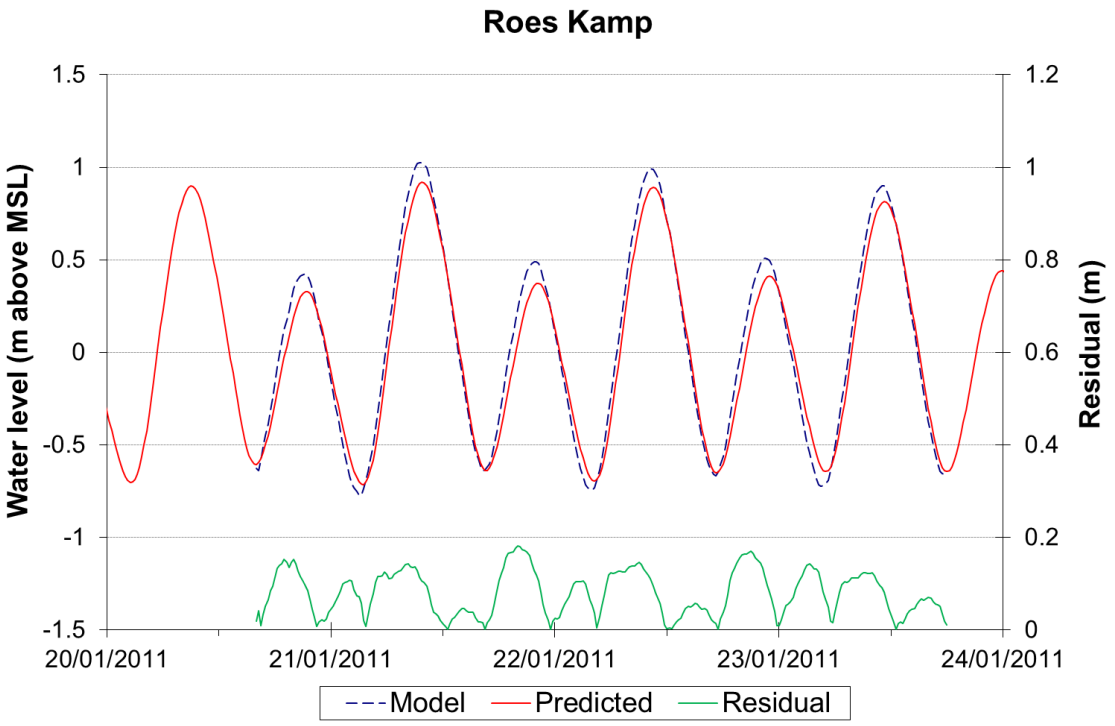

Figure B. 7 – A comparison of the modelled results for the final calibration scenario at Roes Kamp.

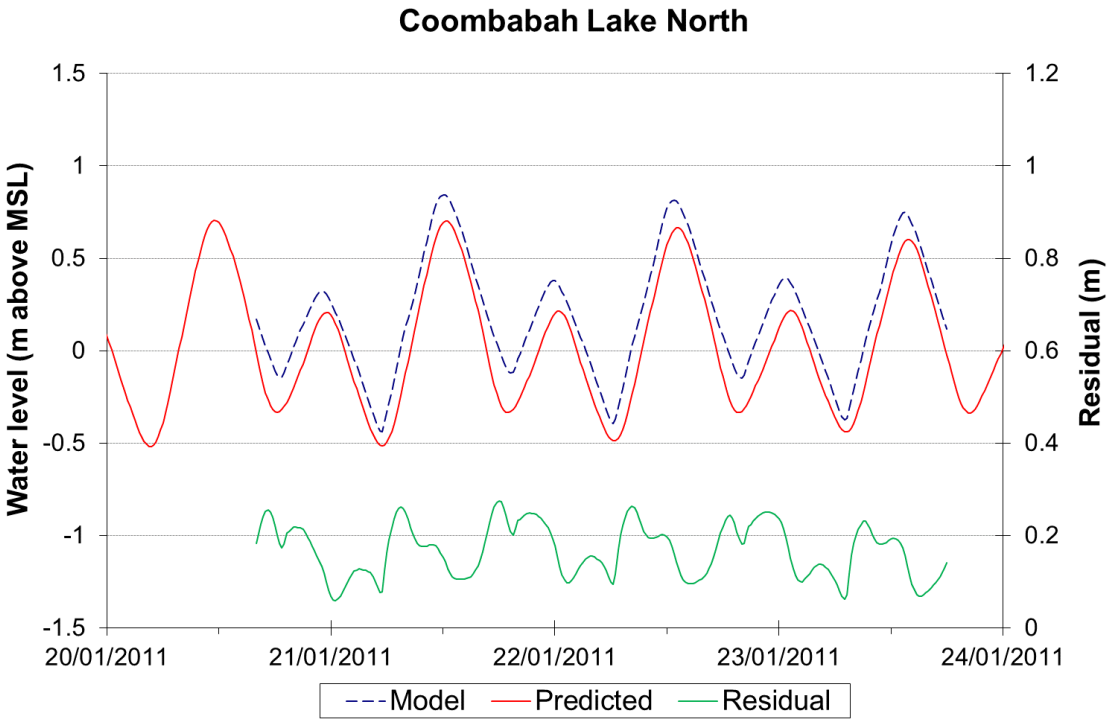

Figure B. 8 – A comparison of the modelled results for the final calibration scenario at Coombabah Lake North.

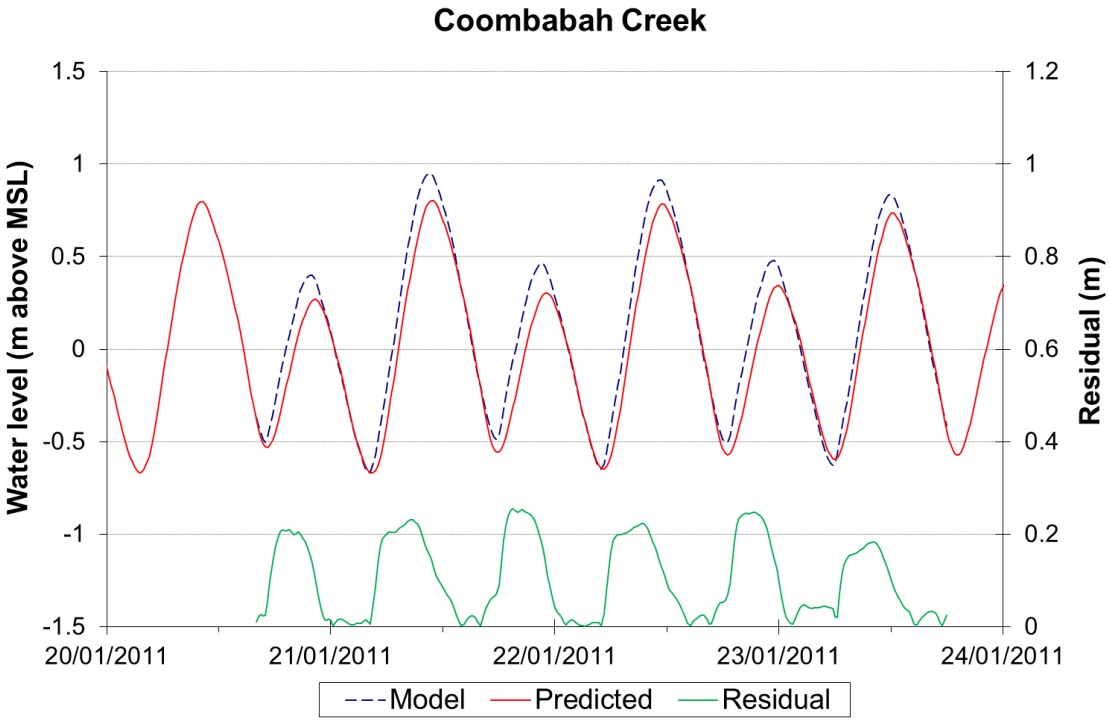

Figure B. 9 – A comparison of the modelled results for the final calibration scenario at Coombabah Creek.

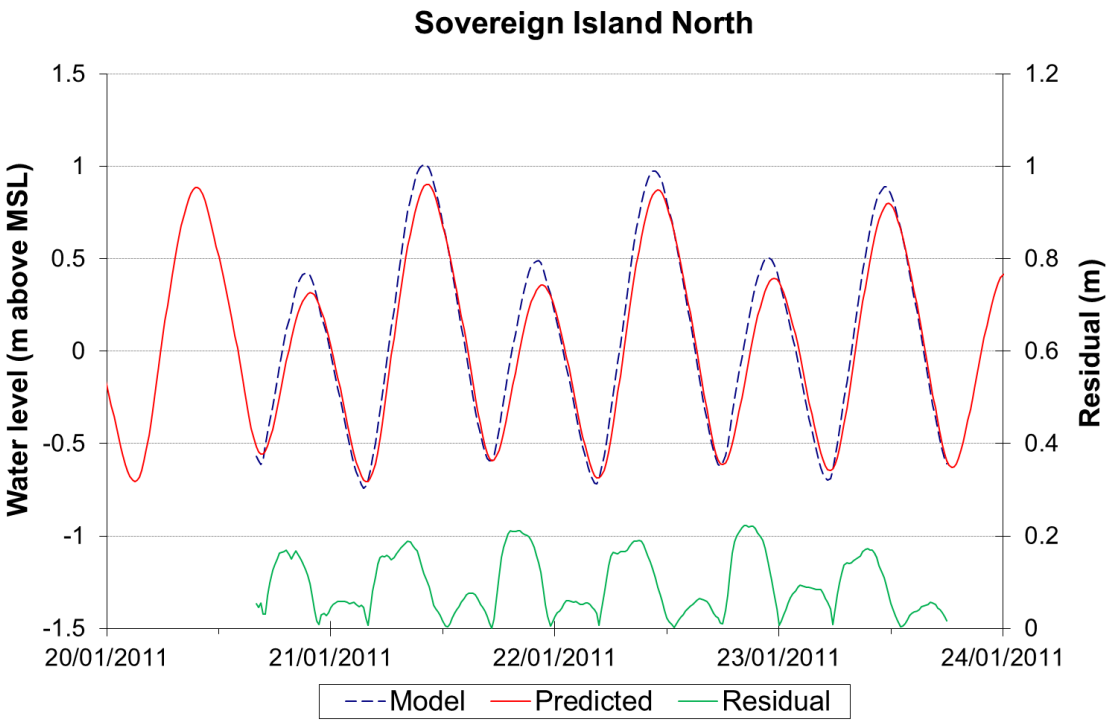

Figure B. 10 – A comparison of the modelled results for the final calibration scenario at Sovereign Island North.

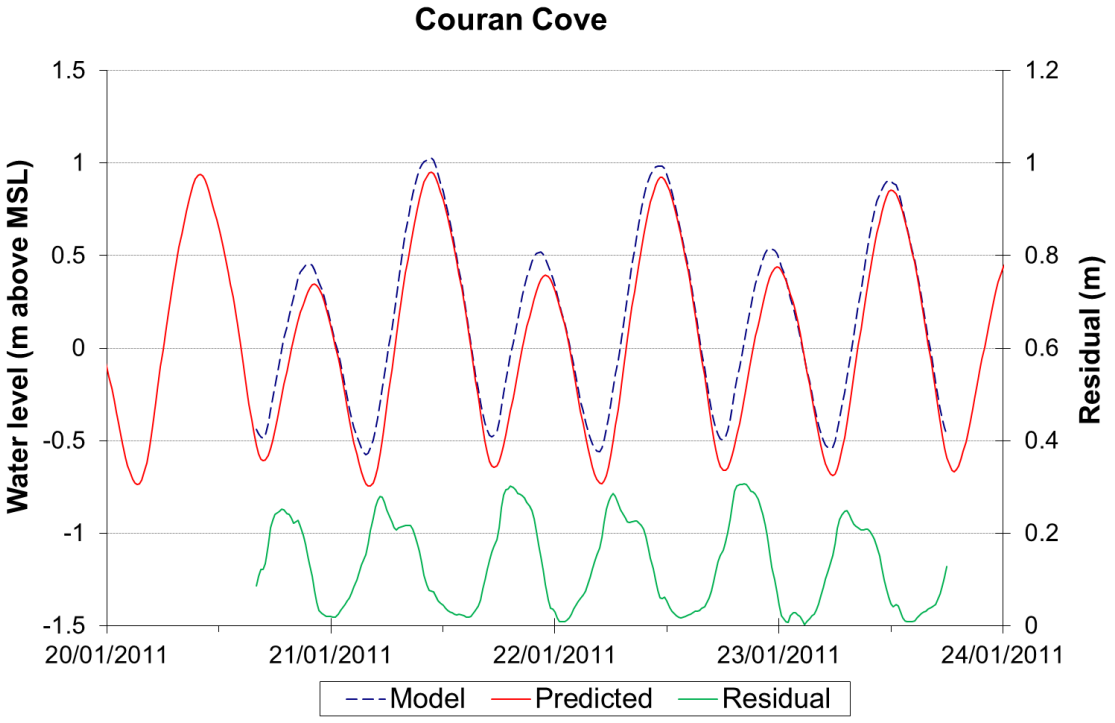

Figure B. 11 – A comparison of the modelled results for the final calibration scenario at Couran Cove.

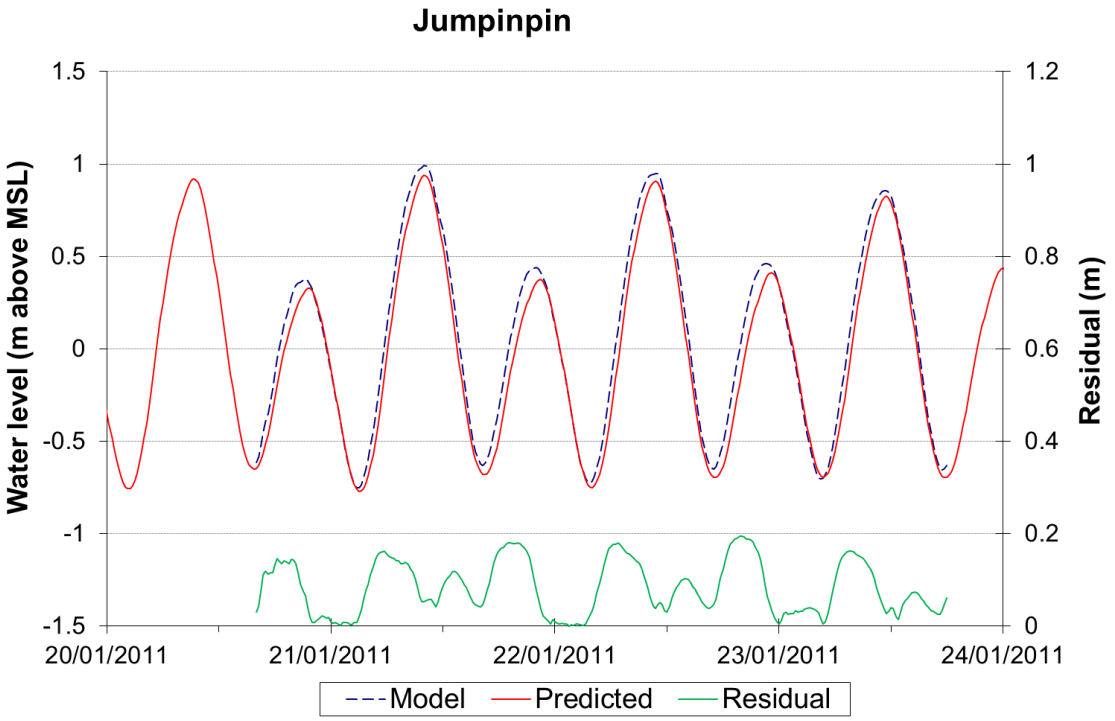

Figure B. 12 – A comparison of the modelled results for the final calibration scenario at Jumpinpin.

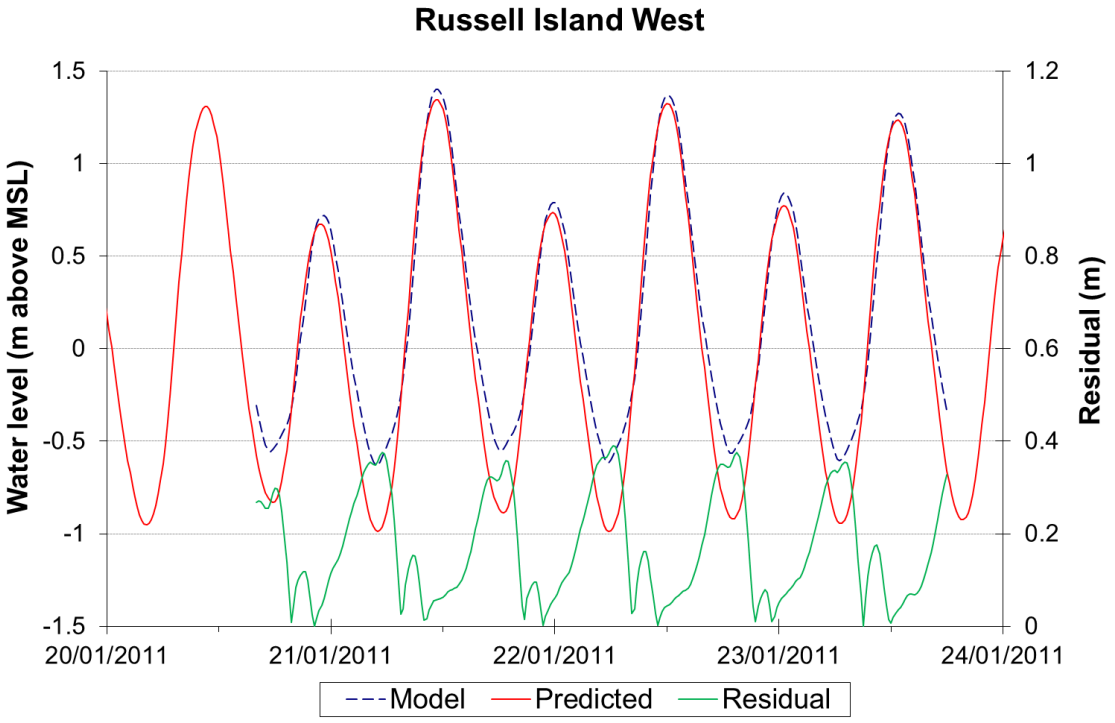

Figure B. 13 – A comparison of the modelled results for the final calibration scenario at Russell Island West.

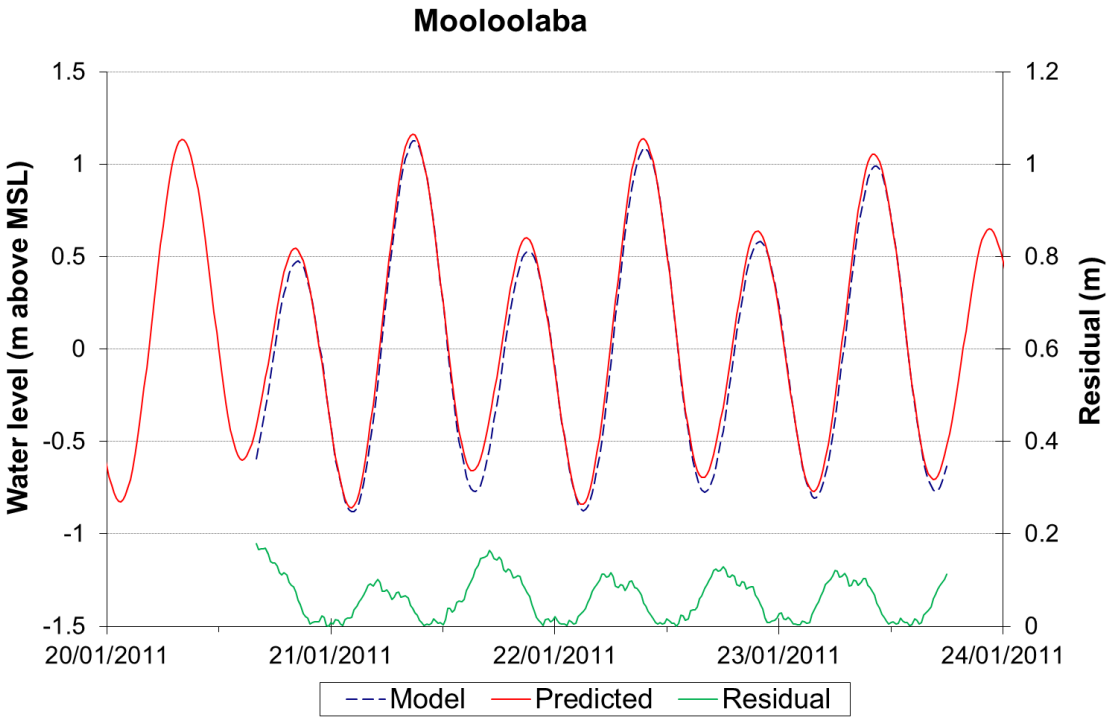

Figure B. 14 – A comparison of the modelled results for the final calibration scenario at Mooloolaba.

Table B. 2 – Skill Score Summary for Manning's roughness, n = 0.02

Criteria	IofA (%)	R^2 (%)	Normalised RMSE (%)
excellent	92.3	100.0	61.5
satisfactory	7.7	0.0	30.77
poor	0.0	0.0	7.69
reject	0.0	0.0	0.0

The tides modelled for both roughness cases are the same for the ocean sites and sites close to the ocean entrance (Figure B. 15). The tides are slightly higher for the upstream sites for Manning's roughness of n = 0.02 but provides a better fit for Russell Island West (Figure B. 16). The model achieves the high tide levels but does not reach the low tide levels. Examination of the low tides shows nonlinear effects, most likely due to the shallow bathymetry in the model that could be constricting low tides that are not entirely representative of the real bathymetry in the area. These effects do not occur closer to the entrance at Jumpinpin. As the study is considering more extreme water levels, this is not expected to be an issue.

There is one poor normalised RMSE score for Coombabah Lake North. This site is in shallow water and the predictions are based on only 90 days of data. The coordinates for the tide site went dry on the low tide indicating differences in the bathymetry. The model extraction point was moved slightly to correspond the channel in the area. There appears to be a shift of approximately 0.16 m between the model results and predictions. Adjusting the predictions provides a good fit with the model results (Figure B. 17).

In any case, the results show good agreement and are slightly conservative, which is acceptable for this study. The results indicate that the model captures the hydrodynamics associated with long period tides.

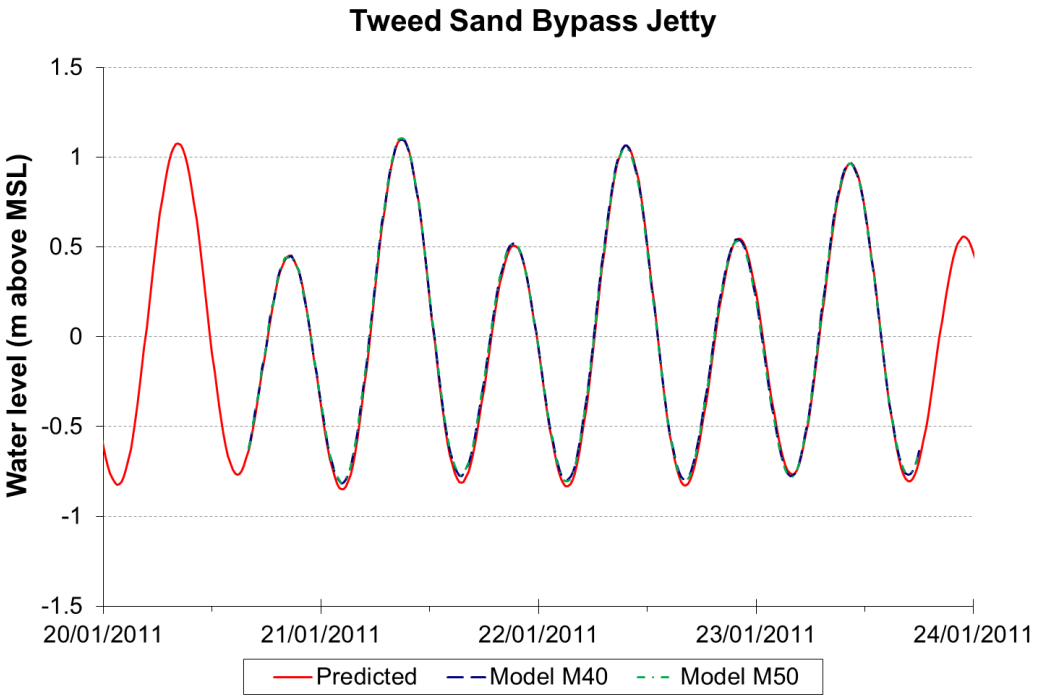

Figure B. 15 – Comparison of tides for both roughness values at Tweed

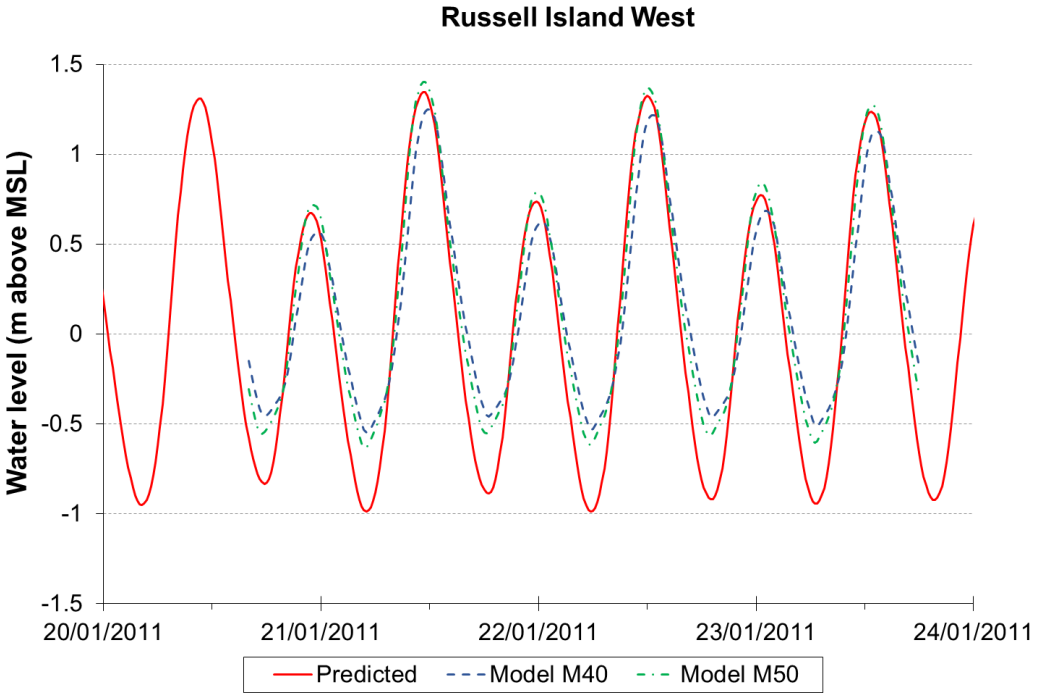

Figure B. 16 – Comparison of tides for both roughness values at Russell Island West.

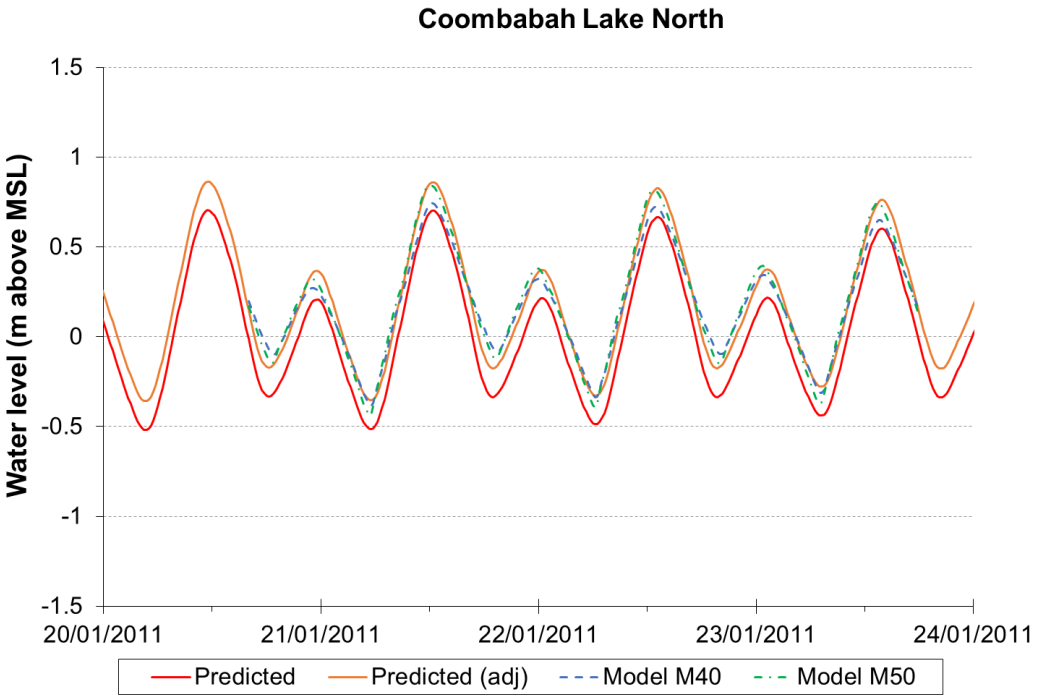

Figure B. 17 – Comparison of tides for both roughness values at Coombabah Lake North.

B.5 Waterway Tides

The model provides an indication of high-water levels within the waterways. To the south of the Gold Coast Seaway entrance in the Nerang River, high tides are within 1 to 1.1 m above MSL. They reduce to 0.85 m in the canal estates around and south of Broadbeach. To the north of the Gold Coast Seaway, the tides are typically 1 m in the Coomera River, and slightly lower in Coombabah Creek, reducing to 0.85 m in Coombabah Lake.

The high tide reaches 1.5 m in the Logan River, whereas it is 1.1 m in Tallebudgera and Currumbin Creeks. In the Tweed River, the tides reach 0.9 m but reduce in Terranora Creek to 0.7 metres.

The model suggests that high tide reaches 1.4 m on the Gold Coast beaches. However, there are no measurements to support this, and the value is likely overestimated.

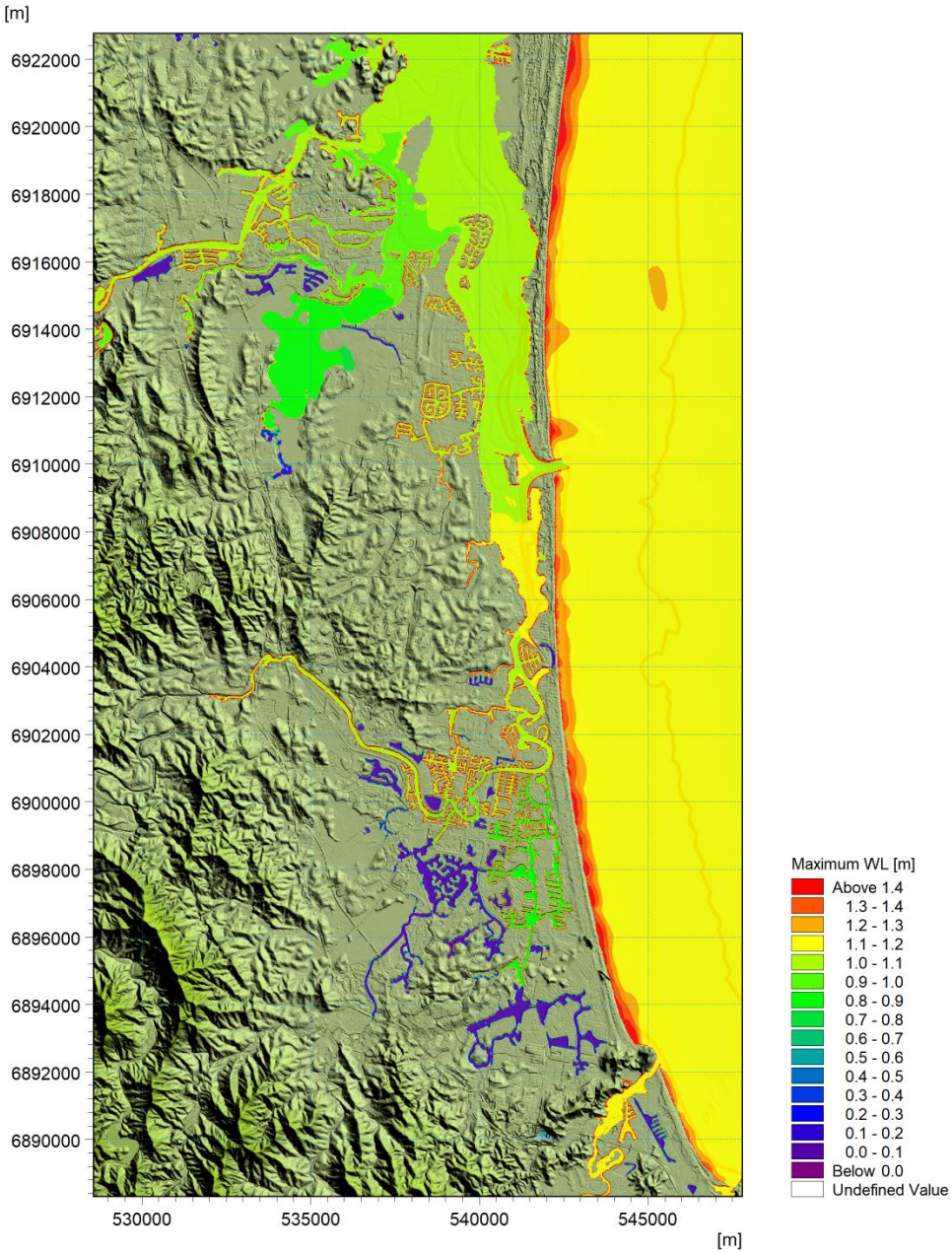

Figure B. 18 – High tide levels on the Gold Coast.

B.6 References

Boswood, P.K., 2013. Tsunami Modelling along the East Queensland Coast, Report 1: Regional Modelling. Brisbane: Department of Science, Information Technology, Innovation and the Arts, Queensland Government, p 111.

Boswood P.K., Wall R., Peach L. 2018. Tsunami Modelling along the East Queensland Coast, Report 3: Moreton Bay. Brisbane: Department of Environment and Science, Queensland Government.

DHI, 2020. Mike 21 Toolbox User Guide, Mike Powered by DHI, p 250.

Kreyszig, E., 1999. Advanced engineering mathematics, Vol. New York: John Wiley, p 1156.

Smagorinsky, J., 1963. General Circulation Experiment with the Primitive Equations, Monthly Weather Review, 91(3), pp 99–164.

Wilmott, C.J., 1981. On the validation of models. Physical Geography, Vol. 2(2), pp 184–194.

Appendix C Validation and Sensitivity Testing

C.1 Introduction

The original Stage 1 model (Boswood, 2013) was validated against the 2007 Solomon Islands tsunami event that was captured by the then Queensland Environmental Protection Agency's (EPA) storm tide monitoring network. Given the purpose of Stage 1 was to assess nearshore amplification up to the 10 m depth contour, this model was coarser than the current mesh and did not include overland flooding (i.e., a fixed land boundary at RL −0.5 m AHD). The previous validation was therefore revisited for the current mesh.

C.2 2007 Solomon Islands Tsunami Event

On 01 April 2007, at about 20:39:58 UTC, an 8.1 magnitude earthquake occurred at latitude 8.481° south and longitude 156.978° east because of shallow thrust faulting along the boundary of the Pacific plate with the Australia, Woodlark, and Solomon Sea microplates (Hayes et al., 2017). The epicentre of the quake was about 43 km south-south-east of Gizo in the Solomon Islands, and approximately 540 km west-north-west of the capital Honiara (EPA, 2007). The earthquake (which lasted for more than one minute) generated a tsunami that devastated the local islands with run-up heights up to 12.1 m, resulting in 52 deaths and destroying 2,500 buildings (McAdoo et al., 2008 and NOAA, 2018b). Over 3 hours later, the tsunami started to reach the Queensland coastline. The waves that were measured by several Queensland tide gauges were of much smaller magnitude. Amplitudes along the east coast of Queensland were typically less than 0.1 m except for Clump Point and Rosslyn Bay, which recorded in the order of 0.25 metres (EPA, 2007).

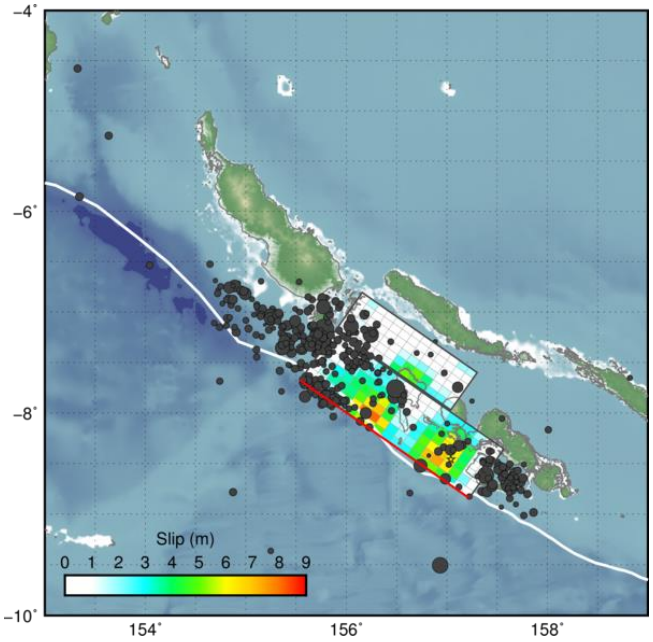

Figure C. 1 – Surface projection of the slip distribution for the 2007 Solomon Islands earthquake superimposed on GEBCO bathymetry (USGS: https://earthquake.usgs.gov/earthquakes/eventpage/usp000f83m#finite-fault).

Several sources describe the seabed deformations with some variations. NOAA (2018b) refers to an uplift of up to 3.6 m and subsidence down to 1.5 m, resulting in reports of tsunami waves between 2 to 10 m. USGS (2018b) has the origin at latitude 8.466° south and longitude 157.043° east with a depth of 24 km (last updated 07 February 2017). Its preliminary finite faults analysis is shown in Figure C. 1 based on 2 segments with a strike of 305 degrees and dip of 14 and 30 degrees respectively. Their modelling of the earthquakes implies a fault area of 200 x 80 kilometres.

Based on a fault area of 180 x 60 km, a 300-degree strike and 14-degree slip, Koshimura (2018) developed the deformation map shown in Figure C. 2. Further information about the earthquake can be found in Fisher et al. (2007) and Chen et al. (2009).

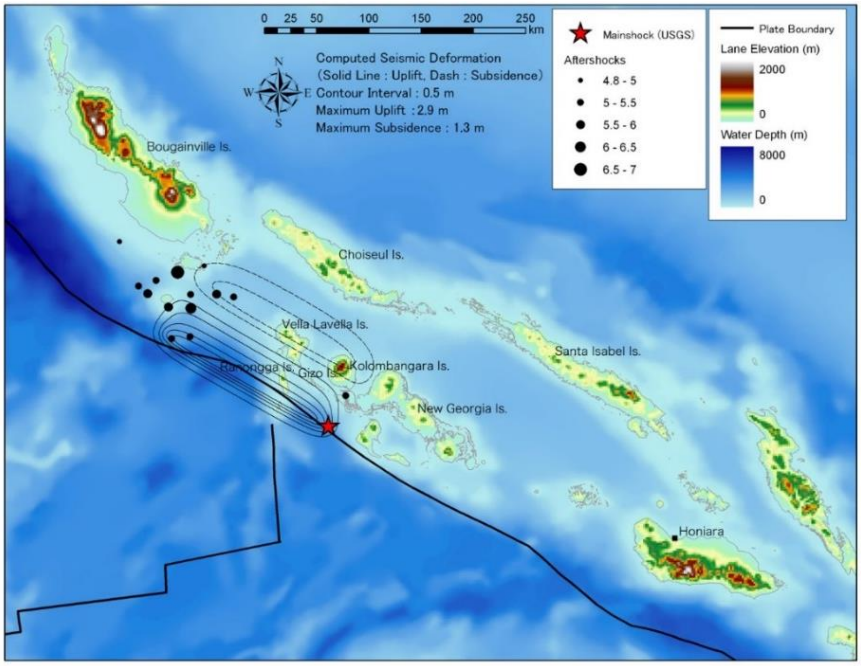

Figure C. 2 – Seabed deformation during 2007 Solomon Islands earthquake (Dr S Koshimura: http://www.tsunami.civil.tohoku.ac.jp/hokusai2/disaster/07_Solomon/event.html)

C.3 Tsunami Event Data and Boundary Conditions

The 2007 Solomon Islands tsunami event was captured by the then EPA's storm tide monitoring network at a 1-min sampling rate. Only 2 sites were available within the Gold Coast model domain: Gold Coast Seaway; and Mooloolaba. The tsunami signal was extracted from the tides by using a 61-minute centred moving average to the raw data.

Boundary conditions for the Stage 5 model, in the form of water level and depth-averaged velocity time series, were obtained from the Stage 1 validation model (as shown in Figure C. 3).

The offshore boundary of the Stage 1 validation model is located at 158° longitude. The north-east corner has been clipped to be more parallel with the wave crest, connecting to the south-east extent of Papua New Guinea (Figure C. 3). As the tsunami was generated from an earthquake approximately 500 km north of the north-east corner of the mesh, boundary conditions in the form of a varying water level time series along the open offshore boundaries were provided courtesy of Geoscience Australia (GA) and consisted of a maximum leading wave ranging between 0.7 m in the north and 0.05 m in the south. Although the land boundary was based on a GIS shapefile polyline representing 0 m AHD, the depths along the boundary interpreted from the gbr100 DEM varied between −1.5 m and −15 m AHD. The mesh consists of 1,179,240 triangular elements with areas generally ranging from 17 km^2 offshore to 31,000 m^2 near the coast. This equates to approximately an equivalent spatial resolution of 6 km offshore to 250 m along the coast. Finer meshes with equivalent spatial resolutions down to 50 m were incorporated in the vicinity of storm tide gauge locations. Tides were excluded, with the tsunami time series applied to a constant water level set to Mean Sea Level (MSL). The mesh extent and modelled maximum water levels are shown in Figure C. 3.

The Stage 1 model was re-run to provide time series outputs of water level and depth-averaged velocities at the offshore Stage 5 model boundary.

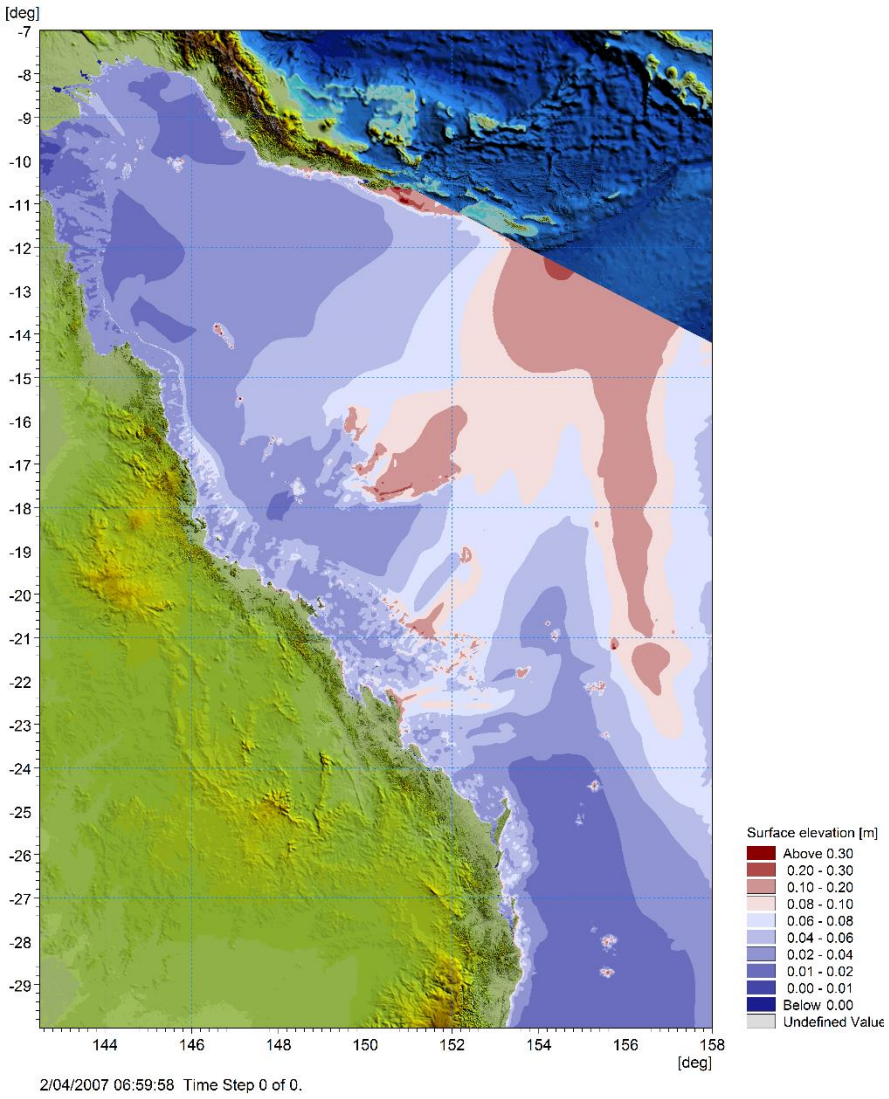

Figure C. 3 – Stage 1 mesh domain and maximum water level for 2007 Solomon Islands tsunami model validation.

C.4 Validation Results

The results of the validation for the Stage 5 mesh are provided in Figure C. 4 and Figure C. 5 for Gold Coast Seaway and Mooloolaba, respectively, and are summarised in Table C. 1 in terms of the maximum amplitude and

Table C. 2 for arrival times. The Gold Coast Seaway site is located within the finer mesh study area, but Mooloolaba is outside of the finer mesh within the study region. The Mooloolaba monitoring site was located at the pilot jetty in the Mooloolah River. The river is not resolved within the Stage 5 mesh as it is outside the study region. A location just offshore was used for this comparison. Being in river entrances, the 2 locations will be influenced by tidal currents, particularly the Gold Coast Seaway. These currents are not represented in the model.

There is also some uncertainty associated with the boundary water level time series as there were no offshore measurement sites in the Coral Sea to validate the Stage 1 model against, and as described in Pedersen et al. (2005) and Luger and Harris (2010), it is possible that there may be some numerical dispersion with a 6 km offshore mesh resolution. Sensitivity testing demonstrated that the model became too dispersive when the offshore mesh resolution was increased. The boundary conditions for the Stage 1 model are also the result of a model run from Geoscience Australia.

Despite these limitations, the modelled results perform well against the measured data in terms of arrival times and the amplitude of the leading wave.

Table C. 2 provides the measured and modelled arrival times relative to the time of the earthquake. The arrival time is defined as the time when the leading edge of the tsunami deviates by more than 1 cm from Mean Sea Level. Determination of the recorded arrival times for the monitoring sites can be complicated by the tsunami amplitude being comparable in magnitude to the background meteorological fluctuations preceding the event. There is only 3 minutes difference for Mooloolaba. There is a 6-minute difference for the Gold Coast Seaway. There are only a few

waves available for the measured tsunami at Gold Coast Seaway. Apart from the tsunami occurring slightly earlier in the model, there is good representation of these waves in the model results with only 1 cm difference in maximum water levels. The Mooloolaba site underestimated the maximum water level and did not capture the higher frequency oscillations observed in the measured data. However, Mooloolaba is outside of the study area, and the mesh is coarser in this area, which could have affected the results. The Mooloolah River was also not captured in the model.

Table C. 1 – Measured and modelled maximum tsunami amplitude for the 2007 Solomon Islands tsunami.

Site	Location	Measured Maximum Amplitude (m)	Stage 1 Max Amplitude (m)	Stage 3 Max Amplitude (m)
Gold Coast Seaway	Within the Broadwater	0.07	0.04	0.06
Mooloolaba	Pilot jetty within Mooloolah River	0.10	0.1	0.06

Table C. 2 – Tsunami arrival times following the 2007 Solomon Islands earthquake for select tide sites.

Site	Measured Arrival Time (h:min)	Stage 1 Model (MSL) Arrival Time (h:min)	Stage 5 Model (MSL) Arrival Time (h:min)
Gold Coast Seaway	4:28	4:20	4:22
Mooloolaba	4:11	4:09	4:08

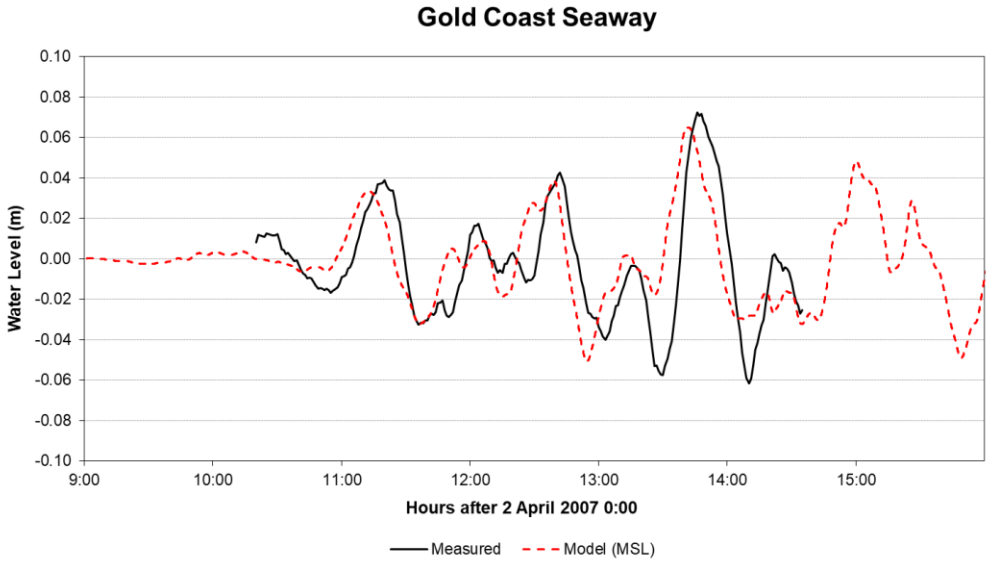

Figure C. 4 – Solomon 2007 tsunami model results near Gold Coast Seaway.

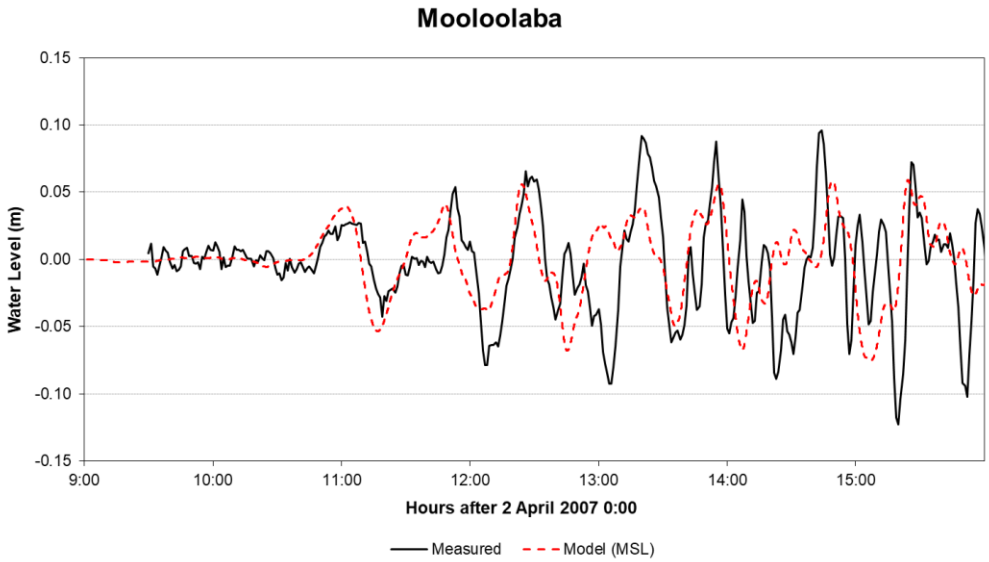

Figure C. 5 – Solomon 2007 tsunami model results near Mooloolaba.

Some sensitivity testing was undertaken by varying the roughness described in the tide calibration (Appendix B). However, there were only marginal changes to the modelled water levels, most likely contributable to the very small amplitudes being modelled.

In general, the validation exercise for the 2007 Solomon Islands tsunami event supports the use of MIKE21FM and the developed mesh for tsunami propagation studies. However, it is noted that this validation has relied solely on one event.

C.5 Sensitivity Testing

The calibration phase demonstrated that for tides, the model behaviour in terms of amplitude and phase were slightly sensitive to roughness within the Broadwater and near Russell Island. Similar checks for the validation phase show lesser sensitivity. Cardno (2013) undertook an assessment of tsunami inundation risk for the New South Wales government. Sensitivity testing undertaken in that study indicated that for seabed roughness, the model was not particularly sensitive, and a Manning's roughness (n), of 0.02 was adopted. The report also discussed sensitivity to tides, structures, and overland roughness. It did not discuss eddy viscosity as a sensitivity parameter.

To further test model sensitivity, several runs were undertaken for a 10,000-year ARI event from Kermadec-Tonga at HAT (event ID 43443). As with tides, Manning roughness values of 0.02 and 0.025 were tested. The results are demonstrated for select locations in Table C. 3 and Table C. 4 for ocean and waterway sites, respectively.

The results for the open ocean showed similar results to Cardno (2013). That is, the tsunami is not particularly sensitive to open ocean seabed roughness with changes typically less than 10 per cent. Within the waterways there were increases of up to 20 per cent. However, the higher increases are associated with maximum water levels below one metre.

The model was found to be more sensitive to mesh size. An initial nearshore mesh size area of 50,000 m^2 (length of approximately 300 m) was compared with the final nearshore mesh size area of 4,000 m^2 (approximate length of 90 m). This resulted in an increase in maximum water level of up to 27 per cent. Figure C. 6 demonstrates the change in maximum water level for several ocean sites. Considerable effort was taken into refining the mesh in consideration of percentage change in maximum water levels and increased computation time.

Based on the tidal analysis, validation and sensitivity testing, a constant seabed and waterways roughness of 0.02 and a constant Smagorinsky (1963) coefficient of 0.28 (default value) were adopted. Overland roughness was defined by interpolation of the roughness mapping described in Appendix D.

Table C. 3 – Percentage change in maximum water level relative to a Mannings number, n = 0.025 for select ocean sites.

Location	Mannings 0.025 (Max WL)	Mannings 0.02 (% increase)
Burleigh Beach	4.02	2.2
Miami Beach	3.96	0.5
Surfers Paradise Beach	4.23	3.4
Seaworld-seaside	4.02	2.7
South Stradbroke	4.29	5
Kirra	4.37	2.6
Palm Beach	3.66	2.9
Coolangatta	4.07	2.1
Fingal Head	4.30	6.9

Table C. 4 – Percentage change in maximum water level relative to a Mannings number, n = 0.025 for select waterway sites.

Location	Mannings 0.025 (Max WL)	Mannings 0.02 (% increase)
Logan River mouth	0.32	18
Coomera River mouth	0.46	13
Coombabah Creek	0.16	7
Runaway Bay	1.63	8
Gold Coast Seaway	2.43	4
Nerang River (Campbell Street Reserve)	0.32	15
Bond University	0.22	7
Lake Awonga Reserve	1.37	4
Currumbin Creek Estuary Bridge	2.02	2
Terranora Creek (Kennedy Drive bridge)	0.39	12
Coolangatta Golf Club	0.47	10

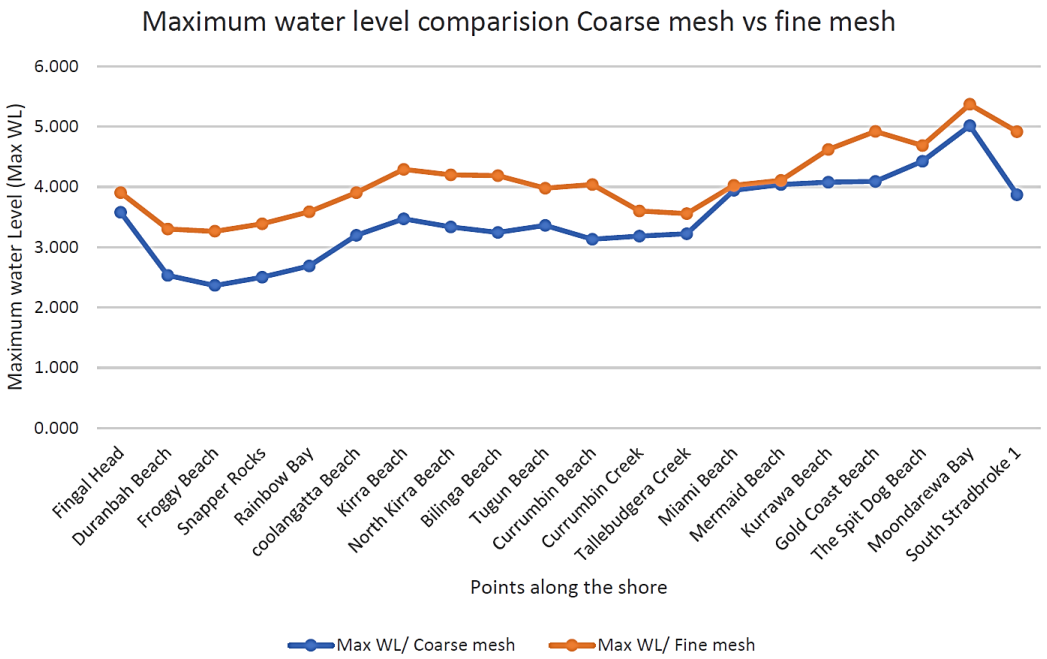

Figure C. 6 – Sensitivity to mesh resolution at select ocean sites.

C.6 References

Boswood, P.K. 2013. Tsunami Modelling along the East Queensland Coast, Report 1: Regional Modelling. Brisbane: Department of Science, Information Technology, Innovation and the Arts, Queensland Government, p 111.

Cardno,.2013. NSW Tsunami Inundation Modelling and Risk Assessment, Report prepared for the NSW State Emergency Service and the Office of Environment and Heritage, p 64.

Chen, T., Newman, A.V., Feng, L., and Fritz, H.M., 2009. Slip distribution from the 1 April 2007 Solomon Islands earthquake: A unique image of near-trench rupture, Geophysical Research Letters, Vol 36, L16307, p 6, URL: https://doi.org/10.1029/2009GL039496.

Hayes, G.P., Myers, E.K., Dewey, J.W., Briggs, R.W., Earle, P.S., Benz, H.M., Smoczyk, G.M., Flamme, H.E., Barnhart, W.D., Gold, R.D., and Furlong, K.P., 2017. Tectonic summaries of magnitude 7 and greater earthquakes from 2000 to 2015: U.S. Geological Survey Open-File Report 2016–1192, p 148, https://doi.org/10.3133/ofr20161192.

Environmental Protection Agency (EPA), 2007. Solomon Islands tsunami, Fact Sheet, FS 2007-2, May, p 3.

Fisher, M.A., Geist, E.L., Sliter, R., Wong, F.L., Reiss, C., and Mann, D.M., 2007. Preliminary Analysis of the Earthquake (M_w 8.1) and Tsunami of April 1, 2007, in the Solomon Islands, Southwestern Pacific Ocean, Science of Tsunami Hazards, Vol. 26(1), p 19.

Koshimura, S., 2018. The Tsunami Disaster of 01 April 2007 in the Vicinity of Solomon Sea (web page accessed in 2018), Disaster Control Research Center, Tohoku University, Japan, URL: http://www.tsunami.civil.tohoku.ac.jp/hokusai2/disaster/07_Solomon/event.html.

Luger, S.A., and Harris, R.L., 2010. Modelling Tsunamis Generated by Earthquakes and Submarine Slumps Using MIKE 21, International MIKE by DHI Conference, Copenhagen, 6–8 September 2010, p 13.

McAdoo, B.G, Fritz, H.M., Jackson, K.L., Kalligeris, N., Kruger, J., Bonte-Grapentin, M., Moore, A.L., Rafiau, W.B., Billy, D., and Tiano, B., 2008. Solomon Islands Tsunami, One Year Later, EOS, Transactions, American Geophysical Union, Vol 89(18), 29 April, pp 169–176.

NOAA, 2018b. 2007 Solomon Island Tsunami Event (web page accessed in 2018), National Centers for Environmental Information, URL: https://www.ngdc.noaa.gov/nndc/struts/results?EQ_0=3037&t=101650&s=9&d=100,91,95,93&nd=display

Pedersen, N.H., Rasch, P.S., and Sato, T., 2005. Modelling of the Asian Tsunami off the Coast of Northern Sumatra. 3rd Asia-Pacific DHI Software Conference, Kuala Lumpur, Malaysia, 21–22 February.

Smagorinsky, J., 1963. General Circulation Experiment with the Primitive Equations, Monthly Weather Review, 91(3), pp 99–164.

USGS, 2018b. M 8.1 – Solomon Islands (web page accessed in 2018), Earthquake Hazards Program, URL: https://earthquake.usgs.gov/earthquakes/eventpage/usp000f83m#executive.

Appendix D Overland Roughness Mapping

D.1 Background

The Mike21 software seeks to balance the external forces acting on a mesh cell with the local resistant forces. As a tsunami travels overland, it will experience obstacles and land cover that will obstruct or impede its motion. Including such structures within the model requires a very fine mesh of 1 to 2 metres. An even smaller scale is required to capture features such as trees. However, the computation time of such a fine resolution over large extents becomes prohibitively long, being considerably slower than the actual real-world time the tsunami would travel and requiring a large storage capacity for result files. At very fine resolutions, the flow interaction with buildings can further complicate the problem. For problems focused on inundation extent and depths, a simplified approach has been broadly and successfully applied (e.g., Gayer et al., 2010). The approach replaces the obstacles with a representative roughness that replicates the behaviour of the obstacle in resisting flows.

Typically, overland grid sizes are limited by computation (and storage) requirements. For inundation extent, 5 to 50 m grid sizes are typical for built-up areas, with larger sizes in areas of mostly uniform vegetation. These models are based on a 'bare earth' digital elevation model (DEM), where the structures have been removed, leaving only the ground surface. To facilitate the effect of obstacles, an apparent roughness is adopted, the value of which depends on the type and coverage of the obstacle relative to the area of consideration. Syme (2008) considered the apparent roughness to be a valid option for freshwater flood modelling, as this tries to replicate the effect of water being restricted as it flows through the building, whilst preserving the full storage covered by the building.

Roughness coefficients are typically adjusted to match measured inundation levels. However, such data for a tsunami event is lacking for the study region. Other approaches include determining roughness coefficients from physical models (e.g., Aida, 1977 or Kotani et al., 1998), or by adjusting numerical model inundation extents to match smaller scale numerical models that include buildings as solid structures (e.g., Gayer et al., 2010 or Cardno, 2013). MLITT (2012) provides guidance for tsunami inundation modelling and gives the roughness coefficients from Kotani et al. (1998) as an example. Stage 2 (Boswood, 2013b) adopted three values representing: ocean and waterways; beach and dune system; and built-up areas based on a range of values from Aida (1977), Kotani et al. (1998), Cardno (2013), and Garber et al. (2011).

Bricker et al. (2015) undertook a review of roughness values used in tsunami modelling. The paper concluded that the values provided by Kotani et al. (1998) were smaller than those based on field measurements and large-scale experiments for open channel flow (for example Chow, 1959; Arcement and Schneider, 1984; and Gibson, 2005). They attributed this to the physical model scales not being large enough to avoid the effects of surface tension and viscosity. Housing-density-dependent and flow-depth dependent urban Manning's n relations (Koshimura et al., 2009) produce values like those found in open channel flow literature. Bricker et al. (2015) conclude that tsunami models would benefit from leveraging roughness values from open channel flow literature and cites the work of Bunya et al. (2010), which provides an extensive list of Manning's values based on land use mapping for a storm surge modelling study.

The approach applied to this study was the development of a detailed roughness map based on land use. Further detail is provided in the subsequent section.

D.2 Roughness Map Generation

Manning's values for onshore areas were chosen following a literature review of values as discussed above. The final list of values is provided in Table D. 1, based on the work of Bricker et al. (2015), Bunya et al. (2010), and Cardno (2013). This list has been purposely kept to a minimum to reduce complicated areas that are currently impossible to verify, given the lack of tsunami inundation levels for actual events. It is expected that this will produce a conservative result.

Several different datasets were used to generate a land use map, listed below (refer to Table D. 1 for details), for which roughness values were then applied:

- Queensland Land Use Mapping – QLUMP.
- Queensland Digital Cadastral Database – QDCDB.
- Queensland Wetland Habitat Mapping.
- New South Wales vegetation Mapping
- NSW Cadastre Web Service
- Biodiversity Wetlands NSW

QLUMP was the principal dataset used in Queensland. This is an aggregated product derived from several sources, including remote sensing and field surveys developed and maintained by DES in collaboration with other

government departments and councils. The dataset provides a series of land use categories and types which are sorted by a code. These were then mapped against the land use types identified in the literature review (refer Table D. 1). This provided the base layer for roughness mapping as it has no gaps. However, for the purposes of detailed roughness mapping it missed a number of key elements including roads and detail in urban and coastal areas.

Table D. 1 – Table of Manning's values used with the model domain.

Land Use Category	Manning's n	Manning's M
Coastal Waters	0.02	50
Roads	0.02	50
Wetland Barren	0.030	33.33
Wetland Shrub	0.045	22.22
Grassland	0.030	33.33
Farmland	0.040	25
Coastal Woody Wetland	0.070	14.28
Forest	0.070	14.28
Low Density Urban	0.050	20
Medium Density Urban	0.100	10

Several subsequent layers were used to improve the QLUMP base dataset; the QDCDB provided detailed cadastral information for roads and urban areas. Manning's numbers were assigned based on attribute information which contained details on land use. The Wetland Habitat Mapping layer was also used to define vegetation areas in the coastal floodplains better, allowing the inclusion of mangroves and wetlands, which have different roughness characteristics but were not separated within the QLUMP data. These supplementary layers were then incorporated into the QLUMP data to produce a more complete roughness map. Results were then reviewed against aerial mapping to produce the final roughness map. Figure D. 1 shows the roughness map for the Broadwater region. A similar approach was adopted for areas within New South Wales.

The final land use map has the associated Manning's n and Manning's M (adopted by the MIKE21 software and is the reciprocal of Manning's n) within the attribute table, to convert the product into a roughness map. These are then tied to the model domain mesh node points using a spatial join and those values are ingested into MIKE21.

It is important to note that the final roughness values applied within the model are interpolations at the mesh nodes and therefore the resolution of the roughness map used within the model domain was dependant on the resolution on the model mesh. Figure D. 1 shows good agreement with the original roughness map.

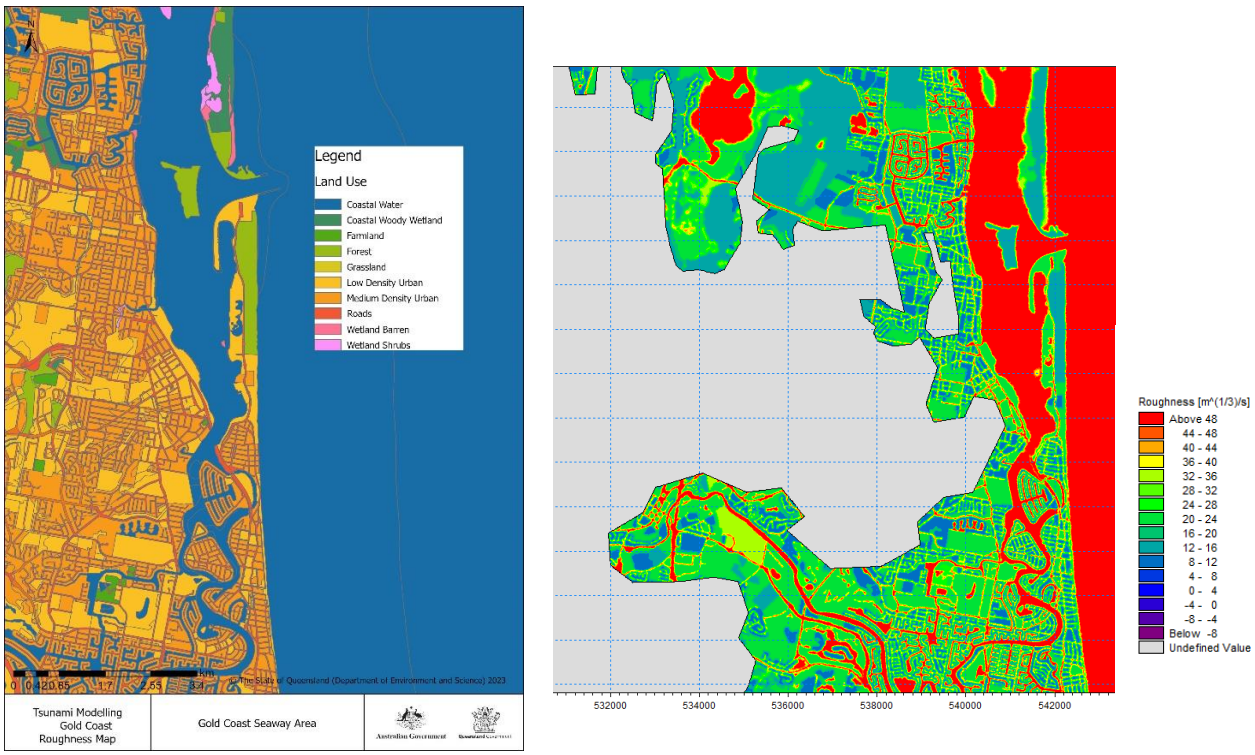

Figure D. 1 – Land use map example for Gold Coast Seaway Area, compared with the roughness map interpolated for the MIKE21 model.

D.3 References

Arcement, G.J. Jr. and Schneider, V.R., 1984. Guide for Selecting Manning's Roughness Coefficients for Natural Channels and Flood Plains, Report No. FHWA-TS-84-204, Federal Highway Administration, also published as US Geological Survey Water Supply Paper 2339 [1989].

Aida, I., 1977. Numerical experiment for inundation of tsunamis. Susaki and Usa, in the Kochi Prefecture. Bulletin of Earthquake Research Institute, University of Tokyo, 52: pp 441–460. (In Japanese).

Boswood, P.K., 2013b. Tsunami Modelling along the East Queensland Coast, Report 2: Sunshine Coast. Brisbane: Department of Science, Information Technology, Innovation and the Arts, Queensland Government, p 96.

Bricker, J.D., Gibson, S., Takagi, H., and Imamura, F., 2015. On the Need for Larger Manning's Roughness Coefficients in Depth-Integrated Tsunami Inundation Models. Coastal Engineering Journal, volume 57(2), June, p 13, https://doi.org/10.1142/S0578563415500059

Bunya, S., Deitrich, J.C., Westerink, J.J., Ebersole, B.A., Smith, J.M., Atkinson, J.H., Jensen, R., Resio, D.T., Luettich, R.A., Dawson, C., Cardone, V.J., Cox, A.T., Powell, M.D., Westerink, H.J., and Roberts, H.J., 2010. A High-Resolution Coupled Riverine Flow, Tide, Wind, Wind Wave, and Storm Surge Model for Southern Louisiana and Mississippi. Part I: Model Development and Validation, Monthly Weather Review, Vol. 18, pp 345–377.

Cardno, 2013. NSW Tsunami Inundation Modelling and Risk Assessment, Report prepared for the NSW State Emergency Service and the Office of Environment and Heritage, p 64.

Chow, V. T., 1959. Open-Channel Hydraulics, McGraw-Hill Book Company, New York, p 113.

Garber, S., Treloar, D., Beadle, C., Hanslow, D., and Opper, S., 2011. Validation of Tsunami Modelling along the NSW Coast, 20th NSW Coastal Conference, Tweed Heads, 8–11 November, 18pp.

Gayer, G., Leschka, S., Nöhren, I., Larsen, O., Günther, H., 2010. Tsunami inundation modelling based on detailed roughness maps of densely populated areas, Natural Hazards and Earth System Sciences, pp 1679–1687.

Gibson, S., 2005. Unsteady HEC-RAS Model of the downtown reach of the Truckee River, HEC, PR-58, p 39.

Koshimura, S., Oie, T., Yanagisawa, H., and Imamura, F., 2009. Developing fragility functions for tsunami damage estimation using numerical model and post-tsunami data from Banda Aceh, Indonesia," Coastal Eng. J. 51(3), pp 243–273.

Kotani, M., Imamura F. & N. Shuto., N., 1998. Tsunami run-up simulation and damage estimation by using GIS. In: Proc. of Coastal Eng., JSCE, vol. 45 (1), pp 356–360. (In Japanese)

MLITT., 2012. Guide to determining the potential tsunami inundation, Seacoast Office, Water and Disaster Management Bureau, Ministry of Land, Infrastructure, Transport and Tourism, Version 2.0 (temporary translation), p 82.

Syme, W.J., 2008. Flooding in Urban Areas – 2D Modelling Approaches for Buildings and Fences, 9th National Conference on Hydraulics in Water Engineering, Engineers Australia, Darwin, 23–26 September, p 8.

Appendix E Tsunami Arrival Times

Tables E. 1 to E. 24 provide the arrival times for various Average Recurrence Intervals (ARIs) and subduction zones. The geographical locations of the sites are depicted in Figure E. 1, which corresponds to Table E. 25. Finally, Table E. 26 and Table E. 27 illustrate the variation in arrival time for the coast and waterways for the given subduction zones.

Differences in water levels between beaches and waterways (with waterways generally maintaining lower water levels) have led to the development of distinct criteria for calculating arrival time as outlined below:

- Beaches – defined as an up-crossing deviation of 4 cm away from the still water level.
- Waterways – defined as an up-crossing deviation of 2 cm from the still water level.

Where no time is provided in the tables, the tsunami did not reach the location or was below the threshold. This could be from attenuation or the presence of control structures such as weirs.

Arrival time statistics (hours: minutes after earthquake) for Northern Beach locations for ARI 10,000 and subduction zones of Kermadec-Tonga (KDT), New Hebrides2 (NH2), and Outer-rise New Hebrides (ONH).

Table E.1 – Arrival time statistics (hours: minutes after earthquake) for Northern Beach locations for ARI 10,000 and subduction zones of Kermadec-Tonga (KDT), New Hebrides2 (NH2), and Outer-rise New Hebrides (ONH).

Arrival Time (hours: minutes after earthquake) Northern Beaches (ARI=10,000 yr)			
Source	**KDT**	**NH2**	**ONH**
Burleigh Beach 1	5:04	3:47	3:29
Nobby Beach	5:05	3:47	3:30
Kurrawa Beach	5:05	3:47	3:30
Surfers Paradise Beach	5:05	3:47	3:30
Seaworld-seaside	5:05	3:47	3:30
Moondarewa Bay	5:06	3:47	3:31
South Stradbroke 2	5:04	3:44	3:28

Table E. 2 – Arrival time statistics (hours: minutes after earthquake) for Northern Beach locations for ARI 2000 and subduction zones of Kermadec-Tonga (KDT), New Hebrides2 (NH2), Outer-rise New Hebrides (ONH), Outer-rise Kermadec-Tonga (OKDT), Solomon2 (S2) and South America (SA).

Arrival Time (hours: minutes after earthquake) Northern Beaches (ARI=2,000 yr)						
Source	**KDT**	**NH2**	**ONH**	**OKDT**	**S2**	**SA**
Burleigh Beach 1	5:14	3:49	3:35	5:13	3:51	18:16
Nobby Beach	5:15	3:50	3:36	5:13	3:51	18:16
Kurrawa Beach	5:15	3:50	3:36	5:02	3:51	18:16
Surfers Paradise Beach	5:15	3:50	3:36	5:02	3:51	18:16
Seaworld-seaside	5:15	3:49	3:36	5:03	3:50	18:17
Moondarewa Bay	5:16	3:50	3:37	5:14	3:50	18:19
South Stradbroke 2	5:14	3:47	3:35	5:12	3:47	18:19

Table E. 3 – Arrival time statistics (hours: minutes after earthquake) for Northern Beach locations for ARI 500 and subduction zones of Kermadec-Tonga (KDT), New Hebrides2 (NH2), Outer-rise New Hebrides (ONH), Outer-rise Kermadec-Tonga (OKDT), Solomon2 (S2) and South America (SA).

Arrival Time (hours: minutes after earthquake) Northern Beaches (ARI=500 yr)						
Source	**KDT**	**NH2**	**ONH**	**OKDT**	**S2**	**SA**
Burleigh Beach 1	5:07	3:46	3:35	5:13	3:52	18:24
Nobby Beach	5:08	3:47	3:35	5:13	3:52	18:25
Kurrawa Beach	5:08	3:47	3:36	5:13	3:52	18:26
Surfers Paradise Beach	5:08	3:47	3:36	5:14	3:52	18:26
Seaworld-seaside	5:08	3:46	3:36	5:14	3:51	18:26
Moondarewa Bay	5:08	3:46	3:36	5:14	3:51	18:27
South Stradbroke 2	5:07	3:44	3:34	5:12	3:48	18:26

Table E. 4 – Arrival time statistics (hours: minutes after earthquake) for Northern Beach locations for ARI 100 and subduction zones of Kermadec-Tonga (KDT), New Hebrides2 (NH2), Outer-rise New Hebrides (ONH), Outer-rise Kermadec-Tonga (OKDT), Solomon2 (S2), South America (SA) and puysegur2 (P2).

Arrival Time (hours: minutes after earthquake) Northern Beaches (ARI=100 yr)							
Source	**KDT**	**NH2**	**ONH**	**OKDT**	**S2**	**SA**	**P2**
Burleigh Beach 1	5:08	3:50	3:42	5:20	3:57	18:39	3:31
Nobby Beach	5:08	3:51	3:43	5:21	3:58	18:39	3:31
Kurrawa Beach	5:09	3:51	3:43	5:21	3:59	18:39	3:31
Surfers Paradise Beach	5:09	3:50	3:43	5:22	3:59	18:39	3:31
Seaworld-seaside	5:10	3:51	3:45	5:22	3:59	18:40	3:31

Table E. 5 – Arrival time statistics (hours: minutes after earthquake) for Southern Beach locations for ARI 10,000 and subduction zones of Kermadec-Tonga (KDT), New Hebrides2 (NH2), and Outer-rise New Hebrides (ONH).

Arrival Time (hours: minutes after earthquake) Southern Beaches (ARI=10,000 yr)			
Source	**KDT**	**NH2**	**ONH**
Kingscliff2	4:54	3:39	3:22
Froggy Beach	4:57	3:39	3:24
Coolangatta Beach	4:59	3:41	3:25
Bilinga Beach	5:00	3:44	3:27
Currumbin Beach	5:02	3:44	3:28
Palm Beach1	5:02	3:45	3:28
Tallebudgera Beach	5:04	3:46	3:29
Maggies Beach	4:53	3:37	3:21
Wooyung Beach	4:54	3:39	3:23
Letitia	4:55	3:39	3:23

Table E. 6 – Arrival time statistics (hours: minutes after earthquake) for Southern Beach locations for ARI 2000 and subduction zones of Kermadec-Tonga (KDT), New Hebrides2 (NH2), Outer-rise New Hebrides (ONH), Outer-rise Kermadec-Tonga (OKDT), Solomon2 (S2) and South America (SA).

Arrival Time (hours: minutes after earthquake) Southern Beaches (ARI=2000 yr)						
Source	**KDT**	**NH2**	**ONH**	**OKDT**	**S2**	**SA**
Kingscliff2	5:05	3:41	3:28	5:07	3:44	18:10
Froggy Beach	5:07	3:41	3:30	5:09	3:44	18:12
Coolangatta Beach	5:09	3:43	3:32	5:11	3:46	18:13
Bilinga Beach	5:11	3:46	3:33	5:09	3:48	18:14
Currumbin Beach	5:12	3:46	3:34	5:13	3:49	18:15
Palm Beach1	5:13	3:47	3:34	5:14	3:50	18:15
Tallebudgera Beach	5:14	3:48	3:35	5:16	3:50	18:16
Maggies Beach	5:03	3:39	3:27	5:05	3:44	18:07
Wooyung Beach	5:05	3:40	3:28	5:06	3:47	18:07
Letitia	5:06	3:41	3:29	5:04	3:44	18:11

Table E. 7 – Arrival time statistics (hours: minutes after earthquake) for Southern Beach locations for ARI 500 and subduction zones of Kermadec-Tonga (KDT), New Hebrides2 (NH2), Outer-rise New Hebrides (ONH), Outer-rise Kermadec-Tonga (OKDT), Solomon2 (S2) and South America (SA).

Arrival Time (hours: minutes after earthquake) Southern Beaches (ARI=500 yr)						
Source	**KDT**	**NH2**	**ONH**	**OKDT**	**S2**	**SA**
Kingscliff2	4:57	3:38	3:28	5:04	3:45	18:16
Froggy Beach	5:00	3:39	3:30	5:04	3:45	18:18
Coolangatta Beach	5:02	3:41	3:31	5:12	3:47	18:20
Bilinga Beach	5:03	3:43	3:32	5:09	3:49	18:21
Currumbin Beach	5:04	3:44	3:33	5:14	3:50	18:22
Palm Beach1	5:05	3:45	3:34	5:12	3:51	18:23
Tallebudgera Beach	5:06	3:45	3:34	5:12	3:51	18:24
Maggies Beach	4:56	3:37	3:27	5:07	3:45	18:14
Wooyung Beach	4:57	3:38	3:28	5:08	3:48	18:15
Letitia	4:58	3:39	3:29	5:04	3:45	18:17

Table E. 8 – Arrival time statistics (hours: minutes after earthquake) for Southern Beach locations for ARI 100 and subduction zones of Kermadec-Tonga (KDT), New Hebrides2 (NH2), Outer-rise New Hebrides (ONH), Outer-rise Kermadec-Tonga (OKDT), Solomon2 (S2), South America (SA) and Puysegur2 (P2).

Arrival Time (hours: minutes after earthquake) Southern Beaches (ARI=100 yr)							
Source	**KDT**	**NH2**	**ONH**	**OKDT**	**S2**	**SA**	**P2**
Kingscliff2	4:58	3:42	3:36	5:12	3:49	18:33	3:24
Froggy Beach	5:00	3:43	3:38	5:13	3:51	18:35	3:25
Coolangatta Beach	5:02	3:46	3:39	5:15	3:53	18:36	3:27
Bilinga Beach	5:04	3:47	3:40	5:17	3:55	18:37	3:28
Currumbin Beach	5:07	3:49	3:42	5:19	3:57	18:38	3:30
Palm Beach1	4:57	3:41	3:34	5:10	3:48	18:31	3:27
Tallebudgera Beach	4:56	3:41	3:34	5:10	3:47	18:31	3:27
Maggies Beach	-	-	-	-	-	-	-
Wooyung Beach	-	-	-	-	-	-	-
Letitia	4:59	3:43	3:37	5:12	3:49	18:34	3:24

Table E. 9 – Arrival time statistics (hours: minutes after earthquake) for Northern Seaway locations for ARI 10,000 and subduction zones of Kermadec-Tonga (KDT), New Hebrides2 (NH2), and Outer-rise New Hebrides (ONH).

Arrival Time (hours: minutes after earthquake) Northern Seaway (ARI=10,000 yr)			
Source	**KDT**	**NH2**	**ONH**
Logan River Mouth	6:07	4:38	4:49
Logan River Boat Ramp	6:28	4:59	5:08
Coomera River Mouth	5:36	4:11	4:00
Coombabah Creek	6:23	4:51	5:07
South Stradbroke - Coombabah Mouth	5:41	4:15	4:06
Coomera River - Jiboora Island	5:44	4:18	4:09
South Stradbroke-Runaway Bay3	4:32	3:54	3:37
Coomera River-Colman Road Reserve	5:49	4:22	4:13
South Stradbroke-Crusoe Island	5:14	3:49	3:33
Runaway Bay-Pacific Park	4:34	3:54	3:38

Table E. 10 – Arrival time statistics (hours: minutes after earthquake) for Northern Seaway locations for ARI 2000 and subduction zones of Kermadec-Tonga (KDT), New Hebrides2 (NH2), Outer-rise New Hebrides (ONH), Outer-rise Kermadec-Tonga (OKDT), Solomon2 (S2) and South America (SA).

Arrival Time (hours: minutes after earthquake) Northern Seaway (ARI=2000yr)						
Source	**KDT**	**NH2**	**ONH**	**OKDT**	**S2**	**SA**
Logan River Mouth	6:16	4:44	4:59	6:51	4:47	19:35
Logan River Boat Ramp	6:36	5:03	5:17	7:04	5:06	19:50
Coomera River Mouth	5:42	4:14	4:06	5:53	4:16	18:46
Coombabah Creek	6:33	5:07	5:25	8:38	5:00	19:42
South Stradbroke - Coombabah Mouth	5:47	4:18	4:26	5:58	4:21	18:52
Coomera River - Jiboora Island	5:50	4:21	4:29	6:02	4:24	18:56
South Stradbroke-Runaway Bay3	5:23	3:56	3:43	5:09	3:57	18:18
Coomera River-Colman Road Reserve	5:56	4:26	4:34	6:10	4:28	18:58
South Stradbroke-Crusoe Island	5:19	3:51	3:40	5:17	3:51	18:20
Runaway Bay-Pacific Park	5:24	3:56	3:44	5:10	3:58	18:19

Table E. 11 – Arrival time statistics (hours: minutes after earthquake) for Northern Seaway locations for ARI 500 and subduction zones of Kermadec-Tonga (KDT), New Hebrides2 (NH2), Outer-rise New Hebrides (ONH), Outer-rise Kermadec-Tonga (OKDT), Solomon2 (S2) and South America (SA).

Arrival Time (hours: minutes after earthquake) Northern Seaway (ARI=500 yr)						
Source	**KDT**	**NH2**	**ONH**	**OKDT**	**S2**	**SA**
Logan River Mouth	6:20	5:19	5:27	6:55	4:52	19:42
Logan River Boat Ramp	6:38	5:02	5:26	7:11	5:10	19:57
Coomera River Mouth	5:37	4:12	4:05	5:52	4:18	18:52
Coombabah Creek	6:36	6:12	6:46	-	5:07	19:48
South Stradbroke - Coombabah Mouth	5:42	4:16	4:25	5:58	4:24	18:59
Coomera River - Jiboora Island	5:46	4:19	4:29	6:01	4:27	19:02
South Stradbroke-Runaway Bay3	5:17	3:53	3:42	5:21	3:58	18:29
Coomera River-Colman Road Reserve	5:51	4:23	4:35	6:08	4:30	19:06
South Stradbroke-Crusoe Island	5:14	3:48	3:39	5:17	3:52	18:30
Runaway Bay-Pacific Park	5:18	3:53	3:43	5:22	3:59	18:31

Table E. 12 – Arrival time statistics (hours: minutes after earthquake) for Northern Seaway locations for ARI 100 and subduction zones of Kermadec-Tonga (KDT), New Hebrides2 (NH2), Outer-rise New Hebrides (ONH), Outer-rise Kermadec-Tonga (OKDT), Solomon2 (S2), South America (SA) and puysegur2 (P2).

Arrival Time (hours: minutes after earthquake) Northern Seaway (ARI=100 yr)							
Source	**KDT**	**NH2**	**ONH**	**OKDT**	**S2**	**SA**	**P2**
Logan River Mouth	7:04	5:38	5:59	8:41	5:00	20:04	6:35
Logan River Boat Ramp	6:40	5:59	6:19	7:18	5:17	20:19	6:02
Coomera River Mouth	5:30	4:13	4:23	5:53	4:22	19:11	3:57
Coombabah Creek	-	-	-	-	5:15	20:12	-
South Stradbroke - Coombabah Mouth	5:43	4:18	4:29	5:59	4:28	19:18	4:03
Coomera River - Jiboora Island	5:46	4:20	4:48	6:17	4:31	19:23	4:18
South Stradbroke-Runaway Bay3	5:09	3:54	3:45	5:22	4:01	18:46	3:38
Coomera River-Colman Road Reserve	5:52	4:25	4:40	6:09	4:34	19:25	4:14
South Stradbroke-Crusoe Island	5:06	3:49	3:43	5:18	3:55	18:47	3:37
Runaway Bay-Pacific Park	5:10	3:54	3:46	5:35	4:02	18:47	3:38

Table E. 13 – Arrival time statistics (hours: minutes after earthquake) for Southern Seaway locations for ARI 10,000 and subduction zones of Kermadec-Tonga (KDT), New Hebrides2 (NH2), and Outer-rise New Hebrides (ONH).

Arrival Time (hours: minutes after earthquake) Southern Seaway (ARI=10,000 yr)			
Source	**KDT**	**NH2**	**ONH**
Loders Creek Mouth	4:29	3:57	3:40
Macintosh Island	4:38	4:04	3:50
Nerang River_Thomas Dr bridge W	4:41	4:08	3:54
Nerang River_Thomas Dr bridge E	4:41	4:08	3:54
Nerang River_Furlong St	4:59	4:19	3:59
Nerang River_Tui Johnson Park	5:01	4:20	4:00
Little Tallebudgera Creek_Boronia Park	5:49	4:23	3:57
Nerang River-River Cres	6:00	4:32	4:12
Nerang River- Witt Ave	6:08	4:38	4:19
Mermaid SHS	6:03	4:33	4:02
Robina Waters Park	-	-	-
Broadbeach Waters-Sunshine Blv	5:51	4:24	3:56
Clear Island Waters-Robina Pkwy	-	-	-
Robina Waters-Kennedy Park	-	-	-
Robina Waters-Bermuda Street Buffer	-	-	-
Bond_Uni	5:32	4:46	4:12
Burleigh Lake	-	-	4:15
Nerang River_Sundale Bridge	4:33	4:01	3:45
Boobegan Creek _St Martin Pl	-	-	-
Nerang River_ Big Tree Park	5:42	4:55	4:35

Table E. 14 – Arrival time statistics (hours: minutes after earthquake) for Southern Seaway locations for ARI 2000 and subduction zones of Kermadec-Tonga (KDT), New Hebrides2 (NH2), Outer-rise New Hebrides (ONH), Outer-rise Kermadec-Tonga (OKDT), Solomon2 (S2) and South America (SA).

Arrival Time (hours: minutes after earthquake) Southern Seaway (ARI=2000yr)						
Source	**KDT**	**NH2**	**ONH**	**OKDT**	**S2**	**SA**
Loders Creek Mouth	5:26	3:59	3:47	5:12	4:00	18:19
Macintosh Island	5:35	4:07	3:56	5:53	4:10	18:28
Nerang River_Thomas Dr bridge W	5:38	4:10	4:00	5:56	4:14	18:32
Nerang River_Thomas Dr bridge E	5:39	4:11	4:00	5:52	4:14	18:32
Nerang River_Furlong St	5:52	4:22	4:14	6:08	4:27	18:48
Nerang River_Tui Johnson Park	5:54	4:23	4:16	6:11	4:28	18:50
Little Tallebudgera Creek_Boronia Park	5:55	4:25	4:18	6:11	4:29	18:54
Nerang River-River Cres	6:06	4:35	4:48	6:26	4:41	19:07
Nerang River- Witt Ave	6:15	4:41	4:56	6:33	4:48	19:14
Mermaid SHS	6:10	4:37	4:50	6:32	4:42	19:13
Robina Waters Park	-	-	-	-	-	-
Broadbeach Waters-Sunshine Blv	5:57	4:27	4:38	6:14	4:32	18:59
Clear Island Waters-Robina Pkwy	-	-	-	-	-	-
Robina Waters-Kennedy Park	-	-	-	-	-	-
Robina Waters-Bermuda Street Buffer	-	-	-	-	-	-
Bond_Uni	6:24	4:49	5:06	6:42	4:56	19:20
Burleigh Lake	-	-	-	-	-	-
Nerang River_Sundale Bridge	5:31	4:03	3:51	5:16	4:05	18:23
Boobegan Creek _St Martin Pl	-	-	-	-	-	-
Nerang River_ Big Tree Park	6:32	4:58	5:13	6:52	5:04	19:30

Table E. 15 – Arrival time statistics (hours: minutes after earthquake) for Southern Seaway locations for ARI 500 and subduction zones of Kermadec-Tonga (KDT), New Hebrides2 (NH2), Outer-rise New Hebrides (ONH), Outer-rise Kermadec-Tonga (OKDT), Solomon2 (S2) and South America (SA).

Arrival Time (hours: minutes after earthquake) Southern Seaway (ARI=500 yr)						
Source	**KDT**	**NH2**	**ONH**	**OKDT**	**S2**	**SA**
Loders Creek Mouth	5:21	3:56	3:45	5:24	4:02	18:26
Macintosh Island	5:31	4:04	3:55	5:53	4:12	18:33
Nerang River_Thomas Dr bridge W	5:35	4:08	3:58	5:56	4:16	18:36
Nerang River_Thomas Dr bridge E	5:35	4:08	3:58	5:51	4:16	18:36
Nerang River_Furlong St	5:48	4:20	4:13	6:08	4:28	18:57
Nerang River_Tui Johnson Park	5:49	4:21	4:15	6:11	4:30	18:59
Little Tallebudgera Creek_Boronia Park	5:51	4:23	4:18	6:11	4:31	19:04
Nerang River-River Cres	6:02	4:33	4:51	6:25	4:43	19:15
Nerang River- Witt Ave	6:11	4:40	5:00	6:33	4:50	19:21
Mermaid SHS	6:06	4:35	5:00	6:34	4:44	19:19
Robina Waters Park	-	-	-	-	-	-
Broadbeach Waters-Sunshine Blv	5:53	4:25	4:40	6:14	4:34	19:08
Clear Island Waters-Robina Pkwy	-	-	-	-	-	-
Robina Waters-Kennedy Park	-		-	-	-	-
Robina Waters-Bermuda Street Buffer	-	-	-	-	-	-
Bond_Uni	6:20	4:48	5:09	6:42	4:58	19:26
Burleigh Lake	-	-	-	-	-	-
Nerang River_Sundale Bridge	5:26	4:00	3:50	5:41	4:07	18:29
Boobegan Creek _St Martin Pl	-	-	-	-	-	-
Nerang River_ Big Tree Park	6:28	4:56	5:17	6:53	5:06	19:33

Table E. 16 – Arrival time statistics (hours: minutes after earthquake) for Southern Seaway locations for ARI 100 and subduction zones of Kermadec-Tonga (KDT), New Hebrides2 (NH2), Outer-rise New Hebrides (ONH), Outer-rise Kermadec-Tonga (OKDT), Solomon2 (S2), South America (SA) and puysegur2 (P2).

Arrival Time (hours: minutes after earthquake) Southern Seaway (ARI=100 yr)							
Source	**KDT**	**NH2**	**ONH**	**OKDT**	**S2**	**SA**	**P2**
Loders Creek Mouth	5:13	3:57	3:47	5:25	4:05	18:49	3:41
Macintosh Island	5:29	4:05	3:56	5:54	4:15	18:58	3:55
Nerang River_Thomas Dr bridge W	5:32	4:09	3:59	5:56	4:19	19:01	3:59
Nerang River_Thomas Dr bridge E	5:32	4:09	4:00	5:53	4:19	19:02	3:55
Nerang River_Furlong St	5:45	4:22	4:41	6:10	4:32	19:16	4:12
Nerang River_Tui Johnson Park	5:47	4:23	4:44	6:12	4:34	19:18	4:14
Little Tallebudgera Creek_Boronia Park	5:48	4:24	4:43	6:12	4:35	19:21	4:15
Nerang River-River Cres	6:00	4:36	5:06	6:30	4:47	19:35	4:30
Nerang River- Witt Ave	6:08	4:42	5:10	6:36	4:54	19:41	4:37
Mermaid SHS	6:04	4:38	6:48	8:17	4:49	19:41	-
Robina Waters Park	-	-	-	-	-	-	-
Broadbeach Waters-Sunshine Blv	5:50	4:27	4:46	6:15	4:38	19:26	4:18
Clear Island Waters-Robina Pkwy	-	-	-	-	-	-	-
Robina Waters-Kennedy Park	-	-	-	-	-	-	-
Robina Waters-Bermuda Street Buffer	-	-	-	-	-	-	-
Bond_Uni	6:16	4:50	5:18	6:44	5:02	19:48	4:46
Burleigh Lake	-	-	-	-	-	-	-
Nerang River_Sundale Bridge	5:20	4:01	3:51	5:41	4:10	18:53	3:45
Boobegan Creek _St Martin Pl	-	-	-	-	-	-	-
Nerang River_ Big Tree Park	6:25	4:59	6:08	7:16	5:11	19:58	4:55

Table E. 17 – Arrival time statistics (hours: minutes after earthquake) for Tallebudgera and Currumbin Creek locations for ARI 10,000 and subduction zones of Kermadec-Tonga (KDT), New Hebrides2 (NH2), and Outer-rise New Hebrides (ONH).

Arrival Time (hours: minutes after earthquake) Tallebudgera and Currumbin Creek (ARI=10,000 yr)			
Source	**KDT**	**NH2**	**ONH**
Lake Awonga Reserve	4:21	3:51	3:33
Lilys Beach	4:21	3:52	3:34
Conservation Park	4:23	3:54	3:36
Schuster Park	4:41	4:10	3:55
Tallebudgera Creek	4:16	3:47	3:26
Currumbin Creek Estuary Bridge	4:18	3:48	3:27
Mainsail St N	4:29	3:59	3:42

Table E. 18 – Arrival time statistics (hours: minutes after earthquake) for Tallebudgera and Currumbin Creek locations for ARI 2000 and subduction zones of Kermadec-Tonga (KDT), New Hebrides2 (NH2), Outer-rise New Hebrides (ONH), Outer-rise Kermadec-Tonga (OKDT), Solomon2 (S2) and South America (SA).

Arrival Time (hours: minutes after earthquake) Tallebudgera and Currumbin Creek (ARI=2000 yr)						
Source	**KDT**	**NH2**	**ONH**	**OKDT**	**S2**	**SA**
Lake Awonga Reserve	5:19	3:53	3:39	5:03	3:56	18:10
Lilys Beach	5:20	3:54	3:40	5:04	3:56	18:11
Conservation Park	5:22	3:56	3:42	5:06	3:59	18:12
Schuster Park	5:41	4:13	4:01	5:51	4:18	18:31
Tallebudgera Creek	5:14	3:49	3:32	4:57	3:51	18:03
Currumbin Creek Estuary Bridge	5:16	3:50	3:34	4:58	3:53	18:05
Mainsail St N	5:27	4:01	3:48	5:12	4:05	18:18

Table E. 19 – Arrival time statistics (hours: minutes after earthquake) for Tallebudgera and Currumbin Creek locations for ARI 500 and subduction zones of Kermadec-Tonga (KDT), New Hebrides2 (NH2), Outer-rise New Hebrides (ONH), Outer-rise Kermadec-Tonga (OKDT), Solomon2 (S2) and South America (SA).

Arrival Time (hours: minutes after earthquake) Tallebudgera and Currumbin Creek (ARI=500 yr)						
Source	**KDT**	**NH2**	**ONH**	**OKDT**	**S2**	**SA**
Lake Awonga Reserve	5:13	3:50	3:38	5:06	3:57	18:17
Lilys Beach	5:14	3:51	3:39	5:06	3:57	18:18
Conservation Park	5:16	3:53	3:41	5:08	4:00	18:19
Schuster Park	5:36	4:11	4:00	5:53	4:20	18:35
Tallebudgera Creek	5:07	3:46	3:31	4:58	3:52	18:11
Currumbin Creek Estuary Bridge	5:09	3:48	3:33	5:00	3:54	18:12
Mainsail St N	5:23	3:59	3:47	5:38	4:07	18:23

Table E. 20 – Arrival time statistics (hours: minutes after earthquake) for Tallebudgera and Currumbin Creek locations for ARI 100 and subduction zones of Kermadec-Tonga (KDT), New Hebrides2 (NH2), Outer-rise New Hebrides (ONH), Outer-rise Kermadec-Tonga (OKDT), Solomon2 (S2), South America (SA) and puysegur2 (P2).

Arrival Time (hours: minutes after earthquake) Tallebudgera and Currumbin Creek (ARI=100 yr)							
Source	**KDT**	**NH2**	**ONH**	**OKDT**	**S2**	**SA**	**P2**
Lake Awonga Reserve	5:05	3:51	3:40	5:30	4:00	18:39	3:31
Lilys Beach	5:06	3:52	3:40	5:30	4:01	18:40	3:32
Conservation Park	5:09	3:54	3:42	5:33	4:04	18:42	3:34
Schuster Park	5:31	4:12	4:00	5:54	4:23	19:01	3:55
Tallebudgera Creek	5:00	3:46	3:34	5:01	3:54	18:33	3:27
Currumbin Creek Estuary Bridge	5:02	3:48	3:36	5:27	3:57	18:34	3:28
Mainsail St N	5:17	4:00	3:48	5:39	4:10	18:47	3:41

Table E. 21 – Arrival time statistics (hours: minutes after earthquake) for Tweed locations for ARI 10,000 and subduction zones of Kermadec-Tonga (KDT), New Hebrides2 (NH2), and Outer-rise New Hebrides (ONH).

Arrival Time (hours: minutes after earthquake) Tweed (ARI=10,000 yr)			
Source	**KDT**	**NH2**	**ONH**
Tweed Heads	4:59	3:42	3:25
Charles-Trutes Bay	5:32	4:08	4:09
Tweed River_Bosun Blvd	5:29	4:05	3:55
Coolangatta Golf Club	5:17	3:55	3:42
Tweed Entrance	4:56	3:40	3:21
Cobaki Broadwater	5:39	4:12	4:11
Tweed River_Murwillumbah	6:32	5:05	4:57

Table E. 22 – Arrival time statistics (hours: minutes after earthquake) for Tweed locations for ARI 2000 and subduction zones of Kermadec-Tonga (KDT), New Hebrides2 (NH2), Outer-rise New Hebrides (ONH), Outer-rise Kermadec-Tonga (OKDT), Solomon2 (S2) and South America (SA).

Arrival Time (hours: minutes after earthquake) Tweed (ARI=2000 yr)						
Source	**KDT**	**NH2**	**ONH**	**OKDT**	**S2**	**SA**
Tweed Heads	5:10	3:44	3:31	5:08	3:47	18:10
Charles-Trutes Bay	5:39	4:11	4:13	6:30	4:18	18:58
Tweed River_Bosun Blvd	5:34	4:08	4:01	5:44	4:14	18:41
Coolangatta Golf Club	5:23	3:57	3:48	5:33	4:02	18:27
Tweed Entrance	5:07	3:41	3:26	4:51	3:44	17:59
Cobaki Broadwater	5:47	4:16	4:20	8:19	4:24	19:02
Tweed River_Murwillumbah	6:39	5:09	5:13	7:27	5:16	19:52

Table E. 23 – Arrival time statistics (hours: minutes after earthquake) for Tweed locations for ARI 500 and subduction zones of Kermadec-Tonga (KDT), New Hebrides2 (NH2), Outer-rise New Hebrides (ONH), Outer-rise Kermadec-Tonga (OKDT), Solomon2 (S2) and South America (SA).

Arrival Time (hours: minutes after earthquake) Tweed (ARI=500 yr)						
Source	**KDT**	**NH2**	**ONH**	**OKDT**	**S2**	**SA**
Tweed Heads	5:01	3:42	3:30	5:08	3:48	18:18
Charles-Trutes Bay	5:36	4:09	4:16	6:31	4:21	19:06
Tweed River_Bosun Blvd	5:31	4:06	4:11	5:45	4:16	18:49
Coolangatta Golf Club	5:17	3:55	3:47	5:33	4:03	18:34
Tweed Entrance	4:59	3:39	3:26	5:04	3:45	18:13
Cobaki Broadwater	5:42	4:14	4:27	-	4:26	19:10
Tweed River_Murwillumbah	6:36	5:07	5:15	7:38	5:19	19:59

Table E. 24 – Arrival time statistics (hours: minutes after earthquake) for Tweed locations for ARI 100 and subduction zones of Kermadec-Tonga (KDT), New Hebrides2 (NH2), Outer-rise New Hebrides (ONH), Outer-rise Kermadec-Tonga (OKDT), Solomon2 (S2), South America (SA) and Puysegur2 (P2).

Arrival Time (hours: minutes after earthquake) Tweed (ARI=100 yr)							
Source	**KDT**	**NH2**	**ONH**	**OKDT**	**S2**	**SA**	**P2**
Tweed Heads	4:55	3:42	3:35	5:09	3:51	18:32	3:21
Charles-Trutes Bay	5:37	4:13	-	-	4:28	19:30	-
Tweed River_Bosun Blvd	5:32	4:07	4:28	6:03	4:20	19:08	5:30
Coolangatta Golf Club	5:10	3:56	4:04	5:34	4:07	18:51	3:35
Tweed Entrance	4:52	3:39	3:30	5:06	3:48	18:27	3:18
Cobaki Broadwater	5:42	4:19	-	-	4:32	19:34	-
Tweed River_Murwillumbah	7:07	5:10	-	12:58	5:25	20:23	-

Table E. 25 – Reference numbers for locations on the beach and within waterways.

Location	Reference
Lake Awonga Reserve	1
Lilys Beach	2
Conservation Park	3
Schuster Park	4
Tallebudgera Creek	5
Currumbin Creek Estuary Bridge	6
Mainsail St N	7
Logan River Mouth	8
Logan River Boat Ramp	9
Coomera River Mouth	10
Coombabah Creek	11
South Stradbroke - Coombabah Mouth	12
Coomera River - Jiboora Island	13
South Stradbroke-Runaway Bay3	14
Coomera River-Colman Road Reserve	15
South Stradbroke-Crusoe Island	16
Runaway Bay-Pacific Park	17
Loders Creek Mouth	18
Macintosh Island	19
Nerang River_Thomas Dr bridge W	20
Nerang River_Thomas Dr bridge E	21
Nerang River_Furlong St	22
Nerang River_Tui Johnson Park	23
Little Tallebudgera Creek_Boronia Park	24
Nerang River-River Cres	25
Nerang River- Witt Ave	26
Mermaid SHS	27
Robina Waters Park	28
Broadbeach Waters-Sunshine Blv	29
Clear Island Waters-Robina Pkwy	30

Location	Reference
Robina Waters-Kennedy Park	31
Robina Waters-Bermuda Street Buffer	32
Bond_Uni	33
Burleigh Lake	34
Nerang River_Sundale Bridge	35
Boobegan Creek _St Martin Pl	36
Nerang River_ Big Tree Park	37
Tweed Heads	38
Charles-Trutes Bay	39
Tweed River_Bosun Blvd	40
Coolangatta Golf Club	41
Tweed Entrance	42
Cobaki Broadwater	43
Tweed River_Murwillumbah	44
Burleigh Beach 1	45
Nobby Beach	46
Kurrawa Beach	47
Surfers Paradise Beach	48
Seaworld-seaside	49
Moondarewa Bay	50
South Stradbroke 2	51
Kingscliff2	52
Froggy Beach	53
Coolangatta Beach	54
Bilinga Beach	55
Currumbin Beach	56
Palm Beach1	57
Tallebudgera Beach	58
Maggies Beach	59
Wooyung Beach	60
Letitia	61

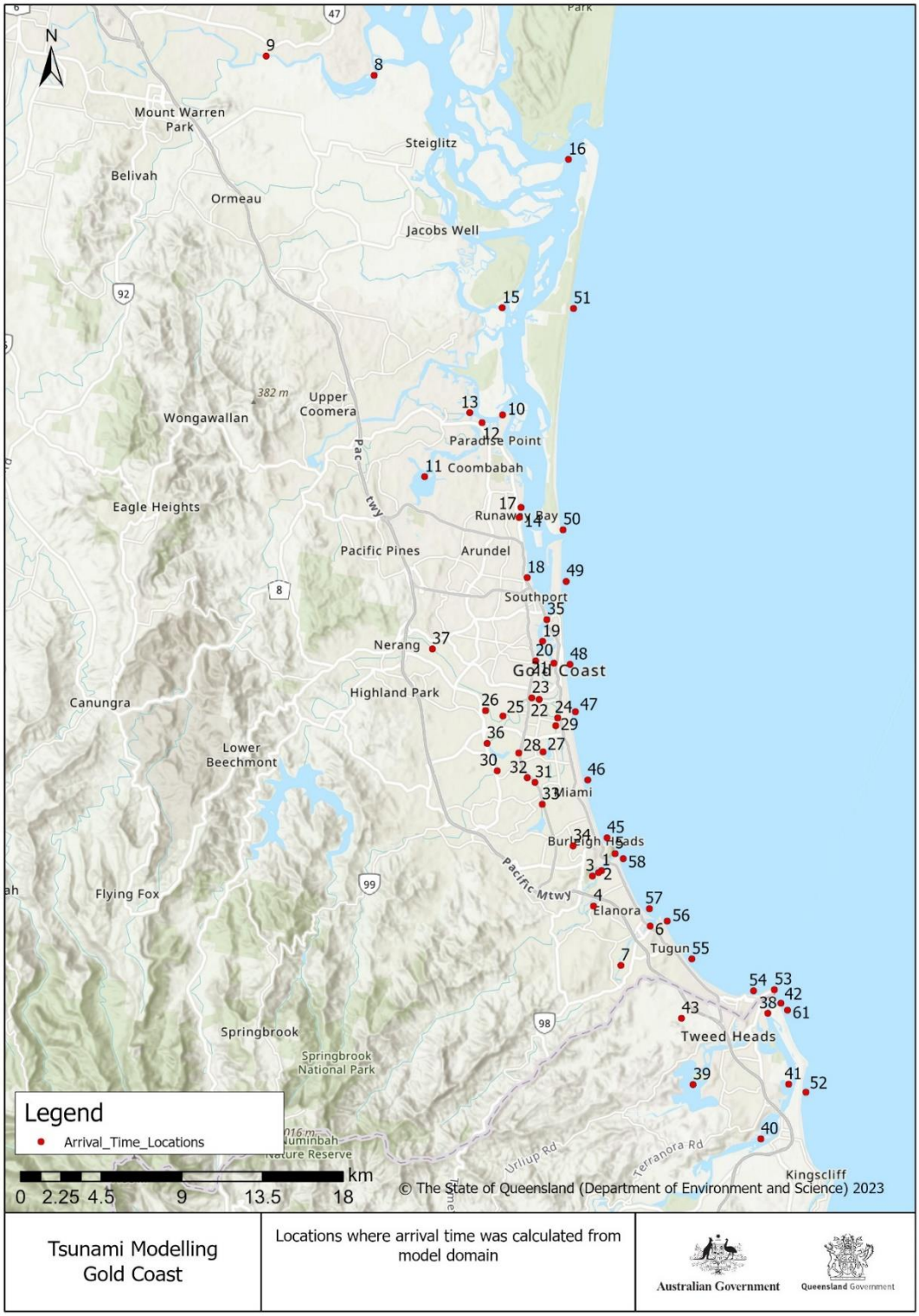

Figure E. 1 – The locations on the beach and within the waterways, along with their corresponding reference numbers, as shown in Table E. 25.

Table E. 26 – Deviation from the arrival time for locations on the beach for given subduction zones.

Average Arrival Time (hours: minutes after earthquake) for each subduction zone for beaches	
Source	**Average and Standard deviation**
Kermadec-Tonga	5:04±06 min
New Hebrides2	3:44±04 min
Outer-rise Kermadec-Tonga	5:11±05 min
Outer-rise New Hebrides	3:32±05 min
Puysegur2	3:28±02 min
Solomon2	3:48±04 min
South America	18:22±09 min

Table E. 27 – Deviation from the arrival time for locations within the waterways for given subduction zones.

Average Arrival Time (hours: minutes after earthquake) for each subduction zone for waterways	
Source	**Average and Standard deviation**
Kermadec-Tonga	5:27±55 min
New Hebrides2	4:09±48 min
Outer-rise Kermadec-Tonga	5:54±78 min
Outer-rise New Hebrides	4:06±56 min
Puysegur2	3:59±60 min
Solomon2	4:15±48 min
South America	18:50±49 min

Based on the above criteria, events from the Puysegur and New Hebrides, regarding the beaches, exhibit the shortest arrival time, approximately 3.5 hours after the earthquake, with events from South America arriving much later at over 18 hours. The same pattern can be observed for waterways, with events at Puysegur and New Hebrides arriving approximately four hours after the earthquake, while South American events arrive approximately 18 to 20 hours later.

Appendix F Scenarios

The following table lists the scenarios that were modelled.

Table F. 1 – List of scenarios modelled.

Run No.	ARI	Source	PTHA Event ID	Max Amplitude (m)	Earthquake Magnitude (Mw)	Nominal Water Level	Water Level (m AHD)
1	100	Kermadec-Tonga	38319	0.19	8.7	MSL	0.0
2	100	Kermadec-Tonga	38319	0.19	8.7	HAT	1.1
3	100	Kermadec-Tonga	38395	0.16	8.9	MSL	0.0
4	100	Kermadec-Tonga	38395	0.16	8.9	HAT	1.1
5	100	New Hebrides	8399	0.16	8.1	MSL	0.0
6	100	New Hebrides	8399	0.16	8.1	HAT	1.1
7	100	New Hebrides	9905	0.16	8.4	MSL	0.0
8	100	New Hebrides	9905	0.16	8.4	HAT	1.1
9	100	Outer-rise Kermadec-Tonga	10788	0.13	8.5	MSL	0.0
10	100	Outer-rise Kermadec-Tonga	10788	0.13	8.5	HAT	1.1
11	100	Outer-rise Kermadec-Tonga	11435	0.14	8.6	MSL	0.0
12	100	Outer-rise Kermadec-Tonga	11435	0.14	8.6	HAT	1.1
13	100	Outer-rise New Hebrides	4578	0.15	8.1	MSL	0.0
14	100	Outer-rise New Hebrides	4578	0.15	8.1	HAT	1.1
15	100	Outer-rise New Hebrides	6071	0.15	8.4	MSL	0.0
16	100	Outer-rise New Hebrides	6071	0.15	8.4	HAT	1.1
17	100	Puysegur	3188	0.14	8.5	MSL	0.0
18	100	Puysegur	3188	0.14	8.5	HAT	1.1
19	100	Puysegur	3269	0.13	8.5	MSL	0.0
20	100	Puysegur	3269	0.13	8.5	HAT	1.1
21	100	Solomon	14181	0.16	8.8	MSL	0.0
22	100	Solomon	14181	0.16	8.8	HAT	1.1
23	100	Solomon	14659	0.16	8.9	MSL	0.0
24	100	Solomon	14659	0.16	8.9	HAT	1.1
25	100	South America	138376	0.16	9.1	MSL	0.0
26	100	South America	138376	0.16	9.1	HAT	1.1

Run No.	ARI	Source	PTHA Event ID	Max Amplitude (m)	Earthquake Magnitude (Mw)	Nominal Water Level	Water Level (m AHD)
27	100	South America	139765	0.17	9.2	MSL	0.0
28	100	South America	139765	0.17	9.2	HAT	1.1
29	500	Kermadec-Tonga	40294	0.25	8.9	MSL	0.0
30	500	Kermadec-Tonga	40294	0.25	8.9	HAT	1.1
31	500	Kermadec-Tonga	40814	0.24	9.0	MSL	0.0
32	500	Kermadec-Tonga	40814	0.24	9.0	HAT	1.1
33	500	New Hebrides	10423	0.31	8.5	MSL	0.0
34	500	New Hebrides	10423	0.31	8.5	HAT	1.1
35	500	New Hebrides	10881	0.30	8.6	MSL	0.0
36	500	New Hebrides	10881	0.30	8.6	HAT	1.1
37	500	Outer-rise Kermadec-Tonga	12160	0.22	8.7	MSL	0.0
38	500	Outer-rise Kermadec-Tonga	12160	0.22	8.7	HAT	1.1
39	500	Outer-rise Kermadec-Tonga	12188	0.22	8.7	MSL	0.0
40	500	Outer-rise Kermadec-Tonga	12188	0.22	8.7	HAT	1.1
41	500	Outer-rise New Hebrides	5564	0.28	8.3	MSL	0.0
42	500	Outer-rise New Hebrides	5564	0.28	8.3	HAT	1.1
43	500	Outer-rise New Hebrides	6484	0.27	8.5	MSL	0.0
44	500	Outer-rise New Hebrides	6484	0.27	8.5	HAT	1.1
45	500	Solomon	15018	0.31	9.0	MSL	0.0
46	500	Solomon	15018	0.31	9.0	HAT	1.1
47	500	Solomon	15034	0.33	9.0	MSL	0.0
48	500	Solomon	15034	0.33	9.0	HAT	1.1
49	500	South America	143881	0.27	9.4	MSL	0.0
50	500	South America	143881	0.27	9.4	HAT	1.1
51	500	South America	143914	0.28	9.4	MSL	0.0
52	500	South America	143914	0.28	9.4	HAT	1.1
53	2,000	Kermadec-Tonga	41602	0.41	9.1	MSL	0.0
54	2,000	Kermadec-Tonga	41602	0.41	9.1	HAT	1.1
55	2,000	Kermadec-Tonga 2	42273	0.39	9.2	MSL	0.0

Run No.	ARI	Source	PTHA Event ID	Max Amplitude (m)	Earthquake Magnitude (Mw)	Nominal Water Level	Water Level (m AHD)
56	2,000	Kermadec-Tonga	42273	0.39	9.2	HAT	1.1
57	2,000	New Hebrides	10877	0.45	8.6	MSL	0.0
58	2,000	New Hebrides	10877	0.45	8.6	HAT	1.1
59	2,000	New Hebrides	11290	0.46	8.7	MSL	0.0
60	2,000	New Hebrides	11290	0.46	8.7	HAT	1.1
61	2,000	Outer-rise Kermadec-Tonga	12851	0.32	8.8	MSL	0.0
62	2,000	Outer-rise Kermadec-Tonga	12851	0.32	8.8	HAT	1.1
63	2,000	Outer-rise Kermadec-Tonga	12858	0.41	8.8	MSL	0.0
64	2,000	Outer-rise Kermadec-Tonga	12858	0.41	8.8	HAT	1.1
65	2,000	Outer-rise New Hebrides	6503	0.33	8.5	MSL	0.0
66	2,000	Outer-rise New Hebrides	6503	0.33	8.5	HAT	1.1
67	2,000	Outer-rise New Hebrides	6915	0.34	8.6	MSL	0.0
68	2,000	Outer-rise New Hebrides	6915	0.34	8.6	HAT	1.1
69	2,000	Solomon	15551	0.49	9.2	MSL	0.0
70	2,000	Solomon	15551	0.49	9.2	HAT	1.1
71	2,000	Solomon	15725	0.47	9.2	MSL	0.0
72	2,000	Solomon	15725	0.47	9.2	HAT	1.1
73	2,000	South America	147780	0.46	9.6	MSL	0.0
74	2,000	South America	147780	0.46	9.6	HAT	1.1
75	2,000	South America	147918	0.45	9.6	MSL	0.0
76	2,000	South America	147918	0.45	9.6	HAT	1.1
77	10,000	Kermadec-Tonga	43313	0.62	9.4	MSL	0.0
78	10,000	Kermadec-Tonga	43313	0.62	9.4	HAT	1.1
79	10,000	Kermadec-Tonga	43443	0.57	9.4	MSL	0.0
80	10,000	Kermadec-Tonga	43443	0.57	9.4	HAT	1.1
81	10,000	New Hebrides	11664	0.67	8.8	MSL	0.0
82	10,000	New Hebrides	11664	0.67	8.8	HAT	1.1
83	10,000	New Hebrides	12034	0.72	8.9	MSL	0.0
84	10,000	New Hebrides	12034	0.72	8.9	HAT	1.1

Run No.	ARI	Source	PTHA Event ID	Max Amplitude (m)	Earthquake Magnitude (Mw)	Nominal Water Level	Water Level (m AHD)
85	10,000	Outer-rise New Hebrides	7380	0.58	8.7	MSL	0.0
86	10,000	Outer-rise New Hebrides	7380	0.58	8.7	HAT	1.1
87	10,000	Outer-rise New Hebrides	7700	0.62	8.8	MSL	0.0
88	10,000	Outer-rise New Hebrides	7700	0.62	8.8	HAT	1.1
89	10,000	Outer-rise New Hebrides	7700	0.62	8.8	HAT + SLR	1.9
90	10,000	Kermadec-Tonga	43313	0.62	9.4	HAT + SLR	1.9

Appendix G Local Tsunami Variability Related to Shelf Interactions, Resonance and Standing Waves.

This research has demonstrated considerable variability in the dominant frequencies of tsunami from various sources for the limited number of scenarios considered for each source zone. Some variability in frequency response is related to the proximity of the study site to the source earthquake that generates the tsunami. For example, the Kermadec-Tonga (KDT) earthquake site is one of the closer potential sources to the Gold Coast (arrival time approximately 5 hours). The KDT tsunami boundary timeseries (run 78, 10,000-yr ARI, *WL* = HAT, PTHA18 event 43313) and corresponding spectrum features many higher-frequency oscillations with a broad range of frequencies (Figure G. 1). Conversely, the selected South America (SA) tsunami scenario (run 74, 2,000-yr ARI, *WL* = HAT, PTHA18 event 147780) features a more organised time series and spectra with a narrower range of frequencies and more energy located in the lower frequencies (Figure G. 2). It is important to note that while these observed trends are true for the events considered for each source zone, they might not characterise the source zones as a whole. However, modelling of a larger number of events would be required to confirm this. Generally, a range of periods is possible and depends on the source zone fault characteristics.

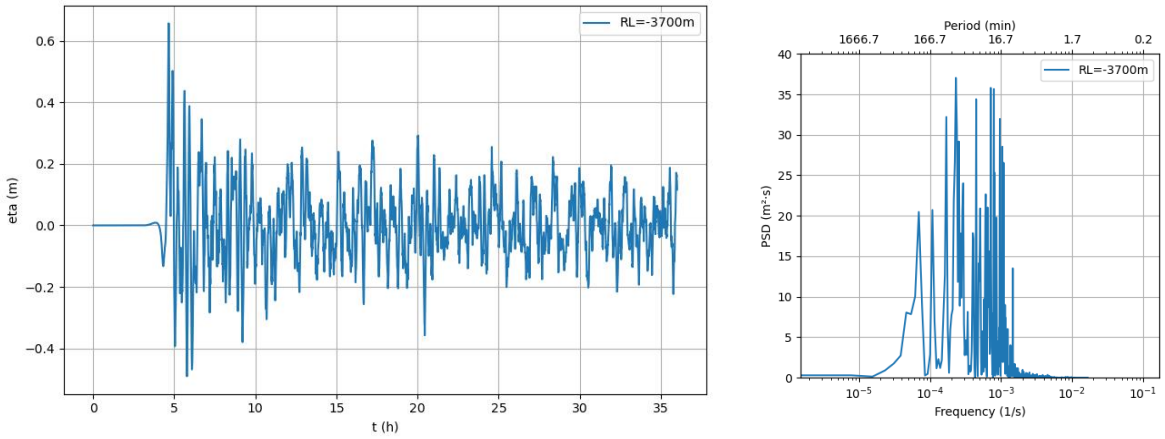

Figure G. 1 – Time series (left) and spectra (right) for the Kermadec-Tonga tsunami (run 78).

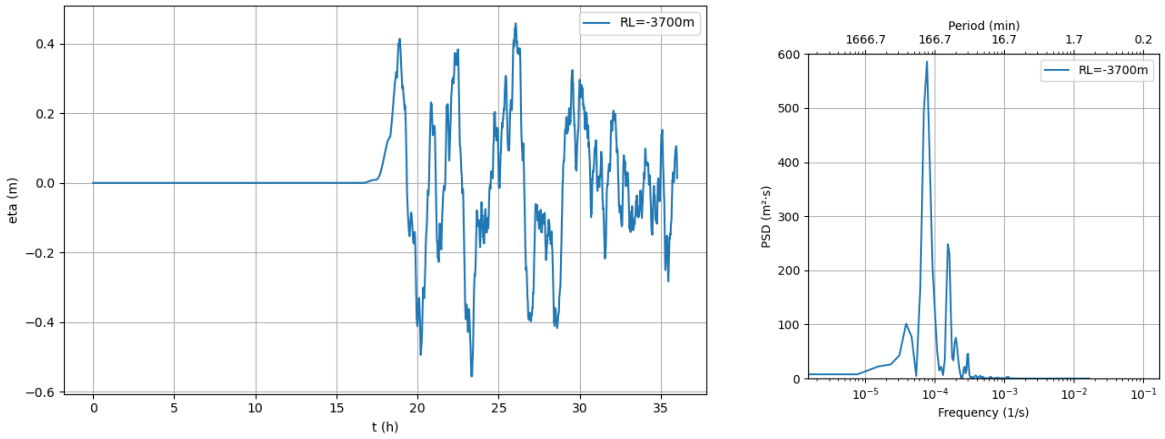

Figure G. 2 – Time series (left) and spectra (right) for the South American tsunami (run 74).

The periods of tsunami are essential factors in potential reflected, standing, and edge wave interactions, and resonant responses of the waves to local bathymetric configurations over the continental shelf and approaching the shoreline (e.g., Rabinovich, 1997; Yamazaki and Cheung, 2011; and Cortés et al. 2017). For given wavelengths, local surface elevation amplitudes can be influenced by the bathymetric contours, shoreline shape (e.g., straight versus curved bedforms and shorelines, resonance and standing waves), and interactions between various incident, reflected, and edge waves.

The following two sections investigate the potential resonant and standing wave responses of the longer period South American tsunami scenarios and the shorter period Kermadec-Tonga tsunami scenarios.

G.1 South America Tsunami Scenarios

Figure G. 3 shows a Hovmöller time stack plot of the water surface elevation at various model output locations at an approximate elevation RL = −5 m MSL. The figure indicates that the South America (SA) scenario time series have a dominant signal that features very long period waves (~98 minutes). The Hovmöller plot shows the progression of the tsunami time series over time in a spatial context. However, it is important to note that the Hovmöller plot y-axis is given in northing coordinates for each model output site, so it does not capture the actual distance between each point. Therefore, for many regions the propagation along the northings over time does not completely resolve velocity due to the curved nature of the 5 m depth contour.

Tsunami with similarly long period waves have been observed for previous events originating from South America. For example, Yamazaki and Cheung (2011) reported on resonance and shelf wave interactions associated with an earthquake off the coast of Chile where the surface elevation time series and associated spectra indicated a significant amount of energy for wave periods of over 100 minutes.

An interesting feature of the Hovmöller plot is the gradually increasing amplification of the signal to the north of Tweed Heads (approximately Duranbah beach in Figure G. 3), with the maximum surface elevations occurring approximately 6 hours (about 24 hours in Figure G. 3) after the initial arrival of the first wave. To the south, the oscillations remain more constant with the incoming tsunami time series, with no apparent gradual increase in amplification. Melgar and Ruiz-Angulo (2018) found that the width of the shelf exerted a strong influence on the duration of a tsunami.

Considering the left map image in Figure G. 3, there are a couple of notable aspects related to the bathymetric configurations to the north and south of Duranbah. First, the Gold Coast ‘embayment’ provides a relatively large concave-curved shoreline with a broader, convex-curved edge to the continental shelf. Conversely, south of the Tweed features a straighter shoreline interspersed with headlands and a narrower and straighter continental shelf edge.

Further time series data analysis has been undertaken to investigate the difference between the continental shelf widths. Two locations were selected to consider more closely where surface elevation gauges (note, the use of gauge, or gauges in this appendix refers to model output points) were available as outputs from the model. Burleigh was selected as the Gold Coast embayment site, and Wooyung Beach was selected as the southern beaches site. The two transects and their nearest extracted surface elevation time series output points for RL = −3700 m, −1000 m, −100 m, and −5 m are indicated in Figure G. 4. Figure G. 5 provides a comparison of the continental shelf profiles for the two transects. In these plots, Linear Wave Theory (LWT) has been applied to estimate the velocity, travel time and wavelengths corresponding to the change in depth. The middle plot indicates the travel time from a depth of 3,000 m to the shoreline for the two profiles.

As described in Section A.3.2.3, the fundamental mode of resonance can be approximated by assuming a semi-enclosed basin, giving (Bryant, 2014):

$$T_s = \frac{4L_b}{\sqrt{gD}}$$

When considering a change in grade from the steeper continental slope to define the shelf length for the Gold Coast (about 450 m depth and length of about 54 km), and an average depth over this length of about 123 m. This equates to a wave period of about 100 minutes. Based on this approach, the required period for resonance for the narrower continental shelf in northern New South Wales would be less than 66 minutes.

Figure G. 6 provides a sample of other Hovmöller plots for lower ARI events. Each is for a South American tsunami event, and the time series patterns are consistent. The amplitude (corresponding to the different ARI) appears to be the main difference.

The water surface elevation (η) time series outputs for each of the output sites indicated in Figure G. 4 are provided in Figure G. 7 (Burleigh) and Figure G. 8 (Wooyung). Little discernible difference exists between the time series for the boundary condition (RL = −3700 m) and RL = −1000m. The differences are much more apparent when considering the shallower contours of RL = −100 m and RL = −5m, particularly after time = 23 hours. After this time, the Burleigh water surface elevation time series continues to increase in amplitude, oscillating at a period of approximately 98 minutes, whereas although Wooyung's signal does have a similar low-frequency fluctuation, the amplitude does not increase after time of approximately 22.5 hours.

As the Hovmöller plot (Figure G. 3) is a time stack oriented from north to south, it also provides some indications of the presence of edge waves (Melgar and Ruiz-Angulo, 2018), where crests or troughs propagate in a diagonal direction through time.

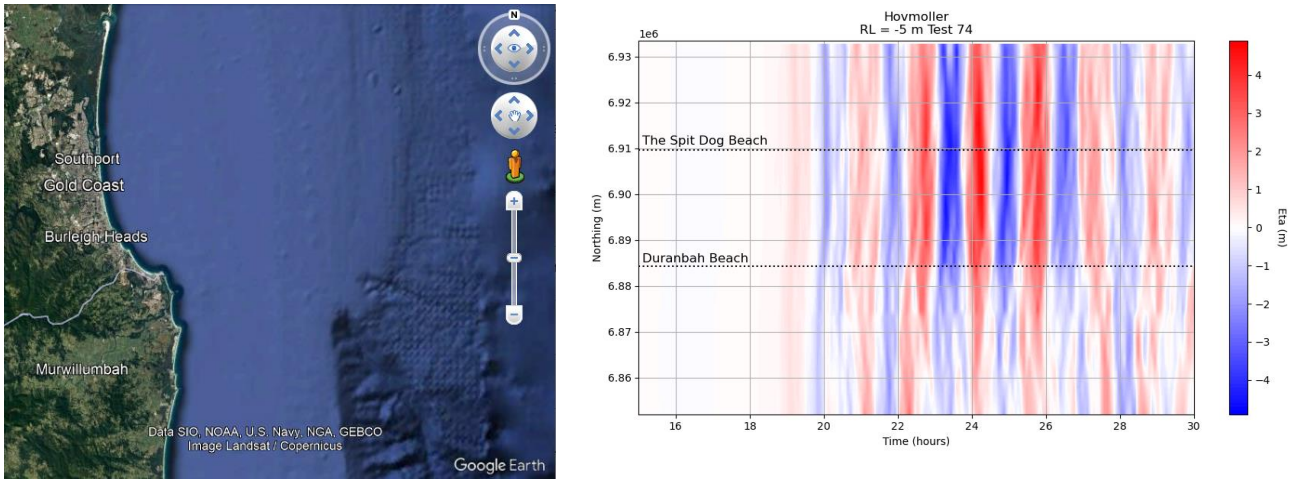

Figure G. 3 – Google Earth screen shot approximately aligned with the Sample Hovmöller plot on the right (2,000-yr ARI at HAT). The greatest wave amplification appears to occur through the Gold Coast Bay, north of Duranbah. Note the increased shelf width compared with the southern beaches.

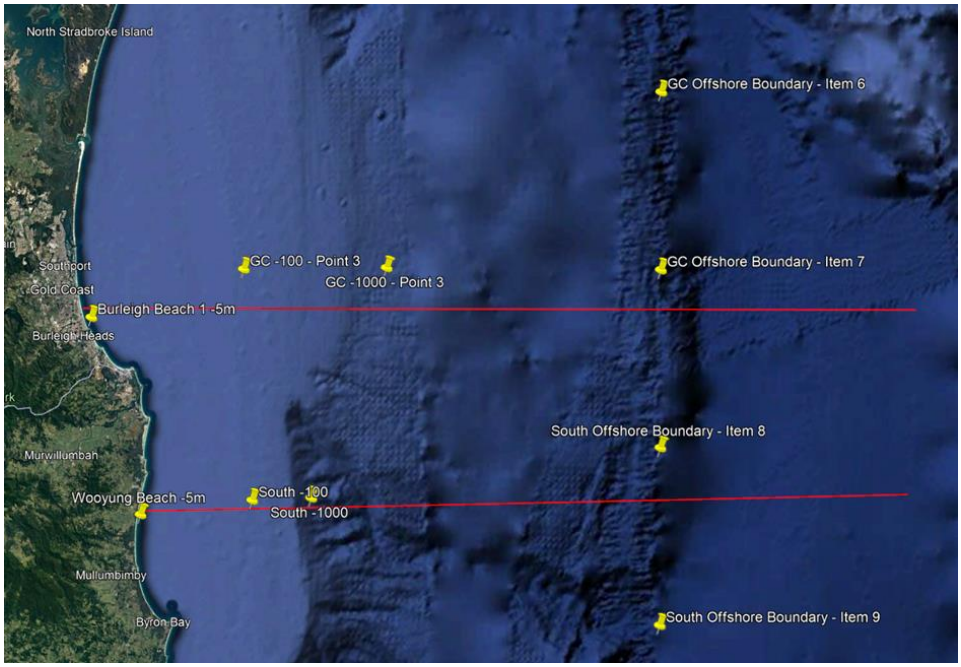

Figure G. 4 – The two W-E profiles for Gold Coast (top red line) and Wooyung Beach (lower red line). The yellow pins show the query points for the surface elevation time series.

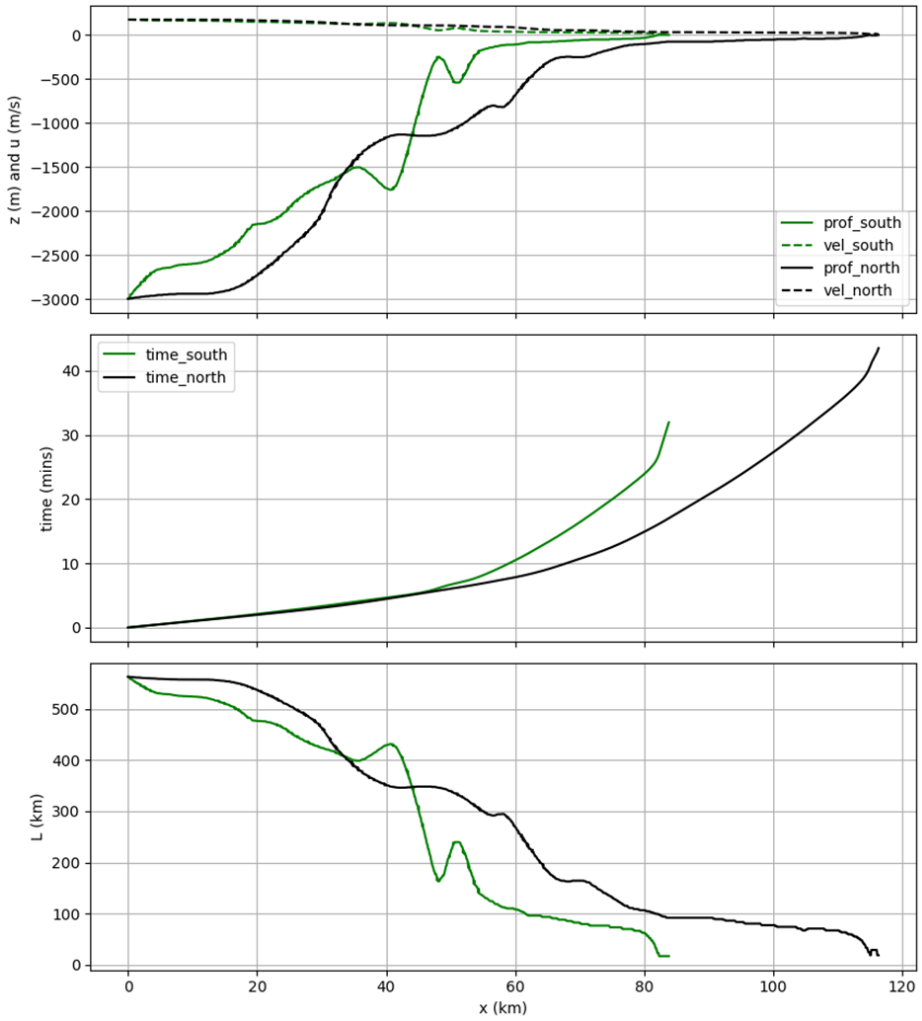

Figure G. 5 – Comparison of continental shelf profiles (top plot) and the shallow water, linear wave theory velocity (top plot), propagation time (middle plot), and wavelength (bottom plot) for the north and south profiles as indicated in the two red lines, shown in Figure G. 4.

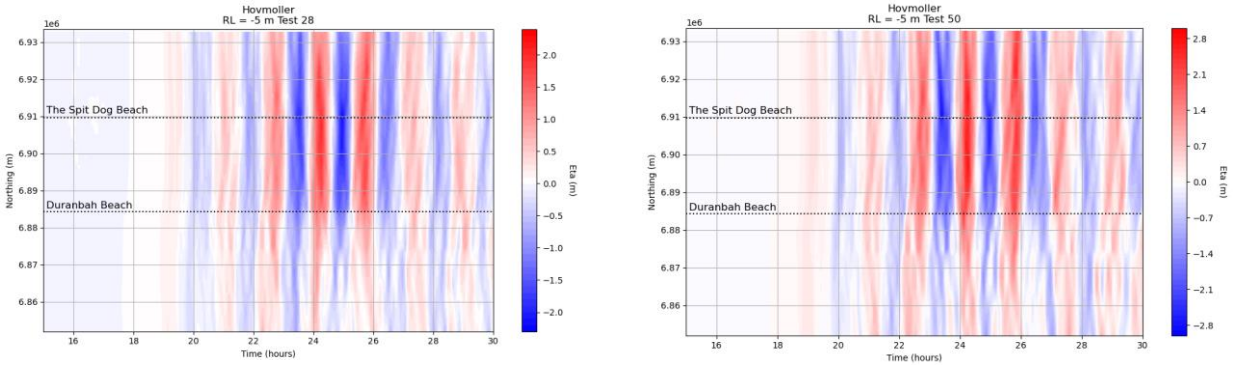

Figure G. 6 – Hovmöller plots for the RL = −5 m elevation contour for the South America tsunami model runs 28 (100-yr ARI at HAT – left) and 50 (500-yr ARI at HAT – right).

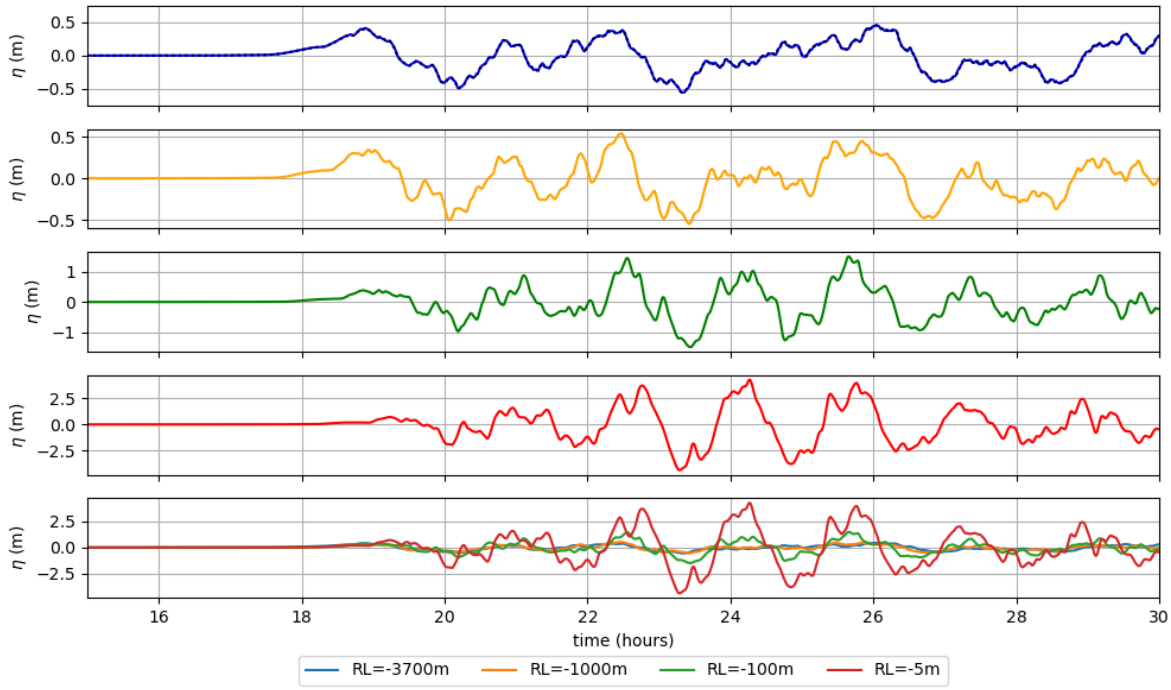

Figure G. 7 – Water surface elevation (η) time series of the SA run 74 (2,000-yr ARI) tsunami at different depth contours for the northern, Burleigh profile. Note the changing eta (y-axis) scales.

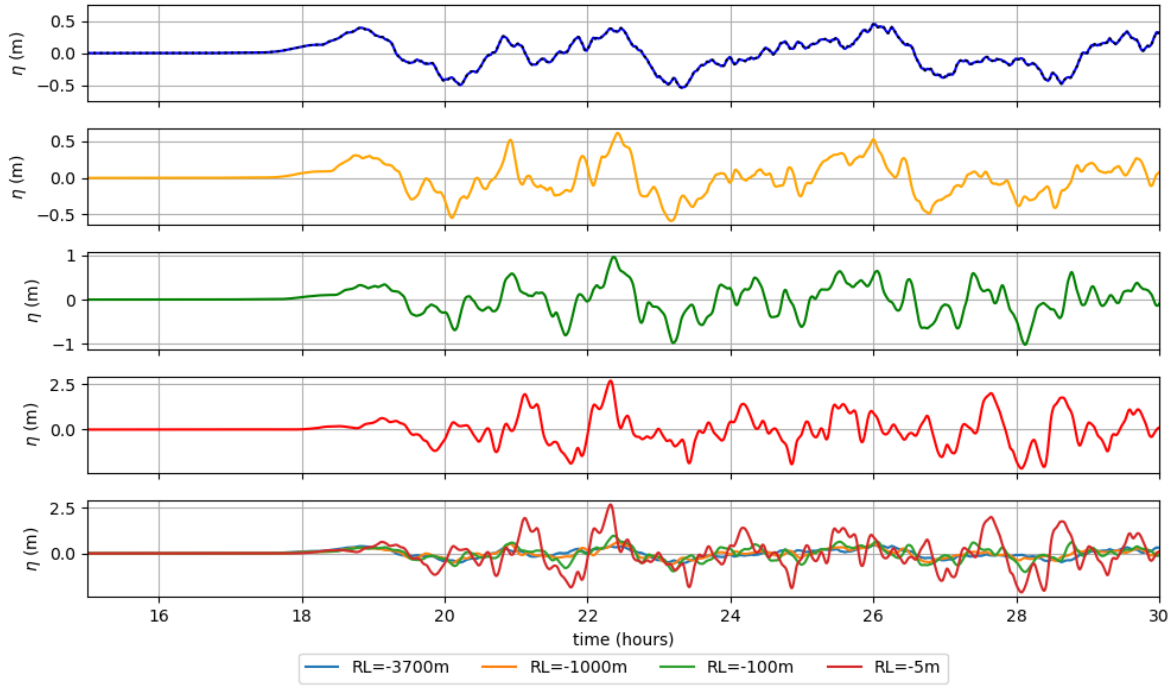

Figure G. 8 – Water surface elevation (η) time series of SA run 74 (2,000-yr ARI) tsunami at different depth contours for the southern, Wooyung profile. Note the changing eta (y-axis) scales.

G.1.1 Frequency Analysis of the South America run 74 (PTHA18 event 147780, 2,000-yr ARI at HAT)

Considering the time series responses described in the previous Section, a spectral analysis (wave energy versus frequency, using Welch's method with a Hann window of 4096 samples at a sampling frequency $f_s \approx 0.033$ Hz for the offshore RL = −3700m time series and 8192 samples at $f_s = 0.2$ Hz for the 3 shallower time series) has been undertaken to investigate the energy associated with each gauge. Figure G. 9 provides the spectra for each of the gauges in Figure G. 7 and Figure G. 8. Except for the RL = −5 m plots, the y-axes have been fixed to facilitate the comparison of the spectra. The spectra for the tsunami time series progressively changes with decreasing depth. The energy associated with the 98-minute period amplifies at the RL = −1000 m gauge for both sites, and becomes

increasingly dominant into shore for both sites, albeit most significantly for the Burleigh transect probes in the shallowest two depths. Note, especially, the change in scale for the y-axis in the RL = −5 m between the Burleigh and Wooyung plots. There is an additional spike at approximately 60 minutes between RL = −100 m and −5 m in the Wooyung probe spectra.

To further consider the two dominant frequencies in the nearshore (corresponding to periods of 60 minutes and 98 minutes), a spectral analysis was applied to the water surface elevation area time series output from the numerical model. Due to the computational limitations associated with the data size, the analysis was constrained to a time step of 60 seconds between time = 17 to 26 hours.

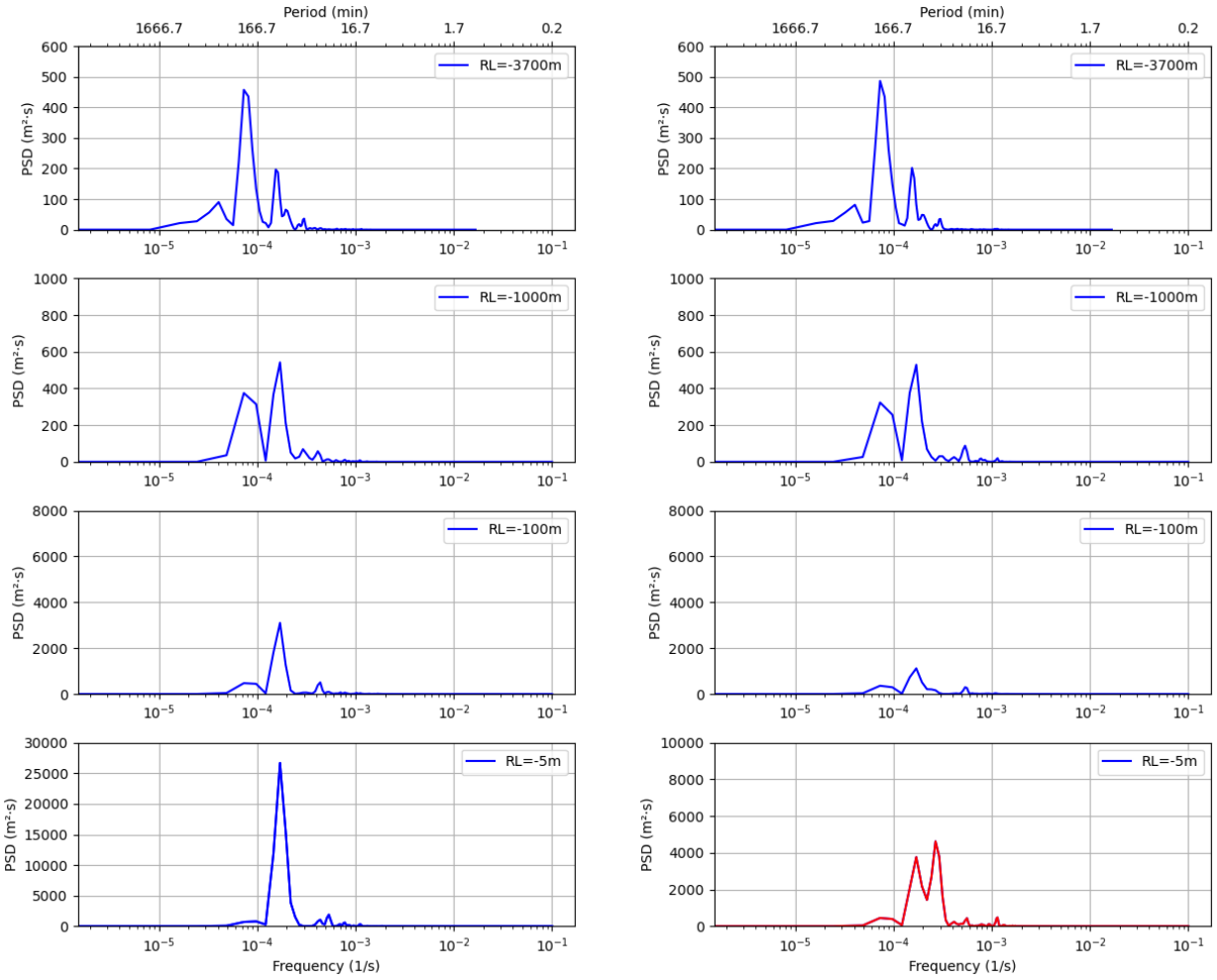

Figure G. 9 – Spectral plots for the Burleigh (Left) and Wooyung (right) probes for SA run 74. Welch method with Hann window. Y-axes limits have been fixed for each corresponding elevation contour (RL) plot, except for the changed y-axis scale between the two bottom plots (RL = −5 m). The corresponding period (in minutes) for a given frequency is provided at the top of the top plot.

Figure G. 10 provides the spectral outputs for the two periods of interest. The contours in the figure represent −5 m (red), −30 m (brown), −50 m (purple) and −100 m (yellow) AHD. The Burleigh probe is located within the Gold Coast embayment, at northing of approximately 6,893,000 metres. The Wooyung probe is located at northing of approximately 6,852,000 m, just north of the southern edge of the plotted spectral data. However, it is noted that the extent of the model domain is far beyond the north and south limits shown in the figures, so model boundary effects will not impact the spectral analysis.

The spectra plots corresponding to the 30-minute period component indicate an increasing amplitude towards the centre of the Gold Coast embayment with the phase plot indicating nodes on either side, which may indicate some form of standing wave associated with edge waves. In addition, some amplification is indicated offshore, between the 50 and 100 m depth contours.

The spectra plots corresponding to the 60-minute period component indicate increasing amplitude to the southern extent of the plotted data, which is supported by the spike in the −5 m Wooyung gauge spectra (Figure G. 9). In addition, the phase plot indicates a node that stretches seaward from the headland, just north of Duranbah

beach at Snapper Rocks (where the coastline turns towards the west around Snapper Rocks) that is supported by the region of minimal amplitude. Other studies have found local features such as headlands and embayments to often have nodes and resonance associated with various periods (e.g., Cortés et al., 2017).

The amplitude associated with the 98-minute period peaks through the centre of the Gold Coast embayment (Burleigh is located close to the southern tip of the highest amplitude contour) and diminishes to the south. The distribution of the maximum amplitude associated with this period also aligns well with the differences to the north and south of the Tweed, as indicated in the Hovmöller plot (Figure G. 3), which may indicate some form of resonance at this frequency for the Gold Coast continental shelf and embayment.

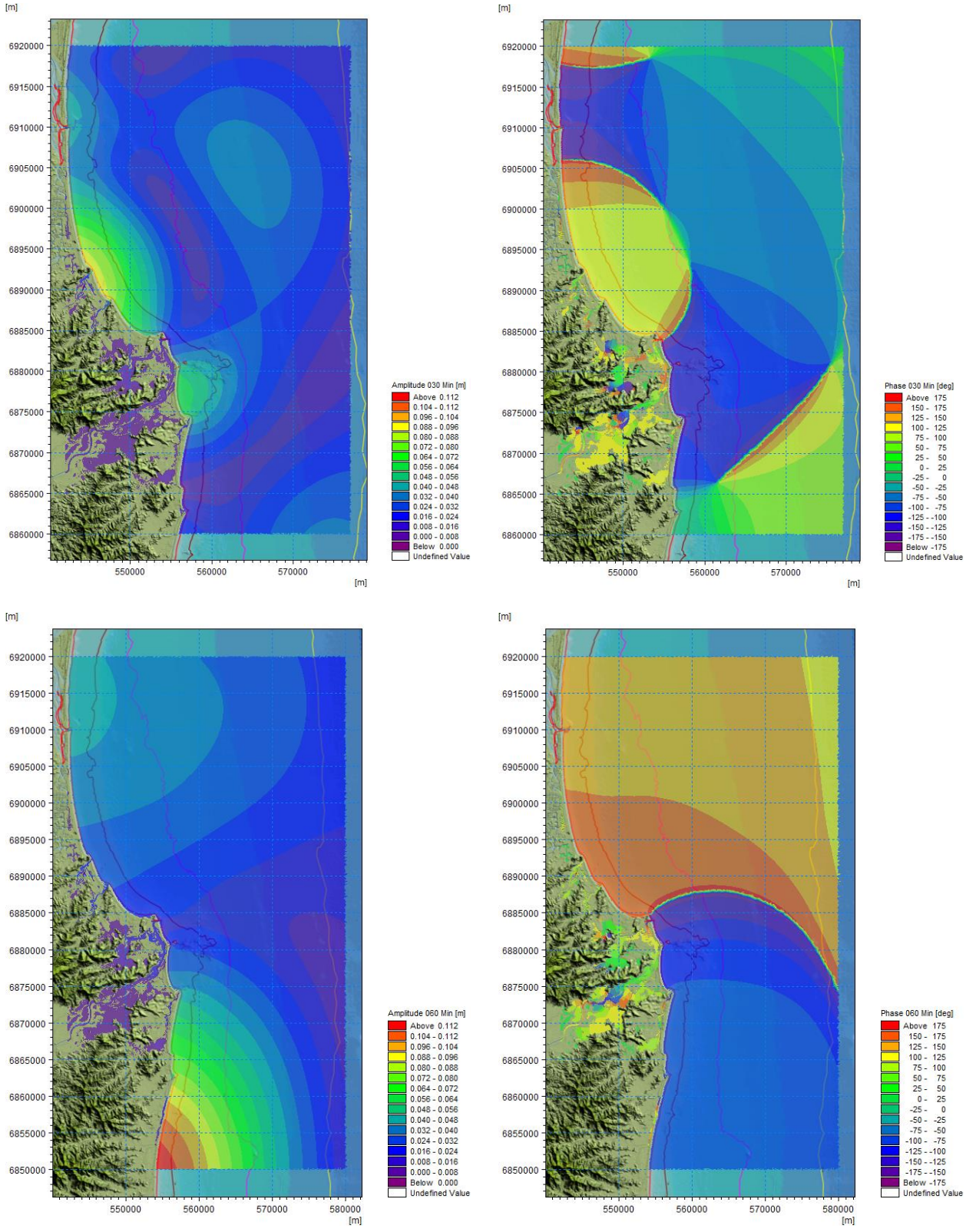

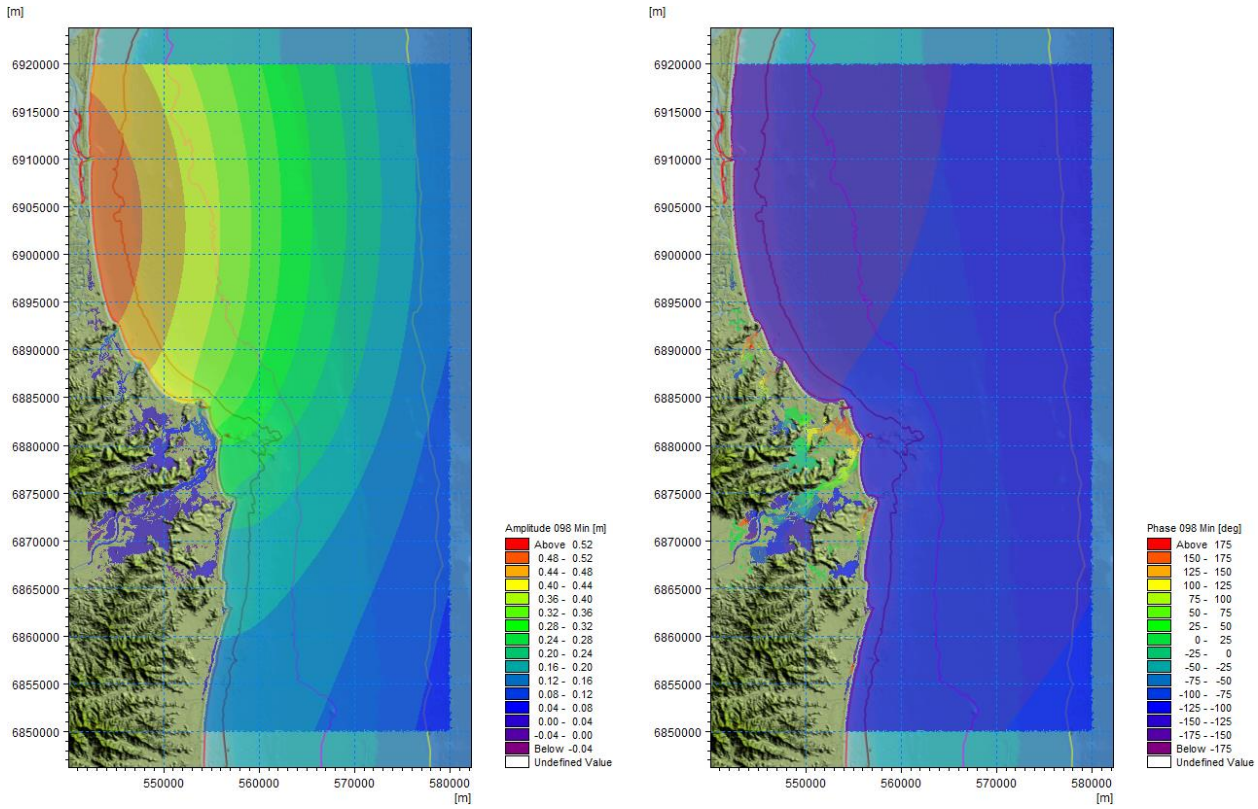

Figure G. 10 – Spectral analysis plots for SA event for the select periods T=30 min (top plots), T = 60 min (middle plots) and T = 98 minutes (bottom plots). Spectral amplitudes are provided on the left and phase is shown on the right. The duration for the spectral analysis was nine hours, between t = 17 and 26 hours.

G.2 Kermadec-Tonga Tsunami (run 78 – PTHA18 event 43313, 10,000-yr ARI at HAT)

To compare the apparent resonant response of the longer period South American tsunami waves in the previous section, the Kermadec-Tonga event was selected as it features much shorter period waves (approximately 17 minutes at 5 m depth). While there appears to be some form of demarcation in the surface elevation fluctuations near Duranbah beach, no distinct amplification over time is apparent in the extent of the Hovmöller plot (Figure G. 11). The apparent demarcation is thought to be a feature of the curved shoreline and widening continental shelf just north of Duranbah, resulting in a delayed arrival time at the gauges to the north of Duranbah Beach. Interestingly, the phase plots in Figure G. 10 indicate that, for a range of frequencies, nodes extend seawards from Snapper Rocks (~0.5 km north of Duranbah). The first crest appears to come close to the maximum amplitude; however, some local hot spots may have greater amplitudes between one to two hours after the first crest. These hot spots may be related to various resonant frequencies and interaction between the incident, reflected and edge waves.

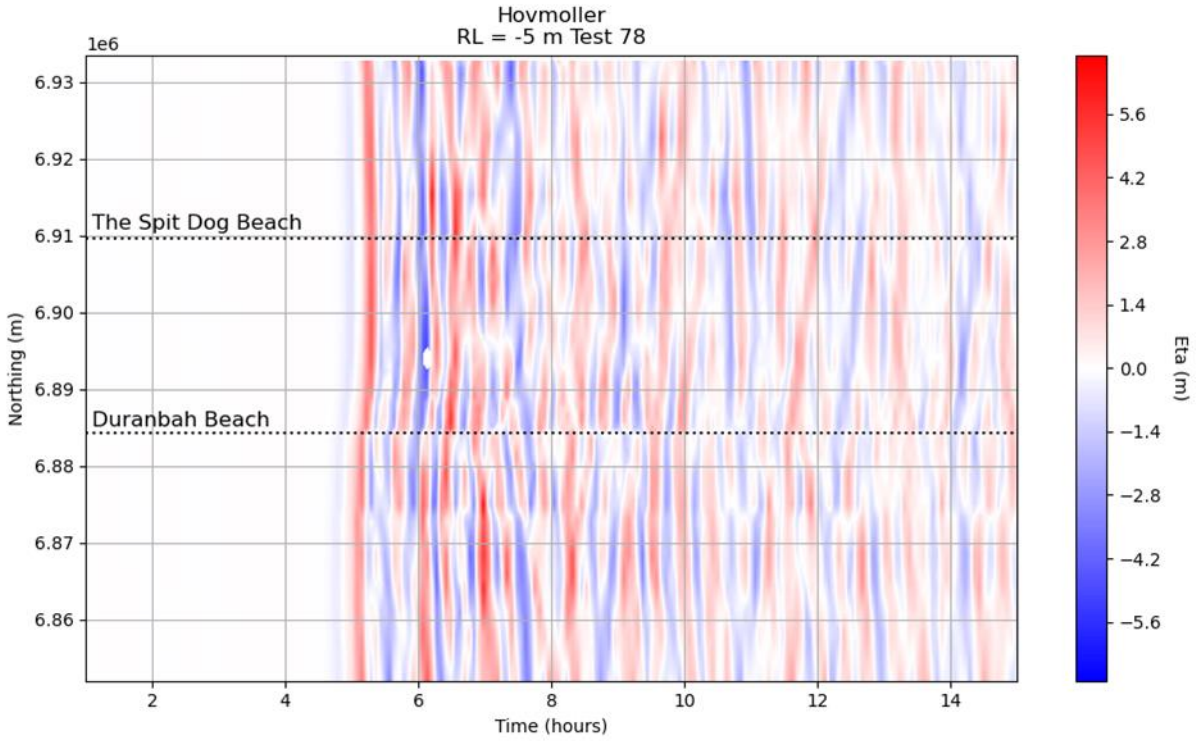

Figure G. 11 – Hovmöller plot for the RL = ~−5 m elevation contour for the Kermadec-Tonga tsunami model run 78. The northing locations for the Spit Dog Beach and Duranbah Beach are provided as geographical markers to visualise the Gold Coast embayment as well as the turning point to the NSW beaches to the south of the Tweed (Duranbah).

For comparison with the South American event above, Figure G. 12 and Figure G. 13 provide the water surface elevation (η) time series for the 8 water level gauges shown in Figure G. 4 for Burleigh Beach and Wooyung Beach transects (Figure G. 4). As shown with the Hovmöller plot above, while there are differences between the different time series at each gauge, it is less easy to visually detect any difference in trends between the gauges across the two transects. Therefore, the following Section investigates the spectral components of the gauges and the area surface elevation time series.

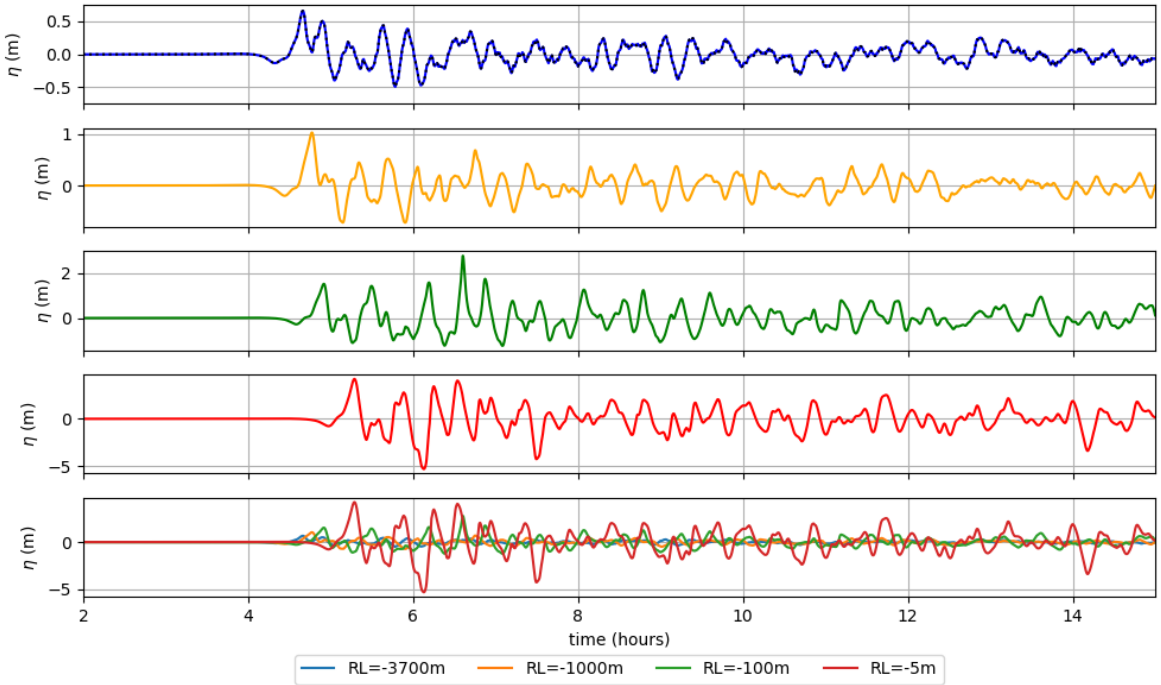

Figure G. 12 – Water surface elevation (η) time series of KDT run 78 tsunami at different depth contours for Gold Coast. Note the changing eta (y-axis) scales.

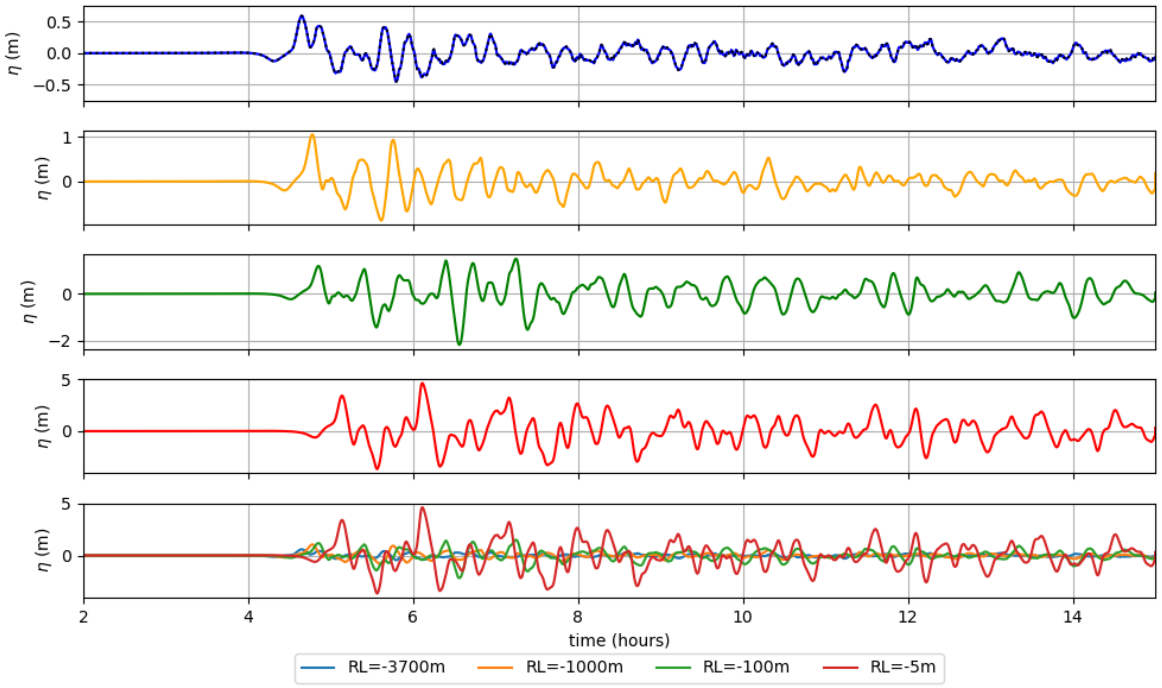

Figure G. 13 – Water surface elevation (*η*) time series of KDT run 78 tsunami at different depth contours for Wooyung. Note the changing eta (y-axis) scales.

G.2.1 Frequency Analysis of the Kermadec-Tonga run 78

The following Section presents the frequency analysis of the Kermadec-Tonga tsunami. Figure G. 14 provides the spectra for each of the eight gauges in the model domain (Figure G. 4), corresponding with the time series in Figure G. 12 and Figure G. 13. As discussed above (Figure G. 1 and Figure G. 2), and compared with the South American event presented before, the boundary time series for this event features a broader range of frequencies with a reasonably uniform energy distribution. However, some notable energy spikes occur as the tsunami propagates into shallower depths. The Burleigh gauge indicates an increase in energy around the frequency corresponding to a 98-minute period, further supporting the potential for this being a resonant frequency of the Gold Coast Embayment. Likewise, for the Wooyung probe, a distinct spike develops, corresponding to a 62-minute period, aligning well with the potential resonant configuration of the southern continental shelf. In addition to these two seemingly resonant frequencies, other notable energy spikes associated with the spectra for RL = −5m and −100 m are detailed in Table G. 1 below.

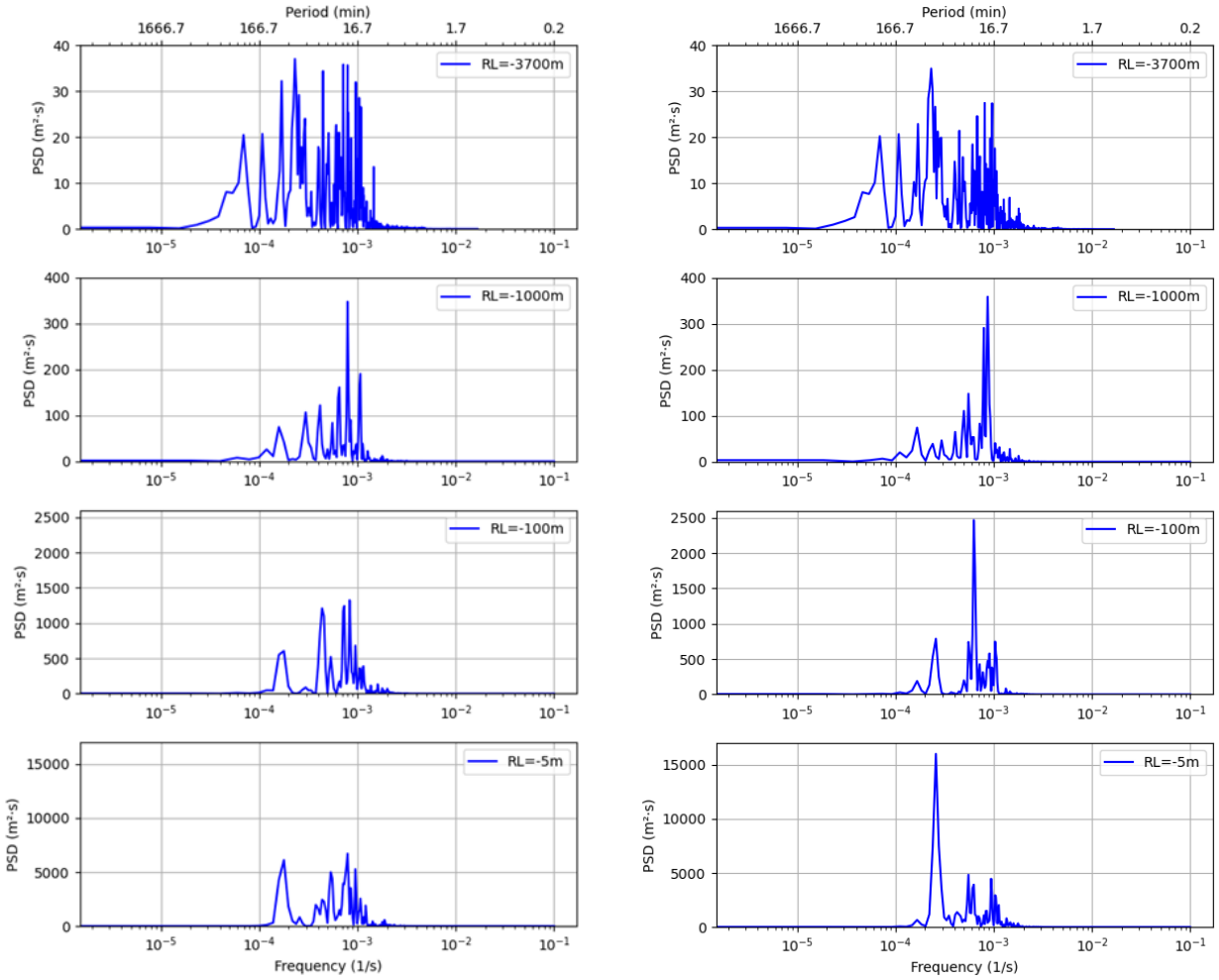

Figure G. 14 – Spectral plots for the Burleigh (Left) and Wooyung (right) Probes for KDT run 78. Welch method with Hann window. Y-axes limits have been fixed for each corresponding elevation contour (RL) plot.

Table G. 1 – Key frequencies and their respective periods associated with the point-data spectra provided in Figure G. 14. The beach and relative levels (RL) where these frequencies are dominant are detailed.

Key frequencies (Hz)	1.70E-04	2.70E-04	4.4E-04	5.4E-04	6.3E-04	7.8E-04
Associated Period (min)	98	62	38	31	26	21
Beach	Burleigh	Wooyung	Burleigh	Burleigh	Wooyung	Burleigh
RL (m MSL)	−100 and −5	−5	−100	−5	−100	−5

Figure G. 15 provides the spectral amplitude and phase plots for each frequency detailed in Table G. 1. The spectral amplitudes and phase plots for the lower frequencies associated with periods 62-minutes and 98-minutes are very similar to those indicated for the spectral plots of comparable periods from South American tsunami (Figure G. 10). The higher frequency components indicate more complex interactions between incident and reflected waves, with multiple nodes and antinodes across the continental shelf and at some locations in the longshore. The spectra corresponding to the 26-minute oscillation indicate some energy close to the RL = −100 m contour in the Wooyung transect, but very little energy in the Burleigh transect. The spectral amplitude plots support this, with lower energy and a nodal line located near Burleigh and increased amplitude away from a node to the south of the analysis region at both the shoreline and offshore over the 100 m depth contour (most easterly extent of the plotted data).

The Wooyung probe is located at northing = 6,852,000 m, further south of the plotted spectral data's southern edge. Unfortunately, this is the most southern extent (6,860,000 m N) for the model run 78 area time series. Nevertheless, general trends towards and up to the southern boundary should indicate the situation at Wooyung, which is located approximately eight kilometres south of the analysis extent.

21 minutes

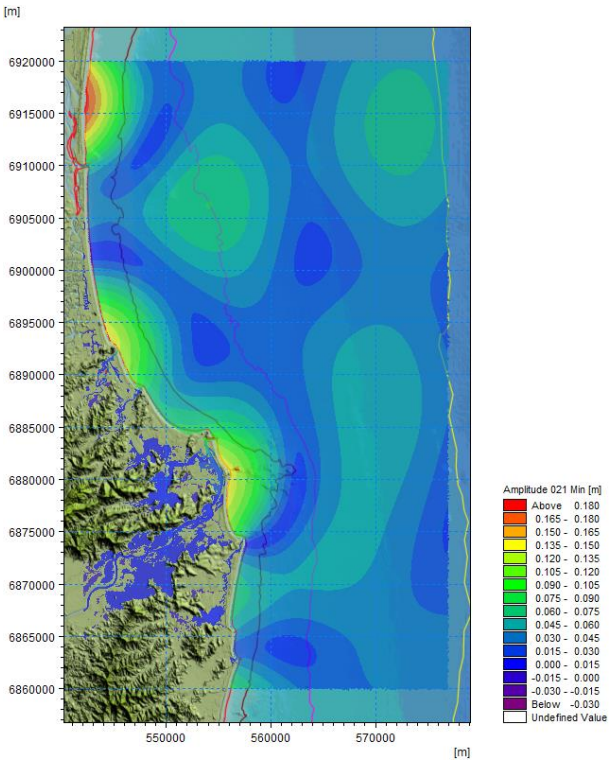

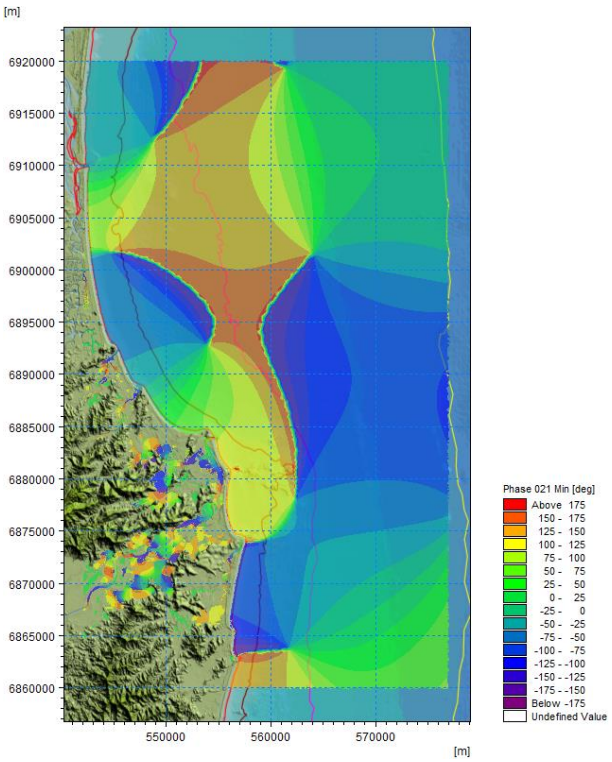

26 minutes

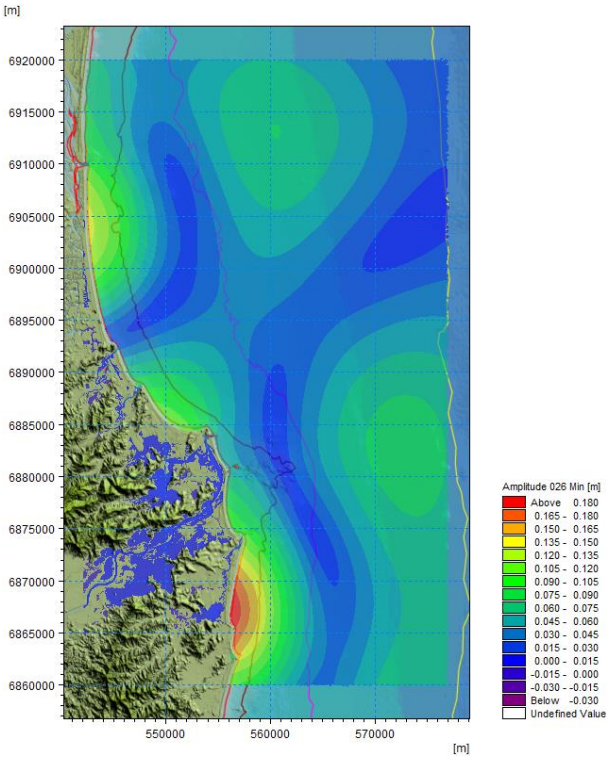

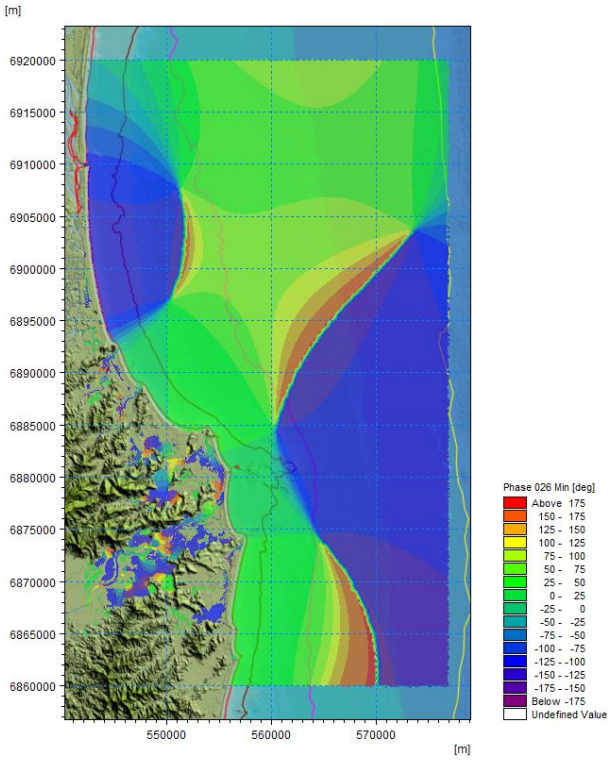

31 minutes

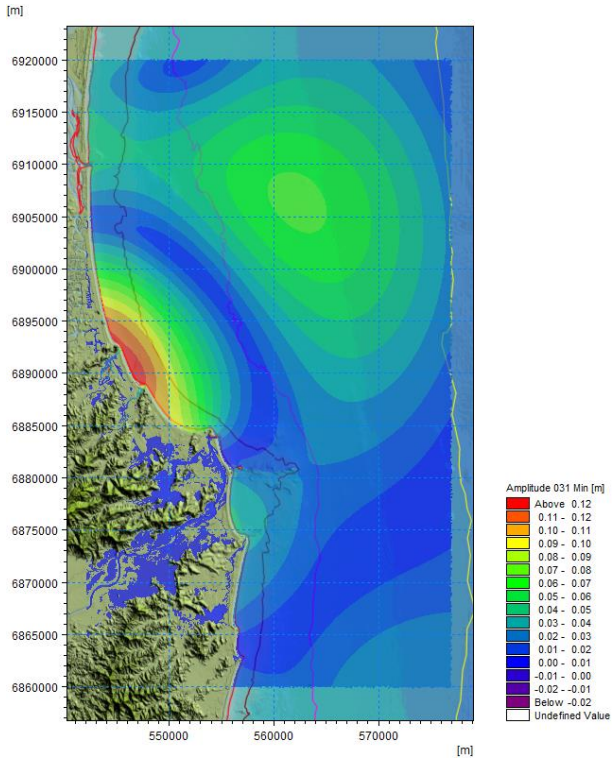

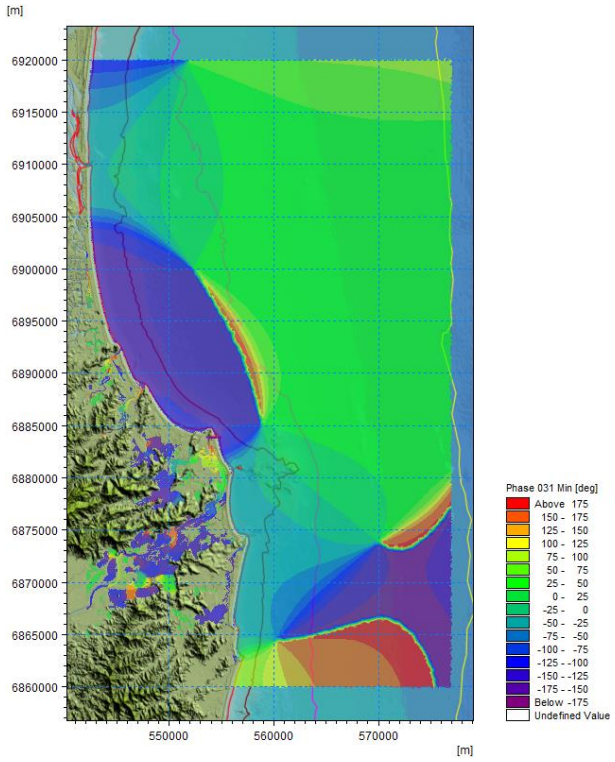

38 minutes

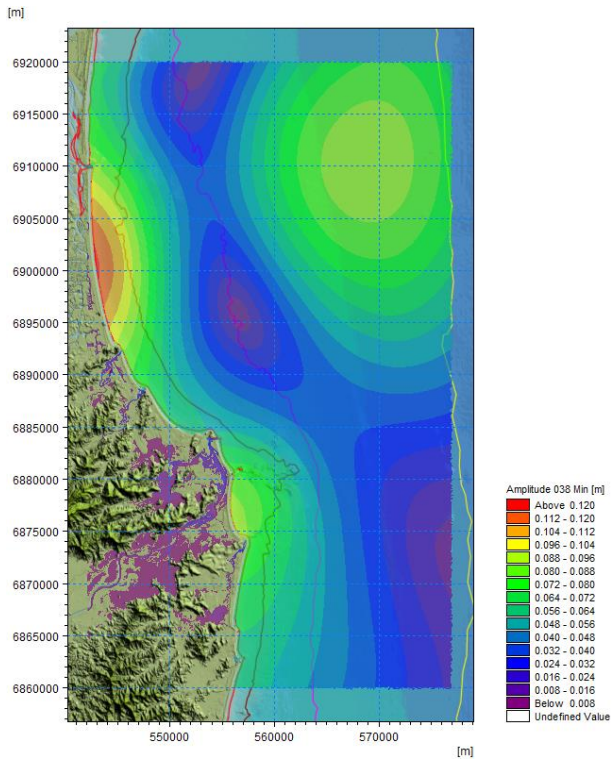

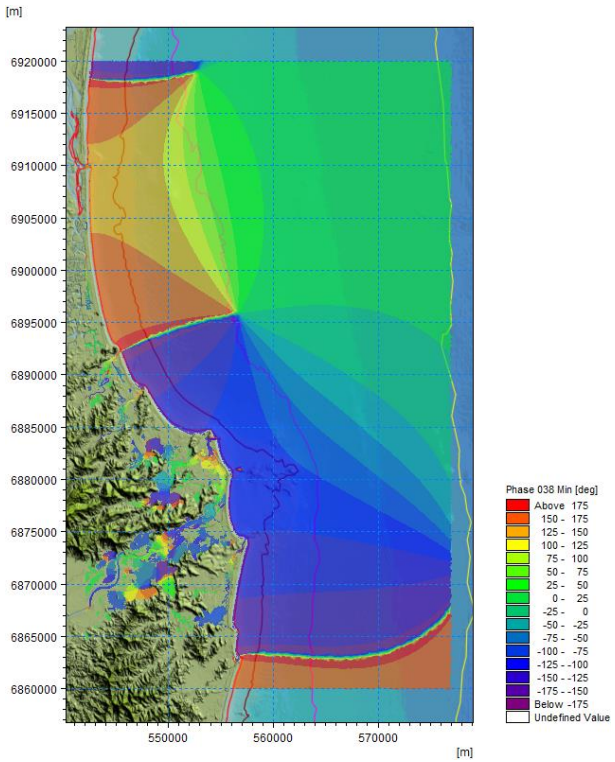

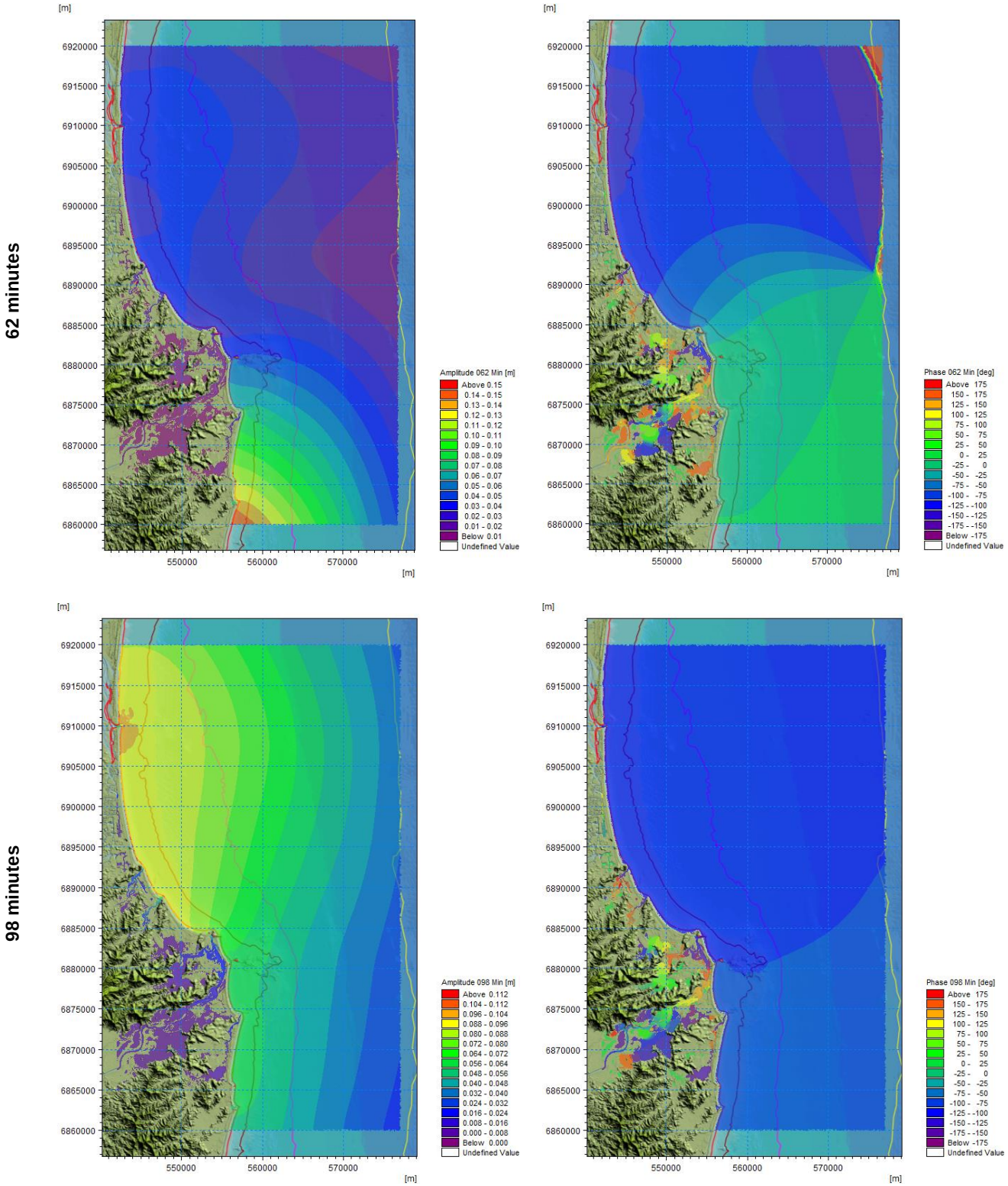

Figure G. 15 – Spectral analysis plots for the select periods (detailed to the left of each row of plots) in

. Spectral amplitudes are provided on the left and phase is shown on the right. The spectral analysis was conducted over an eight-hour duration, between t = 2 hours and t = 8 hours.

G.2.2 Tidal Analysis to Identify Possible Resonant Frequencies

Tidal analysis has been undertaken to investigate the potential for resonant effects at local sites (e.g., Rabinovich, 1997 and Cortés et al., 2017). To further investigate potential resonance at a period of 98 minutes, we performed a spectral analysis on 5 months of tidal data from 2 storm tide gauges located at the Gold Coast Seaway and Tweed Sand Bypass jetties (locations shown in Figure G. 16). Figure G. 17 presents the measured tidal stage time series for each of the gauges, recorded at 60-second intervals with a four-minute smoothing filter applied.

The corresponding spectra for each tide gauge, calculated using Welch's method with a Hann window of length 4,096, are shown in Figure G. 18; no other filtering was applied, such as lower frequencies to remove potential meteorological effects. Notably, there is a peak at around 95 minutes for both datasets, which is in line with the previously hypothesized 98-minute resonance. The data from the Seaway storm tide gauge, demonstrating the highest amplitude values at this peak, correlates well with the spatial amplitude spectra plots (Figure G. 10), showing a pronounced peak near the Seaway and a subsequent reduction at the TSB jetty in the south. Finally, two additional peaks are present at 60-, and 70-minute periods in the TSB jetty data, which correlate well with the Wooyung RL = −5 m spectra for the KDT event (Figure G. 14).

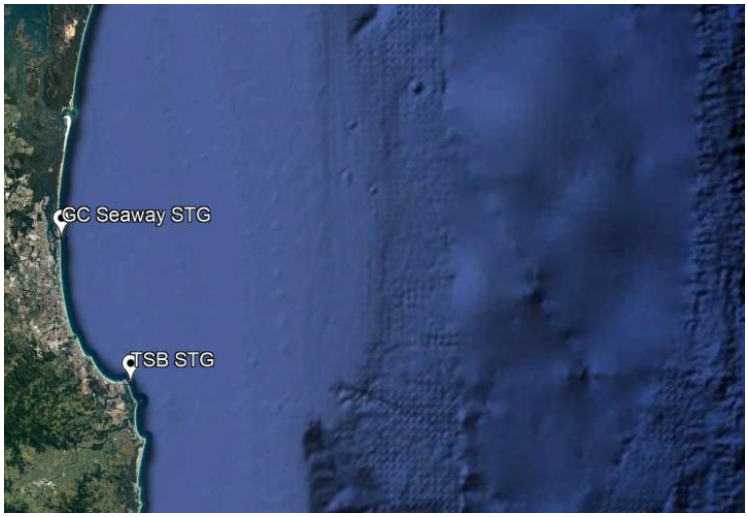

Figure G. 16 – Approximate location of the storm tide gauges for the Gold Coast Seaway and Tweed Sand Bypass jetties.

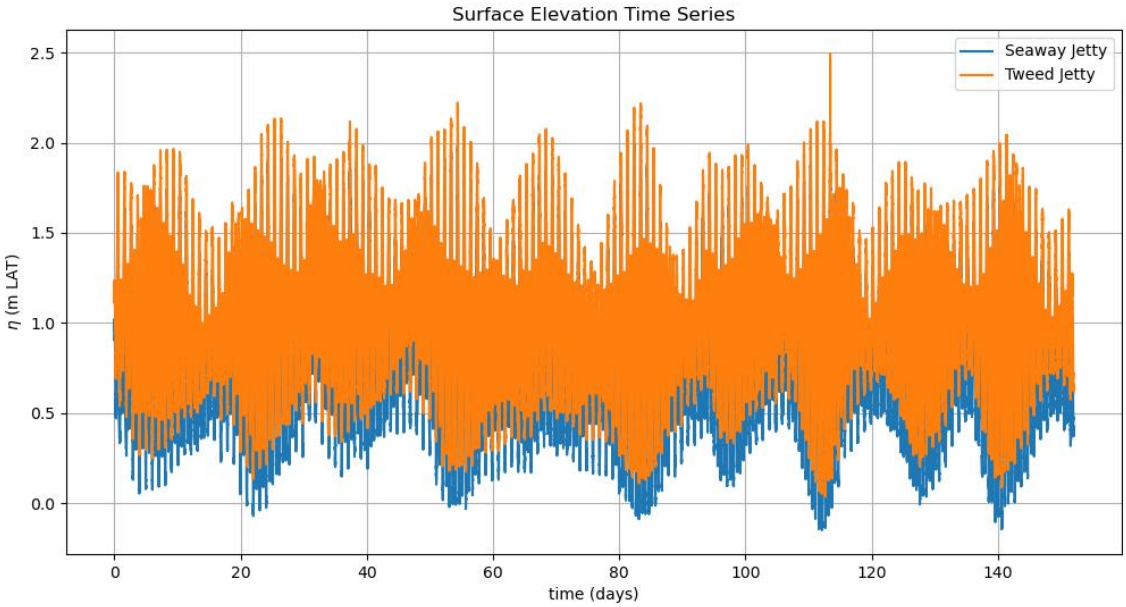

Figure G. 17 – Time series of the tidal stage data from the Gold Coast Seaway Jetty and Tweed Sand Bypass Jetty.

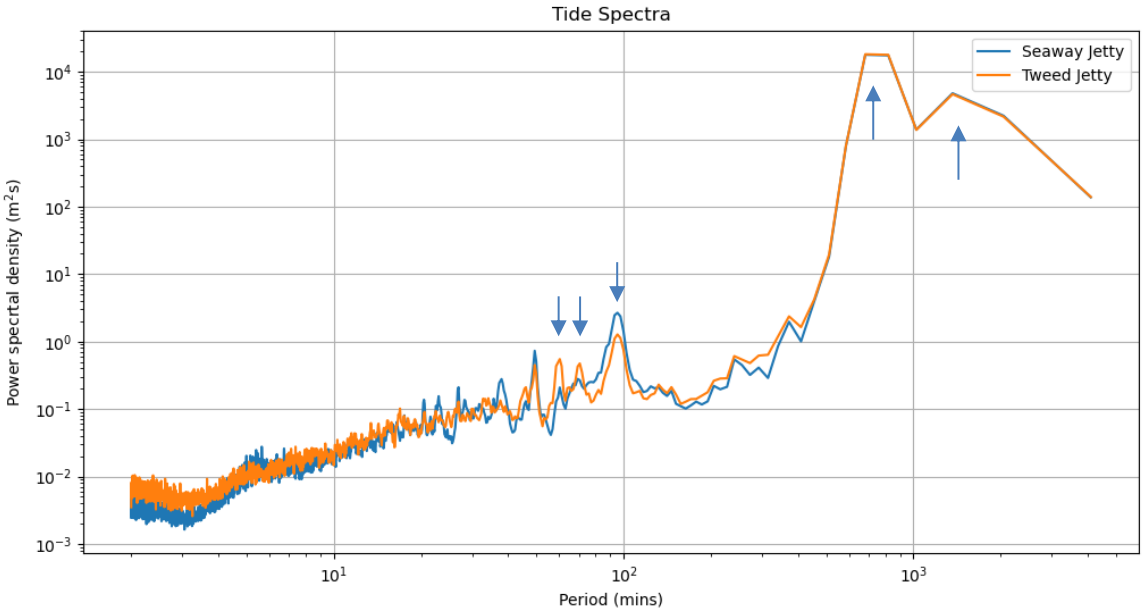

Figure G. 18 – Tidal spectra for the tidal data in Figure G. 17. Upward arrows highlight diurnal (~1440 mins) and semidiurnal (~720 mins) tidal oscillations. Downward arrows point to heightened values at higher frequencies, specifically around 95 and 50 minutes at both sites, with additional peaks at 60 and 70 minutes at the Tweed Jetty.

G.3 Empirical Orthogonal Function Analysis

G.3.1 Introduction

Empirical Orthogonal Function (EOF) analysis (also known as principal component (PC) analysis) is a statistical method used widely across the scientific community, including in the field of oceanography. EOF analysis is a helpful tool that enables extraction of significant spatial and temporal patterns from large and complex datasets. These patterns (or 'modes') can provide insight into the underlying dynamics of a system. In this section, we undertake an EOF analysis on the two datasets described in the preceding sections.

Preisendorfer (1988) provides a practical introduction to PC analysis, especially in the context of climatology and oceanography. His description of EOF analysis to real-valued scalar fields applies to the application to the surface elevation datasets considered in our analysis.

Chang and Chao (2011) carried out an EOF analysis of real-valued scalar fields, not on sea surface oscillations, but on land displacement data from Japan's GEONET an extensive, nationwide GPS network (See, for example, Sagiya, 2004). They extracted EOFs and PCs from the displacement data gathered during two weeks surrounding the 2011 Tohoku earthquake, which triggered a devastating tsunami. Their analysis allowed deeper consideration of the characteristics associated with the natural disaster.

Ren et al. (2021) conducted frequency analysis on a tsunami event, identifying potential resonances and the presence of standing waves in Hangzhou Bay and around the Zhoushan Archipelago, China. They also performed a modal analysis of various periods to detect potential eigenmodes influenced by the bathymetry of the bay. Their findings, aligning with those of Yamazaki and Cheung (2011), indicated that tsunamis containing energy aligned with dominant resonant modes can significantly extend oscillations and amplify energy over the inner shelf, extending from the shoreline to a depth of approximately 200 metres. Similarly, the region of our frequency and EOF analysis is confined to the inner shelf, focusing on depths up to 100 metres.

The following presents the EOF and PC analysis outputs from the SA (run 74) and KDT (run 78) events. This analysis aimed to identify the dominant spatial patterns (EOFs) and corresponding temporal variations (PCs) in our 2 area time series for the events discussed in the preceding section. The patterns presented represent the primary modes of variability in the data. The outputs from the EOF analysis may be considered in conjunction with the spectral analysis applied in the previous sections to consider further the potential resonance associated with the two tsunami time series being analysed.

G.3.2 EOF Analysis Results

The EOFs are ranked by the amount of variance they explain, with the first EOF (EOF1) accounting for the most variability in the dataset. The principal component time series corresponding to each EOF were also extracted, and a spectral analysis was performed to consider the dominant frequencies for each EOF and its PCs. The following provides the first four EOFs and their corresponding PC spectra to consider some potential resonant modes within the model domain.

Figure G. 19 provides the first four EOF's associated with the South America (left plots) and Kermadec-Tonga (right plots) sourced tsunami. Figure G. 20 provides PC time series and their spectra for each of the first four EOFs. Finally, Figure G. 21 provides the eigenvalue variance plots that provide an indication of the proportion of the total variance explained by each EOF. The first EOF explains the highest proportion of the variance, with each subsequent EOF explaining less and less.

The first EOF and PC for the South American tsunami further demonstrates the dominance of the 98-minute period for the Gold Coast embayment, contributing to a fraction of over 0.85 (i.e., 85 per cent) of the total variance observed. The first EOF for the Kermadec-Tonga (KDT) tsunami is more complex, with amplitude peaks located along the shoreline to the south of the Tweed, and offshore near the 50-metre depth contour in the middle of the Gold Coast embayment. The first EOF for KDT accounts for less than 40 per cent of the variance, also indicating the increased complexity of the time series. The spatial pattern aligns with a combination of the 21- to 26-minute amplitude plots associated with the spectral analysis (Figure G. 15). Thus, the spectra associated with the first PC indicates a much broader range of contributing frequencies compared with the South American PC1 spectra that has minimal energy beyond the frequency corresponding to 98-minutes.

The second EOF and associated PCs continue to indicate a dominance of the low-frequency components associated with the South American tsunami. However, the second EOF contributes to less than 10 per cent of the variance. A similar frequency range to EOF1 is present for the PC's associated with the KDT event, with a slight change in the approximate 100-minute and 26-minute periods providing the highest values. The KDT EOF plot indicates contributions to the nearshore fluctuations with a more significant portion of the variability (16 per cent) remaining with EOF2 for KDT, compared with the South American event.

For EOF3 and PC3 for the South American event, more variability is associated with the southern beaches. In this spectral analysis, the energy appears for the frequencies close to the 60-minute oscillations observed in the previous section. However, this accounts for less than 5 per cent of the variance explained. Conversely, and further demonstrating the difference between the 2 tsunamis, EOF3 for the KDT event indicates more contribution to variability in the Gold Coast embayment, again with a higher percentage variance explained compared with EOF3 for the South American event. There is a spike in the spectra around a 30-minute period for the KDT PC3 and the EOF spatial pattern in the Gold Coast embayment, which resembles the amplitude plot for the 31-minute period in the KDT spectral analysis (Figure G. 15).

For EOF4 for SA, there is a hot spot located offshore of the Gold Coast between the 50 m and 100 m depth contours that has a peak at the frequency component likely associated with a 30-minute period (see similar hot spot in Figure G. 10 for the 30-minute period plot). The variance explained is now less than 2 per cent. For the KDT event, the PCs resulting in EOF4 have their energy focussed around the 20-minute period, with the more significant hot spots located north of the spit and in the embayment south of Kingscliff and a lesser one aligned with the centre of the Gold Coast embayment (also in agreement with aspects of the T=21- and 26-minute spectral plots in the preceding section, Figure G. 15). The variance explained retains a comparatively higher value, above 5 per cent.

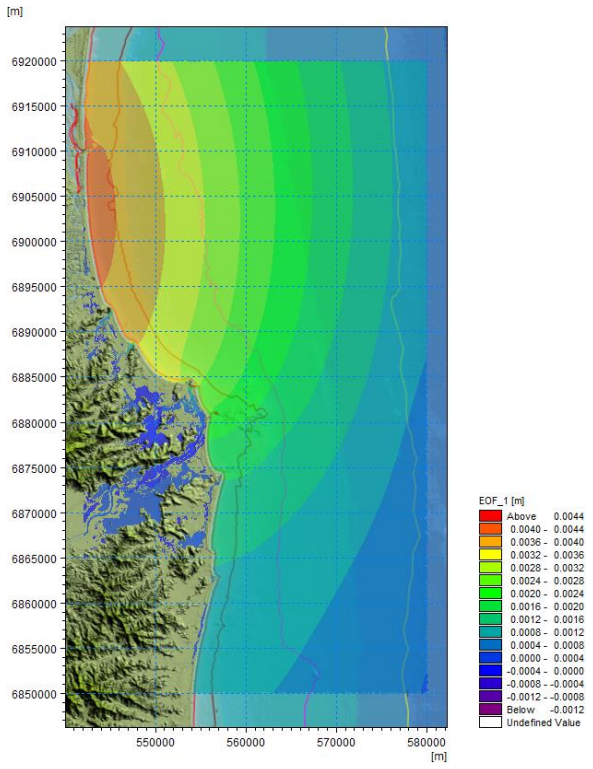
[m]
6920000
6915000
6910000
6905000
6900000
6895000
6890000
6885000
6880000
6875000
6870000
6865000
6860000
6855000
6850000
550000
560000
570000
580000
[m]
EOF_1 [m]
Above 0.0044
0.0040 - 0.0044
0.0036 - 0.0040
0.0032 - 0.0036
0.0028 - 0.0032
0.0024 - 0.0028
0.0020 - 0.0024
0.0016 - 0.0020
0.0012 - 0.0016
0.0008 - 0.0012
0.0004 - 0.0008
0.0000 - 0.0004
-0.0004 - 0.0000
-0.0008 - -0.0004
-0.0012 - -0.0008
Below -0.0012
Undefined Value

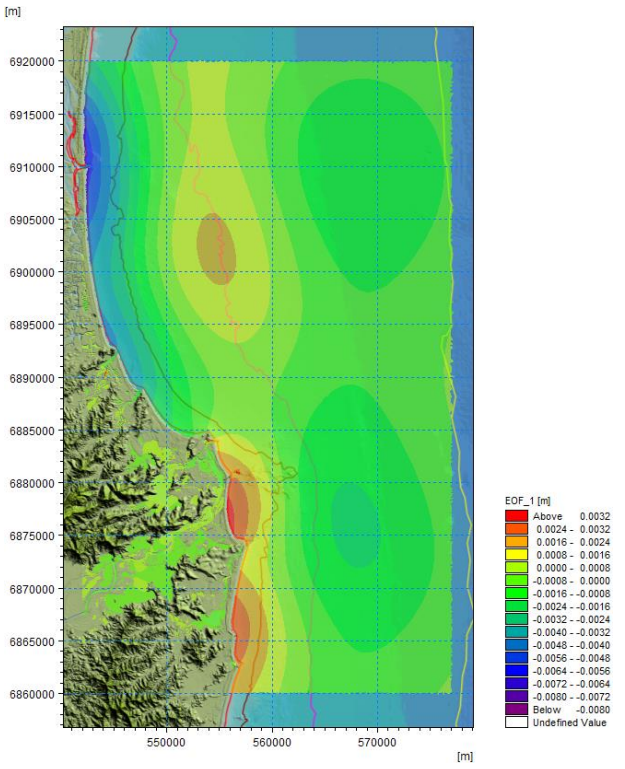
[m]
6920000
6915000
6910000
6905000
6900000
6895000
6890000
6885000
6880000
6875000
6870000
6865000
6860000
550000
560000
570000
[m]
EOF_1 [m]
Above 0.0032
0.0024 - 0.0032
0.0016 - 0.0024
0.0008 - 0.0016
0.0000 - 0.0008
-0.0008 - 0.0000
-0.0016 - -0.0008
-0.0024 - -0.0016
-0.0032 - -0.0024
-0.0040 - -0.0032
-0.0048 - -0.0040
-0.0056 - -0.0048
-0.0064 - -0.0056
-0.0072 - -0.0064
-0.0080 - -0.0072
Below -0.0080
Undefined Value

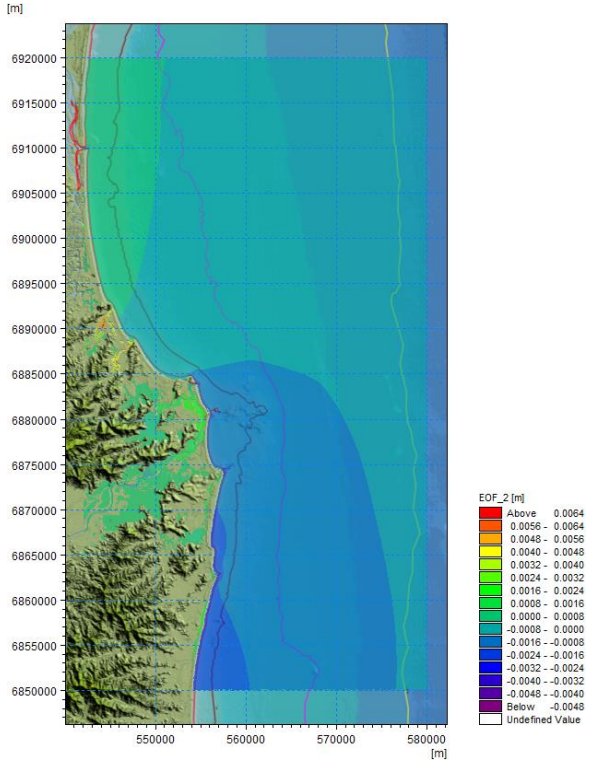
[m]
6920000
6915000
6910000
6905000
6900000
6895000
6890000
6885000
6880000
6875000
6870000
6865000
6860000
6855000
6850000
550000
560000
570000
580000
[m]
EOF_2 [m]
Above 0.0064
0.0056 - 0.0064
0.0048 - 0.0056
0.0040 - 0.0048
0.0032 - 0.0040
0.0024 - 0.0032
0.0016 - 0.0024
0.0008 - 0.0016
0.0000 - 0.0008
-0.0008 - 0.0000
-0.0016 - -0.0008
-0.0024 - -0.0016
-0.0032 - -0.0024
-0.0040 - -0.0032
-0.0048 - -0.0040
Below -0.0048
Undefined Value

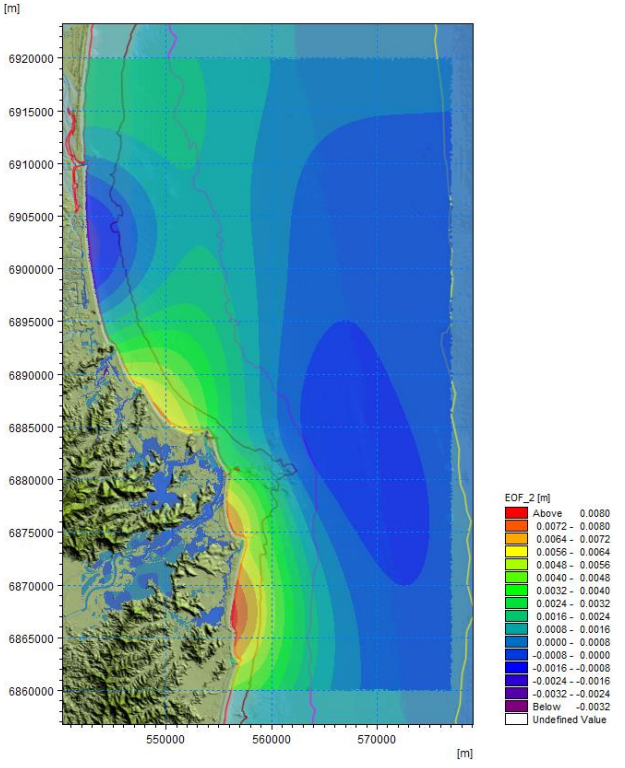
[m]
6920000
6915000
6910000
6905000
6900000
6895000
6890000
6885000
6880000
6875000
6870000
6865000
6860000
550000
560000
570000
[m]
EOF_2 [m]
Above 0.0080
0.0072 - 0.0080
0.0064 - 0.0072
0.0056 - 0.0064
0.0048 - 0.0056
0.0040 - 0.0048
0.0032 - 0.0040
0.0024 - 0.0032
0.0016 - 0.0024
0.0008 - 0.0016
0.0000 - 0.0008
-0.0008 - 0.0000
-0.0016 - -0.0008
-0.0024 - -0.0016
-0.0032 - -0.0024
Below -0.0032
Undefined Value

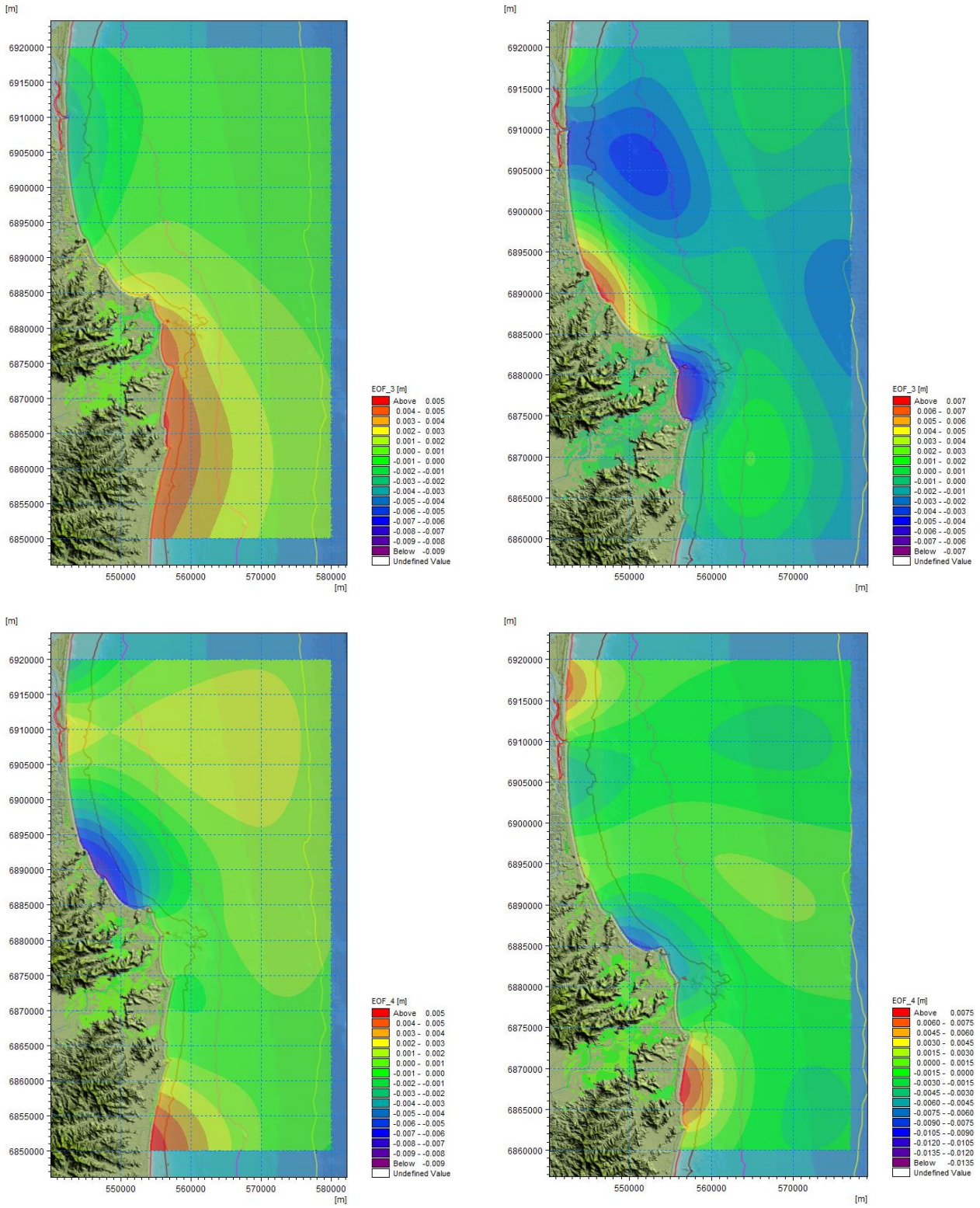

Figure G. 19 – EOF analysis outputs of the first four EOFs for the South America tsunami (left plots) and the Kermadec-Tonga tsunami (right plots).

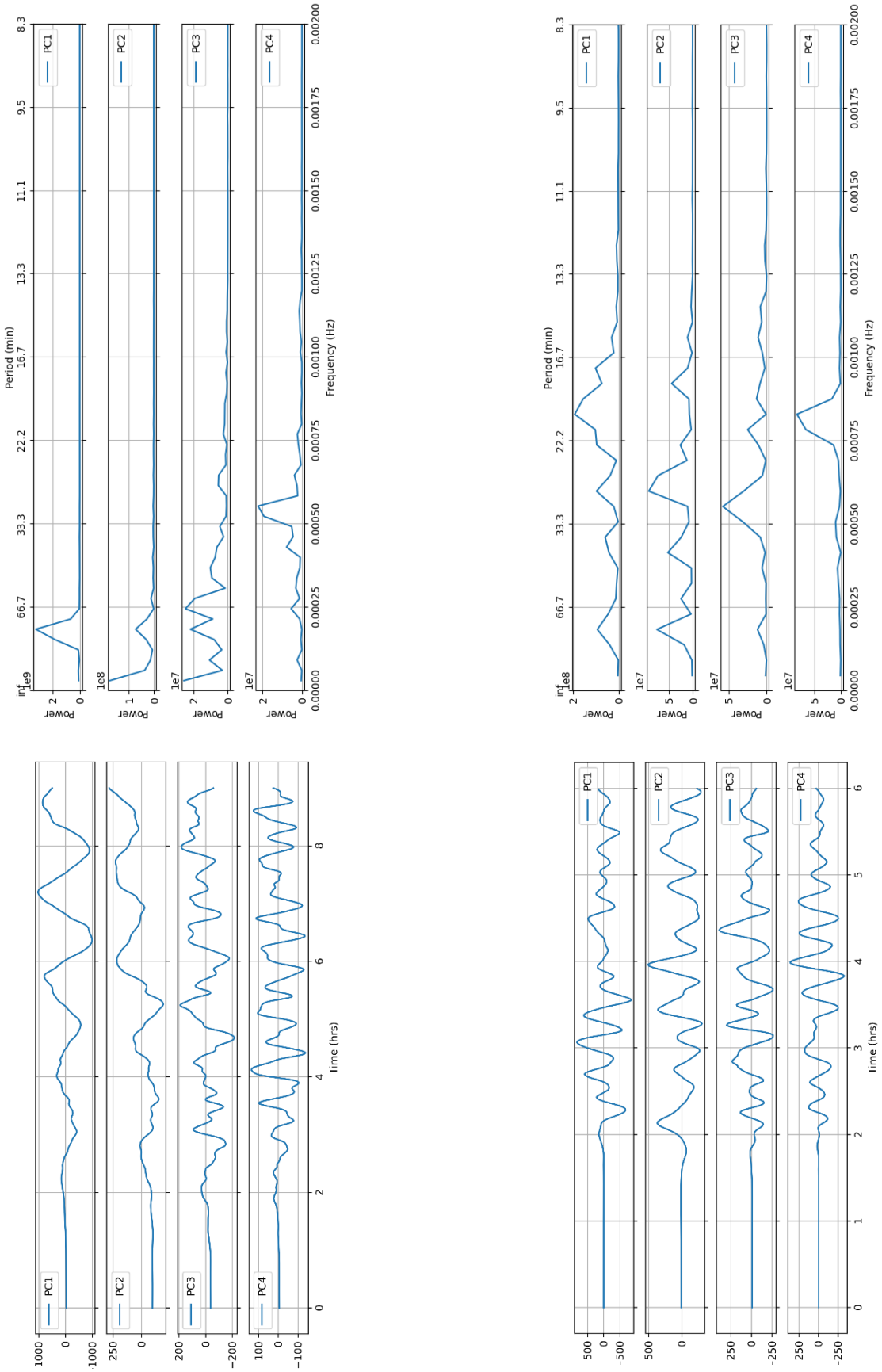

Figure G. 20 – Principal Components (PCs) and their associated spectra for each of the four EOFs for the South America (run 74, top plots) and Kermadec-Tonga (run 78, bottom plots) tsunami. The spectra x-axes have been fixed to facilitate the comparison of the frequency ranges for each PC and periods corresponding to the plotted frequency intervals are given at the top of the plot.

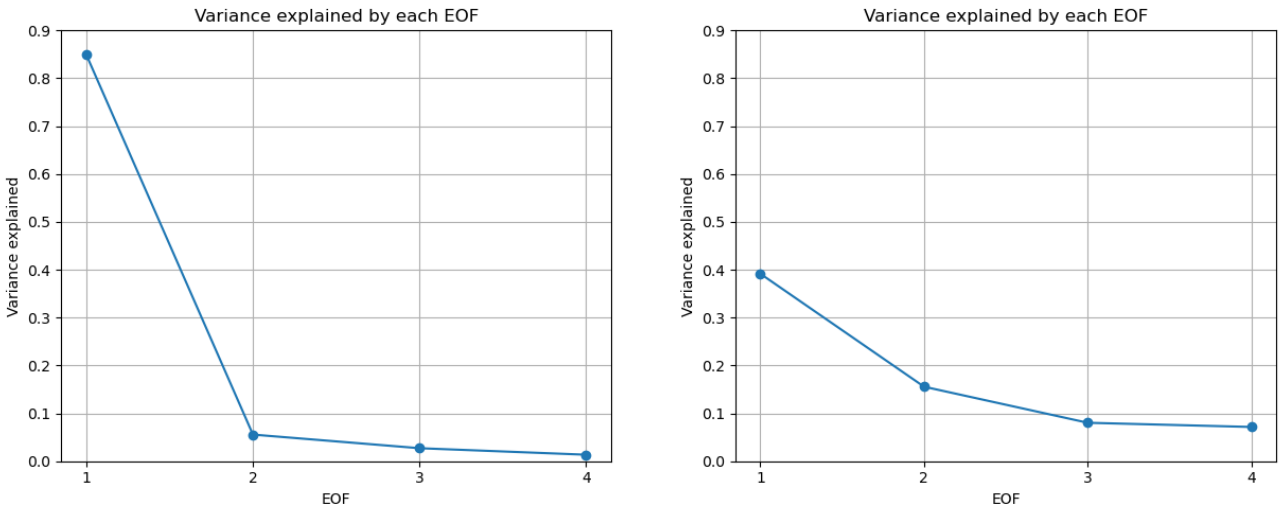

Figure G. 21 – Eigenvalue variance plots for the South American (left) and Kermadec-Tongan (right) events. The x-axis represents the EOFs or PCs and the y-axis shows the proportion of the total variance that each EOF or PC explains.

G.4 Conclusion

A simple calculation based on linear wave theory indicates that shelf resonance on the Gold Coast may occur for periods of approximately 100 minutes and 66 minutes for the narrower continental shelf in northern New South Wales. These values align with the spectral analysis undertaken for the South America event for east-west transects terminating at Burleigh and Wooyung beaches. Although the Kermadec-Tonga event exhibits much shorter wave periods than the South America event, the spectral analysis close to shore also shows a growth in energy for these frequencies. Furthermore, a spectral analysis on five months of tide gauge data was also undertaken for 2 ocean-side jetties. The spectra also featured distinct spikes around these two periods.

Therefore, it is plausible that the 98-minute period of the South America events is experiencing some shelf resonance due to the configuration of the Gold Coast embayment. This resonance may increase wave amplitude over time, particularly when excited by subsequent waves near the resonant frequency. It is worth noting, however, that this amplitude growth is not apparent in the offshore time series or the southern beaches beyond Duranbah, which suggests a localised phenomenon specific to the bathymetric conditions. The narrower shelf further south may also exhibit some resonance, though the associated periods would likely be closer to 60 minutes.
This highlights the significance of bathymetric configuration on wave behaviour, an insight that underscores the value of site-specific understanding in predicting and mitigating the potential impacts of tsunamis.

Finally, it is noted that while all South American tsunamis modelled in this study feature very similar time series with long duration periods that may be close to a resonant frequency for the Gold Coast, this analysis has relied on only a small sample of South American events. Therefore, a larger sample of events may demonstrate more variability associated with differences in slip characteristics, potentially resulting in variations in dominant frequencies.

G.5 References

Bryant, E., 2014. Tsunami: The Underrated Hazard, Third Edition, Springer, p 222.

Chang, E.T. and Chao, B.F., 2011. Co-seismic surface deformation of the 2011 off the Pacific coast of Tohoku Earthquake: Spatio-temporal EOF analysis of GPS data. *Earth, planets and space*, *63*, pp. 649–654.

Cortés, P., Catalán, P.A., Aránguiz, R. and Bellotti, G., 2017. Tsunami and shelf resonance on the northern Chile coast. *Journal of Geophysical Research: Oceans*, *122*(9), pp. 7364–7379.

Melgar, D. and Ruiz-Angulo, A., 2018. Long-lived tsunami edge waves and shelf resonance from the M8. 2 Tehuantepec earthquake. *Geophysical Research Letters*, *45*(22), pp. 12–414.

Preisendorfer, R.Ä.N.Ü., 1988. Principal component analysis in meteorology and oceanography. *Elsevier Sci. Publ.*, *17*, p. 425.

Rabinovich, A.B., 1997. Spectral analysis of tsunami waves: Separation of source and topography effects. *Journal of Geophysical Research: Oceans*, *102*(C6), pp. 12663–12676.

Ren, Z., Hou, J., Wang, P. and Wang, Y., 2021. Tsunami resonance and standing waves in Hangzhou Bay. *Physics of Fluids*, *33*(8), p.081702.

Sagiya, T., 2004. A decade of GEONET: 1994-2003 The continuous GPS observation in Japan and its impact on earthquake studies. *Earth, planets and space*, *56*(8), pp. xxix–xli.

Yamazaki, Y. and Cheung, K.F., 2011. Shelf resonance and impact of near-field tsunami generated by the 2010 Chile earthquake. *Geophysical Research Letters*, *38*(12).